24th International Scientific Conference

APPLIED MECHANICS 2023

BOOK OF ABSTRACTS

Slovak University of Technology in Bratislava
Faculty of Electrical Engineering and Information Technology

Slovak Society of Cybernetics and Informatics

Central European Association of Computational Mechanics

Piešťany, April 19th – 21st 2023, Slovakia

SCHAEFFLER

SVS FEM
Your partner in computing

TES
TEK

Topics of the conference

- dynamics
- experimental mechanics
- noise and vibrations
- multibody dynamics
- computational mechanics
- biomechanics
- fluid mechanics
- mechatronics
- strength of materials, creep, plasticity
- fracture mechanics and fatigue
- durability and reliability of engineering structures
- structural mechanic

Scientific committee

Pawel Bachorz	Pawel.Bachorz@polsl.pl	Department of Applied Mechanics, FME SUT, Gliwice (PL)
Miroslav Byrtus	mbyrtus@kme.zcu.cz	Department of Mechanics, FAS UWB, Pilsen (CZ)
Karel Frydrýšek	karel.frydrysek@vsb.cz	Department of Mechanics of Materials, VSBTUO, Ostrava (CZ)
Michal Hajžman	mhajzman@kme.zcu.cz	Department of Mechanics, FAS UWB, Pilsen (CZ)
Radim Halama	radim.halama@vsb.cz	Department of Mechanics of Materials, VSBTUO, Ostrava (CZ)
Pavel Hutař	hutar@ipm.cz	Institute of Physics of Materials AS CR, Brno (CZ)
Roland Jančo	janco@is.stuba.sk	Institute of Applied Mechanics and Mechatronics, FME STU, Bratislava (SK)
Pawel Jureczko	pawel.jureczko@polsl.pl	Department of Applied Mechanics, FME SUT, Gliwice (PL)
Vladimír Kutiš	vladimir.kutis@stuba.sk	Institute of Automotive Mechatronics, FEI STU, Bratislava (SK)
Luboš Náhlík	nahlik@ipm.cz	Institute of Physics of Materials AS CR, Brno (CZ)
Zdeněk Padovec	zdenek.padovec@fs.cvut.cz	Department of Mechanics, Biomechanics and Mechatronics, FME CTU in Prague, Prague (CZ)
Radek Sedláček	radek.sedlacek@fs.cvut.cz	Department of Mechanics, Biomechanics and Mechatronics, FME CTU in Prague, Prague (CZ)
Michal Sivčák	michal.sivcak@tul.cz	Department of Applied Mechanics, FME TUL, Liberec (CZ)
Milan Vaško	milan.vasko@fstroj.uniza.sk	Department of Applied Mechanics, FME UZ, Žilina (SK)

Series of Applied Mechanics conferences

1st conference AM 1999	March 16–18	Brno, Czech Republic
2nd conference AM 2000	April 3–6	Liberec, Czech Republic
3rd conference AM 2001	April 2–5	Nečtiny, Czech Republic
4th conference AM 2002	April 8–11	Ostrava, Czech Republic
5th conference AM 2003	March 24–27	Jaworzynka, Poland
6th conference AM 2004	March 22–25	Kočovce, Slovakia
7th conference AM 2005	March 29–April 1	Hrotovice, Czech Republic
8th conference AM 2006	April 3–5	Srní, Czech Republic
9th conference AM 2007	April 16–19	Malenovice, Czech Republic
10th conference AM 2008	April 7–10	Wisła, Poland
11th conference AM 2009	April 6–8	Smolenice, Slovakia
12th conference AM 2010	April 19–21	Jablonec nad Nisou Czech Republic
13th conference AM 2011	April 18–20	Velké Bílovice, Czech Republic
14th conference AM 2012	April 16–18	Plzeň, Czech Republic
15th conference AM 2013	April 15–18	Velké Karlovice, Czech Republic
16th conference AM 2014	April 14–16	Kraków, Poland
17th conference AM 2015	April 13–15	Kutná Hora, Czech Republic
18th conference AM 2016	April 11–13	Banská Štiavnica, Slovakia
19th conference AM 2017	April 25–27	Brno, Czech Republic
20th conference AM 2018	April 9–11	Myslovice, Czech Republic
21st conference AM 2019	April 15–17	Ostravice, Czech Republic
22nd conference AM 2021	April 22	Liberec, Czech Republic (online)
23rd conference AM 2022	April 4–6	Liblice, Czech Republic
24th conference AM 2023	**April 19–21**	**Piešťany, Slovakia**

https://am2023.sski.sk/

Table of contents

APPLIED MECHANICS 2023

Grand Hotel Sergijo, April 19th – 21st 2023
Piešťany, SLOVAKIA

APPLICATION OF MSC ADAMS IN TATRA TRUCKS A.S.

JAN BLOKEŠ[1], JAN FOJTÁŠEK[2]

Mathematical modelling enables help to understand problems, to solve problems efficiently, quickly, at low cost, and environmentally friendly. The paper is about the implementation of the multibody software MSC Adams in the development of Tatra Trucks. Equally important is the verification of the virtual mathematical model with testing. Results are shown in several examples.

KEYWORDS

Tatra, Multibody, MBS, Simulation, Verification, MSC ADAMS, Automotive

INTRODUCTION

Tatra Trucks a.s. is the third oldest automotive factory in the world. It is known for its unique chassis (see Fig. 1) which was many times verified in the most difficult races in the world such as Rallye Dakar.

The current model series are T158 Phoenix, T815-7 Force and T810 Tactic. The main industry segments are defense, construction, firefighting, mining, agriculture and more. A necessary section of the development is virtual modelling where one part is a multibody simulation.
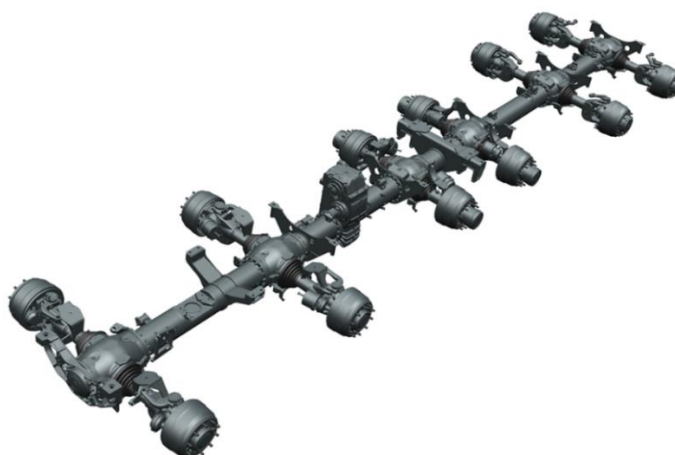
Fig. 1 Typical Tatra suspension with swing axles

[1] **Ing. Jan Blokeš,** Structural Engineer, Tatra Trucks a.s., Areál Tatry 1450/1, 742 21 Kopřivnice, Czechia. Tel +420 556 492 673. Email: jan.blokes@tatra.cz

[2] **Ing. Jan Fojtášek, Ph.D.**, Researcher, Brno University of Technology, Technicka 2896/2, 616 69 Brno, Czechia. Tel. +420 54114 2275. Email: jan.fojtasek@vutbr.cz

SUSPENSION ANALYSIS

This analysis investigates motions of the wheels and load transmission to the chassis, which is attached to the ground, see examples in Fig. 2. It is possible to perform quasi-static as well as dynamic analyses. The topology and all properties can be very easily modified. All the suspension characteristics are possible to observe using plots.

MSC Adams/Car prepared standard set of suspension and steering maneuvers such as:

- parallel wheel travel,
- opposite wheel travel,
- single wheel travel,
- steering,
- roll and vertical force,
- and others.
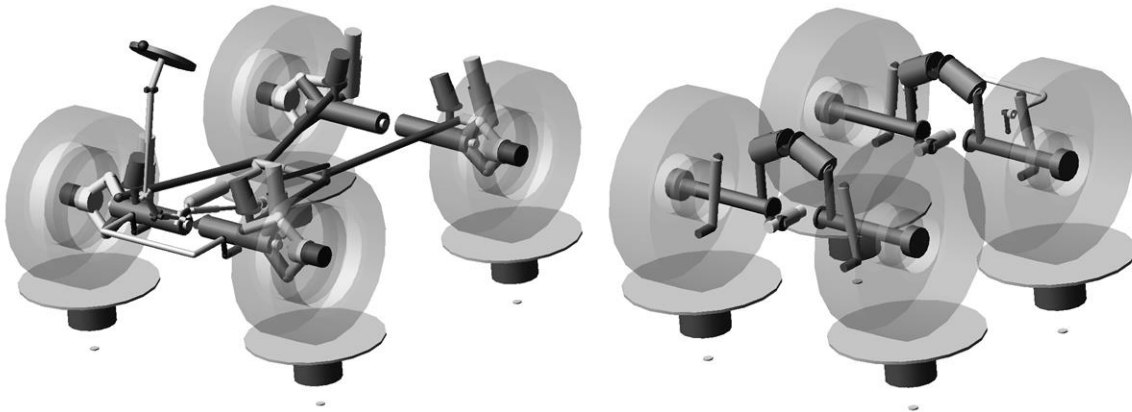
Fig. 2 Examples mathematical models of Tatra suspensions

COMPONENT ANALYSIS

Tatra Trucks development uses Component analysis in MSC Adams/Car for investigation e.g. Cabin mount or Powertrain mount as shown in Fig. 3. These parts are most often mounted flexibly to the chassis via bushings, dampers, and the like. The properties of the mounting parts are tested by test engineers and consequently inserted into the simulation software. Whole assemblies are also tested on the testing rig or directly on the car, and the results are compared to the simulations.
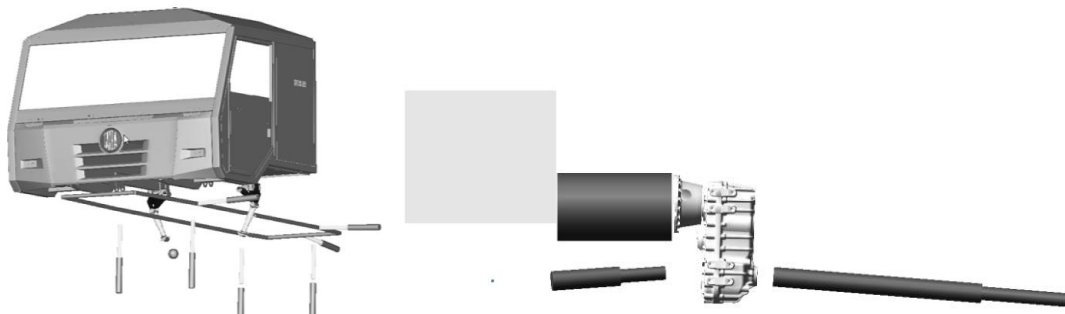
Fig. 3 Testing rig with cabin (left), powertrain assembly (right)

FULL-VEHICLE ANALYSIS

The vehicle assembly is created from so called subsystems. Example of subsystems for the simplest assembly:

- front and rear suspensions,
- powertrain,
- chassis,
- cabin,
- front and rear wheels.

The full vehicle assembly can be used either for Static Events or Dynamic Events. In Tatra, static events are used for checking mass distribution of the car and its reactions on the axles. There are also investigated reactions on the axles with the special superstructures like bridges or cranes in different positions – transport, launching and retrieval conditions. Tatra has different types of suspensions, for example air spring suspension with ride height sensors, mechanical suspension – leaf spring, coil spring, etc. All the types are implemented in the multibody software and can be simply switched.

Dynamic Events represent maneuvers like acceleration, braking, double lane change, steering and so on. Most of them are already implemented in MSC Adams/Car. For example, the parking effort maneuver was used to optimize the steering system.

ADAMS Car contents several levels of driver algorithm for complete vehicle dynamic testing. It allows user to simulate open-loop maneuvers, closed-loop maneuvers and smart driver maneuvers. By open-loop maneuvers user simply prescribe throttle position, steering wheel angle, brake pedal position, gear and clutch position in time and driver algorithm just executes these demands. Closed-loop maneuvers allows user to define velocity, longitudinal and lateral accelerations or vehicle trajectory and driver algorithm try to reach these targets [2]. The most advanced driver model called smart driver allows user to define on which percentage level should the vehicle moves during the maneuver on prescribed trajectory. Thanks to these driver models it is possible to make various simulations of predefined scenarios or user defined scenarios too. The result sets then provide very good idea of complete vehicle behavior [3].

MSC Adams car is made for inputs for the Finite Element Analysis as well. The inputs can be forces, moments, displacements, accelerations and so on.
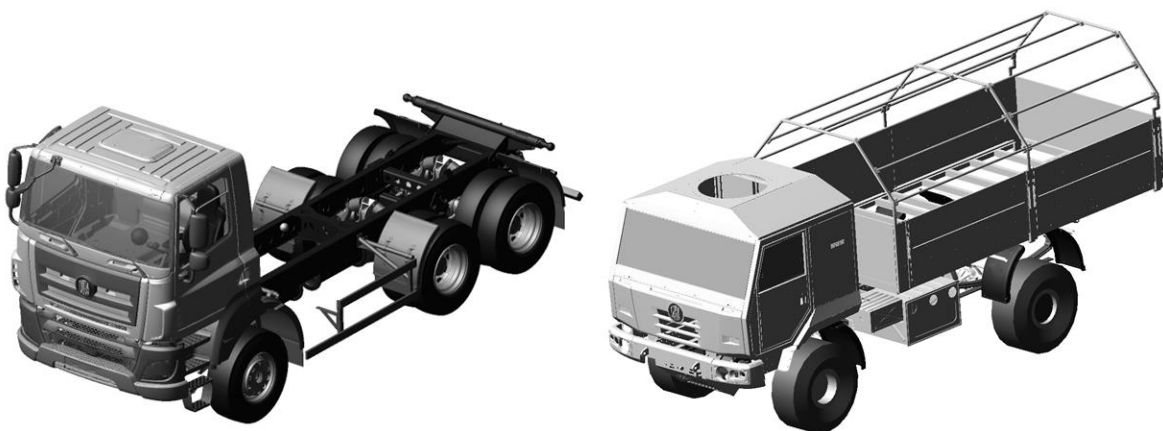
Fig. 4 Examples of full-vehicle models

PYTHON

Python is a programming language often used for data analysis. In the company Tatra Trucks is mainly used for:

- Data processing.

- Automatic evaluation of the measurements.

- Automatic models creation, simulation, and evaluation.

- Optimization – example.

The script for kinematic optimization of the steering mechanism (see Fig. 5) was created. The goal was to reduce Cardan joint error. The optimization parameters were angles of the hooke joints. The solution minimizes the objective function which is the difference between input rotational displacement and out rotational displacement. Nelder-Mead algorithm is used as the solver.
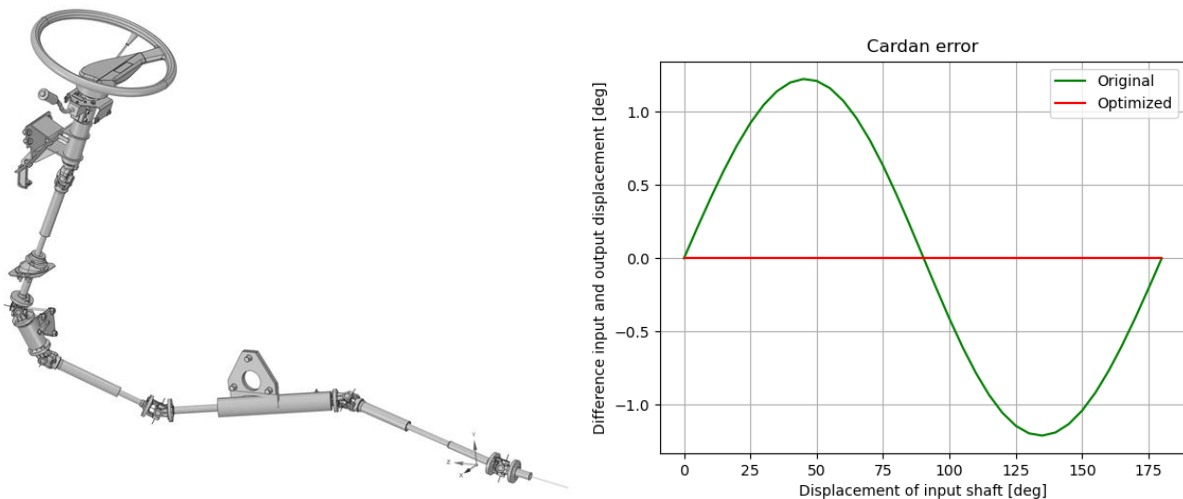
Fig. 5 Steering mechanism and result of optimization

CONCLUSION

The multibody software MSC Adams is a great support in Tatra Trucks development team. It helps to solve the complex problems of the whole car, to accelerate development of different parts, reduce weight and last but not least to reduce emissions.

ACKNOWLEDGMENT

LITERATURE

[1] MSC ADAMS MANUAL
[2] Blundel M., Harty D. The Multibody Systems Approach to Vehicle Dynamics. Elsevier Buterworth-Heinemann, Oxford, 2004.
[3] AL-TABEY, W. Study of Vehicles Handling & Riding Characteristics by Adams Software: full study of automotive handling and riding characteristics using MSC-ADAMS software. Saarbrücken, 2012. ISBN 978-3-8484-3942-3.

RESIDUAL STRESSES IN THE RAILWAY AXLES AND HOW TO DETERMINE THEM

PAVOL DLHÝ[1], PAVEL POKORNÝ[2], ONDŘEJ PETER[3], ROSTISLAV FAJKOŠ[4],
LUBOŠ NÁHLÍK[5], PAVEL HUTAŘ[6], MICHAL JAMBOR[7],

During the railway axle manufacturing process, residual stresses are induced. The residual stresses can influence the initiation and propagation of a potential fatigue crack. Therefore, it is necessary to determine residual stresses in the whole axle cross-section. Most residual stress measurement methods can measure residual stress just in a surface layer of thick samples. Therefore, a new available methodology is presented to penetrate the whole axle cross-section.

KEYWORDS

Residual stresses, railway axle, experimental measurement, finite element modelling, fatigue

INTRODUCTION

The manufacturing process of a sizable component like a railway axle is always linked with inducing residual stresses, especially when surface heat treatment is performed. Compressive residual stress benefits crack propagation by reducing fatigue crack growth or even arresting a fatigue crack. On the other hand, tensile residual stress affects crack growth negatively. It accelerates crack growth and influences the component's critical position (crack initiation position). Therefore, the neglection of the residual stress during the design process can be very dangerous for safe operation.

[1] **Ing. Pavol Dlhý, Ph.D.**, Institute of Physics of Materials of the Czech Academy of Sciences, v.v.i. Žižkova 513/22, Brno, Czech Republic. Tel +420 532 290 347. Email: dlhy@ipm.cz

[2] **Ing. Pavel Pokorný, Ph.D.**, Institute of Physics of Materials of the Czech Academy of Sciences, v.v.i. Žižkova 513/22, Brno, Czech Republic. Tel +420 532 290 362. Email: pokorny@ipm.cz

[3] **Ing. Ondřej Peter,** BONATRANS GROUP a.s., Revoluční 1234, 735 94, Bohumín, Czech Republic. Tel +420 597 082 016. Email: ondrej.peter@ghh-bonatrans.com

[4] **Ing. Rostislav Fajkoš, Ph.D.**, BONATRANS GROUP a.s., Revoluční 1234, 735 94, Bohumín, Czech Republic. Tel +420 597 082 016. Email: rostislav.fajkos@ghh-bonatrans.com

[5] **doc. Ing. Luboš Náhlík, Ph.D.**, Institute of Physics of Materials of the Czech Academy of Sciences, v.v.i. Žižkova 513/22, Brno, Czech Republic. Tel +420 532 290 358. Email: nahlik@ipm.cz

[6] **doc. Ing. Pavel Hutař, Ph.D.**, Institute of Physics of Materials of the Czech Academy of Sciences, v.v.i. Žižkova 513/22, Brno, Czech Republic. Tel +420 532 290 351. Email: hutar@ipm.cz

[7] **Ing. Michal Jambor, Ph.D.**, Institute of Physics of Materials of the Czech Academy of Sciences, v.v.i. Žižkova 513/22, Brno, Czech Republic. Tel +420 532 290 414. Email: jambor@ipm.cz

The choice of the residual stress measurement technique is a demanding process itself. Fig.1 summarizes standard residual stress measurement techniques. The choice is even more complicated in the case of the railway axle with expected high residual stress magnitudes. First of all, one needs to consider available equipment. Only surface (tens/hundreds of μm) measurement techniques, like X-ray diffraction or hole drilling, are typically available in industrial conditions. Therefore, the measurement of the whole cross-section of the railway axle is inconceivable at first moment. However, with the right manufacturing process of the specimen in combination with a numerical modelling procedure, it is possible to obtain residual stress through the whole cross-section of the axle.
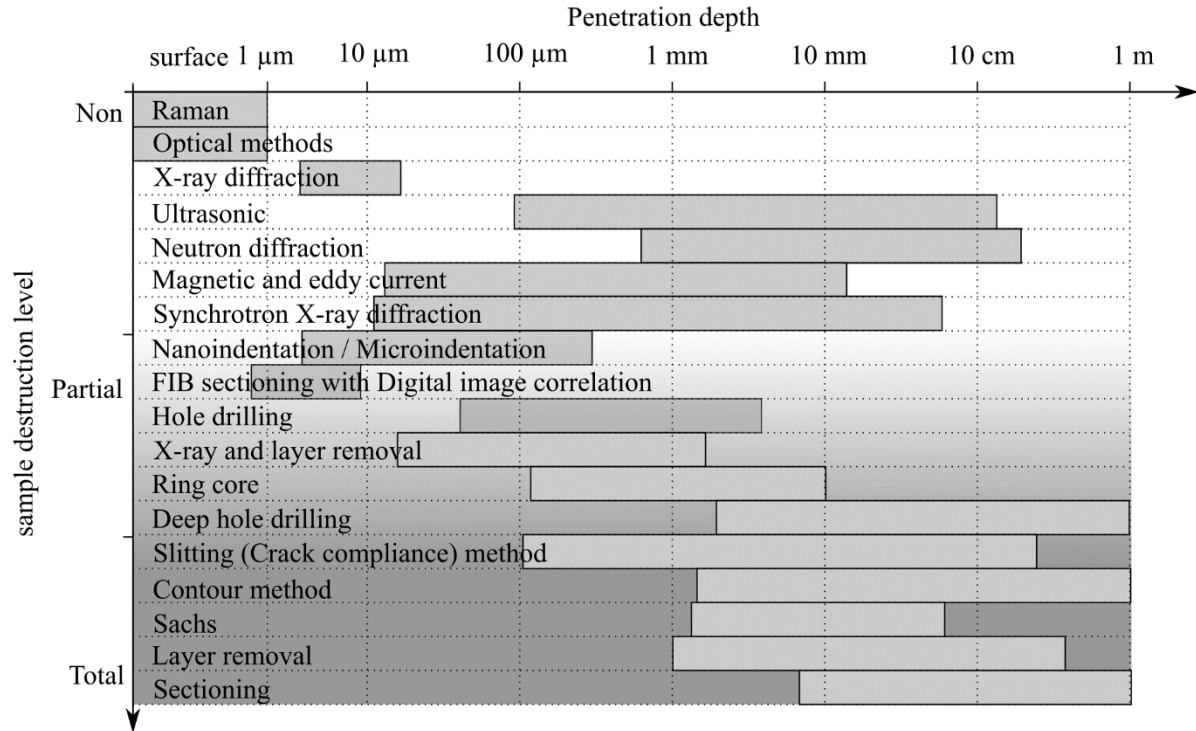
Fig. 1 Overview of different residual stress measurement techniques [1–3]

METHODOLOGY

Fig 2 shows scheme of the developed methodology. The residual stress determination procedure consists of two parts. First is the experimental part, where experimental measurements are designed considering axle geometry, free surface effects, density of measurement points, manufacturing possibilities, etc. It is necessary to manufacture the measurement sample so that it is possible to get to the free surfaces that were originally inside the axle. Then it is possible to access and measure the residual stress profile which was inside the original axle. However, this obtained residual stress profile is not the same as in the original axle. Therefore, it is necessary to determine the original profile by numerical simulations.

The second part of the developed methodology is the numerical part. A numerical model of a measured specimen is developed. The measured residual stress is used as the first input data to the model. Then equilibrium state is determined by solving the numerical model of just internal loads (residual stress). Results from the simulations are taken in the same position as measurement was performed, and results are compared with experimental values. Input data are changed according to the obtained difference. New input data are used again as residual stress input to the numerical model, the equilibrium state is determined, and results

are compared with experimental values. The process is repeated until numerical results are not similar to measured values with an acceptable error.

After the optimization process and finding the correct input data, the obtained input data is used for the original railway axle model. The final equilibrium state is again obtained by solving the numerical simulation, and the result is the determined original residual stress field.
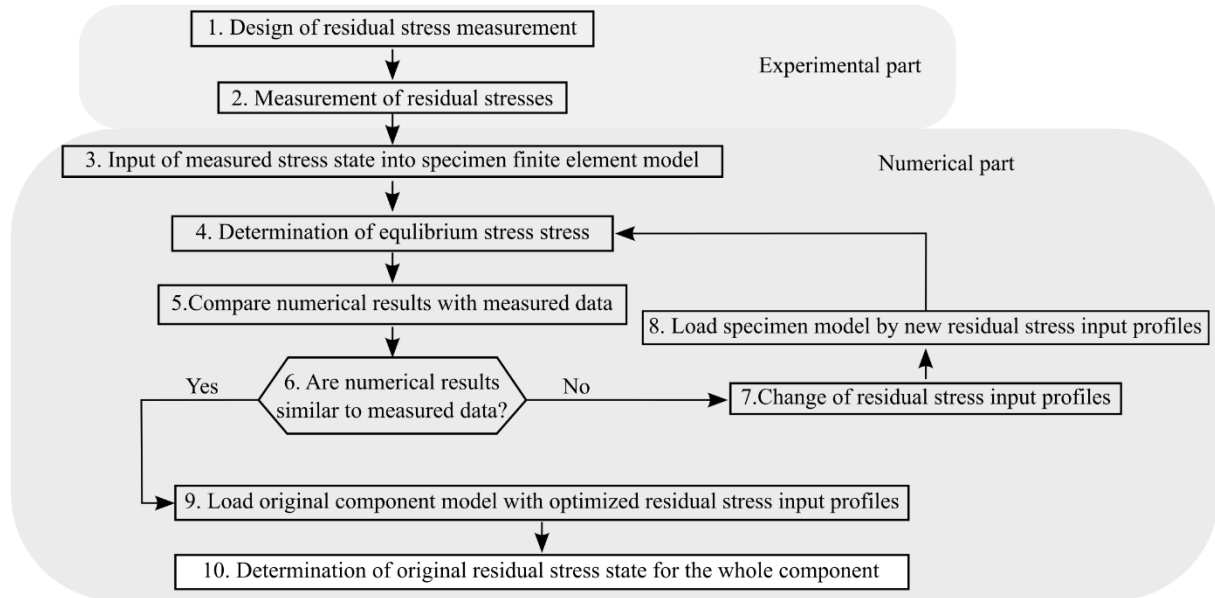
Fig. 2 Scheme of the developed optimization process of residual stresses determination in sizeable components

RESULTS

Axle from the typical railway axle steel EA4T (25CrMo4) was considered. The new developed procedure was applied to obtain residual stress field after the induction hardening manufacturing process. Two specimens were designed for one measurement to obtain all necessary data. One specimen was a thin ring with tangential and radial residual stresses (axial residual stress was released due to the free surface effect). The second specimen was a symmetrical axially cut axle segment with axial and radial residual stresses (tangential residual stress was released due to the free surface effect). Measurement was performed in the middle of specimens, from the outer to the inner original surface. Fig 3 a) and b) show numerical specimen models with the final input profile and equilibrium state, respectively. After the optimization process, the final residual stress distribution was obtained.
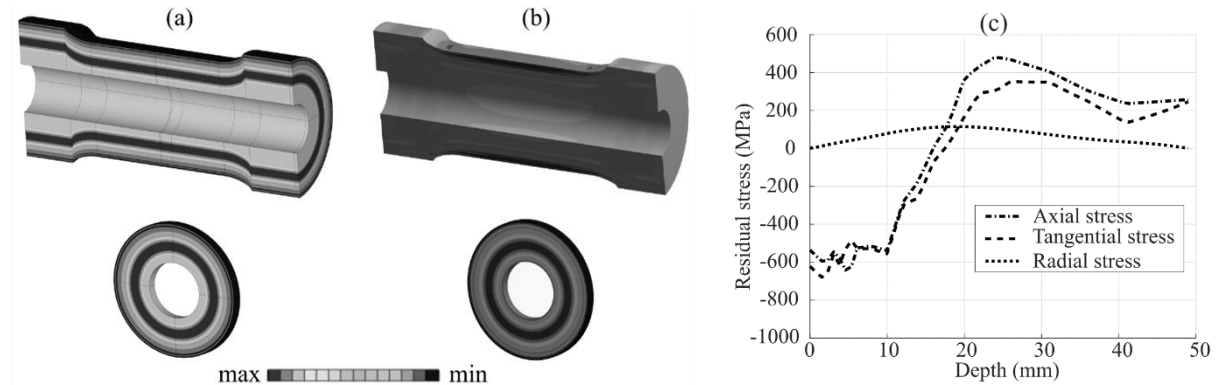
Fig. 3 a) finite element model with visualized residual stress input profile, b) finite element model with residual stress in equilibrium state, c) determined original residual stress profile

Fig 3 c) shows the determined original residual stress field distribution at the railway axle. Obtained results show the compressive axial distribution of about −600 MPa up to 10 mm depth under the surface. Then axial residual stress rises to +420 MPa in 23 mm depth under the surface. Consequently, the axial residual stress decreases gently in the rest of the cross-section. The tangential residual stress shows similar distribution as axial residual stress. The radial residual stress is an order of magnitude smaller than axial and tangential ones.

CONCLUSION

The developed methodology is suitable for residual stress determination of the railway axle. Obtained results show the compressive axial residual stress of about −600 MPa at the surface, where loading and environmental conditions are the worst. Knowledge of residual stress distribution in the whole cross-section is crucial for determining the effect of heat treatment and can be used in subsequent analyses, e.g. for determining the residual fatigue lifetime of railway axles.

ACKNOWLEDGMENT

LITERATURE

[1]   SCHAJER, Gary S. *Practical Residual Stress Measurement Methods* [online]. Chichester, UK: John Wiley & Sons, Ltd, 2013. ISBN 9781118402832. Dostupné z: doi:10.1002/9781118402832

[2]   KANDIL, F. A., J. D. LORD, A. T. FRY a P. V. GRANT. *A Review of Residual Stress Measurement Methods - A Guide to Technique Selection*. 2001.

[3]   FICQUET, Xavier, Ashley BOWMAN, Devkumar GOUDAR, Manuel KÖRNER a Ed J. KINGSTON. Measurement of bending residual stress on a hull section of a submarine. *Proceedings of the International Conference on Offshore Mechanics and Arctic Engineering - OMAE* [online]. 2012, **6**, 117–127. Dostupné z: doi:10.1115/OMAE2012-83378

SOFTWARE IMPLEMENTATION OF THE FEM VELOCITY FORMULATION INTO PRANDTL-REUSS RELATIONS FOR SOLVING ELASTOPLASTIC CONTINUUM MECHANICS PROBLEMS

BARBORA DRVÁROVÁ[1], MILAN SÁGA[2], KATARÍNA PIJÁKOVÁ[3], VLADIMÍR DEKÝŠ[4]

This paper describes the theory and software development in MATLAB for solving elastoplastic continuum mechanics problems using the finite element method (FEM). The core of the work is the incorporation of the tetrahedron element into the nonlinear analysis, which is based on a rate formulation of the solution of the equations of state. The authors consider the implementation of the physical equations for elastoplastic material behavior according to the Prandtl-Reuss theory.

KEYWORDS

plastic creep, Prandtl-Reuss equations, nonlinearity, velocity formulation

INTRODUCTION

The role of applied mechanics is to study the behavior of structures. When an external load is applied to a body, it can deform it, distinguishing between elastic and plastic deformation. We will look more closely at plastic deformation. We speak of non-linear material behavior when the interdependence between the load and the displacement of the material points is not linear. This nonlinear dependence can be caused by significant changes in the geometry of the body during loading, change in boundary conditions, non-conservative loading, and others. Continuum mechanics problems are mostly nonlinear and can be linearized. In the analysis of a compliant body, the nonlinearities can be characterized in terms of the kinematics of the deformation process and the physical/constitutive equations. According to this point of view, we can characterize geometrical nonlinearities and physical or material nonlinearities. Elasto-plastic deformation is a combination of both types of nonlinearities. In the case of large deformations, the elastic component of the deformation can be neglected, in which case we are no longer talking about elasticity and plasticity theories, but about superplasticity theory.

[1] **Ing. Barbora Drvárová,** Faculty of Mechanical Engineering, University of Žilina, Univerzitná 8215/1, 010 26, Žilina, Slovakia. Tel +421 41 513 2965. Email: barbora.drvarova@fstroj.uniza.sk

[2] **prof. Dr. Ing. Milan Sága,** Faculty of Mechanical Engineering, University of Žilina, Univerzitná 8215/1, 010 26, Žilina, Slovakia. Tel +421 41 513 2961. Email: milan.saga@fstroj.uniza.sk

[3] **Ing. Katarína Pijáková**, Faculty of Mechanical Engineering, University of Žilina, Univerzitná 8215/1, 010 26, Žilina, Slovakia. Tel +421 41 513 2965. Email: katarina.pijakova@fstroj.uniza.sk

[4] **doc. Ing. Vladimír Dekýš CSc.**, Faculty of Mechanical Engineering, University of Žilina, Univerzitná 8215/1, 010 26, Žilina, Slovakia. Tel +421 41 513 2954. Email: vladimir.dekys@fstroj.uniza.sk

PRINCIPLES OF PLASTIC CREEP THEORY

The aim of the elastic-plastic analysis of the structural state is to determine the stress, transformation, and boundaries between the elastic and plastic regions of the structure subjected to external forces throughout the loading process. In the plastic creep theory, we assume that the state of stress and strain depends on the loading history. Thus, we solve the problem in steps or as a function of time. Although the theory is more time-consuming and theoretical, it is closer to the real state. It is built into most FEA software packages. This theory is based on the following assumptions and principles: the assumption of the distribution of the total relative deformation into elastic and plastic parts. This is possible up to the value of the equivalent plastic deformation (0.02) even under the assumption of large displacements and rotations, from the Drucker condition of material stability, from the assumption of the existence of a suitable plasticity condition (criterion), from the assumption of a simplifying approximation of the tensile diagram, from the constitutive assumption on the direction of plastic deformation, from a suitable description of the loading process.

Mathematical models describing the non-linear behavior of the material using differential equations are coming to the fore. They have a control mechanism that distinguishes whether we are still in the elastic or already in the plastic region. We call these models continuous differential models.

VELOCITY SOLUTION OF THE MODEL WITH KINEMATIC STIFFENING AND MISES CRITERION

Let us introduce a modified stress vector $\boldsymbol{\sigma}_k$, defined as $\boldsymbol{\sigma_k} = \boldsymbol{\sigma} - \boldsymbol{\alpha}$, the vector $\boldsymbol{\alpha}$ in the six-dimensional stress space is the displacement vector of the hydrostatic axis of the plasticity surface. Let analogous relations hold in the space of components of the stress deviator $\mathbf{s_k} = \mathbf{s} - \boldsymbol{\beta}$, where $\boldsymbol{\beta}$ is the deviatoric stress vector $\boldsymbol{\alpha}$. The stiffening is realized by shifting the plasticity surface in the direction of the vector $d\boldsymbol{\alpha}$. The plastic loading function after the introduction of the von Misses plasticity condition has the form (1):

$$f = (\sigma_{red})_k - \sigma_K = \sqrt{\frac{3}{2} s_k^T . s_k} - \sigma_K = 0 \tag{1}$$

The direction and rate of increment of the vector $\boldsymbol{\alpha}$ and $\boldsymbol{\beta}$, respectively, need to be determined. In determining the direction of the increment and the velocity of the vector $\boldsymbol{\alpha}$ we start from Ziegler's assumption (2) that:

$$\dot{\boldsymbol{\alpha}} = \boldsymbol{H} \cdot \dot{\bar{\varepsilon}}_P \cdot \frac{\sigma_k}{\sigma_K} \tag{2}$$

Parts of the Piola-Kirchhoff stress tensor II can be found in matrix **H**. The matrix **H** comprises the Cauchy real stresses in both the total Lagrange formulation of the issue and the modified Lagrange formulation.

The same method used to generate the isotropic model's constitutive relation is employed to obtain it. We get the relation for computing the equivalent plastic strain speed by progressively evaluating and modifying the equations (3)

$$\dot{\bar{\varepsilon}}_P = \frac{3G}{\sigma_K(3G+H)} \cdot \boldsymbol{s}_k^T \cdot \dot{\boldsymbol{\varepsilon}} \tag{3}$$

Substituting relation (3) into the basic constitutive relation for σ-ε, we can write the resulting form (4) as follows:

$$\dot{\boldsymbol{\sigma}} = \boldsymbol{D}^{EP}\dot{\boldsymbol{\varepsilon}} \tag{4}$$

$$\mathbf{D}^{EP} = \mathbf{D} - \frac{9G^2}{\sigma_K^2(3G+H)} \mathbf{s}_k \cdot \mathbf{s}_k{}^T \tag{5}$$

while the $\mathbf{D}^{EP}$ elastic-plastic matrix (5) is used for the incremental stress calculation. The differential equations (4) are called the **Prandtl-Reuss equations**.

In this paper, we will discuss the rate formulation for solving the equations of state. The derivation of the rate formulation of the solution is realized from the variational principle of minimum rates of the total potential energy or minimum rates of the complementary energy of the system. To derive the velocity formulation from the principle of virtual works (for quasi-static problems), we can start from the form (6):

$$\int_V \dot{S}_{ij} \cdot \delta\dot{E}_{ij} \cdot dV - \int_A \dot{t}_i \cdot \delta\dot{u}_i \cdot dA = 0 \tag{6}$$

where S_{ij} is a member of II. Piola-Kirchhoff stress tensor, E_{ij} is a term of the Green-Lagrange ratio transformation tensor, t_i is a term for the intensity vector of external forces on the surface A, and u_i is a term for the displacement vector. Since we know the Green-Lagrange tensor, we can determine its velocity. If the Green-Lagrange tensor is (7) and its speed will be (8)

$$E_{ij} = \frac{1}{2} \cdot (u_{i/j} + u_{j/i} + u_{k/i} \cdot u_{k/j}) \tag{7}$$

$$\dot{E}_{ij} = \frac{1}{2} \cdot (\dot{u}_{i/j} + \dot{u}_{j/i} + \dot{u}_{k/i} \cdot u_{k/j} + u_{l/i} \cdot \dot{u}_{l/j} \tag{8}$$

For simplicity, we will consider infinitesimal deformations. The matrix expression between the relative strains and displacements in the FEM will be simpler, namely $\boldsymbol{\varepsilon} = \boldsymbol{B}_L \cdot \boldsymbol{u}$. Assuming the elastoplastic behavior of the material, we obtain equations of state for the unknown velocity vector of the form (9)

$$\int_V \mathbf{B}_L{}^T \cdot \mathbf{D}^{EP} \cdot \mathbf{B}_L \cdot dV \cdot \dot{\mathbf{u}} - \dot{\mathbf{f}} = \mathbf{0} \quad \Rightarrow \quad \mathbf{K(u)} \cdot \dot{\mathbf{u}} = \dot{\mathbf{f}} \tag{9}$$

In MATLAB, we created a version of the calculation program based on the theory for elastoplastic analysis. The program combines the principles of FEM, a rate formulation for solving nonlinear continuum mechanics problems, and is applied to the material nonlinearity described by the Prandtl-Reuss equations.

TESTING TASK

Fig. 1 shows the finite-element model (FEM model) that we will load. Tetrahedron 3D elements with a linear shape function were used to create the mesh. The number of elements is 1718 and the number of node points is 643. The created model is loaded with a force F(t), whose waveform can also be seen in Fig. 1.
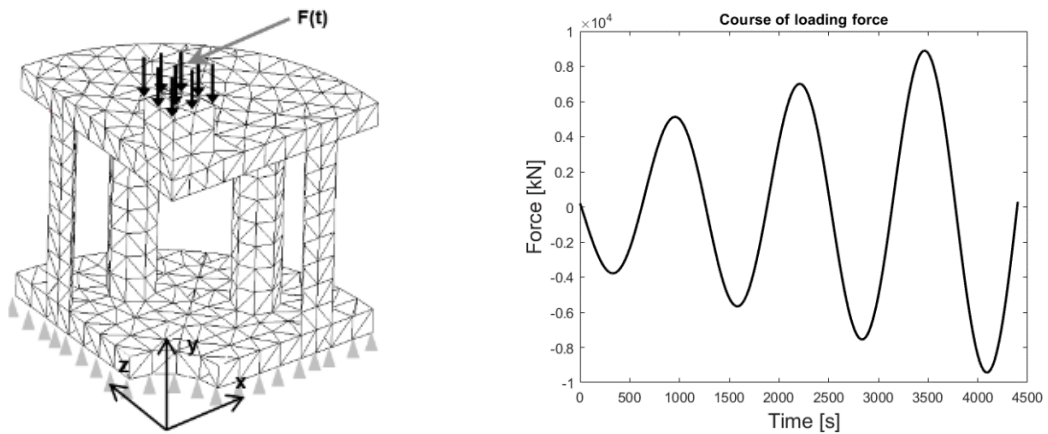
Fig. 1 FEM model and course of loading force F(t)

We have entered the material properties into the material matrix: Young's modulus of elasticity is E=200 GPa, Poisson's number $\mu=0,3$, and the yield strength R_e 280 MPa. After defining the force that loads a given body, the program processes these input data and prepares the model for the velocity solution of the nonlinear problem. The subroutine calculates the predicted values of stresses and strains along the elements. The main program then prepares this data to plot the dependencies of the stresses on the relative deformations in the elements.

Fig. 2 and Fig. 3 plot the hysteresis loops for element 58. In Fig. 2, the normal stress σ_x is plotted in grey. The normal stress σ_z is plotted in black. Fig. 3 graphically depicts the shear stresses τ_{yz} and τ_{zx} in grey and black, respectively.
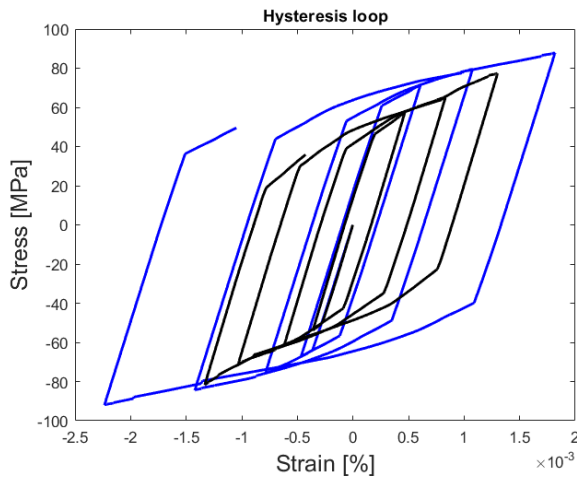
Fig. 2 Hysteresis loop for normal stress σ_x (grey) and normal stress σ_z (black)
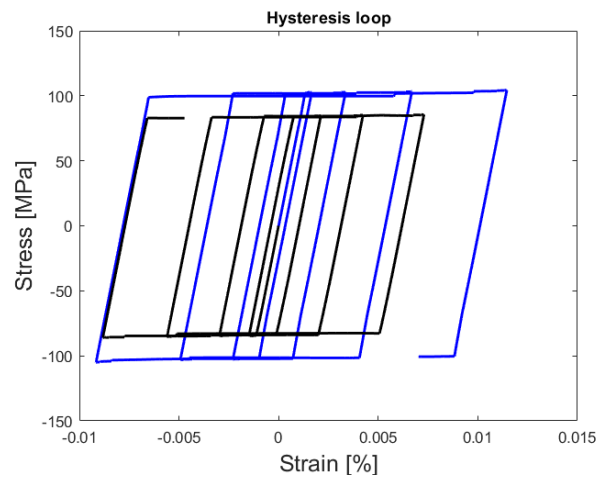
Fig. 3 Hysteresis loop for shear stresses τ_{yz} (grey) and shear stresses τ_{zx} (black)

CONCLUSION

This article was written to make the reader understand that in mechanics we deal with nonlinearities and we can reliably solve this type of problem. The article summarizes the theory of plastic creep, which is necessary to know to be able to solve the problem using the rate solution of the equations of state. A model with kinematic stiffening and the Mises criterion, from which we can determine the Prandtl-Reuss equations, is described in more detail. These equations then enter the nonlinear analysis solved in the MATLAB software environment. This problem was a test problem. The creation of the paper was motivated by the subject of computational methods of continuum mechanics and the subject of plasticity theory. The evaluation of these courses will take into account both the paper's outputs and the program's efforts. The program will hopefully be enhanced in the future to allow for the investigation of other models' dynamics and durability.

ACKNOWLEDGMENT

LITERATURE

[1] Sága, M., Vavro, J., Kopecký, M. Počítačová analýza a syntéza mechanických sústav. 1.edition. ZUSI Žilina, 2002. Ppt. 267. ISBN-13: 978-80-968605-4-8.

[2] Sága, M., Dekýš, V., Žmindák, M., Mazúr, J., Kocúr, R. Príspevok k analýze kumulácie únavového poškodenia pri viacosovom namáhaní. Acta Mechanica Slovaca, Košice 1/2006, ppt. 475 – 484. ISSN 1335-2393.

NUMERICAL MODELLING OF DRY MASONRY

MONIKA FRÉMUNDOVÁ[1], JAN PAŠEK[2]

Abstract: The article deals with the analysis of numerical modelling of a masonry wall made of dry-assembled aerated concrete blocks and a comparison of the behaviour of this numerical model with the behaviour of a real wall model. The wall model was loaded by controlled displacement. RFEM Dlubal software, based on finite element method (FEM), was used. The conclusions of these simulations will be used in the analyses of the behaviour of important historical monuments.

KEYWORDS

Dry masonry, FEM modelling, deformations

INTRODUCTION

Mortar masonry research and modelling has been researched for a long time. On the other hand, there is much less research interest in dry masonry. This type of masonry from different materials is used in modern constructions as well as in world-famous monuments.

When creating a numerical model of a masonry structure, one of the following variants according to [1] is generally used. The first variant is a micromodel, where blocks and the contact zone between them are modelled separately. This procedure is more time-consuming in terms of model creation and numerical calculation itself. The second variant is a macro model, where blocks and contact zones are replaced by a continuum. The model behaves as a homogeneous anisotropic continuum. To use this variant, it is necessary to use some of the homogenization techniques. The homogenization process is mostly based on real or numerical tests performed on a part of the structure.

NUMERICAL MODEL

RFEM Dlubal software was used for numerical simulations. Newton-Raphson method was chosen for calculation. Micromodel was chosen for the construction of wall to obtain the behaviour of individual blocks. There are mainly two approaches to modelling micromodels of masonry in RFEM. The first approach is the modelling of surfaces with the appropriate thickness and contact zones as a line release (2D model) and modelling of solids with a surface release (3D model). The second approach involves modelling the solids of all blocks, as well

---

[1] **Ing. Monika Frémundová**, Department of Mechanics, Faculty of Applied Sciences, University of West Bohemia. Univerzitní 2732/8, Pilsen, Czech Republic. Email: mfremund@kme.zcu.cz

[2] **Doc. Ing. Jan Pašek, Ph.D.**, Department of Mechanics, Faculty of Applied Sciences, University of West Bohemia. Univerzitní 2732/8, Pilsen, Czech Republic. Email: pasek@kme.zcu.cz

as modelling the solids of the contacts between blocks (only 3D model). By our own procedure, it was found that it is appropriate to choose contacts with a thickness of 1 mm with regard to the stability of the calculation [2].
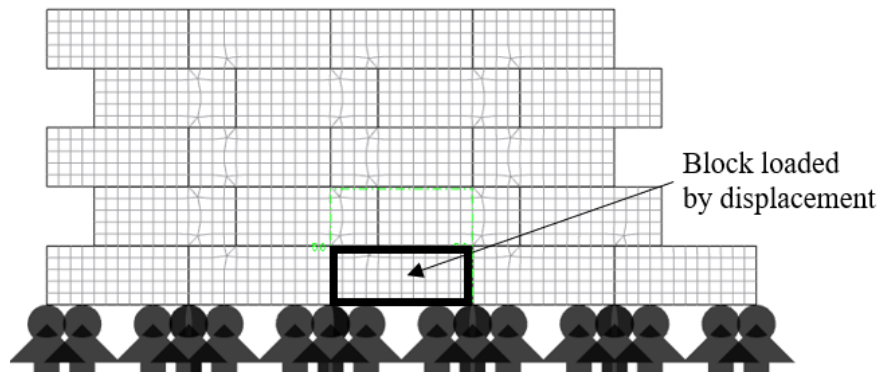
Fig. 1 Numerical model of the wall

The model of the real wall was built from aerated concrete blocks. These blocks were used to create and verify the models due to their precise dimensions. The model is based on the dimensions and properties of material obtained in situ, laboratory tests and information provided by the manufacturer. The dimension of the block is 0,599 x 0,3 x 0,249 m ± tolerance. The blocks were selected so that they were the same height in a row. The binding is about 1/3 of the length of the block Simplified, the used material was specified as an isotropic, linear elastic material. The friction between the blocks was considered by Mohr-Coulomb with the exclusion of tension in perpendicular to the surfaces. The measurement revealed a range in the values of density and horizontal friction, see Table 1. The length of the finite elements was determined to be 0,05 m in order to have 5 elements per block height. The wall model was loaded with its own weight and by controlled displacement of the representative block of 5 mm.

Tab. 1 Material properties of aerated concrete

Young's Modulus [MPa]	Poisson's Ratio [-]	Density [kN/m³]	Friction of horizontal joints [-]	Friction of vertical joints [-]
1100	0,25	5,00/4,85	0,70/0,78	0,80
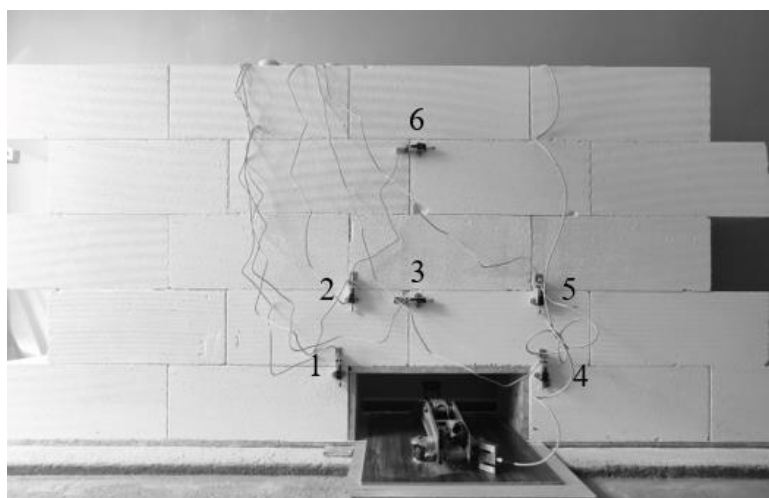
Fig. 2 Real model of the wall

22

CONCLUSION

By our own research and consultation with the software developer, it was found that the first modelling approach (2D model with line release) is limited by the size and shape of the model. The calculation did not converge and the results are not applicable. 2D modelling is less time-consuming in general and it is going to be used for more suitable shapes of masonry structures. The results of the calculations of the second approach (3D model with contacts) are applicable.

Several models with different parameters have been calculated. First, the appropriate support of the model was examined. Sliding supports with stiffness C = 15 MPa in horizontal directions (imitation of subsoil) appear to be more plausible than fixed supports. The shape of the deformation is more similar to the real experiment. Figure 3 shows the global deformation of the wall model.
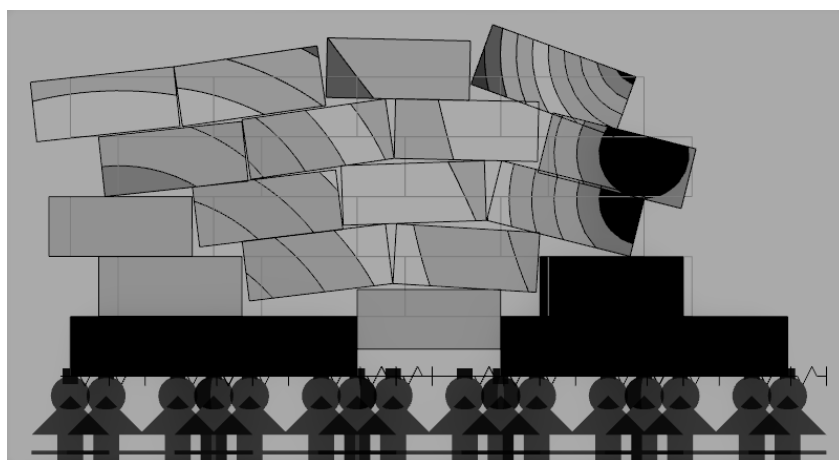
Fig. 3 Example of global deformation

Second, calculations with different friction of horizontal joints were calculated. Six shift sensors with sensitivity 0,001 mm were placed on the experimental wall viz Fig. 2. The resulting behaviour affects multiple parameters. There are differences in the deformation values in the real and numerical models viz Tab. 2.

Tab. 2 Deformation of the model

	Pos. 1	**Pos. 2**	**Pos. 3**	**Pos. 4**	**Pos. 5**	**Pos. 6**
Real model 1	4,996	4,312	3,642	4,576	0,220	5,271
Real model 2	5,004	4,261	3,674	4,679	0,235	5,403
Num. model 1	5,000	5,000	3,040	5,000	0,260	4,110
Num. model 2	5,000	5,000	2,810	5,000	0,620	4,230
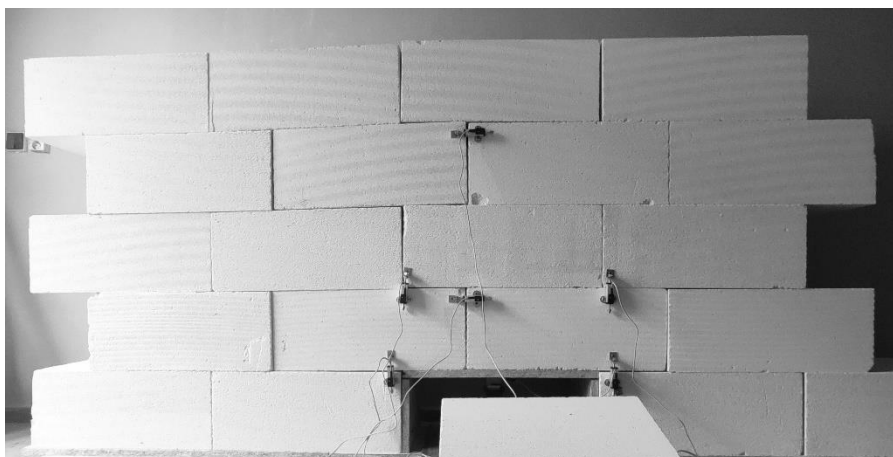
Fig. 4 Deformation of the real wall

In this article, trends in the behaviour of numerical models in comparison to a real experiment were researched and can be considered satisfactory. Nevertheless, it is necessary to optimize the simulation model and look for parameters that fundamentally affect the deformation differences. These numerical simulations are preparation for the future modelling larger models, such as the constructions of the Archaeological park Angkor.

Fig. 5 Structures of medieval monuments in Angkor *(author: Jan Pašek)*

ACKNOWLEDGMENT

LITERATURE

[1] Lorenço, P. B. Computational strategies for masonry structures. Ph.D. Dissertation, Delft University of Technology, Delft, 1996. ISBN 90-407-1221-2.

[2] Frémundová, M. Numerická simulace chování konstrukcí kamenných chrámů v archeologickém parku Angkor, Kambodža. 22. odborná konference doktorského studia, JUNIORSTAV 2020, Brno. ISBN 978-80-86433-73-8.

EXPERIMENTAL MEASUREMENTS OF NYLON COIL SPRING THERMAL PROPERTIES

GABRIEL GÁLIK[1], TIBOR SEDLAR[1], VLADIMÍR GOGA[1], MICHAL ULIČNÝ[1] AND JUSTÍN MURÍN[1]

Nylon coil springs are thermally controlled linear actuators. They have a perspective application as artificial muscles. This article describes thermal experiments that were conducted on samples to determine thermal properties of these coiled springs. The experiments were performed in a temperature regulated environmental chamber. Measurements correctly shown negative value for the coefficient of apparent thermal expansion The results of these experiments will be used to validate numerical models.

KEYWORDS

artificial muscle, nylon, actuator, coiled spring

INTRODUCTION

The following article describes experiments performed on a Coiled Nylon Spring Actuator. These soft actuators (also called Artificial muscles) which are suitable to realize smooth and soft motion in machines and robots are also referred to as Twisted-Polymeric-Fibre Actuators (TPFA) [1]. These actuators are fabricated by twisting nylon fibres into a helical state and in the finished form look like preloaded tensile springs. The working principle of such an actuator is governed by its temperature. Increasing the temperature of the nylon coils causes the loaded spring to contract. Actuator heating can be realized by multiple different methods e.g. hot air flow, heated water/fluid bypass or electric Joule heating. The advantages of these actuators are simple and cheap production, compactness, simplicity and relatively small mass.

EXPERIMENT SETUP

A thermal experiment to obtain kt was performed on newly wound springs. Six springs were wound from one material (brand). The nylon fiber [2] was 0.6 mm thick and was wound using a 500g mass.

Base coil parameters:

- Fiber thickness 0.6mm
- Coil spring length at rest 75mm
- Wound with 500g weight

---

[1] Faculty of Electrical Engineering and Information Technology, Slovak University of Technology in Bratislava, Institute of Automotive Mechatronics, Ilkovičova 3, 81219 Bratislava, Slovak Republic

Initially, the basic parameters of the springs were determined using a tensile test. These tests were used to determine the spring constant k and the preload F_0. Tensile tests were performed at an ambient temperature of 25C.
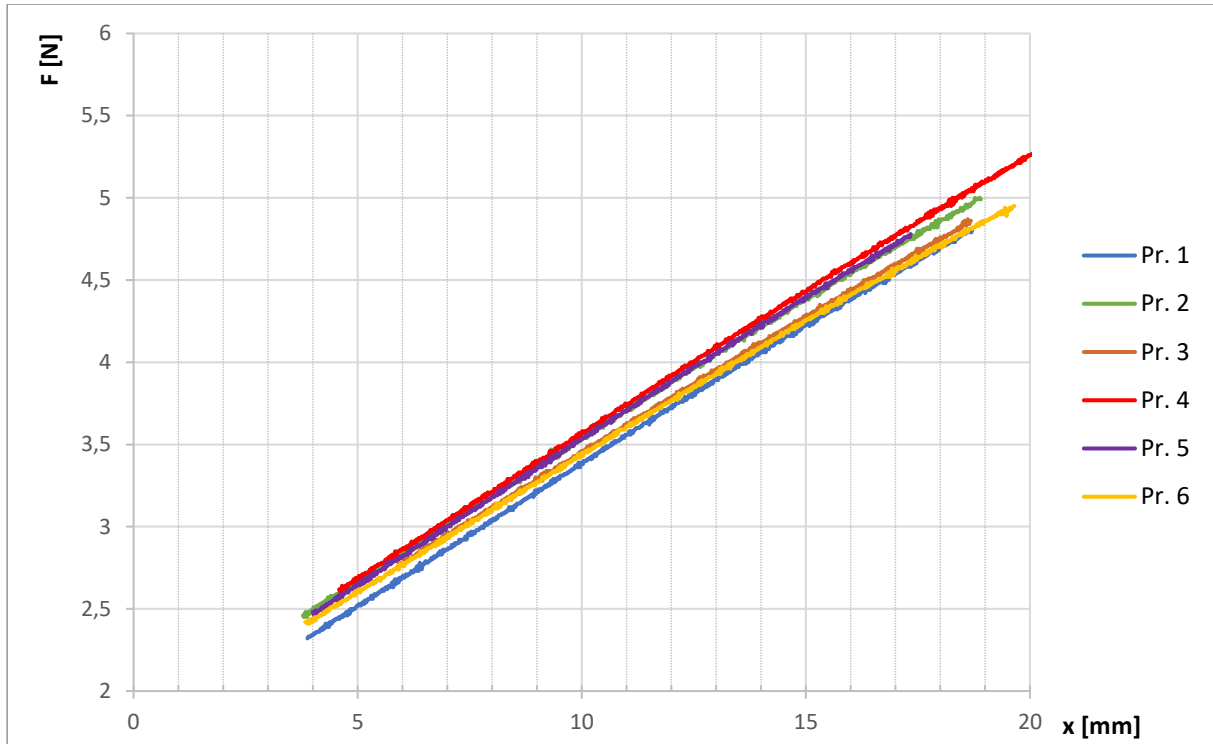
Fig. 1 The linear area of the springs determined from the tensile test.

Fig. 1 shows individual measured dependences of tensile force and spring deformation. From this linear part, the basic spring parameters were determined using the relation

$$F = kx + F_0$$

Tab. 1 Spring parameters for thermal analysis

Spring no.	k [N/m]	F_0 [N]
1	164.3	1.806
2	170.7	1.854
3	162.2	1.805
4	169.2	1.834
5	174.0	1.783
6	168.7	1.686

Mean values of parameters:

- k = 168.2 N/m
- F0 = 1.795 N

THERMAL EXPERIMENT

The next step of the experiment was to determine the response of the springs to a change in temperature. This measurement was performed using a thermostatic chamber where the springs were heated cyclically.

Thermal conditions during the experiment:

- Ambient temperature T_0 = 20C

- Maximum temperature T_1 = 53C

- The temperature of the springs periodically changed between T_0 and T_1, i.e. ΔT = 33C

- Temperature equilibrium was always reached when the temperature changed, each temperature changes lasted min. 20 min to reach a steady temperature of the springs.

Mechanical conditions during experiment:

- The springs were hung vertically.

- They were loaded in tension with a constant axial force of mass m_1=300g and m_2=410g

To reach the working point of the spring, it was necessary to overcome several load cycles. The response of the springs to load cycles is shown in the following graphs.
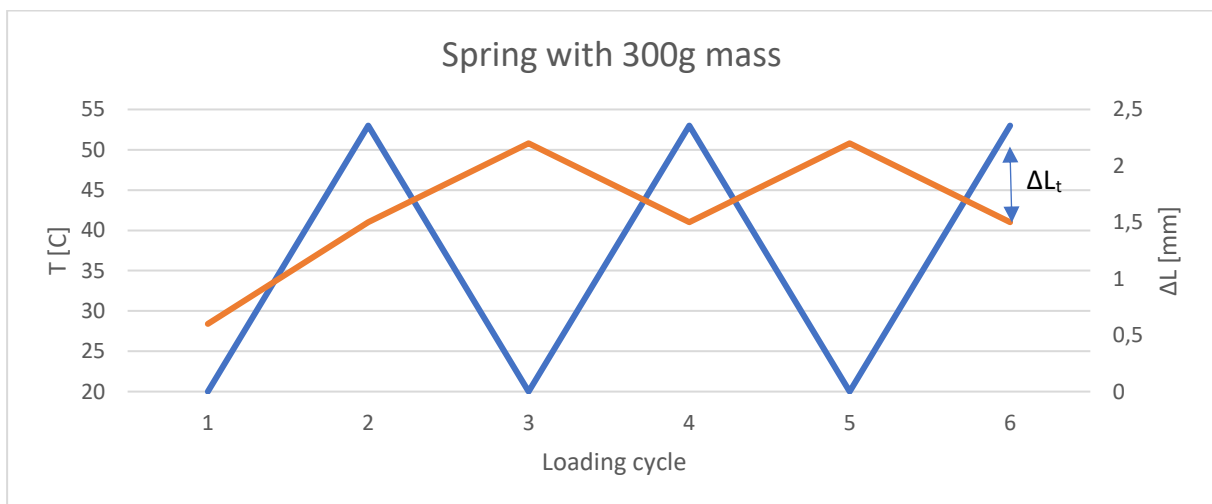
Fig. 2 Spring extension ΔL at mass m_1
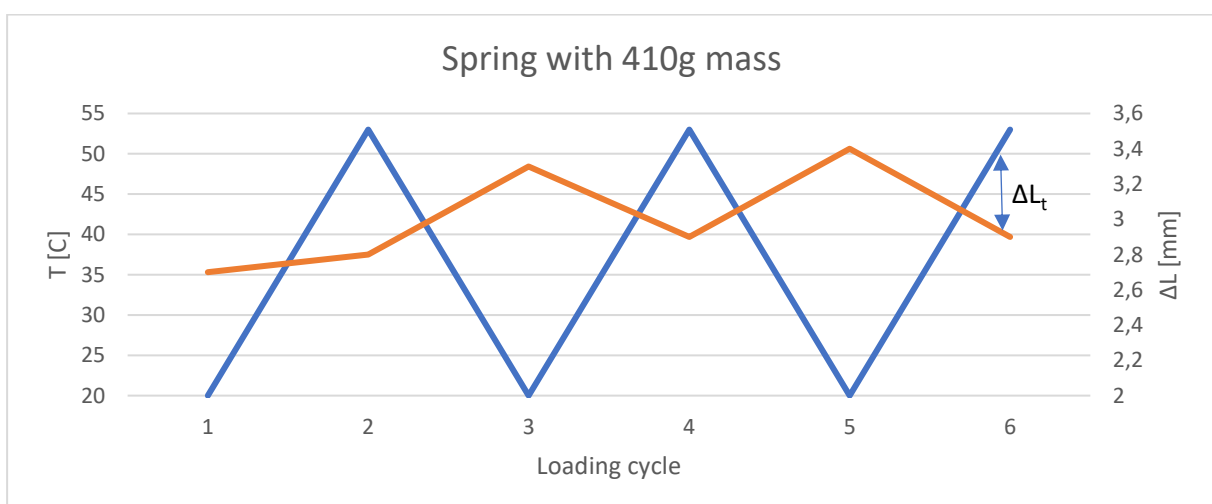
Fig. 3 Spring extension ΔL at mass m_2

As can be seen in Fig. 2 and 3, the extension of the spring from the axial force increases during repeated strokes until it reaches a steady working point. On the basis of these measured

characteristics, it was possible to compile a table of processed parameters, which contains the parameters of the spring extension from the axial force ΔLm and changes in the extension when the temperature increases ΔLt ("Stroke").

Tab. 2 Temperature parameters of springs

m	300	410	g
ΔL_m	15	29	mm
ΔL_t	7	5	mm
F_m	3	4,1	N
k_t	0,212	0,151	mm/K

Tab. 2 contains expressed parameters kt, which were determined based on the equation [3]

$$\Delta L_t = k_t * \Delta T \qquad (1)$$

The parameter k_t can be expressed as a function of the axial force Fm, where this dependence is assumed to be linear and is shown in Fig. 4
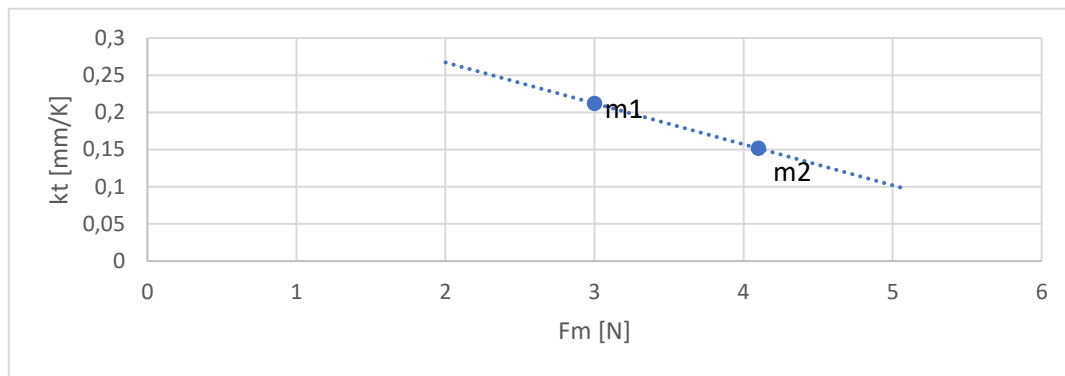
Fig. 4 Parameter k_t

CONCLUSION

As can be seen in Figure 4, the line of dependence has a decreasing character. The elongation of the spring from the axial force increases with repeated strokes until it reaches a steady working point.

ACKNOWLEDGMENT

LITERATURE

[1] A. Cherubini, G. Moretti, R. Vertechy, M. Fontana, "Experimental characterization of thermally-activated artificial muscles based on coiled nylon fishing lines", AIP Advances 5, 067158 (2015).

[2] Martin Minár, Vladimír Goga, Romana Čápková, Kristián Ondrejička and Justín Murín "Basic Parameters of Coiled Fishing Line Actuator", 2020 Cybernetics & Informatics (K&I), Velké Karlovice, Czech Republic

[3] Murin, Justin & Goga, V & Paulech, Juraj & Hrabovský, J & Sedlár, T & Kutiš, V & Aminbaghai, Mehdi. (2021). Thermo-elastostatic analyzes of new dampers made of polymer springs with negative thermal expansion. IOP Conference Series: Materials Science and Engineering. 1199. 012056. 10.1088/1757-899X/1199/1/012056.

ON THE MULTIBODY MODELLING AND NUMERICAL SIMULATIONS OF ROAD AND RAIL VEHICLES

MICHAL HAJŽMAN[1], PAVEL POLACH[2]

Approaches to the modelling of road and rail vehicles considered multibody systems will be summarised in this paper. Further, their implementation and procedures for numerical simulations will be introduced together with suitable software tools. In order to demonstrate the usage of the presented methodology, several examples of real road and rail vehicle problems related to their dynamics will be shown.

KEYWORDS

Dynamics, Multibody dynamics, Vehicle, Model, Parameters.

INTRODUCTION

Approaches of multibody system dynamics [1] are suitable ways how to model systems of rigid and flexible bodies performing large motion with mutual interactions and nonlinear forces. Road and railway vehicles are typical representatives of such systems that are composed of kinematically constrained bodies. This paper is aimed at the summary of various vehicle dynamics tasks solved in the Research and Testing Institute Plzen mainly in connection with industrial partners or in the framework of applied research projects.

The multibody modelling methodology is based on the decomposition of the whole mechanical system into a set of rigid bodies connected by various kinematical joints (constraints) and subjected to the actions of various forces and torques (they can represent springs, dampers, contacts, etc.). The rest of the paper is divided into two parts, one deals with the problems of road vehicles while the second is devoted to railway vehicles.

ROAD VEHICLES

Multibody modelling of road vehicles comprises the vehicle decomposition to suitable structural parts which can be modelled as rigid (or alternatively flexible) bodies and are mutually coupled by kinematical constraints (joints). The third important part of the road vehicle multibody models is various spring-damper elements with linear or non-linear characteristics. Special attention should be paid to the modelling of tires and their interaction

[1] **doc. Ing. Michal Hajžman, Ph.D.**, Department of Applied Mechanics, Research and Testing Institute Plzen. Tylova 1581/46, Plzeň, Czech Republic. Tel +420 371 430 731. Email: hajzman@vzuplzen.cz

[2] **doc. Dr. Ing. Pavel Polach**, Department of Applied Mechanics, Research and Testing Institute Plzen. Tylova 1581/46, Plzeň, Czech Republic. Tel +420 371 430 773. Email: polach@vzuplzen.cz

with a specified road. The proper model selection and the identification of tire model parameters is a separate discipline in the framework of road vehicle modelling. Concerning the particular implementation of models, several commercial software tools have been used in the Research and Testing Institute Plzen (alaska, SIMPACK) and simplified in-house models were created in the MATLAB system [2].
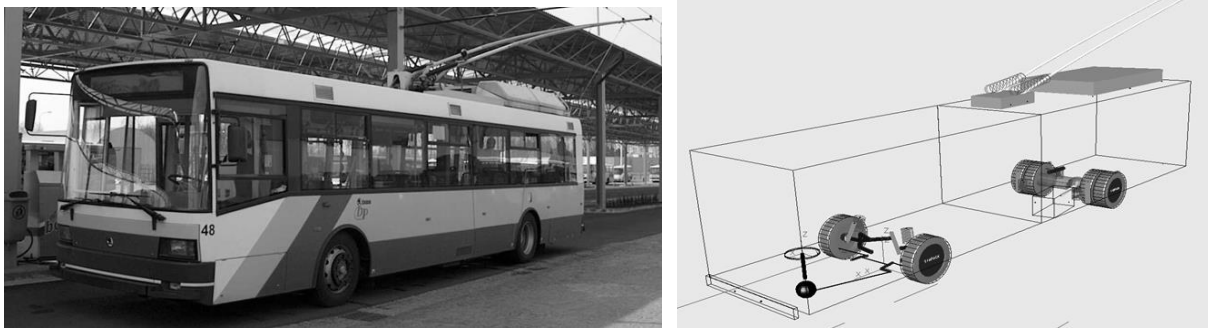
Fig. 1 Real trolleybus and the visualisation of its multibody model in SIMPACK

The overview of the main tasks solved by the authors in the framework of bus and trolleybus vehicle dynamics was given in [2] and [3]. Real ŠKODA trolleybus and its SIMPACK multibody model are shown in Fig. 1. Typical goals of numerical simulations of road vehicles concern both vertical dynamics (durability and driving comfort) and horizontal dynamics (stability and handling). An example of the kinematical scheme of a simplified trolleybus multibody model is shown in Fig. 2, where rectangles denote rigid bodies and circles denote kinematical constraints.
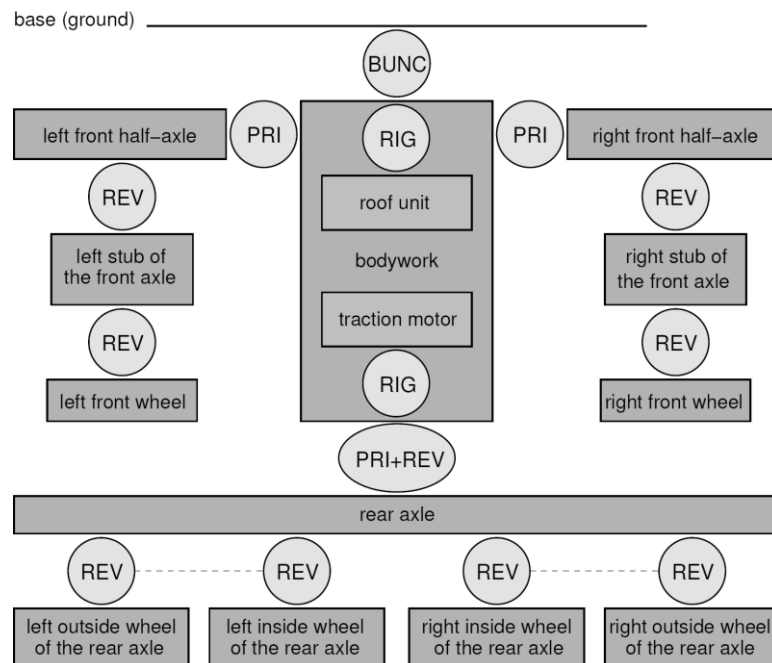
Fig. 2 Illustrative example of the trolleybus model kinematical scheme

RAILWAY VEHICLES

The concept of multibody modelling of railway vehicles is analogous to road vehicles. A studied vehicle should be decomposed into rigid (and flexible) interconnected bodies with various spring-damper elements. The specific model part is the interaction of wheels and rails using contact forces of a different complexity. One of the first problems in the railway industry

solved in the Research and Testing Institute Plzen was the comparison of the dynamic behaviour of the wagon with conventional (steel) and composite leaf springs in suspension [4].
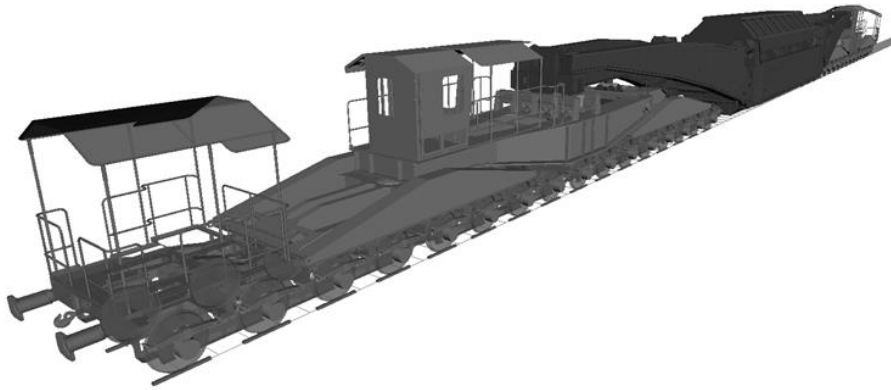
Fig. 3 Visualisation of the 32-axle wagon multibody model in SIMPACK
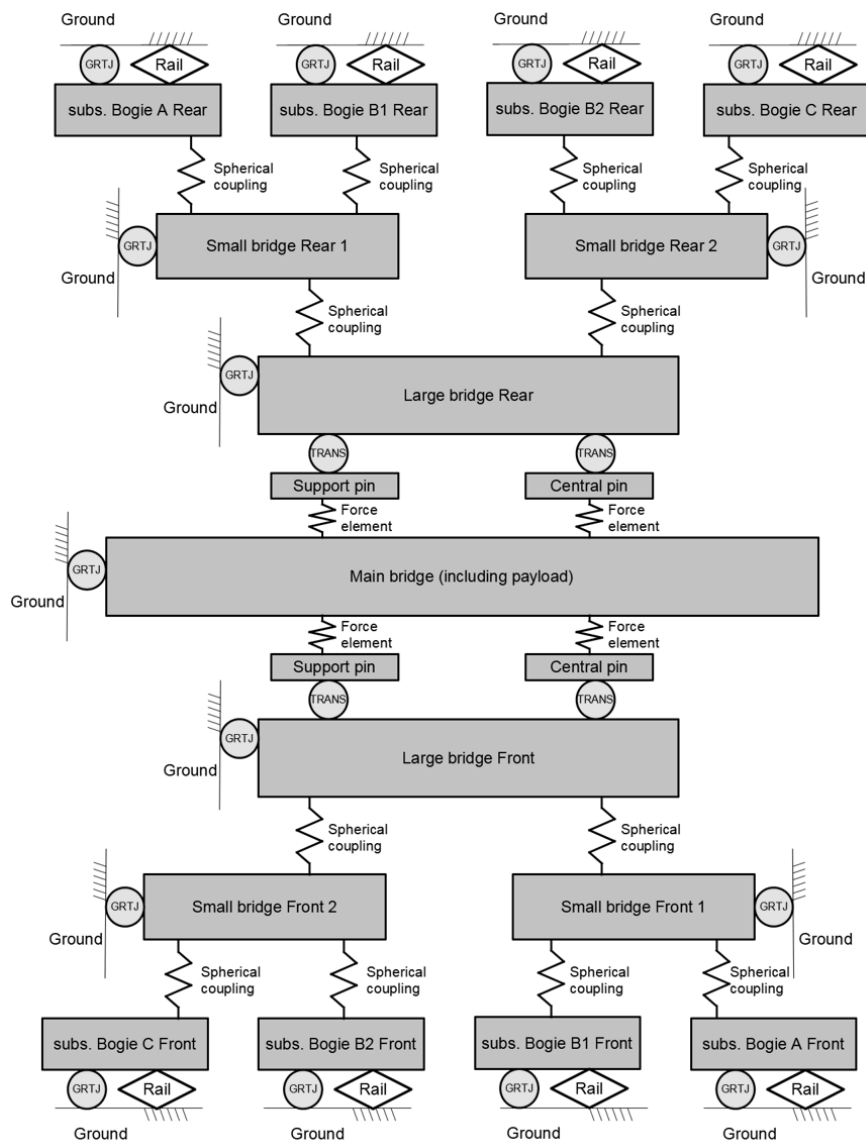
Fig. 4 Kinematical scheme of the 32-axle wagon multibody model

Another complex task was the modelling and numerical simulations of the railway vehicle for heavy load transport in SIMPACK [5]. Except for particular bogies (each with four wheelsets), the modelled wagon (see Fig. 3) is designed with several functional components called bridges carrying a payload. The wagon multibody model contains these main rigid bodies: 32 wheelsets, 8 bogie frames, 4 small bridges, 2 large bridges, and 1 main bridge (+payload and/or platforms), see Fig. 4 for the kinematical scheme of the whole model.

The computational multibody model of the wagon was implemented to perform various numerical simulations prescribed in railway standards. The main code utilized for railway vehicles is EN 14363 standard "Railway applications – Testing and simulation for the acceptance of running characteristics of railway vehicles – Running behaviour and stationary tests" [5]. At first, the running of the wagon on a straight track at various velocities was numerically simulated. It was followed by linearized modal analysis to investigate stability properties. The extensive set of numerical simulations was dedicated to running on tracks with prescribed curvature and given velocity. All tests were evaluated by means of the standard using derailment coefficient and wheel lateral forces.

CONCLUSION

This paper deals with the overview of the multibody modelling problems solved in the Research and Testing Institute Plzen in the framework of vehicle dynamics. The modelling methodology is based on the vehicle decomposition into particular design elements characterized as rigid bodies and further connected by various kinematical joints and constraints. Road vehicle and railway vehicle models are used mainly for the purpose of design evaluation and verification of correct vehicle operation. The created models were used also for the optimization of certain components such as hydraulic shock absorbers or stabilizer bars. Almost all real vehicle models were also experimentally investigated in order to validate simulation results.

ACKNOWLEDGMENT

LITERATURE

[1] Shabana, A. A. Dynamics of Multibody Systems. Fifth edition. London, Cambridge University Press, 2020. ISBN 978-1-108-48564-7.

[2] Polach, P. Utilization of multibody simulations in the development of buses and trolleybuses. Habilitation thesis. Plzeň, University of West Bohemia, 2020.

[3] Polach, P., Hajžman, M. Selected problems in bus development solved using multibody simulations. Technologie wytwarzania, analizy procesów i symulacje obliczeniowe, Monografia. Bielsko-Biala, Wydawnictwo naukowe Akademii Techniczno – Humanistycznej w Bielsku-Bialej, 2021, 17-28. ISBN 978-83-66249-87-5.

[4] Polach, P., Hajžman, M. Computer simulations of the freight wagon laboratory excitation. Mechanics Based Design of Structures and Machines. 2011, 39(2), 194-209. ISSN 1539-7742.

[5] Hajžman, M., Polach, P. Multibody modelling methodology of the railway vehicle for heavy loads transport. Proceedings of the International Colloquium Dynamics of Machines and Mechanical Systems with Interactions DYMAMESI 2022. Prague, Institute of Thermomechanics of the CAS. 2022, 7-10. ISBN 978-80-87012-78-9.

LOW-CYCLE FATIGUE AND CYCLIC PLASTICITY OF VERTICALLY BUILT SPECIMENS FROM RECYCLED POWDER OF ALSI10MG

HALAMA RADIM[1], PAŠKA ZBYNĚK[2], NATARAJAN VIGNESH AJAY[3], HAJNYŠ JIŘÍ[4]

This contribution describes the chosen results of the low-cycle fatigue tests performed on AlSi10Mg printed by SLM technology in vertical orientation on the built plate. Two proportional loading cases were realised: push-pull and pure torsion. The non-proportional loading tests were performed as the third case in the form of 90 degree out-of-phase tests. Cyclic plastic properties and lifetimes have been evaluated. The longest lifetimes correspond to cyclic torsion and the shortest ones to the non-proportional loading case. A new experimental technique for the cyclic stress-strain curve estimation based on DIC measurement was also validated.

KEYWORDS

AlSi10Mg, SLM, cyclic plasticity, LCF, nonproportional loading, DIC

INTRODUCTION

Selective laser melting (SLM) is an additive manufacturing (AM) technology used to print functional parts from metallic powders using a high-energy laser beam. Compared to the static tensile properties of the parts produced, fatigue performance is not reported so often in recent research studies [1]. The fatigue properties of AM materials are necessary for industrial use in technical practise. The AlSi10Mg alloy is one of the most popular materials used in light structures produced by SLM and is commonly used in the aviation and automotive industries due to its high resistance and fatigue properties [2].

---

[1] **prof. Ing. Radim Halama, Ph.D.**, Department of Applied Mechanics, Faculty of Mechanical Engineering, VSB-Technical University of Ostrava. 17.listopadu 2172/15, Ostrava, Czech Republic. Tel +420 59 732 1288. Email: radim.halama@vsb.cz

[2] **Ing. Zbyněk Paška**, Department of Applied Mechanics, Faculty of Mechanical Engineering, VSB-Technical University of Ostrava. 17.listopadu 2172/15, Ostrava, Czech Republic. Tel +420 59 732 5273. Email: zbynek.paska@vsb.cz

[3] **Bc. Ajay Vignesh Natarajan**, Department of Applied Mechanics, Faculty of Mechanical Engineering, VSB-Technical University of Ostrava. 17.listopadu 2172/15, Ostrava, Czech Republic. Tel +420 59 732 3290. Email: ajay.vignesh.natarajan@vsb.cz

[4] **Ing. Jiří Hajnyš, Ph.D.**, Department of Machining, Assembly and Engineering Metrology, Faculty of Mechanical Engineering, VSB-Technical University of Ostrava. 17.listopadu 2172/15, Ostrava, Czech Republic. Tel +420 59 732 9064. Email: jiri.hajnys@vsb.cz

This study shows a comparison of the low-cycle fatigue (LCF) properties of AlSi10Mg for three loading cases: tension-compression, torsion, and tension-compression/torsion (90 degrees out of phase test). Cyclic plasticity behavior has also been studied using Python codes and measurements by digital image correlation (DIC).

EXPERIMENTS

All fatigue tests were performed on vertically printed tubular samples in the as built state using a recycled powder of AlSi10Mg [3]. Renishaw AM400 was used to manufacture the samples. The laser power of 400W and the layer thickness of 25μm were applied. The resulting porosity was less than 0.3%. The LabControl 100kN/1000Nm hydraulic testing machine was used in conjunction with the Epsilon 3550 extensometer with a gauge length of 25 mm to control the axial and shear strain under axial / torsion loadings. The DIC method was applied to obtain full-field data during testing at the highest strain amplitude for each loading case to estimate the cyclic stress-strain curve. Subsequently, the estimated cyclic stress-strain curves were compared with the conventionally obtained ones.

CONCLUSION

Preheating the build plate leads to a cyclically stable response of the material, which is useful to follow computational fatigue predictions. LCF lifetimes in strain control increased compared to printing without preheating. On the other hand, the durability observed in stress-controlled tests with zero mean stress leading to strain accumulation (ratcheting) is significantly lower. Estimates of the cyclic stress-strain curve obtained by the DIC technique for all three loading cases correlate very well with the conventional ones [4].

ACKNOWLEDGMENT

LITERATURE

[1] E. Brandl, U. Heckenberger, V. Holzinger. Additive manufactured AlSi10Mg samples using Selective Laser Melting (SLM): Microstructure, high cycle fatigue, and fracture behavior. Materials & Design, 2012, 34 (159-169).

[2] A. Raja, S.R. Cheethirala, P. Gupta, J. V. Nilesh, R. Jayaganthan. A review on the fatigue behaviour of AlSi10Mg alloy fabricated using laser powder bed fusion technique. Journal of Materials Research and Technology, 2022, 17 (1013-1029).

[3] Renishaw, Magics Training: Material Profile Editing. RENISHAW: Apply Innovation, Renishaw, United Kingdom, 2016.

[4] Paška, Z. Application of appropriate optical methods for strain field determination in elasto-plastic domain. Dissertation Thesis. VSB - Technical University of Ostrava. Tutor: prof. Ing. Radim Halama, Ph.D. (In Czech)

COMPARISON OF MANUFACTURING COSTS AND MECHANICAL PROPERTIES OF SPECIMENS PRINTED BY EXTRUSION TECHNOLOGIES

MARIÁN HANDRIK[1], JAROSLAV MAJKO[2], MILAN VAŠKO[3]

The article focuses on the mechanical properties and prices of products made from different materials. The specimens were printed using the Markforged Mark Two printer, which working principle is based on the FFF method. The advantage of the printer is the printing of objects reinforced with continuous reinforcing fibres (carbon, aramid, glass, and HSHT glass). The cost of materials varies greatly, whereas stronger materials are significantly expensive.

KEYWORDS

3D printing, mechanical properties, material costs

INTRODUCTION

The article focuses on the economic efficiency of thermoplastic composite manufacturing using the CFF (Continuous Filament Fabrication) printer. The main criterion for the assessment is the manufacturing costs of printed structures reinforced with various types of fibres. The published studies claimed that the deposition of continuous fibres substantially affects the resulting mechanical properties [1-3]. In general, the presence of fibres leads to increasing composite strength. However, the influence of individual fibre types is various and higher fibre volume fracture of fibres with less strength also allows the achievement of the same or even better mechanical properties than offers high-strength (and more expensive) fibres. The article's aim is to compare the manufacturing costs of various specimens with the same theoretical tensile strength.

---

[1] **Ing. Marián Handrik, PhD.**, Department of Applied Mechanics, Faculty of Mechanical Engineering, University of Žilina. Univerzitná 8215/1, Žilina, Slovakia. Tel +421 41 513 2965. Email: marian.handrik@fstroj.uniza.sk

[2] **Ing. Jaroslav Majko, PhD.**, Department of Applied Mechanics, Faculty of Mechanical Engineering, University of Žilina. Univerzitná 8215/1, Žilina, Slovakia. Tel +421 41 513 2974. Email: jaroslav.majko@fstroj.uniza.sk

[3] **Doc. Ing. Milan Vaško, PhD.**, Department of Applied Mechanics, Faculty of Mechanical Engineering, University of Žilina. Univerzitná 8215/1, Žilina, Slovakia. Tel +421 41 513 2981. Email: milan.vasko@fstroj.uniza.sk

CHAPTER 1 SPECIFICATION OF MECHANICAL PROPERTIES AND UNIT COSTS

The economic efficiency assessment is performed on data provided by the printer manufacturer. The mechanical properties of individual materials are shown in Table 1.

Table 1. Mechanical properties of materials specified by manufacturer [4]

Material	Tensile Strength [MPa]	Tensile Modulus [MPa]	Tensile Strain at Break [%]	Unit price [USD]
Nylon	36	2 400	25	170
Onyx	37	1 700	150	190
Carbon	800	60 000	1.5	450
Aramid	610	27 000	2.7	300
Glass	590	21 000	3.8	230
HSHT glass	600	21 000	3.9	300

In the case of fibres, the manufacturer specifies the strength of the composite structure, which contains the maximal amount of reinforcing fibres oriented parallel to the loading axis. For our analysis, an important aspect is that the type of reinforcing fibres affects the thickness of the laminate and the number of fibres deposited in a layer (Table 2).

Table 2. Determination of force per fiber for various reinforcement types

Material	Layer Thickness [mm]	Specimen thickness [inch]	Number of Fibers [-]	Force per Fiber [N]
Carbon	0.125	1.22	130	95.3
Aramid	0.100	2.03	260	60.5
Glass	0.100	2.03	260	58.5
HSHT glass	0.100	2.03	260	59.5

Continuous reinforcing fibres have a dominant effect on the resulting strength of the produced composite structure. When comparing the fibres' costs, it is necessary to take into account the strength of individual types of fibres. Based on their strength, the fibres can be divided into two groups:

• Carbon fibres with a strength of 95 N per fibre.

• Aramid, glass, and HSHT glass fibres with a strength of approximately 60 N per fibre.

The lower strength per fibre implies that the substitution of carbon fibres in the structure requires the deposition of approximately 1.6 times more fibres from the second group. The calculated unit cost of fibres deposited in specimens which achieve the strength of specimens reinforced with carbon fibres is in Table 3. The subsequent comparison reveals that aramid and HSHT glass fibres have a higher unit cost than carbon fibre. Only the glass fibres have unit costs approximately 20% lower.

Table 3. Unit cost per cubic centimeter of selected fibres. Calculated unit cost required to obtain the strength of carbon fibre

Material	Unit Cost [USD/cc]	Strength multiplayer [-]	Unit cost required to achieve the strength of carbon fibre [USD]
Carbon	3.0000	1	3.0000
Aramid	2.0000	1.575	3.1500
Glass	1.5333	1.629	2.4978
HSHT glass	2.0000	1.601	3.2020

CHAPTER 2 COMPARISON OF SELECTED MATRIX AND FIBRE MATERIALS

The comparison of real printing costs was carried out using a slicing program EIGER, originally intended for the printing preparation process for Markforged printers. Firstly, the authors designed the specimens of block shape with dimensions 100x20x10 millimetres. Each layer comprised two walls of matrix material around the circumference of the specimen. Generally, the walls improve printing accuracy and reduce the roughness of the object's surface.

A more detailed description of the structure configuration for the selected combinations of materials Onyx/carbon and nylon/glass is presented in Table 4. If the condition of the same strength of the laminate is desired, the proportion of glass fibre in the structure must be 1.6 times greater compared to carbon fibre. Since in the investigated example, almost the entire layer comprised reinforcing fibres with an arrangement -45°/45°, the laminate reinforced with glass fibres contains 1.6 times more reinforced layers than laminate with carbon fibres.

Table 4. Specification of laminate composition

Material	Layer Thickness [mm]	Matrix Layers [-]	Fiber Layers [-]	Total Layers [-]
Onyx / Carbon	0.125	60	2 x 10	80
Nylon / Glass	0.1	68	2 x 16	100

The layout of the printing layers in the structure of the laminate is shown in Fig. 1. The arrangement is as follows:

• 4 roof and floor layers (matrix).

• 10 or 16 reinforcing layers with continuous fibres layers divide into two groups. The number of reinforcing layers depends on the fibre type.

• Infill layers between the reinforced laminas (matrix).
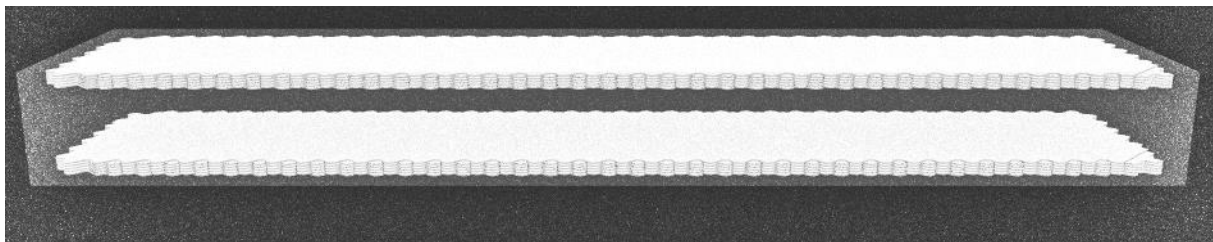
Fig. 1. Composition of the laminate. White colour represents fibres

The consumption of matrix and reinforcement material for the observed types of specimens is specified in Table 5. From the point of total costs, the group of specimens reinforced with less strong fibres are the more appropriate choice. On the other hand, the printing time increases significantly.

Table 5. Printing parameters including total price and printing time

Material	Matrix Volume [cc]	Fiber Volume [cc]	Matrix Unit Cost [USD/cc]	Fiber Unit Cost [USD/cc]	Total Price [USD]	Print Time [min.]
Onyx / Carbon	17.69	3.90	0.2375	3.0000	15.90	198
Nylon / Glass	14.95	5.12	0.2125	1.5333	11.03	273

CONCLUSION

In general, carbon fibre-reinforced composites are classified as high-strength materials. The fibre volume fraction is usually low, although printing parameters modification typically allows the deposition of a higher amount of reinforcing fibres. The significant aspect of manufacturing is production cost hence in many cases engineers look for a cheaper alternative instead of expensive carbon fibre and nylon reinforced with chopped carbon fibre. The authors compared the production costs of two specimen groups (nylon reinforced with chopped carbon fibres and continuous carbon fibres versus pure nylon and continuous glass fibres), while the groups had to achieve the same strength. According to the results, the usage of latter showed a price reduction from 15.9 USD to 11.03 USD (44%). On the other hand, the calculation of total production costs must also consider an increase in printing time by 38% (from 198 min. to 273 min.).

ACKNOWLEDGMENT

LITERATURE

[1] Jones, R.M. Mechanics of Composite Materials, 2nd ed.; Taylor & Francis Group: New York, NY, USA, 1999. ISBN 978-1-5603-2712-7

[2] Xionghao, L.; Zhongjin, N.; Shuyang, B.; Baiyang, L. Preparation and Mechanical Properties of Fiber Reinforced PLA for 3D Printing Materials. IOP Conf. Ser.: Mater. Sci. Eng. 2018, 322 (2). DOI: 10.1088/1757-899X/322/2/022012.

[3] Chapiro, M. Current achievements and future outlook for composites in 3D printing. Reinforced Plastics 2016, 60 (6), 372-375, ISSN 0034-3617.
DOI: https://doi.org/10.1016/j.repl.2016.10.002.

[4] Markforged. Material Datasheet. Available online: Markforged.com (accessed on 10 March 2023).

EFFECT OF TEMPERATURE OF ADHESIVELY BONDED COMPOSITE ON LOADING OF PURE MODE I AND II

LUKÁŠ HORÁK[1], JAN KRYSTEK[2]

In this paper, the effect of temperature on the pure mode I and II loading of an adhesively bonded carbon-epoxy composite was investigated. Specimens for mode I and II loading were exposed to several different temperatures. These temperatures were chosen below the glass transition temperature of both the adhesive and the composite sample. From the experiments performed, the energies of the critical failure mode were calculated for mode I and II.

KEYWORDS

Adhesive bonding, Cohesive properties, Composite, Mode I, Mode II, Temperature

INTRODUCTION

Due to the increase of polymer composite materials in today's manufacturing process across the entire industry, new ways of bonding these materials are needed. Adhesion is one which is not destructive to composite material with uniform stress distribution, high fatigue resistance, and other advantages. Also, these joints are now used more in difficult operating conditions like higher temperatures, humidity, and other extreme conditions.

Adhesion bonding comes with difficulties like sensitivity to the correct application process, choosing the correct adhesive for proper bonding with composite matrix, and others. This uncertainty makes a usable prediction of the bonded joint and its mechanical properties much more difficult to model correctly. [3]

The adhesive layer is primarily exposed to two modes of loading. One is caused by crack opening, which corresponds to pure mode I, and the other is caused by layer-by-layer sliding, which corresponds to mode II. For both modes, it is possible to obtain their strain energy release rate. [4]

In this paper, two modes are experimentally examined. Experiments were performed under increased temperatures during tests. Two temperatures were chosen, room temperature 23˚C and increased temperature 50˚C. According to the manufacturer, these temperatures are below the glass transition of adhesive and adherent.

---

[1] **Ing. Lukáš Horák**, Department of Mechanics, Faculty of Applied Sciences, University of West Bohemia, Pilsen. Univerzitní 8, 301 00, Pilsen, Czech Republic. Email: horakl@kme.zcu.cz

[2] **Ing. Jan Krystek, Ph.D.**, Department of Mechanics, Faculty of Applied Sciences, University of West Bohemia, Pilsen. Univerzitní 8, 301 00, Pilsen, Czech Republic. Email: krystek@kme.zcu.cz

EXPERIMENTS

Specimens were manufactured from a prepreg KORDCARBON−CPREG−200−T−3K−EP1−42−A. This type of polymer composite was chosen because of its good cohesive properties. Adhesive 3M™ Scotch-Weld™ Epoxy Adhesive DP490 was applied on two sheets of composite with dimensions 150x160 mm. The adhesive was not applied on the part of the initialization of the crack. This was achieved by putting Teflon tape between specimens. The adhesive was cured at room temperature (22 ˚C) for seven days, as specified in the datasheet. Then, prismatic specimens (150x20 mm) were created by water jet. By this, we achieved specimens without any residue adhesive on the sides of specimens.

Experiments were performed on universal testing machine Zwick/Roell Z050. For temperature conditioning, a thermal chamber was used. Specimens under increased temperature $T_h = 50$ ˚C were heated to the desired temperature for 60 minutes before testing.

For proper evaluation of fracture toughness using the experimental compliance method and modified beam theory, it is necessary to observe crack length. Observation is difficult even in normal circumstances. Due to the small space in the thermal chamber, it was impossible to use high-resolution recording equipment. For these experiments, a small camera which was not designed to function under extreme conditions was used directly inside of the thermal chamber.
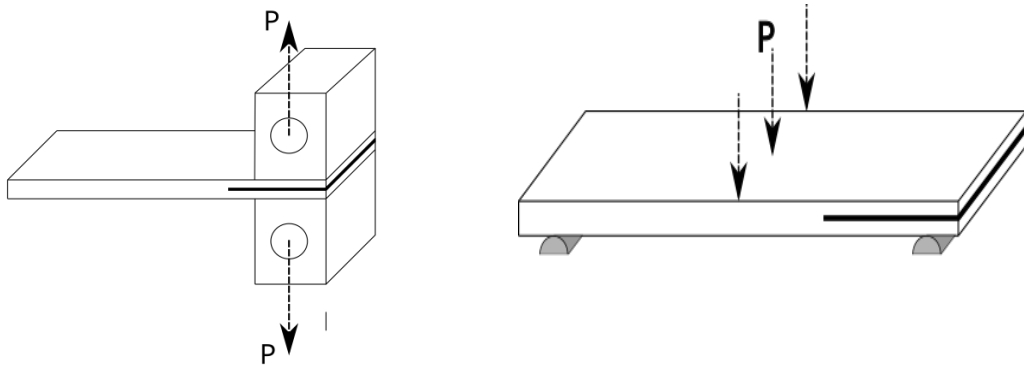
Fig. 1 Scheme of DCB (left) and ENF (right) specimens and their loading points

Double cantilever beam (DCB) experiment was performed according to ASTM D5528 [1]. Specimens were loaded at a constant cross head rate of $v_{DCB} = 5$ mm/min. End notched flexure (ENF) experiment was performed according to ASTM D7905 [2]. Specimens were loaded at a constant cross head rate $v_{ENF} = 1.6$ mm/min. A schematic of specimens is shown in Fig. 1.

RESULTS

Adhesive fracture toughness for mode I was computed according to modified beam theory as

$$G_I = \frac{3P\delta}{2B(a+|\Delta|)},$$

(1)

where P is applied load during crack propagation with length a. δ is load point displacement, B is width of specimen and Δ is term for correction due to possible rotation.

Fig. 2 on the left presents force vs. displacement ($P-\delta$) data and resistance curves (G_I-a) on the right. Different beginning of R−curves is because of different initial crack lengths. Fracture toughness values for increased temperature are beginning to stabilize on the mean value $G_I^{50} = 2208.50$ J/m^2. This value is shown as a bold dashed line in Fig. 2 on the right. For room temperature, the mean value was $G_I^{RT} = 351.83$ J/m^2. This value does not reflect actual

fracture toughness because of brittle fracture. Different adherents would be necessary for future testing. Brittle fracture was also observed in test results in work [3], where different adherents were used.
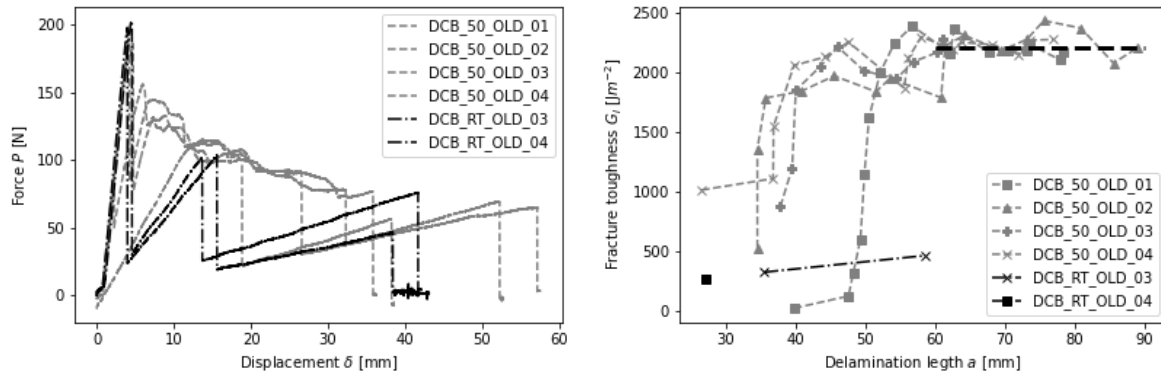
Fig. 2 Evaluation of DCB specimens, Left: Force vs displacement,
Right: Resistance curve (R−curve)

During an evaluation, it was observed that adhesive behaves very differently in elevated temperatures. For specimens at room temperature were observed brittle mode of fracture, this was not satisfactory for complex evaluation. During increased temperature, a gradual fracture was observed.

Mode II was measured on four specimens total, two for room temperature and two for increased temperature $T_h = 50$ ˚C. Due to the fault mode of fracture, one specimen from each group had to be eliminated from the evaluation. Because of this, it was not possible to present statistically accurate data for mode II. During the testing of ENF specimens were verified necessary steps for future testing.
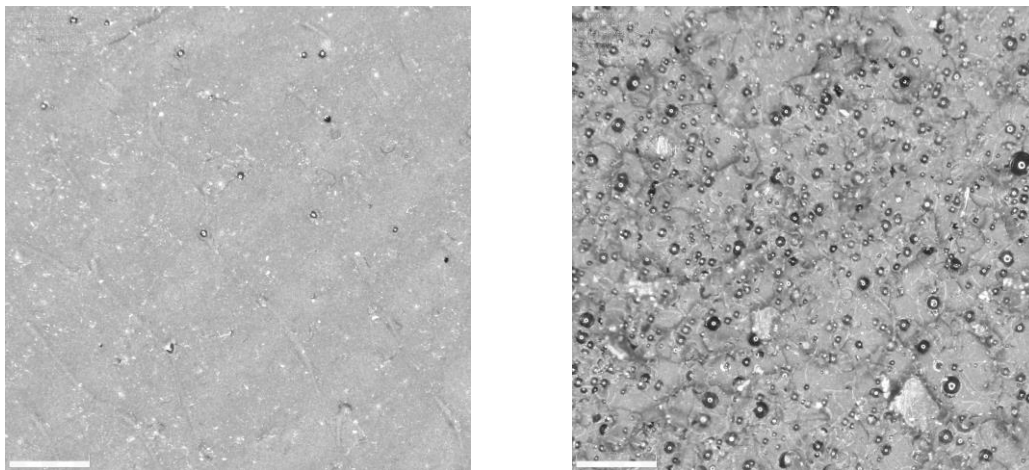
Fig. 3 Detail of adhesive on DCB specimens
after fracture. Left: specimen which was tested in 23˚C, Right: specimen which was tested at increased temperature 50˚C

From data of fracture toughness and microscope photographs it is clear that even temperature below glass transition greatly influences fracture toughness and the whole interaction between adhesive and adherent. In Fig. 3 are presented photographs from the microscope where the image size for both photographs is 2.9x2.9 mm. It seems that the

chemical structure of the adhesive was affected by temperature. Tiny bubbles and a non-uniform surface are seen on the right photograph of adhesive on the DCB specimen after a fracture with elevated temperature.

CONCLUSION

The presented methodology of testing was proven to evaluate fracture toughness for the increased temperature of mode I and mode II for DCB and ENF specimens. Mean values of fracture toughness for increased temperature were obtained. Non-negligible effect of temperature on specimens and their properties was find-out even below glass transition temperatures. This was further observed under detailed photographs from the microscope.

ACKNOWLEDGMENT

LITERATURE

[1] ASTM international. Standard Test Method for Mode I Interlaminar Fracture Toughness of Unidirectional Fiber-Reinforced Polymer Matrix Composites. 2007. Designation: ASTM D 5528 – 01.

[2] ASTM international. Standard Test Method for Determination of the Mode II Interlaminar Fracture Toughness of Unidirectional Fiber-Reinforced Polymer Matrix Composites. 2014. Designation: ASTM D7905/D7905M − 14.

[3] Petr Bernardin. Spojování kompozitních materiálů s kovem. Dissertaion thesis. 2016. University of West Bohemia.

[4] Tomas Walander, Anders Biel, Ulf Stigh. Temperature dependence of cohesive laws for an epoxy adhesive in Mode I and Mode II loading. International Journal of Fracture. 2013. 183 (pp. 203-221).

EFFICIENT IMPLEMENTATION OF CONSTRAINT EQUATIONS IN MULTIBODY DYNAMICS

MARTIN HRABAČKA[1], MICHAL HAJŽMAN[2], RADEK BULÍN[3]

This work deals with the implementation of software automatically constructing mathematical models of the dynamics of multibody systems. The main target of the paper is to compare two different ways of implementing constraint equations and choose the suitable one. Examined approaches are the implementation of constraints as final matrix formulas using matrix variables, and constraints in the form of expanded scalar equations using only scalar variables.

KEYWORDS

Constrained dynamics, multibody software, constraint equations, evaluation efficiency.

INTRODUCTION

Software for simulating multibody systems' (MBS) dynamics allows engineers to study and investigate mechanical and mechatronic systems' motion. It enables them to generate and solve virtual 3D models to predict and visualize motion, coupling forces, or stresses [3].

Because simulation of MBS dynamics is usually quite time demanding, MBS software must be efficient in calculations if it is to be employable in practice. This work focuses on joint constraint formulas and their evaluation efficiency, as these equations are calculated many times during simulations.

MATHEMATICAL MODEL OF DYNAMICS OF CONSTRAINED MBS

The mathematical basis of the in-house developed MBS software is formed by Lagrange's equations of the first kind that represent a set of findings achieved by applying Hamilton's principle. The dynamics of a spatial system of n interconnected rigid bodies can be described according to [1] by a system of $6n + r$ algebraic-differential equations (DAEs)

$$\begin{bmatrix} M & C_q^{\mathrm{T}} \\ C_q & 0 \end{bmatrix}\begin{bmatrix} \ddot{q} \\ \lambda \end{bmatrix} = \begin{bmatrix} Q_e + Q_v \\ Q_d \end{bmatrix}, \tag{1}$$

---

[1] **Ing. Martin Hrabačka**, Department of Mechanics, Faculty of Applied Sciences, University of West Bohemia. Technická 8, 301 00 Pilsen, Czech Republic. Email: hrabackm@kme.zcu.cz

[2] **doc. Ing. Michal Hajžman, Ph.D.**, Department of Mechanics, Faculty of Applied Sciences, University of West Bohemia. Technická 8, 301 00 Pilsen, Czech Republic. Email: mhajzman@kme.zcu.cz

[3] **Ing. Radek Bulín, Ph.D.**, New Technologies for the Information Society, Faculty of Applied Sciences, University of West Bohemia. Technická 8, 301 00 Pilsen, Czech Republic. Email: rbulin@ntis.zcu.cz

where $\boldsymbol{M}$ is the system mass matrix, $\boldsymbol{q}$ is the vector of generalized coordinates of all bodies consisting of generalized coordinates $\boldsymbol{q}^i = [\boldsymbol{R}^i \quad \boldsymbol{\theta}^i]^\mathrm{T}$ of particular bodies ($\boldsymbol{R}^i$ are the absolute Cartesian coordinates and $\boldsymbol{\theta}^i$ are the orientation angles), $\boldsymbol{\lambda}$ is the vector of Lagrange multipliers, $\boldsymbol{Q}_e$ is the vector of generalized applied forces, and $\boldsymbol{Q}_v$ is the quadratic velocity vector. The constraint Jacobian matrix $\boldsymbol{C}_q$ and the vector $\boldsymbol{Q}_d$ are products of time derivatives of kinematic constraints (kinematic relationships describing mechanical joints or specified motion trajectories) represented by an algebraic system of r constraint equations

$$\boldsymbol{C}(\boldsymbol{q}, t) = \boldsymbol{0}, \tag{2}$$

where $\boldsymbol{C}$ is the constraint vector. If system (2) is twice partially differentiated with respect to time, the kinematic acceleration equations are obtained, forming the last r equations in (1), where the vector $\boldsymbol{Q}_d$ can be expanded to

$$\boldsymbol{Q}_d = -\boldsymbol{C}_{tt} - (\boldsymbol{C}_q \dot{\boldsymbol{q}})_q \dot{\boldsymbol{q}} - 2\boldsymbol{C}_{qt} \dot{\boldsymbol{q}}. \tag{3}$$

Lower indices $\cdot_t$ and $\cdot_q$ indicate partial derivatives with respect to time and with respect to generalized coordinates.

One of many possible approaches to solve the problem of MBS dynamics is, for instance, to convert system (1) of DAEs of index 1 to the underlying system of ordinary differential equations (ODEs) and subsequent usage of some standard ODE solver. The transformation of (1) to a system of ODEs can be done via the elimination of the Lagrange multipliers, obtaining

$$\ddot{\boldsymbol{q}} = \boldsymbol{M}^{-1}\boldsymbol{C}_q^\mathrm{T}(\boldsymbol{C}_q \boldsymbol{M}^{-1}\boldsymbol{C}_q^\mathrm{T})^{-1}\big[\boldsymbol{Q}_d - \boldsymbol{C}_q \boldsymbol{M}^{-1}(\boldsymbol{Q}_e + \boldsymbol{Q}_v)\big] + \boldsymbol{M}^{-1}(\boldsymbol{Q}_e + \boldsymbol{Q}_v). \tag{4}$$

System (4) of ODEs can be solved directly, and it is possible to improve numerical accuracy via stabilization techniques, e.g., Baumgarte's stabilization, which can be found in [2].
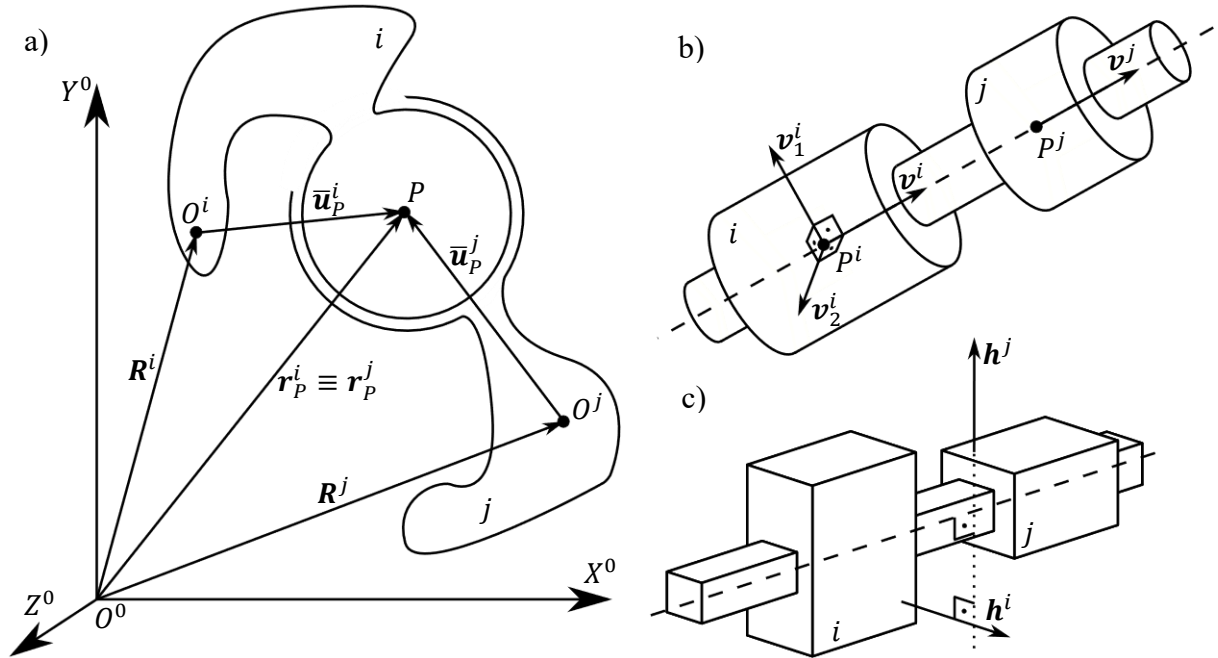

Fig. 1 Spherical, cylindrical, and prismatic joint.

FORMULATION OF BASIC JOINT CONSTRAINTS

Equation (2) represents kinematic restrictions, so-called kinematic constraints, placed on the motion of an MBS. Such constraints can be classified as driving constraints or joints. This paper is focused on the second group. A joint defines the connectivity usually between two

bodies in the system. The basic joints are, e.g., spherical, revolute, cylindrical, prismatic, or rigid.

A spherical joint depicted in Fig. 1a) eliminates relative translations between two bodies i and j, it allows only three degrees of freedom in the form of relative rotations. Its kinematic constraints require that two points, namely P^i on body i with its absolute position $\boldsymbol{r}_P^i$ and P^j on body j with its absolute position $\boldsymbol{r}_P^j$, coincide throughout the motion. The condition can be formally specified as

$$C(q^i, q^j) = \boldsymbol{r}_P^i - \boldsymbol{r}_P^j = \boldsymbol{0}. \tag{5}$$

Generally, the absolute position $\boldsymbol{r}_P^k$ of point P on body k can be expressed using the absolute coordinates $\boldsymbol{R}^k$ of referential point O^k on body k, the transformation matrix $\boldsymbol{A}^k(\boldsymbol{\theta}^k)$ from the absolute coordinate system to the local coordinate system of body k, and position $\overline{\boldsymbol{u}}_P^k$ in the local coordinate system of body k as

$$\boldsymbol{r}_P^k = \boldsymbol{R}^k + \boldsymbol{A}^k \overline{\boldsymbol{u}}_P^k. \tag{6}$$

A cylindrical joint has two degrees of freedom. The relative mobility of bodies connected by the cylindrical joint is apparent from Fig. 1b). One of the possible ways how to specify constraint equations is by using two cross products

$$C(q^i, q^j) = \begin{bmatrix} \boldsymbol{v}^i \times \boldsymbol{v}^j \\ \boldsymbol{v}^i \times (\boldsymbol{r}_P^i - \boldsymbol{r}_P^j) \end{bmatrix} = \boldsymbol{0}, \tag{8}$$

where axial vectors $\boldsymbol{v}^{i,j}$ are again convenient to express using their local forms $\overline{\boldsymbol{v}}^{i,j}$ generally expressed with body index k as

$$\boldsymbol{v}^k = \boldsymbol{A}^k \overline{\boldsymbol{v}}^k. \tag{9}$$

Expression (8) is formed by six equations. Since each cross product defines only two independent equations, these six equations define four kinematic relationships, correlating with the number of joint's degrees of freedom.

A revolute joint has one degree of freedom enabling only one relative rotation of two connected bodies along the joint axis. It can be considered, for instance, as a special case of a cylindrical joint, or as a special case of a spherical joint by eliminating all relative off-axis rotations (more efficient way for the usage in the MBS software). This restriction can be secured by adding two equations

$$C(q^i, q^j) = \begin{bmatrix} \boldsymbol{v}_1^{i\,\mathrm{T}} \boldsymbol{v}^j \\ \boldsymbol{v}_2^{i\,\mathrm{T}} \boldsymbol{v}^j \end{bmatrix} = \boldsymbol{0} \tag{10}$$

to system (5), while vectors $\boldsymbol{v}_1^i$ and $\boldsymbol{v}_2^i$ create an orthogonal triad together with $\boldsymbol{v}^i$.

The last examined constraint, a prismatic joint shown in Fig. 1c), is another joint with one degree of freedom. Similarly to the revolute joint, the prismatic joint can also be derived from the cylindrical joint. However, unlike the revolute one, it is necessary to eliminate relative rotation between two coupled bodies while keeping the ability of relative translation. In order to preclude the relative rotation, a constraint equation

$$\boldsymbol{h}^{i\,\mathrm{T}} \boldsymbol{h}^j = 0 \tag{11}$$

is added to system (8). Orthogonal vectors $\boldsymbol{h}^i$ and $\boldsymbol{h}^j$, both perpendicular to the joint axis, can be expressed using their local forms similarly to (9).

IMPLEMENTATION OF JOINT CONTRAINTS TO MBS SOFTWARE

During the implementation of any joint constraint described in the text above to mentioned MBS software, it is necessary to have access not only to the constraint vector C but mainly to its derivatives C_q and C_{qq}, while the second expression is included in the modified form of (3). Equation (3) also contains derivatives with respect to time t, but since all mentioned kinematic constraints are scleronomic, all time derivatives of C are zero.

This work compares two different ways of implementation of C_q and Q_d in the manner of time consumption of constraint derivatives' evaluation. Approach no. 1 is implementing C_q and Q_d as final matrix formulas obtained by manual derivation, and approach no. 2 is the implementation of the set of final scalar equations using only scalar variables, while these equations were obtained by automatic calculation using MATLAB's symbolic toolbox. The second approach is far less challenging in derivation, but the final formulas are enormously complex expressions. Both variants are tested with the same input values by evaluation in a simple loop with a different number of iterations in order to examine the ability of MATLAB to optimize the calculation when repeated many times. Tab. 1 contains total evaluation times of C_q and Q_d.

Tab. 1 Time consumption of constraints' evaluation using both implementation approaches.

	Spherical joint		Cylindrical joint		Revolute joint		Prismatic joint	
Iterations	Appr. 1	Appr. 2	Appr. 1	Appr. 2	Appr. 1	Appr. 2	Appr. 1	Appr. 2
10^3	0.25 s	0.05 s	1.63 s	1.93 s	0.84 s	0.51 s	2.03 s	2.33 s
10^4	1.48 s	0.12 s	15.0 s	5.33 s	7.06 s	1.40 s	18.1 s	6.17 s
10^5	13.6 s	0.85 s	142.8 s	37.1 s	65.0 s	10.3 s	169.3 s	42.3 s

CONCLUSION

From Tab. 1, it is clear that approach no. 2, evaluation of expanded scalar equations containing scalar variables only, is overall more efficient within all tested joints. Considering constraints, whose single evaluation is relatively more demanding (cylindrical, prismatic joint), approach no. 1 is slightly faster if evaluated a few times ($\leq 10^3$ times). However, when the constraint is evaluated many times ($\geq 10^4$ times), approach no. 2 is always the best option because MATLAB optimizes the repeated calculation far better in this case compared to approach no. 1.

Regardless of the implementation approach used, the particular choice of equations characterizing the constraint is also crucial from the efficiency point of view since various sets of equations may describe one constraint.

ACKNOWLEDGEMENT

LITERATURE

[1] A. A. Shabana. Computational dynamics. Third edition. John Wiley & Sons, 2010. ISBN 978-0-470-68615-7.

[2] M. Hajžman, P. Polach. Application of stabilization techniques in the dynamic analysis of multibody systems. Applied and Computational Mechanics, 2007, 1, pp. 479-488.

[3] W. Schiehlen. Advanced multibody system dynamics. Kluwer Academic Publishers, 1993. ISBN 978-90-481-4253-8.

APPLIED MECHANICS 2023

Grand Hotel Sergijo, April 19th – 21st 2023
Piešťany, SLOVAKIA

CURRENT POSSIBILITIES OF NUMERICAL SOLUTION OF WELDING PROCESS

ROLAND JANČO[1]

In the paper will be presented today way how to numerical solve the process of welding using numerical method of solution. Fiest will be describe the classical welding by electrode and second will be describe the solution of Friction Stir Welding for the material with and without the phase transformation. Comparison of numerical simulation (SYSWeld, ANSYS) results with experiments.

KEYWORDS

Welding process, Friction Stir Welding, Finite Element Method

INTRODUCTION

Welding is a technological process that is most commonly used in manufacturing of industrial equipment for the creation of rigid joints as well as for the repair of various design defects found after manufacturing or in various defectoscopic service inspections. The disadvantage of this technology is that in the structure there may be permanent deformations and stresses, often of undesirable sizes. Unfortunately, it is not possible to carry out an experiment on a real construction when repairing components [1, 3, 5, 6, 7]. Therefore, a process with such technological parameters must be chosen so that the resulting deformation-voltage state is permissible, and the surrounding part of the structure is minimally affected. When choosing the welding technology parameters, the options of numerical solutions, where it is possible to simulate different welding designs to achieve the required minimization of negative welding effects, are numerous.

Friction stir welding (FSW) is a relatively new joining technology which was developed and patented in 1991 by The Welding Institute (TWI), in the United Kingdom [1, 5]. This is a solid-state welding process providing good quality of butt and lap joints. The FSW process has been proved to be ideal for creating high quality welds in several materials including those which are extremely difficult to weld by conventional fusion welding.

1   Solution of GTA welding by program SYSWELD

Based on the geometry was created 2D computational model reflecting the conditions of quasi-stationary cutting in the middle of welding. The mesh of the computational model representing a quarter of the pipe section is shown in Fig. 1. The computational model contained

---
[1] **prof. Ing. Roland Jančo, PhD., ING-PAED IGIP**, Institute of Applied Mechanics and Mechatronics, Faculty of Mechanical Engineering, Slovak University of Technology in Bratislava. Nám. slobody 17, 812 31 Bratislava, Slovakia. Tel +421 2 57296 395. Email: roland.janco@stuba.sk

2772 elements and 6504 nodes. The computational model of welding a longitudinal weld formed by the real weld beads contained 26 welded in seven layers. It was considered pre-heating to 150 °C. The results of thermal analysis are shown in Fig. 2, which captures the temperature field after welding the twenty-sixth bead at the 2 s after the source passes over the modeled cross-section. All heat parameters and material properties are dependent on the temperature, see example [5, 6].
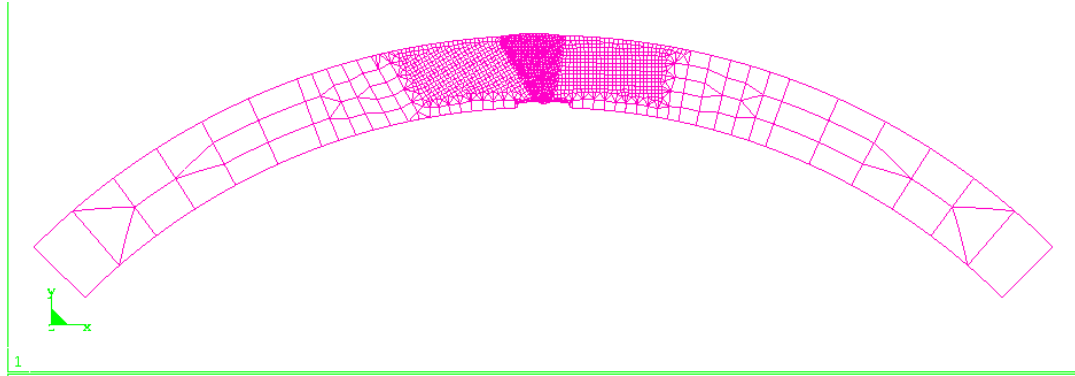
Fig. 1 Geometry and mesh of V weld
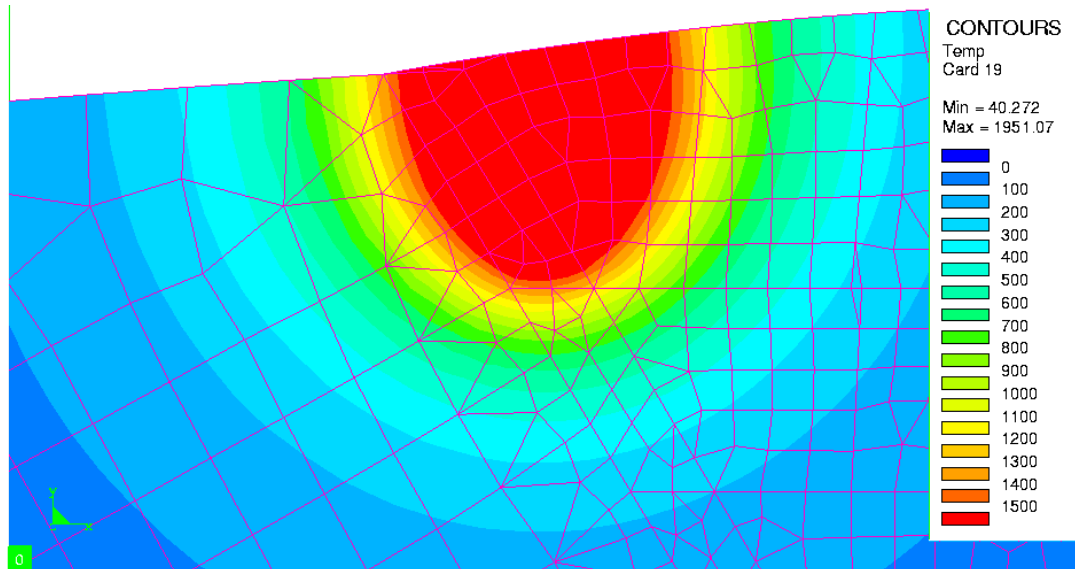
Fig. 2 Temperature field in 2 seconds after electrode passage during welding
of the twenty-sixth layer

The stress-strain analysis results in the final values of the residual stress after welding and the resulting plastic deformation value. In Fig. 3 shows the final state of residual stress after welding.

2   Solution of FSW-welding by program SYSWELD

A schematic of friction stir welding process is illustrated in Fig. 6. For the numerical solution we used the SYSWeld software with the FSW (Friction Stir Welding) module. The FSW module solves the weld joint in the three steps. The boundary conditions and finite element model with the results was presented in [5, 6]. The result of the numerical solution of the thermal field with SYSWeld and the measurements taken with the camera are in a good agreement. The numerical result of thermal field is shown in the Fig. 4.
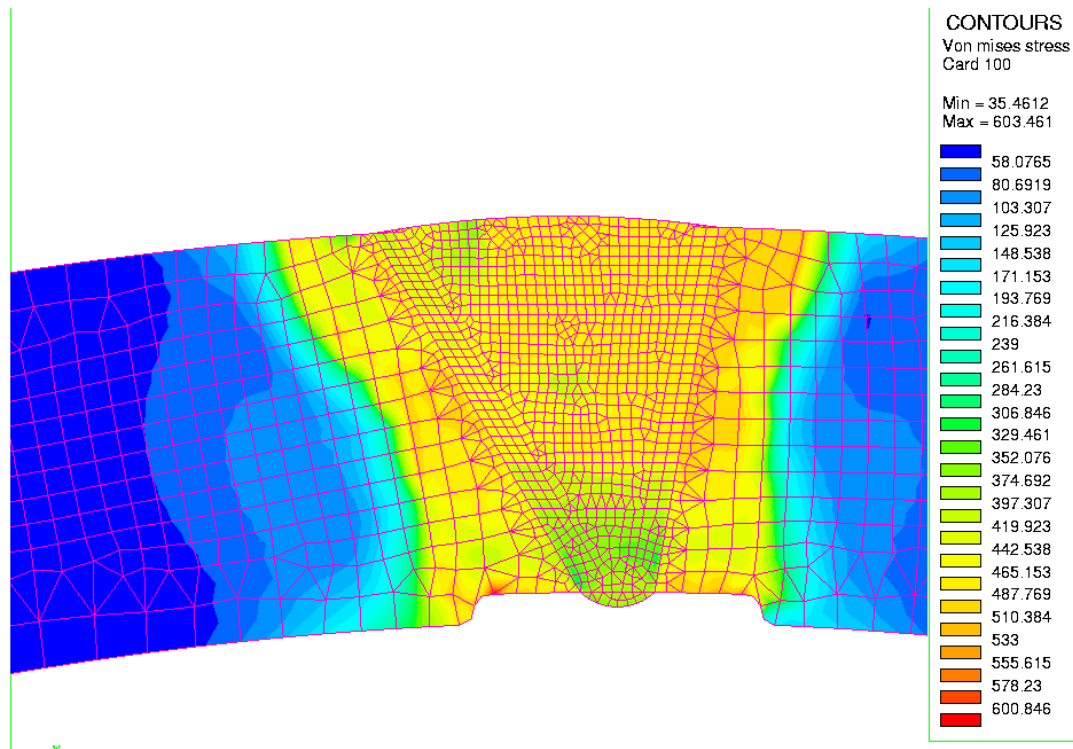
Fig. 3 Von Mises stress after welding the longitudinal weld of the pre-heated fitting 150 °C
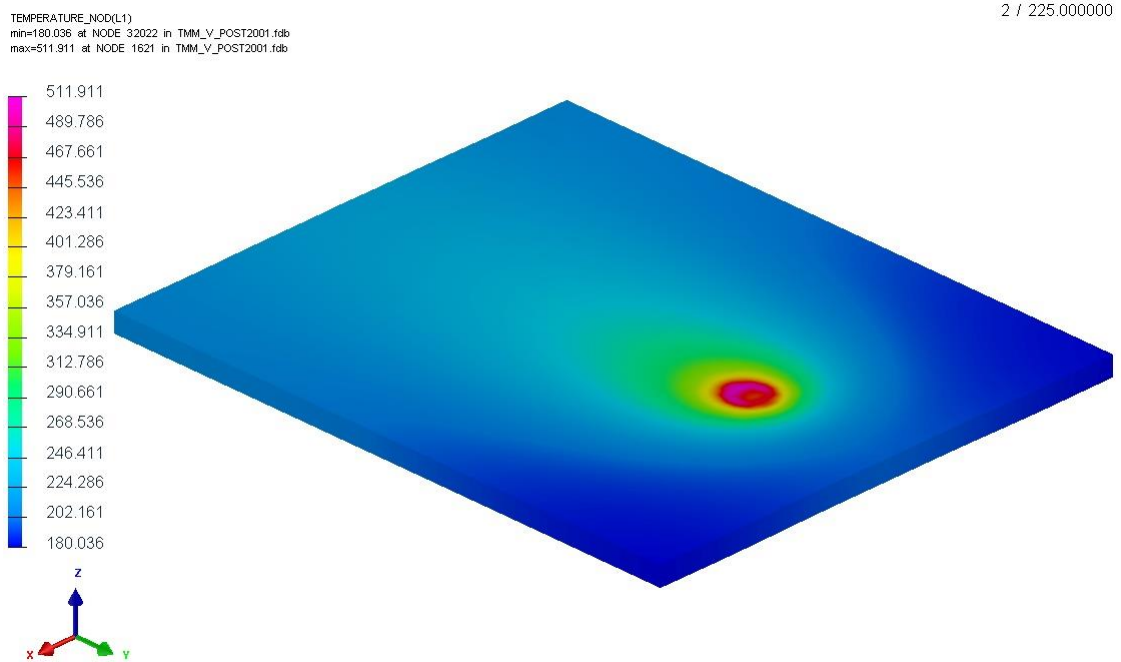
Fig. 4 Temperature field of FSW simulation at time 225 s

Mechanical properties are very important for solving the residual stress state, and therefore they have been the focus of our attention. Mechanical properties of the material AlMg4.5Mn0.7 were taken from literature. The mechanical properties (modulus of elasticity, thermal expansion, yield stress) used for numerical simulation of FSW of two plates from material AlMg4.5Mn0.7 [6]. Results from thermo-mechanical analysis are presented in the Fig. 5.
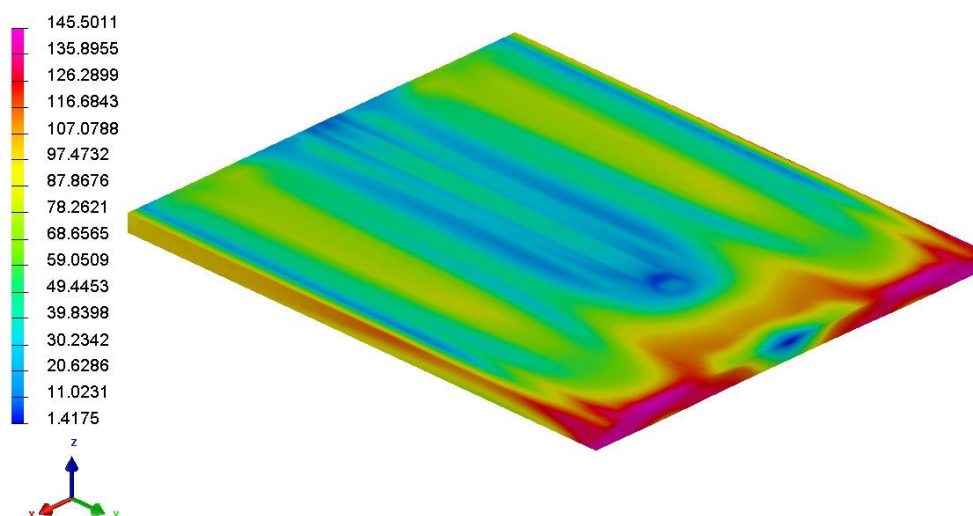
Fig. 5 Von Mises stress field of FSW simulation

CONCLUSION

The present article presents current methods of solving the welding process by conventional as well as friction stir welding processes. Various material parameters, which are a function of temperature, enter the welding process. Many of the parameters need to be experimentally determined. Fig. 2 to 3 are electrode-welded results for V weld joint in 26 layers. In the Fig.4 and Fig. 5 are presented results for friction stir welding. The possibilities of welding simulation in the ANSYS program for both methods of welding will be presented at the conference.

ACKNOWLEDGMENT

LITERATURE

[1] Goldberg, D.E.: Genetic algorithm in Search, Optimization, and Machine Learning, Addison Wesley, Reading, MA 1989.

[2] Goldak, J. A., Chakravarti, A., Bibby, M.: A new finite element model for welding heat sources. In Metallurgical Trans B, 15B, 1984, pp. 299 - 305, ISSN 0039-2472.

[3] L. Chambers. Practical Handbook of Genetic Algorithms, aplications, CRC Press, New York 2001.

[4] Chen, C.M., Kovacevic, R.: Finite element modeling of friction stir welding - thermal and thermomechanical analysis, International Journal of Machine Tools & Manufacture, Vol. 43, 2003, pp. 1319-1326, ISSN 0890-6955

[5] Jančo, R., Écsi, L., Élesztős, P.: FSW numerical simulation of aluminium plates by Sysweld – Part 1. In Strojnícky časopis - Journal of Mechanical Engineering, Vol. 66, No. 1, 2016, pp. 47 - 52, ISSN 0039-2472.

[6] Jančo, R., Écsi, L., Élesztős, P.: FSW numerical simulation of aluminium plates by Sysweld – Part 2. In Strojnícky časopis - Journal of Mechanical Engineering, Vol. 66, No. 2, 2016, pp. 29 - 36, ISSN 0039-2472.

[7] Élesztős, P., Jančo, R., Voštiar, V.: Optimization of welding process using a genetic algorithm. In Strojnícky časopis - Journal of Mechanical Engineering, Vol. 68, No. 2, 2018, pp. 17 - 24, ISSN 0039-2472.

APPLIED MECHANICS 2023

Grand Hotel Sergijo, April 19th – 21st 2023
Piešťany, SLOVAKIA

FLUID–STRUCTURE INTERACTION ANALYSIS OF THE VVER-1000 REACTOR PRESSURE VESSEL INTERNALS AT THE LARGE BREAK LOSS OF COOLANT ACCIDENT ON THE HOT LEG OF THE MAIN COOLANT PIPELINE

MAREK KLEMENC[1], PETR GÁL[2]

The paper presents the results of simulations of the Large-Break Loss of Coolant Accident (LB LOCA) on the hot leg of the main coolant pipeline of the VVER-1000 reactor. The simulations were performed using Fluid-Structure Interaction (FSI) with the two-way coupling approach, where both parts of the model (fluid and structure) interact during the simulation.

KEYWORDS

LOCA, VVER, FSI, Fluid-Structure Interaction, Dytran

INTRODUCTION

The Fluid Structure Interaction (FSI) method is used to solve engineering problems where structural components and the medium interact, e.g., where a structural component is loaded by flow or pressure pulses of the medium and the flow of the medium is affected by the response of the structural component. The application of this approach to nuclear power plants (NPPs) is mainly in the areas of flow-induced vibrations (FIV) and hydraulic shocks, such as water hammer or hydraulic shock at reactor vessel internals (RVI). FIV problems include issues such as fuel assembly vibration, steam line vibration and possibly RVI vibration. The most common application of hydraulic shock is the assessment of Loss of Coolant Accidents (LOCA) caused by rupture of the main coolant pipeline (MCP) loop. LB LOCA is defined as a "guillotine" rupture of one of the MCP legs associated with a sudden loss of coolant. In addition to the loss of coolant, the rupture is characterised by a rapid pressure drop at the rupture site, resulting in a pressure wave propagating at the speed of sound in the medium towards the reactor pressure vessel (RPV). The rapid pressure drop in the ruptured leg and the slow pressure drop in the other intact legs of the MCP form a highly inhomogeneous pressure field with a large pressure difference between the outer and inner surfaces of the RVI, which places a significant load on the RVI.

---

[1] **Ing. Marek Klemenc**, Department of Strength and Lifetime Evaluation, Division of Integrity and Technical Engineering, ÚJV Řež, a. s. Hlavní 130, Řež, 250 68 Husinec, Czech Republic. Tel +420 266 172 085. Email: marek.klemenc@ujv.cz

[2] **Ing. Petr Gál**, Department of Strength and Lifetime Evaluation, Division of Integrity and Technical Engineering, ÚJV Řež, a. s. Hlavní 130, Řež, 250 68 Husinec, Czech Republic. Tel +420 266 172 516. Email: petr.gal@ujv.cz

The analysis evaluates, for example, the elastic and plastic deformation of the RVI, the stress distribution, the resistance to brittle fracture, the pressure difference on the component walls or the possibility of disassembly based on the relative component displacements.

STRUCTURAL AND FLUID MODEL

The model contains both a structural part (RVI) and a fluid part (primary coolant). The model of the RVI consists of 315 400 linear 3D finite elements with 477 413 nodes. Due to the non-symmetrical orientation of the RVI with respect to the RPV nozzles and the RPV consoles (relative rotation of 7°), it was necessary to create a complete model of the RVI without the possibility of taking advantage of symmetry. All internal parts of the reactor (core barrel, core baffle, protective tube unit (PTU)) are made of austenitic titanium-stabilised stainless steel 08Ch18N10T. The fuel assemblies and control rods are replaced in the model by beam elements with similar properties such as overall stiffness and natural frequency. The RPV is modelled by a rigid surface acting as a rigid boundary for the primary coolant (the deformation of the RPV during a LOCA event can be neglected due to the significant stiffness of the RPV). The RVI model is shown in Fig. 1. To evaluate the plastic deformation after the LOCA event, a calculation was performed with a non-linear elastic-plastic material model. The material true stress-true plastic strain curve (Fig. 2) is constructed based on the mechanical properties of the material given in the NTD A.S.I. standard, section II [1]. The effect of irradiation is neglected. This approach is conservative because irradiation increases the yield strength and ultimate strength. In addition, irradiation is negligible or non-existent in the regions of the RVI where the greatest plastic deformation occurs during LOCA.

To model a fluid mesh, the General Coupling method of the Dytran solver is used, which is based on creating a spatial orthogonal mesh of finite volumes around the entire structural model (called MESHBOX). This mesh (MESHBOX) is then trimmed according to the defined surfaces so that it fills only the required volumes. The total number of fluid elements before trimming is 7,000,175 hexahedral volume elements. After trimming the mesh consists of 3 471 646 hexahedral elements. The trimmed fluid mesh is shown in Fig. 1. The primary coolant is considered to be an ideal non-viscous, incompressible fluid. Additives contained in the primary coolant, such as H_3BO_3, are also not considered. The liquid is characterised by bulk modulus K and density ρ. This is sufficient as the temperature in the coolant is assumed to be constant during the calculation. A phase change in the coolant is not considered during the solved time interval (time interval up to 0.1 s in which the liquid phase is present in the reactor).
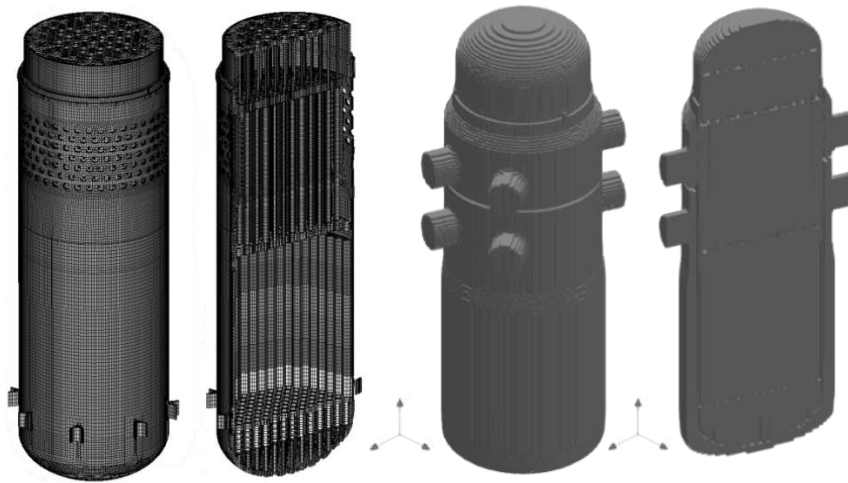

Fig. 1 VVER-1000 reactor vessel internals (left); fluid domain (right)

The time histories of the coolant pressure in the individual reactor nozzles, obtained by thermo-hydraulic simulation in the RELAP5-3D programme, are used as boundary conditions for the solution of the dynamic behaviour of the RVI. In Fig. 2, the pressure time histories in the cold (CL) and hot (HL) legs of the loop 4, whose rupture is postulated, are plotted.
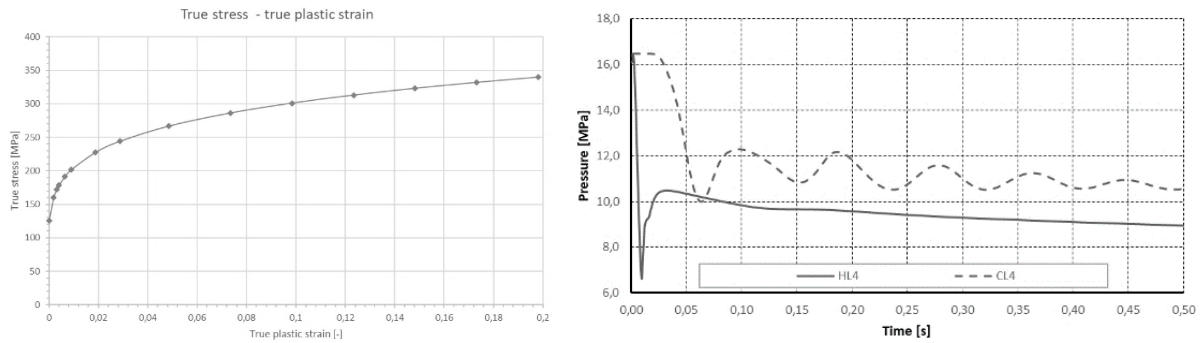

Fig. 2 True stress-true plastic strain curve (left); pressure boundary condition (right)

The interaction between the medium and the structure is achieved by the General coupling function of the Dytran solver. The actual solution of the simulation is performed by two coupled solvers - an explicit solver for solving the dynamics of the HPC (stress and strain in the HPC) and an Eulerian solver for solving the propagation of the pressure wave in the coolant. The two solvers communicate with each other during the computation and transfer information about the mutual force interaction and deformation of the elastic bodies.

RVI INTEGRITY EVALUATION

Based on the results of the analysis, a number of assessments can be made. One of the basic evaluations is the evaluation of the integrity under dynamic loading during LOCA, which consists in evaluating the possibility of fracture initiation from the tip of the postulated crack during the event (the crack is not considered in the model). In accordance with the methodology given in the NTD A.S.I. standard, section IV [1], this evaluation is performed by calculating the J-integral at the nodes of the tip of the postulated crack and comparing its maximum value with the critical value of J_c. According to the criterion given in [1], the elastic part of the J-integral, J^e, multiplied by the safety factor n_J, must be less than the critical value of the J-integral at each at each moment during the event:

$$n_J \cdot J^e < 2{,}5 \cdot 10^{-4} \cdot \sigma_Y(F, T, T_{irr}) \cdot \left[1 - A_{J(e)}\sqrt{1 - exp(-0{,}2 \cdot F)}\right], \qquad (1)$$

where $A_{J(e)} = 0.93$, $\sigma_Y(F,T,T_{irr})$ is the yield stress of the material, which depends on the neutron dose F, the radiation swelling S (which depends on the irradiation temperature T_{irr}) and the instantaneous temperature T, and is determined according to [1]. The calculation of J^e is performed according to the formula:

$$J^e = (1 - \nu^2) \cdot \frac{K_I^2}{E}, \qquad (2)$$

where K_I is the stress intensity factor, ν is Poisson's constant, E is Young's modulus. The stress intensity factor K_I can be determined from the stresses calculated on a linear-elastic model without crack using the formulae given in NTD A.S.I. standard, section IV [1]. It should be noted that relation (2) is valid only for the plane strain state, which is valid for the deepest point of the crack. For the point on the surface (plane stress state), the calculation of the parameter J^e is performed according to formula (2) without the factor $(1 - \nu^2)$. Cracks are postulated in the regions of maximum values of applied stress. The crack is oriented so that its plane is perpendicular to the maximum (first) principal stress. The stress entering the brittle fracture assessment is taken from the linear-elastic model. The locations of the postulated cracks are

shown in Fig. 3. At the locations of the postulated cracks, the component wall bulges due to the pressure difference of the medium on the outer and inner surfaces of the component wall. The time history of the pressure difference is plotted on Fig. 3.
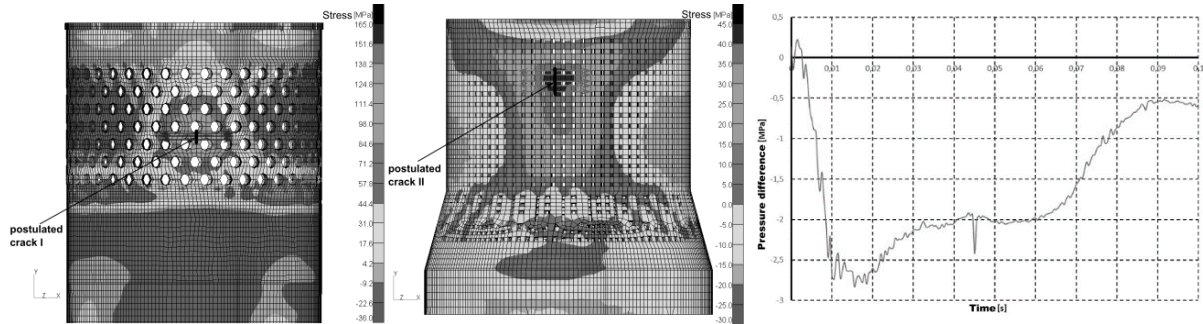
Fig. 3 Crack I - outer surface of the core barrel at the point opposite the hot nozzle of loop 4 (axial) - maximum principal stress at time 17,9 ms; crack II - inner surface of the PTU opposite the hot nozzle of loop 4 (axial) - maximum principal stress at time 11,4 ms; time history of the pressure difference on the outer and inner surface of the core barrel wall opposite the hot nozzle of the ruptured loop 4

The time histories of $n_J \cdot J^e$ for the two postulated cracks calculated from equation (2) are plotted in Fig. 4. During the postulated hot leg rupture, the critical value of the J-integral determined by equation (1) of 54.6 kJ/m^2 is not exceeded, indicating that the structural integrity of the RVI is preserved after the LB LOCA.
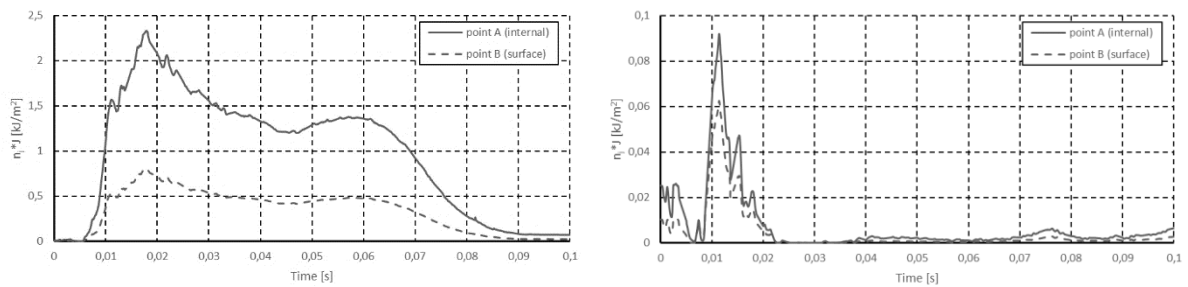
Fig. 4 Time histories of $n_J \cdot J^e$ for the deepest and surface point of the axial crack postulated on the outer surface of the core barrel, crack I (left); crack II (right).

CONCLUSION

This paper presents the procedure for evaluating the RVI of the VVER-1000 reactor during the LB LOCA design accident on the MCP hot leg using FSI analysis in the Dytran solver, and evaluates the integrity of the RVI during the event.

FSI analysis is widely used in the nuclear industry to evaluate hydraulic pressure shocks or component vibrations induced by fluid flow. This approach provides detailed results throughout the event on complex models such as nuclear reactor internals or fuel assemblies that would otherwise be very difficult to obtain. At ÚJV Řež, a. s., we have evaluated the RVI of the VVER-1000 and VVER-440 reactors in a similar way for a postulated rupture of the cold leg of the MCP.

LITERATURE

[1] Normativně Technická Dokumentace A.S.I., sekce II, III, IV, 2020
[2] DytranTM 2018 Theory Manual, MSC Software

COMPARISON OF MULTILAYER PERCEPTRON AND HIGHER ORDER NEURAL NETWORK'S ABILITY TO SOLVE INITIAL VALUE PROBLEM

PATRIK KOVÁŘ[1], JIŘÍ FÜRST[2]

In engineering applications, there are many physical phenomena governed by ordinary differential equations which are solved using approximative approaches called numerical methods. This paper deals with an alternative method, i.e., initial value problem solution using artificial neural networks. Basics of the method are introduced and comparison of multilayer perceptron network and higher order neural network ability to solve the test initial value problem is performed.

KEYWORDS

Ordinary differential equations; Approximative solvers; Higher order neural networks

INTRODUCTION

When ordinary differential equations (ODEs) desribing natural phenomena are solved, only rarely can an analytic formula be found for the solution [5]. To obtain results, numerical methods are used istead in engineering tasks. An alternative approach is solve ODE by artificial neural network (ANN) [4].

In a field of artificial intelligence and machine learning (AI&ML) there are many means of architectures and learning approaches. One of them is supervised learning which is relatively fast and the implementation is very straightforward. Unfortunately, there is one huge disadvantage - learning data set. It contains inputs and corresponding targets for each sample in the data set. As one can see, cornerstone of the learning is training data set which is correct and precise and in this case the problem can occur.

The present paper deals with an alternative method called physics informed neural network (PINN) which is not training data set dependent in that sense we do not have to have labeled targets with its correct value. The only necessary information we need are differential equations which have to be solved. Basic ideas of the method are introduced and ability to solve ODE by well known [6] multilayer perceptron network (MLP) and higher order neural network (HONN) is compared in terms of degrees of freedom (DoFs) of individual approximative solver and defined loss or cost function value.

---

[1] **Ing. Patrik Kovář**, Center of Aviation and Space Research, Czech Technical University in Prague. Jugoslávských partyzánů 1580/30, Prague, Czech Republic. Email: Patrik.Kovar@fs.cvut.cz

[2] **Prof. Ing. Jiří Fürst, Ph.D.**, Department of Technical Mathematics, Faculty of Mechanical Engineering, Czech Technical University in Prague. Karlovo náměstí 13, Prague, Czech Republic.

TEST INITIAL VALUE PROBLEM

As it has been already discussed, the only information we need is differential equation with appropriate initial conditions. Let us assume initial value problem in form

$$y' = -2xy, y(0) = 1. \tag{1}$$

One can see that exact solution of this equation can be obtained as

$$y = \exp(-x^2). \tag{2}$$

METHODOLOGY

From a mathematical point of view, processing of the information within neuron is consisted of two separated mathematical operations [3]. The first, synaptic operation contains weights of the synapse which represents storage of knowledge and thus the memory for previous knowledge. The second is somatic operation which provides various mathematical operations such as thresholding, non-linear activation, aggregation, etc. Neural output of the unit $\tilde{y}$ is scalar as it is indicated in Figure 1 (left).

$$\tilde{y} = \sigma(s). \tag{3}$$

Let us assume N-th order neural unit, then neural output can be expressed as [2]

$$s = w_0 x_0 + \sum_{i=1}^{n} w_i x_i + \sum_{i=1}^{n} \sum_{j=i}^{n} w_{ij} x_i x_j + \cdots + \sum_{i_1=1}^{n} \cdots \sum_{i_N=i_{N-1}}^{n} w_{i_1 i_2 \ldots i_n} x_{i_1} x_{i_2} \ldots x_{i_n}, \tag{4}$$

where $x_0 = 1$ denotes threshold and n stands for length of input feature vector.

Designed neural network is consisted of two neurons in the first layer and single neuron in the output layer as it can be seen in the Figure 1 (right). Synaptic operation of all neurons was assumed as quadratic polynomial in the designed ANN. As the activation function $\sigma(\cdot)$ linear was used in the first layer and in the output layer. Error propagation through the network is performed using multilayer backpropagation algorithm described in [2].
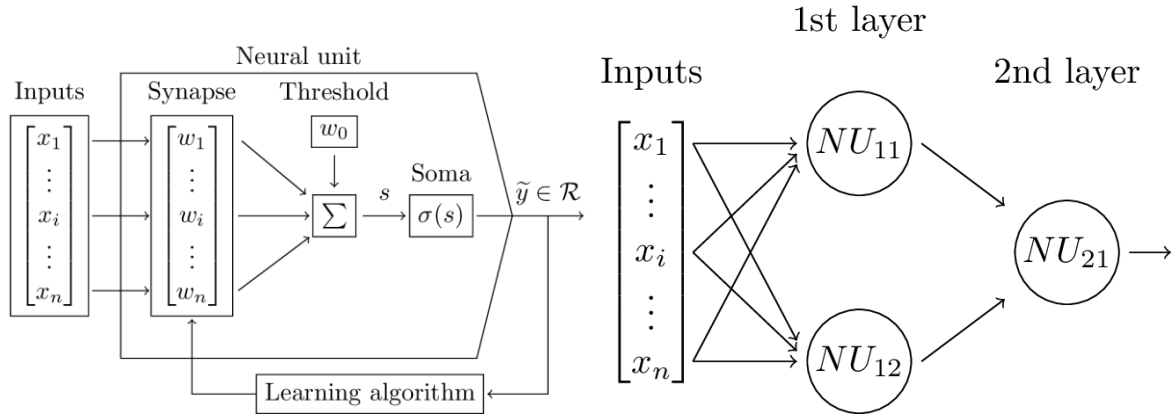
Fig. 1 Neural network: single neural unit (left); shallow neural network (right).

As we could see, the neural output is strongly dependent on the neural memories represented by vector of the weights $\vec{W}$. Thus, processing of the information should be done in a way which leads neural unit to be learned. Batch Levenberg-Marquardt algorithm for weights updating [4] is employed in this work

$$\vec{W} = \vec{W} + \Delta\vec{W}; \text{where} \quad \Delta\vec{W}^T = -\left(\vec{J}^T\vec{J} + \frac{1}{\mu}\vec{I}\right)^{-1} \vec{J}^T\vec{e}. \tag{5}$$

Coefficient μ is learning rate, $\vec{I}$ is $n_w \times n_w$ identity matrix, n_w number of weights and $\vec{J}$ represents $n \times n_w$ Jacobian matrix.

Since desired outputs are known, machine learning is called as supervised learning which is the task of learning a function that maps input to an output represented with cost function $\vec{e}$ that has to be minimized. In case of physics informed neural networks, loss function is defined according to equation (1) as

$$\vec{e} = \left\|\tilde{y}' + 2x\tilde{y}\right\|^2 + K_1\left\|\tilde{y}(0) - 1\right\|^2, \tag{6}$$

where coefficient $K_1 = 1$ imposes initial conditions, x are inputs for the PINN and $\tilde{y}$ are outputs of the network. Derivatives of the neural outputs $\tilde{y}'$ are obtained through reverse mode of automatic differentiation algorithm described in [1]. Referring to equation (1), the first term on the right-hand side quantifies how much the solution predicted by ANN differs from ODE definition and second term is the initial condition loss and it quantifies how much the predicted solution deviates from satisfying the initial condition.

RESULTS

Comparison of multilayer perceptron (MLP) and higher order neural network's (HONN) ability to solve initial value problem is presented. MLP network was consisted of ten neurons in the first layer and one neuron in the output layer which results into 31 optimizable parameters. On the other hand, designed HONN had only 13 learnable weights. In both cases, learning rate μ was set to constant value $\mu = 0.05$ and end of the training was set to $4e4$ epochs.

Twenty-one discrete points are assumed for the test initial value problem which are equally distributed in range $x \in \langle 0; 2\rangle$. There is a learning progress comparison in Figure 2 (left). Firstly, although there is a decrease in the training error performed by MLP is much faster than HONN at the beginning, resulting value of the loss function is not as small as in case of HONN. Secondly, convergence history showed as that HONN got learned the pattern of the model problem more than twofold earlier.
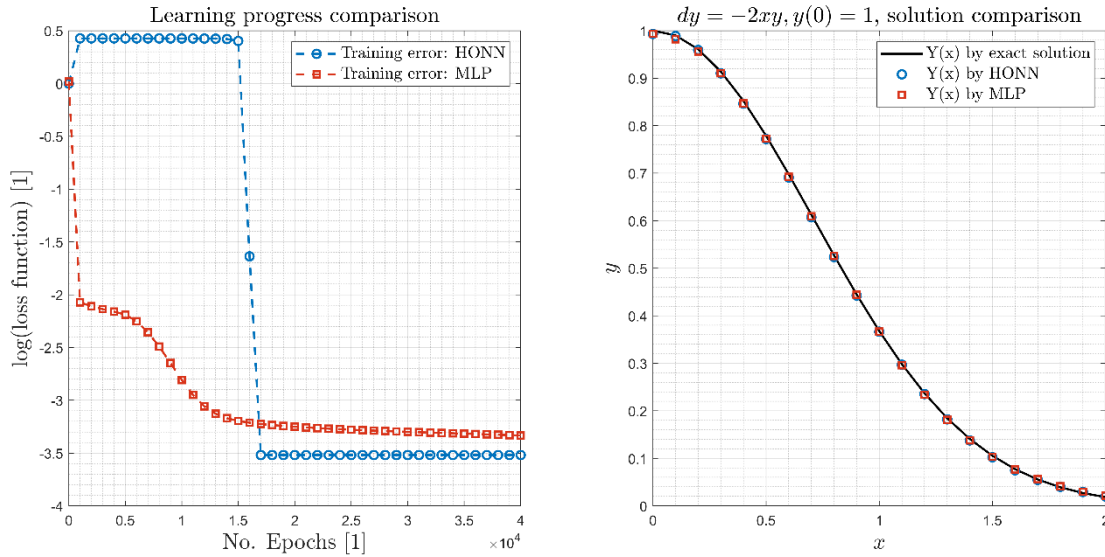
Fig. 2 Results: Progress of the loss function value in logarithmic scale (left); comparison of results obtained using different neural networks against exact solution (right).

At the first sight, both solutions are in a good correspondence with the exact solution expressed with equation (2) as it can be seen in the Figure 2 (right). To quantify how much obtained solutions differ from the exact solution, mean squared error (MSE) is employed

$$MSE = \frac{1}{n}\sum_{i=1}^{n}(y_i - \tilde{y}_i)^2. \tag{7}$$

Main results and comparisons are listed in the following table Tab. 1. It turned out that ability to solve test initial value problem by MLP network was outperformed by designed HONN. Number of learnable parameters (DoFs) and speed of convergence were more than twofold favorable. Loss function value and MSE were also smaller in case of HONN.

Tab. 1 Comparison of the mean squared errors performed by individual neural networks.

Neural network	No. parameters	Loss function	After epochs	MSE
MLP	31	$3.644e-4$	$40e3$	$1.487e-5$
HONN	13	$3.029e-4$	$17e3$	$1.357e-5$

CONCLUSION

Basic ideas of the alternative approach to solve ordinary differential equations were introduced. The main advantage of presented physics informed neural networks (PINNs) is that they are not burdened by errors that may appear in the training data set.

Based on the defined loss function by equation (6), two network architectures were trained to solve simple test initial value problem and the comparison of multilayer perceptron and higher order neural network's ability to solve discussed problem was presented. MLP was outperformed by HONN in number of DoFs, speed of the convergence and solution accuracy.

Further work should aim to more complex problem solution using PINN assembled with higher order neural units. Firstly, include boundary value problem and mixed problem. Higher order derivatives should be also more discussed. At last, but not least, partial differential equations and extension to higher dimensional problems should be more studied.

ACKNOWLEDGMENT

LITERATURE

[1] Baydin, A. G., Pearlmutter, B. A, Radul, A. A. and Siskind, J. M. Automatic differentiation in machine learning: a survey. Journal of Machine Learning Research 18, p. 1-43. 2018.

[2] Gupta, M. M., Jin, L. and Homma, N. Static and dynamic neural networks: from fundamentals to advanced theory. John Wiley & Sons, 2004.

[3] Gupta, M. M., Bukovsky, I., Homma, N., Solo, A. and Hou, Z. G. Fundamentals of higher order neural networks for modeling and simulation. In Artificial Higher Order Neural Networks for Modeling and Simulation, IGI Global. p. 103-133. 2013.

[4] Lagaris, I. E., Likas, A. and Fotiadis, D. I., Artificial neural networks for solving ordinary and partial differential equations. IEEE transactions on neural networks, 9(5), p. 987-1000.

[5] LeVeque, R. J., Finite difference methods for ordinary and partial differential equations: steady-state and time-dependent problem. Society for Industrial and Applied Mathematics, 2007.

[6] Rosenblatt, F. The perceptron: a probabilistic model for information storage and organization in the brain. Psychological review 65(6), p. 386. 1958.

Mechanics of Stabilization in Reverse Shoulder Arthroplasty

Adam Kratochvíl[1], Matej Daniel[2], Jan Votava[3], David Pokorný[4], Petr Fulín[5]

The stability of the shoulder joint depends mostly on dynamic stabilization mechanisms. Success of the reverse shoulder arthroplasty depends mostly on the deltoid muscle to achieve movement and stability. Therefore, insertion of deltoid muscle is moved inferiorly by prolonging humerus. This cause prestress in the muscle and help stabilize the shoulder joint, but on the other hand this also leads to overloading the muscle, which can lead to the loss of mobility.

KEYWORDS

Shoulder Joint, Reverse shoulder arthroplasty, Deltoid muscle, Prolonging humerus

INTRODUCTION

Musculoskeletal geometry of the glenohumeral joint is altered during total reverse shoulder arthroplasty (TSA) [1]. The change is caused by both, the displacement of the center of rotation of the shoulder joint, and the prolongation of the humerus. Hence, it leads to the displacement of distal muscles, and this results in prolonging and prestressing of these muscles. The exact determination of real postoperative changes in the musculoskeletal geometry and the determination of the prolonging of the humerus is a complex problem. Solution leads to optimizing postoperative stability in the shoulder and thereby optimizing the replacement life.

---

[1] **Ing. Adam Kratochvíl**, Department of Mechanics, Biomechanics and Mechatronics, Faculty of Mechanical Engineering, Czech Technical University in Prague. Technická 6, Prague, Czechia. Tel +420 224 352 542. Email: adam.kratochvil@fs.cvut.cz

[2] **prof. RNDr. Matej Daniel, Ph.D.**, Department of Mechanics, Biomechanics and Mechatronics, Faculty of Mechanical Engineering, Czech Technical University in Prague. Technická 6, Prague, Czechia. Tel +420 224 352 518. Email: matej.daniel@cvut.cz

[3] **Ing. Jan Votava**, Department of Mechanics, Biomechanics and Mechatronics, Faculty of Mechanical Engineering, Czech Technical University in Prague. Technická 6, Prague, Czechia. Tel +420 224 352 542. Email: jan.votava@fs.cvut.cz

[4] **prof. MUDr. David Pokorný, CSc.**, Department of Orthopaedics, First Faculty of Medicine, Charles University and University Hospital Motol. V Uvalu 84, Praha 5, Czechia. Tel +420 +420 224 433 933. Email: david.pokorny@lf1.cuni.cz

[5] **doc. MUDr. Petr Fulín, Ph.D.**, Department of Orthopaedics, First Faculty of Medicine, Charles University and University Hospital Motol. V Uvalu 84, Praha 5, Czech Republic. Tel +420 224 433 980. Email: petr.fulin@lf1.cuni.cz

METHODS

A retrospective study included patients that have previously undergo TSA at the Motol University Hospital, Czechia. Only patients with SMR Reverse Shoulder System (Lima Corporate, San Daniele del Friuli, Italy) were analyzed [2] (Fig. 1). The humerus prolonging of the humerus in each patient was evaluated using semi-automatic method. This method uses preoperative X-ray and CT scan and postoperative X-ray. These datasets need to be used in each patient due to lack of knowledge about precise resection line of the humerus and rotation of the humerus in both X-rays. X-rays are fitted on each other by contour of clavicle and resection line position is evaluated by fitting postoperative X-ray on 3D model from preoperative CT scan (Fig. 2). Thirty patients were evaluated in this pilot study.
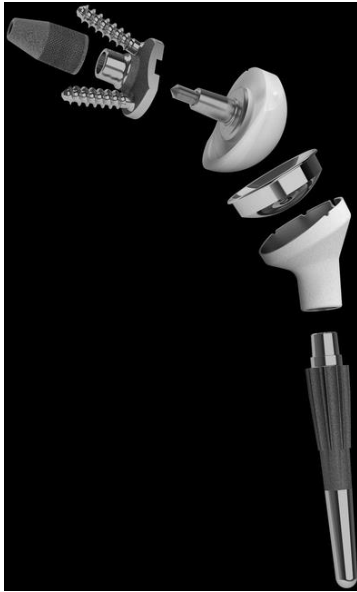
Fig. 1 SMR Reverse Shoulder System [2]
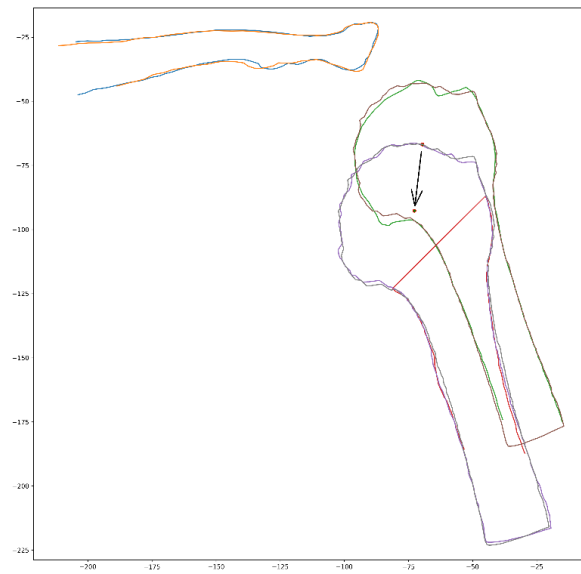
Fig. 2 Shift of the humerus during TSA using reverse replacement, dimensions are in mm.

An average prolonging of the humerus was evaluated out of the thirty patients and the shift of the center of rotation (CoR) was used as determined by Saltzman et. al. [3] (12 mm inferiorly and 27 mm medialy). This data was used in kinematic model of shoulder joint based on model published by Wu et. al. [4] [5, 6, 7]. Changes in muscle forces, the load in the shoulder joint and the direction of resultant force were evaluated.
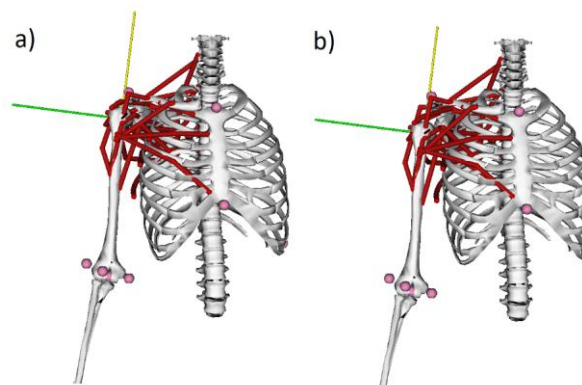
Fig. 3 Musculoskeletal model of shoulder – a) anatomical shoulder, b) with prolonged humerus and shifted CoR

RESULTS

Average displacement of the humerus is 19 mm inferiorly and 8 mm medially. Muscle forces in total and in each muscle and were evaluated during arm elevation in anatomical shoulder, in shoulder with shifted CoR and in shoulder with shifted CoR and prolonged humerus (Fig. 4, Fig. 5). The last state is the most plausible according to the changes in musculoskeletal geometry during reverse TSA. The movement of the arm was calculated without any load and with 2 kg load.
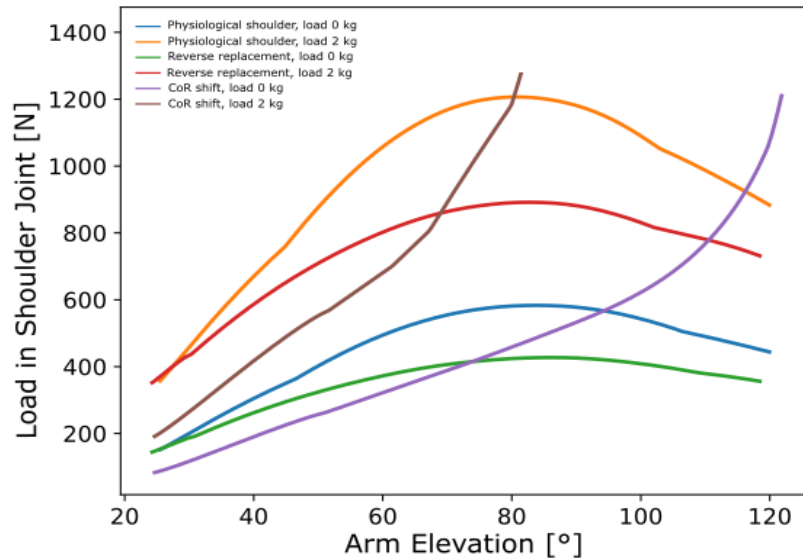
Fig. 4 Total load in shoulder during arm elevation
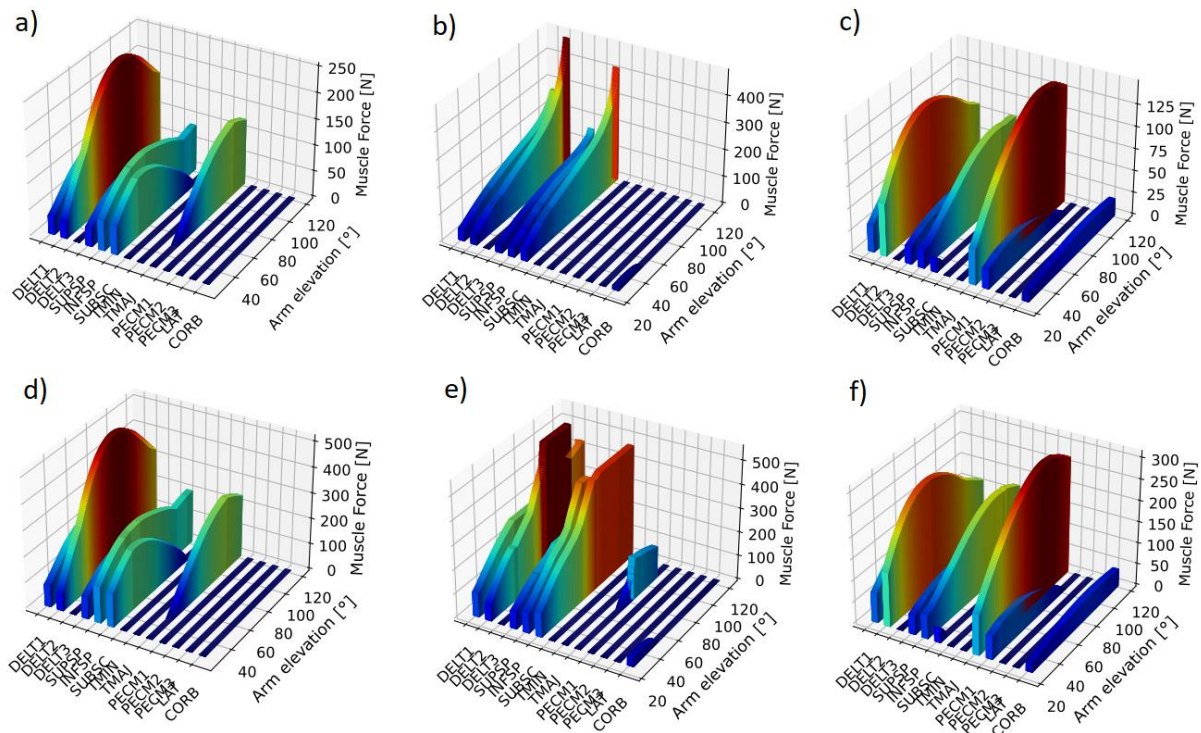
Fig. 5 Forces in muscles during arm elevation without load (a–c) and with 2 kg load (d–e). Anatomical shoulder a), d); with shifted CoR b), e); with shifted CoR and prolonged humerus c), f).

Stability of the shoulder depends on magnitude and angle of the shoulder load vector in glenohumeral plane. The magnitude is shown in Fig. 4 and the angle is shown in Fig. 6 as well as its decomposition to frontal and transversal plane.
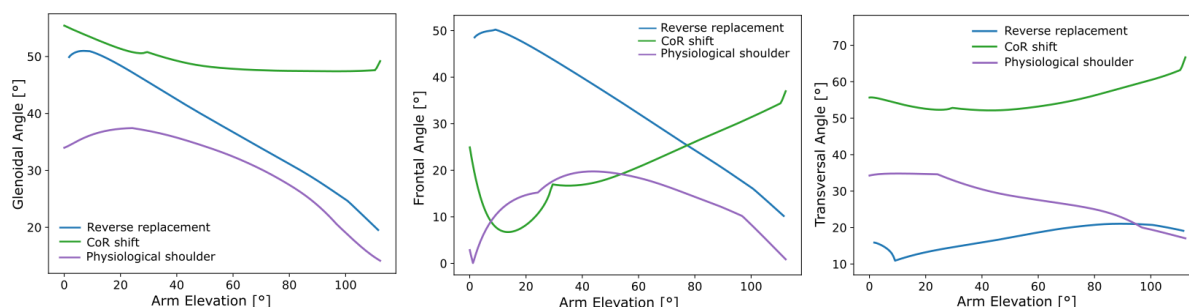
Fig. 6 Angle of shoulder load vector in different planes

CONCLUSION

The study shows that the humerus is displaced inferiorly and medialized as well as the CoR during reverse TSA [3]. Both displacements lower the force in muscles by enhancing moment arm of abductor muscles as shown in Fig. 4.

The glenohumeral angle of the resultant force is lower in anatomical shoulder than in reverse TSA. Thus, stability of anatomical shoulder is higher than in reverse TSA as shown in Fig. 6. However, in transversal plane the angle of resultant force is smaller in reverse TSA than in anatomical shoulder.

ACKNOWLEDGMENT

LITERATURE

[1] Rugg CM, Coughlan MJ, Lansdown DA. Reverse Total Shoulder Arthroplasty: Biomechanics and Indications. Curr Rev Musculoskelet Med. 2019 Dec 1;12(4):542–53.

[2] Hans-Rudolf Bloch. The SMR® Shoulder System of Lima Corporate. In Mark Frankle, Scott Marberry, and Derek Pupello, editors, Reverse Shoulder Arthroplasty, pages 417–424. Springer International Publishing, Cham, 2016.

[3] Saltzman MD, Mercer DM, Warme WJ, Bertelsen AL, Masten FA. A method for documenting the change in center of rotation with reverse total shoulder arthroplasty and its application to a consecutive series of 68 shoulders having reconstruction with one of two different reverse prostheses. Journal of Shoulder and Elbow Surgery [online]. 2010, 19(7), 1028-1033.

[4] Wu W, Lee PVS, Bryant AL, Galea M, Ackland DC. Subject-specific musculoskeletal modeling in the evaluation of shoulder muscle and joint function. Journal of Biomechanics. 2016 Nov;49(15):3626–34.

[5] Goetti P, Denard PJ, Collin P, Ibrahim M, Hoffmeyer P, Lädermann A. Shoulder biomechanics in normal and selected pathological conditions. EFORT Open Rev. 2020 Sep 10;5(8):508–18.

[6] Charlton IW, Johnson GR. A model for the prediction of the forces at the glenohumeral joint. Proc Inst Mech Eng H. 2006 Aug 1;220(8):801–12.

[7] Ghafurian S, Galdi B, Bastian S, Tan V, Li K. Computerized 3D morphological analysis of glenoid orientation. Journal of Orthopaedic Research. 2016;34(4):692–8.

APPLIED MECHANICS 2023

Grand Hotel Sergijo, April 19th – 21st 2023
Piešťany, SLOVAKIA

POSSIBILITIES OF MECHANICAL TESTING AND EVALUATION OF RIB FRACTURES

KRISTÝNA KUBÁŠOVÁ[1], RADEK SEDLÁČEK[1], TOMÁŠ SUCHÝ[1,2], LUCIE VIŠTEJNOVÁ[3], MARIA ŠTĚPÁNKOVÁ[4], PAVEL KLEIN[3], JITKA LUŇÁČKOVÁ[5], MARTIN BARTOŠ[5]

Rib fractures are very common injuries, but there is no definitive answer to their treatment. There are two main approaches to this treatment – the conventional method and the surgical method. Different approaches are used to evaluate their effectiveness, one of which is mechanical evaluation. Several methodologies can be chosen for mechanical testing – using material or structural parameters. Therefore, all advantages and disadvantages need to be considered.

KEYWORDS

Mechanical properties; ribs; fractures; experiment.

INTRODUCTION

Rib fractures are the most common injuries to the chest wall, most often resulting from car accidents, falls, or sports. Typically, one rib is fractured or cracked in more than one place (segmental fractures) or several ribs above each other (serial fractures). Fatigue fractures induced by severe coughing, usually accompanied by cancer or osteoporotic disease, is also a possible cause. Despite their frequency, the indication for the conservative (without stabilization) or for the surgical therapy (with fixation) varies. Unstabilized rib fractures are painful, require analgesic supplementation and result in long-life complications. This clinical outcome, without certain success, led clinicians and biomechanists to revise the benefits of the

---

[1] **Ing. Kristýna Kubášová**, **Ing. Radek Sedláček, Ph.D., doc. Ing. Tomáš Suchý, Ph.D.** Department of Mechanics, Biomechanics and Mechatronics, Faculty of Mechanical Engineering, CTU in Prague. Technicka 4, 160 00 Praha 6. Email: kristyna.kubasova@fs.cvut.cz, radek.sedlacek@fs.cvut.cz.

[2] **doc. Ing. Tomáš Suchý, Ph.D.** Institute of Rock Structure and Mechanics, Czech Academy of Sciences, V Holešovičkách 41, 182 09 Prague 8, Czech Republic. Email: suchy@irsm.cas.cz.

[3] **Ing. Lucie Vištejnová, Ph.D.**, **Ing. Pavel Klein, Ph.D.** Charles University, Medical Faculty in Pilsen, Biomedical Center, alej Svobody 1655/76, 301 00 Pilsen. Email: lucie.vistejnova@lfp.cuni.cz.

[4] **MUDr. Maria Štěpánková**. Department of Thoracic Surgery, University Hospital Basel. Spitalstrasse 21, 4031 Basel, Switzerland. Email: stepankov.maria@gmail.com.

[5] **MDDr. Jitka Luňáčková, MUDr. MDDr. Martin Bartoš, Ph.D.**. Institute of Dental Medicine, First Faculty of Medicine, Charles University, General University Hospital in Prague, Katerinska 32, 12108 Prague 2. Email: jitka.lunackova@lf1.cuni.cz, martin.bartos@lf1.cuni.cz.

surgical therapy. Today, this procedure is mainly chosen for unstable chest and in case of progressive decline in pulmonary function, however, the evidence for introducing of this treatment into routine practice is missing. Therefore, we aimed to evaluate the mechanical aspects of stabilized and unstabilized rib fractures by different mechanical approaches and parameters [1].

MECHANICAL TESTING

In our study, we evaluated the healing progress of ribs with surgically induced fractures (pig, age 7–10 months) that were left without fixation or were stabilized with a metal splint for 3 and 8 weeks. From a biomechanical aspect, all long bones are subjected to combined stresses, but unlike flat bones, bending predominates. The experimental methodology was based on the determination of different mechanical properties during three-point bending test. Six different parameters were calculated to quantify and to compare the differences between the two surgical procedures, namely maximum force, maximum bending moment, maximum bending stress (strength), external bending stiffness, flexural strength, and strain energy. However, each of these parameters reflects the different characteristics (quality and quantity) of healed fractures.

The experimental biomechanics results suggested the possibility that the healing process of fixed and unfixed ribs is fundamentally different in response to different biological needs. In ribs, strength is the most important factor [1]. Therefore, the difference in the healing process of fixed and unfixed ribs is mainly manifested in terms of callus organization and geometry, which are significantly more excessive in the case of unfixed ribs. It is the different geometry of the bones and callus that can lead to such differences as have been observed in mechanical tests. Different healing processes, especially different rib geometries, raise the question of how to evaluate the resulting healing process, whether using material or structural parameters. The determination of the material parameters of healed bone is complicated by the presence of callus, which is composed of both newly formed bone and fibrocartilage tissue in unknown proportions and whose material composition changes during the healing process. In other words, material parameters (e.g. flexural strength) fail in the absence of the ability to accurately determine the cross-sectional areas of newly formed bone, and structural parameters (e.g. failure loads) cannot compare ribs that have different geometries.

To better understand the results from mechanical tests of differently treated ribs, we further evaluated the structural parameters in the intact ribs and utilized them to normalize the values from surgically treated ribs. The healing process was evaluated using the ratio of structural parameters obtained from mechanical tests of geometrically similar ribs before and after surgical intervention followed by the two healing periods. In this way, it was possible to assess to what extent and at what time the healed ribs were able to regain their original mechanical properties.

CONCLUSION

The structural parameters reflect the size of the defect and the material parameters of its composition, and it always depends on what we want to find out from the analysis – whether the quality or the quantity of the healed new tissue is important.

ACKNOWLEDGMENT

LITERATURE

[1] Davy D.T., Connolly J.F. The biomechanical behavior of healing canine radii and ribs. Journal of Biomechanics. 1982, Vol. 15, No. 5 (235-247).

APPLIED MECHANICS 2023

Grand Hotel Sergijo, April 19th – 21st 2023
Piešťany, SLOVAKIA

FINITE ELEMENT ANALYSIS OF CRACK TIP PLASTIC ZONES IN 3D

RADEK KUBÍČEK[1], TOMÁŠ VOJTEK[2], PAVEL POKORNÝ[3], LUBOŠ NÁHLÍK[4], PAVEL HUTAŘ[5]

Many studies dealing with fatigue crack tip plastic zones assume only two-dimensional plane strain or plane stress condition. This has non-negligible impact on a shape and a size of plastic zones. The purpose of this study was to emphasize the difference between plastic zones obtained from 2D simulations and 3D simulations in CT specimen made of the EA4T steel. The results confirmed the importance of 3D simulations with real crack front curvature.

KEYWORDS

Plastic zone, crack front shape, finite element method, plane strain, plane stress

INTRODUCTION

Fatigue crack growth rate is influenced by the crack closure phenomenon, which is important for estimations of residual fatigue life of components. One of the most described closure mechanisms is the plasticity-induced crack closure (PICC). The plastic deformation around the crack tip is an important factor for studying PICC. This plastic zone can be estimated analytically by applying the von Mises yield criterion on the stress fields ahead of the crack tip, yielding occurs when von Mises stress is equal to yield strength σ_y. Forward plastic zone is given at the maximal loading $K_{\max}$ and it can be obtained either by Irwin's second order plastic zone size estimation assuming redistribution of stresses [1,2], see Eq. (1), or from the Dugdale-Barenblat [3,4] strip-yield model in case of plane stress, see Eq. (2). Another estimation using flow stress σ_0 was used by Dougherty [5] or Solanki [6], see Eq. (3), where $\alpha = 1$ for plane

[1] **Ing Radek Kubíček**, Institute of Physics of Materials, Czech Academy of Sciences, Zizkova 22, 612 62 Brno, Czech Republic; Department of Engineering Mechanics, Faculty of Mechanical Engineering, Brno University of Technology. Technicka 2896/2, 61669 Brno, Czech Republic. Tel +420 532 290 347. Email: kubicek@ipm.cz

[2] **Ing. Tomáš Vojtek, Ph.D.**, Institute of Physics of Materials, Czech Academy of Sciences, Zizkova 22, 612 62 Brno, Czech Republic. Tel +420 532 290 362. Email: vojtek@ipm.cz

[3] **Ing. Pavel Pokorný, Ph.D.**, Institute of Physics of Materials, Czech Academy of Sciences, Zizkova 22, 612 62 Brno, Czech Republic. Tel +420 532 290 362. Email: pokorny@ipm.cz

[4] **doc. Ing. Luboš Náhlík, Ph.D.**, Institute of Physics of Materials, Czech Academy of Sciences, Zizkova 22, 612 62 Brno, Czech Republic. Tel +420 532 290 358. Email: nahlik@ipm.cz

[5] **doc. Ing. Pavel Hutař, Ph.D.**, Institute of Physics of Materials, Czech Academy of Sciences, Zizkova 22, 612 62 Brno, Czech Republic. Tel +420 532 290 351. Email: hutar@ipm.cz

stress and $\alpha = 3$ for plane strain. Plastic zone in the middle of a specimen is suppressed by crack-tip triaxiality which leads to three times smaller size in comparison with plastic zone size at the free surface [2].

$$r_p = \frac{1}{\alpha\pi}\left(\frac{K_{max}}{\sigma_y}\right)^2,$$ (1)

$$r_p = \frac{\pi}{8}\left(\frac{K_{max}}{\sigma_y}\right)^2,$$ (2)

$$r_p = \frac{1}{2\alpha\pi}\left(\frac{K_{max}}{\sigma_0}\right)^2,$$ (3)

Reverse plastic zone $r_{p,c}$, also called as cyclic plastic zone, is developed during the unloading and is approximately one quarter of the forward plastic zone [7].

FINITE ELEMENT MODEL

The study deals with CT (compact tension specimen) which is loaded and unloading by forces inducing stress intensity factor range $\Delta K = 15$ MPa $\cdot$ m$^{1/2}$ at the load ratio $R = 0.1$, modelling the real experimental conditions. Since the given geometry allows using two symmetries, only one-fourth of CT was modelled, see Fig. 1. The width $W = 50$ mm and the crack length $a = 15$ mm were assumed and the thickness B of 3D model was set to 10 mm.

The material (EA4T railway axle steel) was assumed to be homogenous, isotropic, elastic-plastic material model with kinematic hardening and Young modulus $E = 200$ GPa and Poisson ratio $\nu = 0.3$, see Fig. 2. According to these material data, the forward plastic zone size can be calculated by formulas (1)–(3), see Tab. 1.

Tab. 1: Plastic zone size assumptions

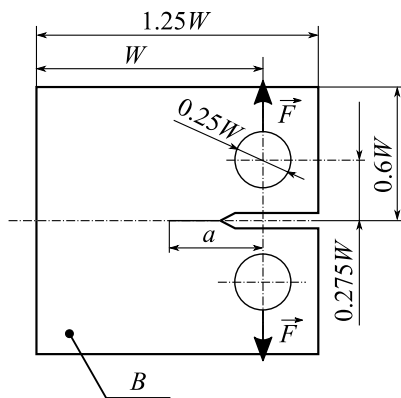|	Irwin Eq. (1)	Dugdale-Barenblat Eq. (2)	Dougherty, Solanki Eq. (3)
Plane stress	0.40 mm	0.49 mm	0.14 mm
Plane strain	0.13 mm	–	0.05 mm

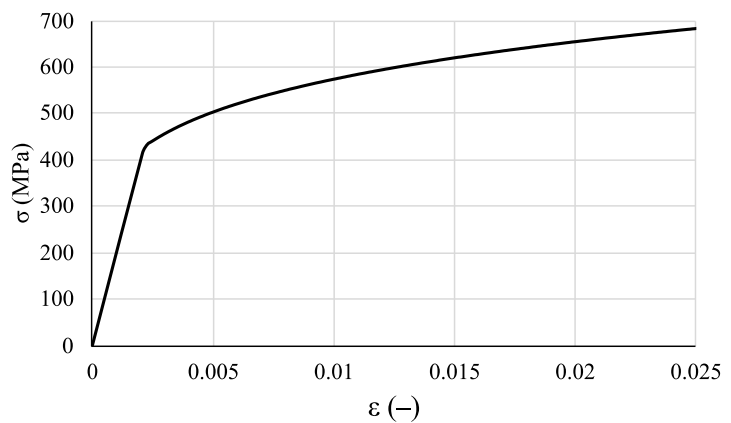Fig. 1: Geometry of the CT specimen

Fig. 2: Cyclic stress-strain curve of the investigated material

PLASTIC ZONES

The plastic zones obtained by 2D finite element method simulations assuming either plane stress or plane strain condition are plotted in Fig. 3. Quadratic eight-node plane elements were used for both simulations. The plane strain condition assumes no out-of-plane deformation, which is widely used to study processes in the middle of specimens with non-negligible thickness. On the other hand, the plane stress condition assumes no stresses in the direction perpendicular to the plane. This should represent stress-strain state at the free surface. Fig. 3 shows a much bigger plastic zone in plane stress condition, which agrees with the theory that the plastic zone is three times smaller in plane strain. The Irwin's second order plastic zone size estimation for plane stress and plane strain condition in the crack growth direction are 0.4 mm and 0.13 mm respectively. Assuming radial zone, it leads to the radii (heights in the opening direction y) of 0.2 mm and 0.065 mm.
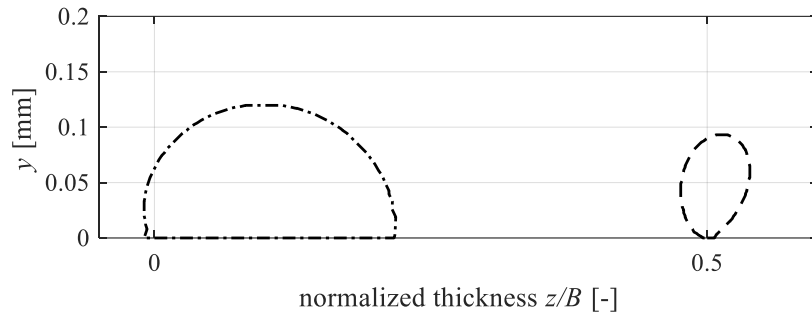
Fig. 3: Plastic zones – 2D simulations

Fig. 4 and Fig. 5 show contours of plastic zones from the free surface, $z/B = 0$, to the middle of the CT specimen, $z/B = 0.5$, obtained from 3D FEM simulation using higher order solid elements with three degrees of freedom per node. There were no big differences in plastic zone size through the thickness, when the straight crack front was modelled. However, straight crack fronts do not naturally occur in fatigue cracks. Therefore, the simulation with real crack front shape described by exponential function Eq. (4) was conducted. Modelling the real crack, the plastic zones close to the free surface increased in comparison with the straight crack. Opposite situations occurred in the middle of the specimen, where the plastic zone contours were slightly smaller. The difference between the plastic zone at the free surface and in the midplane was substantial. The height and width of the plastic zone at the free surface of the CT specimen if approximately two times larger, resulting in a quadruple area.

$$f(z) = -0.6 \cdot e^{-0.35 \cdot z} \tag{4}$$
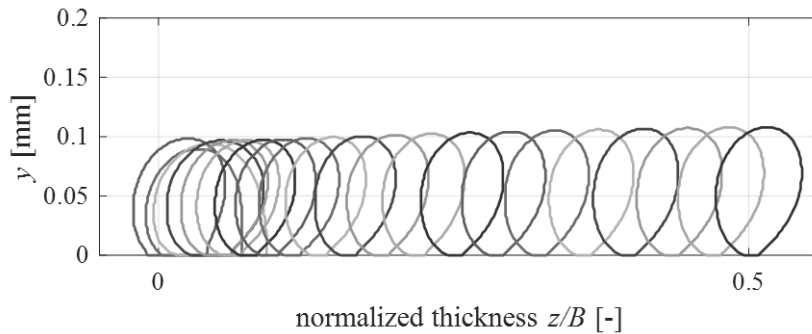
Fig. 4: Plastic zone contours of the straight crack through the thickness
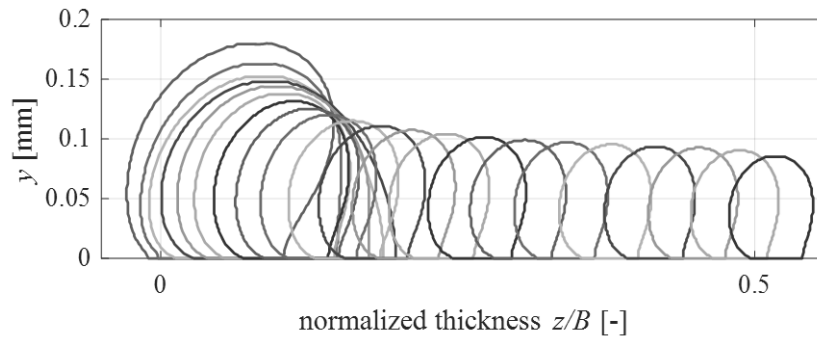
Fig. 5: Plastic zone contours of the curved crack through the thickness

CONCLUSION

Plastic zones were numerically studied in CT specimens made of the EA4T steel using 2D and 3D FE models. Plastic zones through the thickness of a CT specimen were obtained in 3D FE simulations in ANSYS, taking the real elastic-plastic material model into account. It was found that the 2D plane stress solution was much different from the situation at the free surface of the 3D cracked body. There is a principal mistake in replacing the free surface deformation by 2D plane stress solutions due to the effect of the corner-point singularity. The difference between the plastic zones in the middle of the 3D specimen and the 2D plane strain solution was also present but it was not so significant. In addition, the results in 3D were influenced by the crack front curvature. Therefore, modelling of a straight crack front in 3D is not correct for real cracks either.

ACKNOWLEDGMENT

LITERATURE

[1] Irwin GR. Plastic Zone Near a Crack and Fracture Toughness. Sagamore Res Conf Proc 1961;4:63–78.

[2] Anderson TLL. Fracture Mechanics: Fundamentals and Applications. 3rd ed. Boca Raton, FL : Taylor & Francis; 2005.

[3] Dugdale DS. Yielding of steel sheets containing slits. J Mech Phys Solids 1960;8:100–4. https://doi.org/10.1016/0022-5096(60)90013-2.

[4] Barenblatt GI. The Mathematical Theory of Equilibrium Cracks in Brittle Fracture. Adv Appl Mech 1962;7:55–129. https://doi.org/10.1016/S0065-2156(08)70121-2.

[5] Dougherty JD, Srivatsan TS, Padovan J. Fatigue crack propagation and closure behavior of modified 1070 steel: Finite element Study. Eng Fract Mech 1997;56:167–87. https://doi.org/10.1016/S0013-7944(96)00103-8.

[6] Solanki K, Daniewicz SR, Newman JCJ. A new methodology for computing crack opening values from finite element analyses. Eng Fract Mech 2004;71:1185–95. https://doi.org/10.1016/S0013-7944(03)00113-9.

[7] Rice JR. Mechanics of Crack Tip Deformation and Extension by Fatigue. Fatigue Crack Propag.

NORMALITY TEST AND CORRELATION ANALYSIS OF TENSILE TEST RESULTS OF ADDITIVELY MANUFACTURED COMPOSITES

JAROSLAV MAJKO[1], MARIÁN HANDRIK[2], MILAN VAŠKO[3]

The authors are preparing a comprehensive study focused on the directional dependence of mechanical properties of laminates made of nylon reinforced with chopped carbon fibre using the Fused Filament Fabrication method. The article aims to perform a normality test of the measured outputs for each series of specimens. In addition, the authors assessed the relationship between the number of laminates and yielding forces.

KEYWORDS

Tensile testing, normal distribution, linear relation, Anderson-Darling test, trend line.

INTRODUCTION

Fused Filament Fabrication is an additive technology that enables the production of objects by layering various materials. Thanks to the gradual development of the technology, a recent achievement is the printing of nylon reinforced with chopped carbon fibres [1-3]. The authors of this study previously published an article in a peer-reviewed journal focused on the influence of printing parameters (infill type, infill orientation) on the tensile properties of printed laminates [4]. The next goal is the identification of the directional dependence on the tensile strength and specification of the individual laminas' strength. This comprehensive study requires an assessment of the measured tensile test outputs on laminates with different numbers of laminae (5, 7, 9, and 11). Therefore, this article's purpose is the analysis whether the usage of the mean values is correct for experimental measurement evaluation. In the case of a positive result, these mean values allow the identification of the dependence between the increasing number of laminas in the laminate and the average values of yielding forces. The lamina thickness of the observed cross-ply laminates with infill orientation 0/90 degrees is 0.1 millimetres, and in the future, the authors aim to perform the same analysis for other lamina thicknesses.

---

[1] **Ing. Jaroslav Majko, PhD.**, Department of Applied Mechanics, Faculty of Mechanical Engineering, University of Žilina. Univerzitná 8215/1, Žilina, Slovakia. Tel +421 41 513 2965. Email: jaroslav.majko@fstroj.uniza.sk

[2] **Ing. Marián Handrik, PhD.**, Department of Applied Mechanics, Faculty of Mechanical Engineering, University of Žilina. Univerzitná 8215/1, Žilina, Slovakia. Tel +421 41 513 2965. Email: marian.handrik@fstroj.uniza.skz

[3] **Doc. Ing. Milan Vaško, PhD.**, Department of Applied Mechanics, Faculty of Mechanical Engineering, University of Žilina. Univerzitná 8215/1, Žilina, Slovakia. Tel +421 41 513 2965. Email: milan.vasko@fstroj.uniza.sk

CHAPTER 1 GOODNESS-OF-FIT TEST

Firstly, the authors performed a goodness-of-fit test on how well the empirical cumulative distribution function fits the true cumulative distribution function of the standard normal distribution using the Anderson-Darling test. At the significance level, α = 0.05, the null hypothesis - the data follow the normal distribution

$$H_0: F(x) = F_0(x)$$

was tested against alternative hypothesis – the data do not follow the normal distribution

$$H_1: F(x) \neq F_0(x).$$

The formula for the test statistic is:

$$AD = \frac{1}{n}\sum_{i=1}^{n}(1-2i)\left[\ln F_0(x_{(i)}) + \ln(1 - F_0(x_{(n+1-i)}))\right] - n \tag{1}$$

where F_0 is the cumulative distribution function, x_i presents ordered data, and n is the number of measured values. The null hypothesis H_0 is rejected at a significance level of α if the test statistic AD is higher than AD_α. The tested data were yielding forces of various laminates, which differed in number of laminas. Each laminate series contained five specimens (Fig. 1).
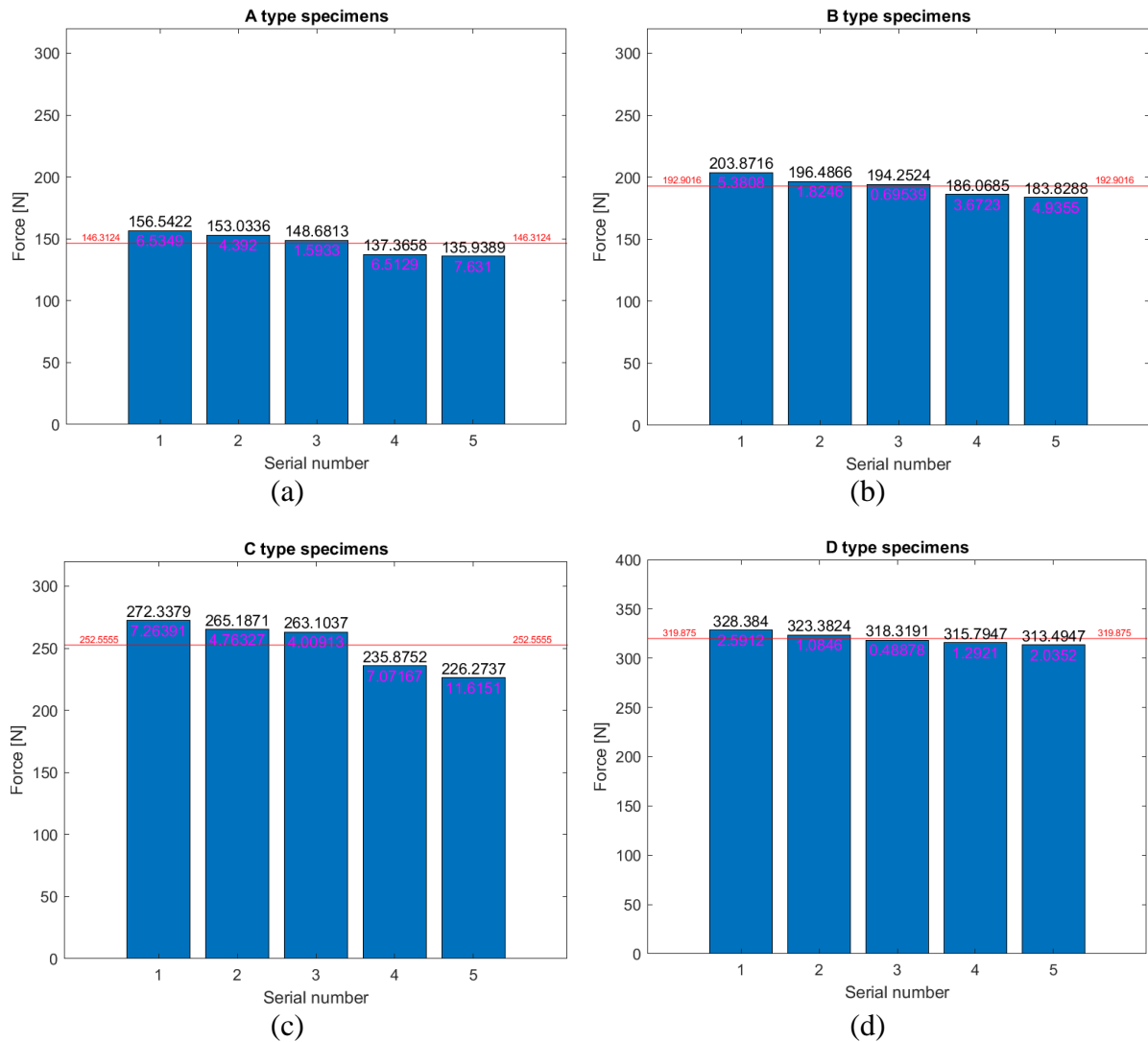

Fig. 1. Yielding forces. The laminates consisted of: (a) 5 laminas (A series), (b) 7 laminas (B series), (c) 9 laminas (C series), (d) 11 laminas (D series)

The primary task was to perform identification whether the measured values represent a random sample from a normal distribution. The goodness-of-fit test was executed using MATLAB software, which allows simple computation of the following parameters:

- Average value of measured yielding forces calculated using function mean.

- Standard deviation determined using function std.

- Cumulative distribution function of the standard normal distribution evaluated using function normcdf.

- Test statistic value defined in Equation 1.

- Critical value calculated using Equation 2

$$AD_\alpha \approx \frac{0,752}{1 + \frac{0,75}{n} + \frac{2,25}{n^2}} \tag{2}$$

If the test statistic value AD is less than the critical value AD_α, the null hypothesis H_0 at the significance level α is not rejected. The results of the described goodness-of-fit testing of the measured values are in Table 1.

Table 1. Values required for evaluation of goodness-of-fit test

Series	Mean [N]	Standard deviation [N]	Test statistic	Critical values
A	146.3130	9.2618	0.3230	0.8347
B	192.9016	8.1244	0.2191	0.8347
C	252.5555	20.1936	0.3936	0.8347
D	319.875	6.0101	0.2117	0.8347

Based on the results from Table 1, the Anderson-Darling test does not reject the null hypothesis H_0. It allows us to state with 95% confidence, that the set of measured data for each series fits a normal distribution.

CHAPTER 2 CORRELATION ANALYSIS

The next step was the identification of the relationship between the number of laminas and the average values of the yielding forces for each series of specimens. The first part of correlation analysis was the generation of a scatter plot with a linear trend line (Fig. 2). The relationship between the observed parameters describes the following linear equation:

$$y = 29.017 * x - 4.2247 \tag{3}$$

The trend equation is most reliable when the R-squared value equals 1. In this case, the reliability value is:

$$R^2 = 0.9936 \tag{4}$$

what indicates very good fit of the estimated trend line values to the data. Finally, the authors performed the Pearson correlation test. The result is the correlation coefficient, which value range between <-1,1>. The interpretation of the result is the following:

- If the correlation coefficient equals 0, the observed variables are uncorrelated.

- If the correlation coefficient equals -1, the observed variables are negatively correlated.

- If the correlation coefficient equals 1, the observed variables are positively correlated.

The value of the Pearson correlation coefficient is:

$$r = 0.9968 \tag{5}$$
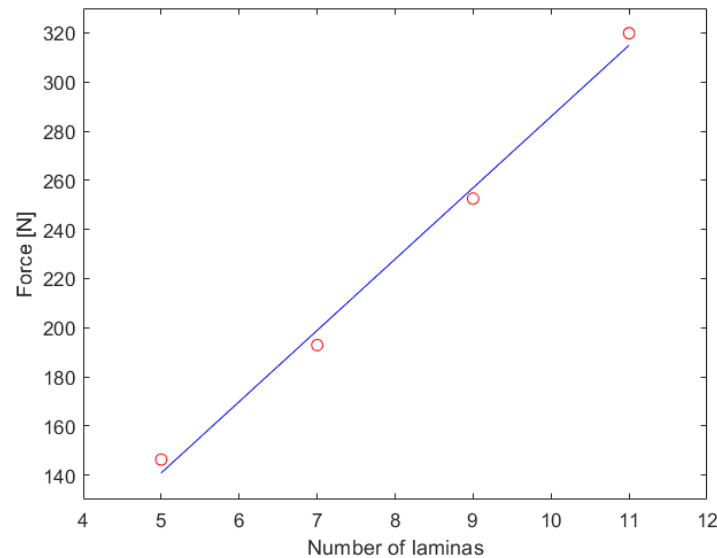
Fig. 2. Scatter plot. Blue curve represents trend line.

According to the coefficient, the relationship between the number of laminates and yielding forces is linear. In addition, the rise in the number of laminas leads to higher yielding forces.

CONCLUSION

This article aimed to evaluate the measured results from a tensile test, which will be used in the comprehensive study focused on the directional dependence of mechanical properties of composites manufactured by the FFF method. Each observed series consisted of five specimens. The Anderson-Darling test showed that the measured data with 95% confidence follow a normal distribution. In the next step, the correlation analysis identified a linear relationship between the number of lamina and the forces required to reach the yield point. In the future, the findings about the measured data allow reliable specification of laminas yielding strength.

ACKNOWLEDGMENT

LITERATURE

[1] Chua, C.K.; Leong, K.F.; Lim, C.S. Rapid Prototyping: Principles and Applications, 5th ed.; World Scientific: Singapore, 2010. 400 pp. ISBN: 978-0-471-73001-9.
[2] Ngo, T.D.; Kashani, A.; Imbalzano, G.; Nguyen, K.T.; Hui, D. Additive manufacturing (3D printing): A review of materials, methods, applications and challenges. Compos. Part B Eng. 2018, 143, 172–196.
[3] Goh, G.D.; Yap, Y.L.; Agarwala, S.; Yeong, W.Y. Recent progress in additive manufacturing of fiber reinforced polymer composite. Adv. Mater. Technol. 2019, 4, 1800271.
[4] Majko J, Vaško M, Handrik M, Sága M. Tensile Properties of Additively Manufactured Thermoplastic Composites Reinforced with Chopped Carbon Fibre. *Materials.* 2022; 15(12):4224. https://doi.org/10.3390/ma15124224

HIGH-STRENGTH STEELS: FATIGUE AND CORROSION

LUCIE MALÍKOVÁ[1], ANNA BENEŠOVÁ[2], MOHAMMAD AL KHAZALI[3],
STANISLAV SEITL[4]

Investigations on mutual interaction of a corrosion pit and a short fatigue crack in a high-strength steel specimen are presented. Particularly, propagation of an inclined crack in the vicinity of a corrosion pit is analyzed via finite element method and the direction of the further crack propagation is estimated via multi-parameter form of the strain energy density fracture criterion.

KEYWORDS

High-strength steel; Fatigue; Corrosion; Finite element method; SED criterion

INTRODUCTION AND METHODOLOGY

High-strength steels (HSS) very often yield to combination of two damage phenomena: fatigue and corrosion. In this work, finite element method was utilized to model an inclined edge crack near a corrosion pit and then, the multi-parameter form of the Strain Energy Density (SED) criterion was applied to estimate the crack deflection angle.

Schema of the HSS specimen can be seen in Fig. 1. The values of the parameters are: $const = 0.1$ mm, $2P = 4$ mm, $D = 1$ mm, $L = 100$ mm, $W = 10$ mm, $a = 0.05, 0.25, 0.5, 1, 1.5, 2, 3$ and 4 mm, $\gamma = -45, -30, -15, 0$ $15, 30$ and $45°$ and $\Delta\sigma = 300$ MPa.
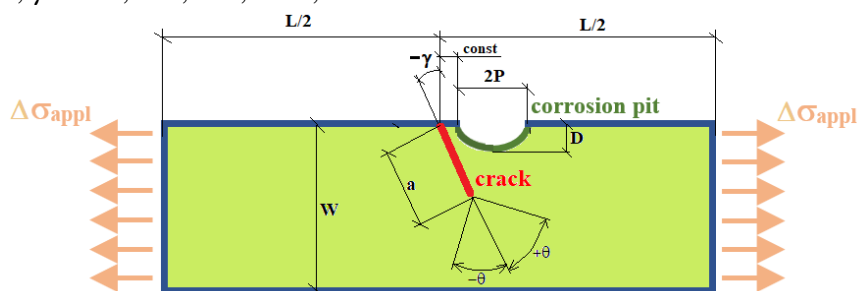
Fig. 1 Schema of the rectangular specimen with an inclined crack and a corrosion pit

[1] **Ing. Lucie Malíková, Ph.D.**, Institute of Physics of Materials, Czech Academy of Sciences (IPM CAS), v.v.i.. Žižkova 513/22, Brno, Czech Republic & Institute of Structural Mechanics, Faculty of Civil Engineering, Brno University of Technology (ISM FCE BUT). Veveří 331/95, Brno, Czech Republic. Tel +420 54114 7381. Email: malikova.l@fce.vutbr.cz

[2] **Bc. Anna Benešová**, ISM FCE BUT. Email: anna.benesova1@vutbr.cz

[3] **Ing. Mohammad Al Khazali**, ISM FCE BUT. Email: mohammad.al.khazali@vutbr.cz

[4] **Doc. Ing. Stanislav Seitl, Ph.D.**, IPM CAS & ISM FCE BUT. Tel +420 532 290 361. Email: seitl@ipm.cz

The model was created in ANSYS considering the linear elastic material properties as $E = 210$ GPa and $\nu = 0.3$. The numerical simulations served to get inputs for the over-deterministic method used for estimation of the higher-order terms of the Williams expansion (WE) [1] which had been derived for approximation of crack-tip stress tensor components. These expressions are necessary for SED criterion [2] which assumes that a crack will deflect into a direction where the strain energy density is minimum. It should be also noted that the criterion needs to be applied on a particular radial distance, referred to as the critical distance, r_c. Within the study, $r_c = 0.1$ and 0.5 mm were considered.

RESULTS

Selected results of the directions of further crack propagation obtained for the initial crack inclination angle $\gamma = +30°$ can be seen in Fig. 2.
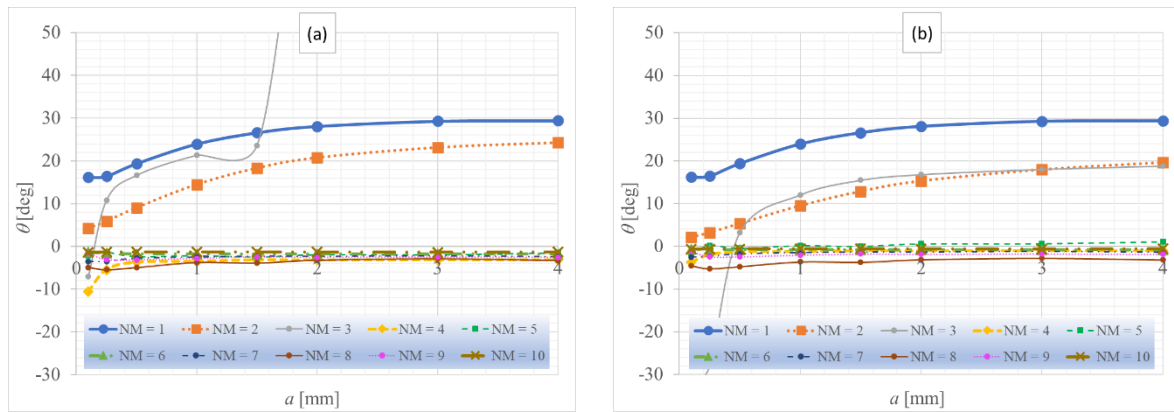
Fig. 2 Dependence of the crack deflection angle on the crack length for various numbers of the WE terms used for stress components approximation: (a) $r_c = 0.1$ mm; (b) $r_c = 0.5$ mm

CONCLUSION

The crack deflection angle affected by a corrosion pit in the defined HSS specimen was estimated via multi-parameter SED criterion. The mutual influence is apparent only for very short cracks. The presence of the corrosion pit keeps the very short initial crack away from its effort to deflect to the direction perpendicularly to the tensile loading. Results obtained on both critical distances seems very similar. All the conclusions mentioned are based on the dependences obtained for the WE assuming only 1 or 2 initial terms of the series. The results show that considering higher-order terms in the SED criterion in this cracked configuration does not improve the prediction of the fracture and fatigue behavior. According to SED assuming more WE terms, the crack would not deflect from its original direction at all. Thus, experimental campaign is to be recommended to be able to compare the results of numerical simulations with real behavior of the crack in the suggested specimen.

ACKNOWLEDGMENT

LITERATURE

[1] Ayatollahi, M.R. and Nejati, M. An over-deterministic method for calculation of coefficients of crack tip asymptotic field from finite element analysis. Fatigue & Fracture of Engineering Materials & Structures, 2011, 34, 3 (159–176).
[2] Sih, G. C. Some basic problems in fracture mechanics and new concepts. Engineering Fracture Mechanics, 1973, 5 (365–377).

MEASUREMENT OF MECHANICAL PROPERTIES OF ALUMINUM ALLOY IN HIGH STRAIN RATE

MARTIN MÁNEK[1], MARTIN FUSEK[2]

This article describes Split Hopkinson Pressure Bar test of aluminum alloy EN AW 7075-T6. This method is used for material testing under high strain rate loading. The strain rate is approximately $10^2 – 10^4 \, s^{-1}$. Based on measured data for three strain rates were set Johnson-Cook material model for FEM analyses. With the use of the material model and Ansys Explicit software, were simulated Split Hopkinson Pressure Bar test and compared the results.

KEYWORDS

Split Hopkinson Pressure Bar, Aluminum alloy 7075, Dynamic behavior, Finite element analyses, Johnson-Cook strength

INTRODUCTION

The aluminum alloy 7075 is one of the most used materials in aerospace, military, racing, etc. In these areas, it is necessary to deal with high velocity impact associated with high strain rates. For accurate computational model, is important knowledge of material parameters in different strain rate. For measurement of material behavior in condition, where it is not possible to neglect wave propagation of stress in material and inertia effect, it is appropriate to use the Split Hopkinson Pressure Bar test. A thin bar to measure mechanical properties was reported by B. Hopkinson [1]. H. Kolsky designed test with two bars and specimen between them [2].

SPLIT HOPKINSON PRESSURE BAR TEST

The apparatus for Split Hopkinson Pressure Bar test consists of incident and transmitter bars, specimen, striker bar, gas gun and strain gauge (Figure 1). The striker bar is accelerated against the incident bar and generates the incident strain pulse ε_i (t) in the input bar. When the pulse reaches the interface between input bar and specimen, part of the pulse is reflected ε_r (t) to incident bar, and the rest is transmitted ε_t (t) through the specimen to the transmitter bar. The

---

[1] **Ing. Martin Mánek**, Department of Applied Mechanics, Faculty of Mechanical Engineering, VSB – Technical University of Ostrava, 17. listopadu 2172/15, Ostrava, Czech Republic. Tel +420 596 993 290. Email: martin.manek@vsb.cz

[2] **doc**. **Ing. Martin Fusek, Ph.D.**, Department of Applied Mechanics, Faculty of Mechanical Engineering, VSB – Technical University of Ostrava, 17. listopadu 2172/15, Ostrava, Czech Republic. Tel + 420 596 993 027. Email: martin.fusek@vsb.cz

amplitude of the incident pulse is dependent on the striker's velocity. The velocity can be regulated by the air pressure in the gas gun. Pulses are measured by strain gauges and recorded in a digital oscilloscope.
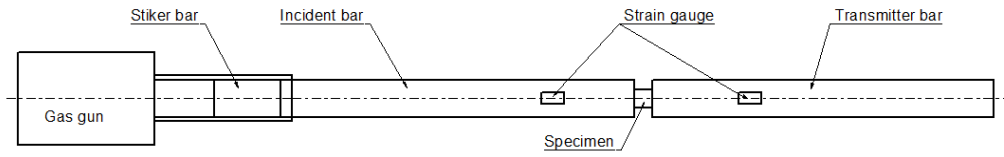
Figure 1: Split Hopkinson Pressure Bar scheme

Based on the experiment can be direct evaluated stress σ(t), strain ε(t) and strain rate ε̇(t). For evaluation of stress and strain, reflected and transmitted waves are used.

$$\sigma(t) = \frac{A_b \cdot E}{A_s} \cdot \varepsilon_t(t),$$ (1)

$$\dot{\varepsilon}(t) = \frac{2 \cdot c_b}{l_s} \cdot \varepsilon_r(t),$$ (2)

$$\varepsilon(t) = \frac{2 \cdot c_b}{l_s} \cdot \int_0^t \varepsilon_r(t) dt.$$ (3)

Where A_b is cross-section of incident and transmitter bar, E is Young´s modulus of bars, A_s is cross-section of specimen, c_b is velocity of the wave propagation, and l_s is length of the specimen.

EXPERIMENT AND EVALUATION

For the experiment was used a set of 9 circular specimens with diameter 10 mm and length 10 mm. In the gas gun 3 pressures, 5, 10 and 15 bars were set. The striker with a length of 200 mm was selected. The impact velocity for each pressure is shown in Table 1.

Table 1: Striker impact velocity

Pressure [bar]	Impact velocity [m/s]
5	18.5
10	26.1
15	31.9

Strain waves were recorded into an oscilloscope and separated to reflected and transmitted waves for the calculation of stress, strain, and strain rate (Figure 2).
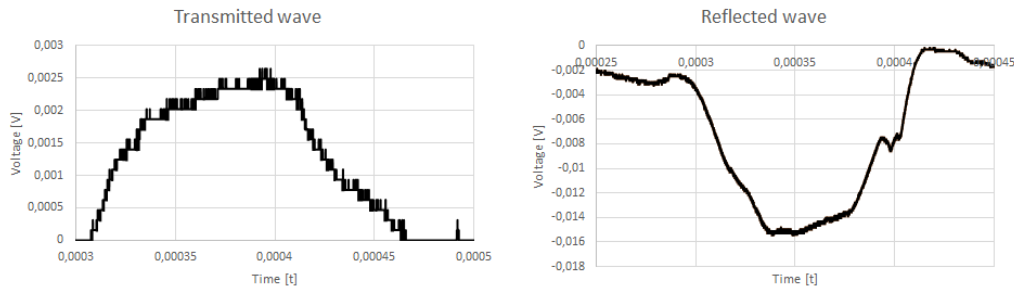
Figure 2: Transmitted and reflected wave for pressure 15 bars

With use of equations (1), (2) and (3) stress-strain curves for each impact velocity were evaluated. The strain rate for 5 bars is 1740 s^{-1}, for 10 bars 3000 s^{-1}, for 15 bars 3430 s^{-1}. For

smoothing of the stress strain curves was used a third order Savitzky-Golay filter with window length 499 [3].
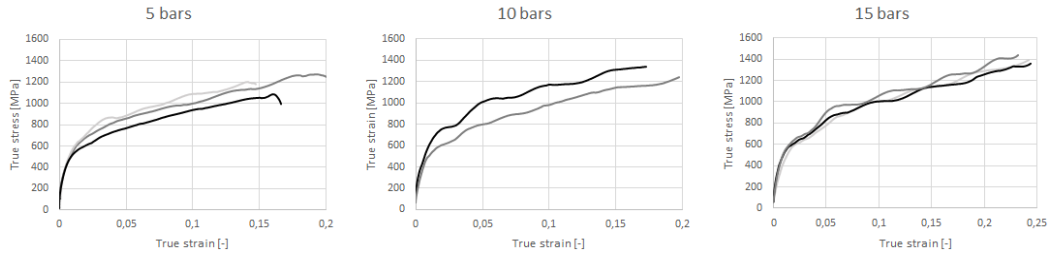
Figure 3: Evaluated Stress-Strain curves

JOHNSON-COOK MODEL PARAMETERS

Johnson-Cook strength is one of the most widely used material model. Its use is suitable in applications, where high strain-rate loading or temperature changing is possible during the deformation process. For fitting the material constant stress–strain curves for low strain rates 0.001, 0.01 and 0.1 s–1 [6] were found. As a reference strain rate was chosen 0.1 s-1. The model defines the yield stress as [4], [5]:

$$Y = \left[A + B\varepsilon_p^n\right]\left[1 + Cln\frac{\dot{\varepsilon}_p}{\dot{\varepsilon}_{ref}}\right]\left[1 - T_H^m\right]. \tag{4}$$

Where A is the basic yield stress for the reference strain rate. B and n represent the effect of strain hardening, ε_p is the effective plastic strain, $\dot{\varepsilon}_p$ is effective plastic strain rate, $\dot{\varepsilon}_{ref}$ is reference strain rate, C is the constant of strain rate hardening, TH is the homologous temperature and m is temperature exponent [4].

Because the experiments were performed at the same temperature, it was possible to neglect the temperature term. For set strain and strain rate coefficient was model separated into strain and strain rate term (Figure 4). The constants of the material model are in Table 2.
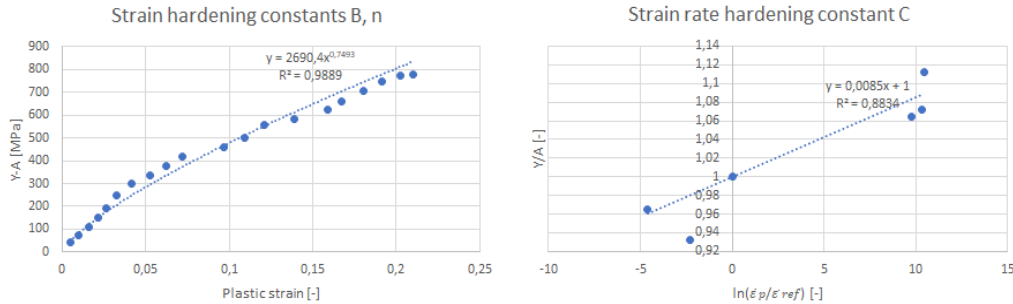
Figure 4: Fitting material coefficients

Table 1: Johnson-Cook material parameters

A [MPa]	B [MPa]	n [-]	C [-]	$\dot{\varepsilon}_{ref}$ [s^{-1}]
515	2690	0,7493	0,0085	0,1

FINITE ELEMENT ANALYSES

Experiments with set material model were performed using Ansys Explicit solver [4]. The models were prepared based on real parts of the testing device and were used specimen of 10 mm length and 10 mm diameter (Figure 5.). The striker velocity was set according to the pressure in the gas gun (Table 1). Stress strain curves from experiments and FEA were compared; see Figure 6.
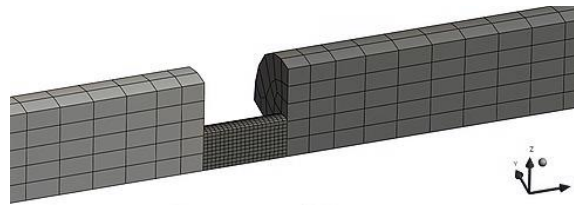
Figure 5: FEA model
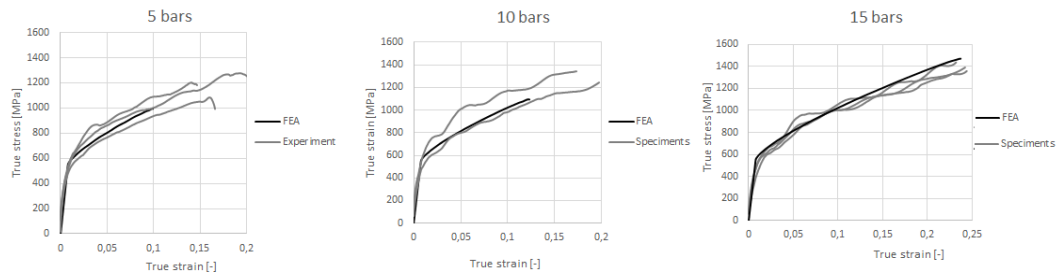
Figure 6: Experiment and FEA comparison

CONCLUSION

In paper, is shown Split Hopkinson Pressure Bar test of aluminum alloy EN AW 7075. The material was tested using three striker velocities. Based on measured data and found data for low strain rate were set material coefficients for the Johnson-Cook material model. This model was used for FEA and the results were compared with the experiment. This research was the first experiment and verification by simulation. 3D printed material and testing apparatus adjustment for tensile loading will follow.

ACKNOWLEDGMENT

LITERATURE

[1] Hopkinson Bertram. 1914 X. A method of measuring the pressure produced in the detonation of high, explosives or by the impact of bullets. Philosophical Transactions of the Royal Society of London. Series A, Containing Papers of a Mathematical or Physical Character 213: 437–456. http://doi.org/10.1098/rsta.1914.0010

[2] Kolsky, H. (1949) An Investigation of the Mechanical Properties of Materials at Very High Rates of Loading. Proceedings of the Physical Society. Section B, 62, 676-700. http://dx.doi.org/10.1088/0370-1301/62/11/302

[3] R. W. Schafer, "What Is a Savitzky-Golay Filter? [Lecture Notes]," in IEEE Signal Processing Magazine, vol. 28, no. 4, pp. 111-117, July 2011, doi: 10.1109/MSP.2011.941097.

[4] Ansys Explicit Dynamics Analysis Guide. Southpointe, July 2022

[5] Johnson, G.R. and Cook, W.H. (1983) A Constitutive Model and Data for Metals Subjected to Large Strains, High Strain Rates, and High Temperatures. Proceedings 7th International Symposium on Ballistics, The Hague, 19-21 April 1983, 541-547.

[6] Bałon, Paweł & Rejman, Edward & Smusz, Robert & Szostak, Janusz & Kiełbasa, Bartłomiej. (2018). Implementation of high speed machining in thin-walled aircraft integral elements. Open Engineering. 8. 162-169. 10.1515/eng-2018-0021.

EXPERIMENTAL AND ANALYTICAL EVALUATION OF THE BIOMECHANICS OF LIPOSOMES

KATARÍNA MENDOVÁ[1], JOSEF ŠEPITKA[1], MARTIN OTÁHAL[2], MATEJ DANIEL[1],

The aim of our study is to prepare artificial cells (liposomes) using a microfluidic device and use them as standard for testing living cells of different phenotypes by force probe microscopy. Two types of liposomes were prepared: liposomes with HA (hyaluronic acid) and pure ones. The artificial cell was shown to have a mechanical behavior similar to living cells. An analytical model has been developed to determine Young´s modulus of elasticity obtained from nanoindentation and AFM loading curves.

KEYWORDS

Liposomes, mechanical properties, AFM, nanoindentation, Young´s modulus

INTRODUCTION

The biological processes occurring in the living organism are closely linked to the mechanical properties of cells (adhesion, migration, etc.). The mechanical properties of the cell are related to many various different external or internal factors. Each cell is exposed to external forces, which might result in the degradation of the cell itself. Change in internal environment induced for example by virus infection or maligns process can be manifested in cell stiffness as well. However, each cell is unique and there is large variability between the measurements of individual cells. That is why our study aims to create artificial cells (liposomes) with controlled mechanical properties. The formed liposomes should serve as a reference in obtaining the mechanical properties by means of nanoindentation and AFM (atomic force microscopy). Evaluation of loading curve is performed by an analytical model.

EXPERIMENTAL AND ANALYTICAL EVALUATION

---

[1] **Ing. Katarína Mendová., Ing. Josef Šepitka, Ph.D., prof. RNDr. Matej Daniel Ph.D.** Department of Mechanics, Biomechanics and Mechatronics, Faculty of Mechanical Engineering, CTU in Prague. Technicka 4, 160 00 Praha 6, Czech Republic, Email: Katarina.Mendova@fs.cvut.cz

[2] **Ing. Martin Otáhal, Ph.D.** Department of Natural Sciences, Faculty of Biomedical Engineering, CTU in Prague, Sítna 3105, 272 01 Kladno, Czech Republic

Liposomes are created by single-step emulsification in a microfluidic device. Our method of producing liposomes with HA rests on the double drop emulsification of controlled solutions dosed with injected syringes. One of the solutions is phosphate buffer, the second one consist of phospholipids dissolved in the organic solvent while the HA is added optionally. The microfluidic device maintains lamellar flow allowing for liposome production by mixing of solutions. AFM (atomic force microscopy) and nanoindentation, two common force probe techniques, were used to examine the mechanical properties of the liposomes. AFM evaluate force interaction between the spherical probe while nanoindentation was used to determine the mechanical properties of cells by compression test using flat indenter. Hertz model and Overbeck model were used to determine the mechanical properties using AFM and nanoindentation, respectively. The adhesion interaction between the spherical AFM probe and liposomes attached to the surface is determined by our adjusted mathematical model based on FEA analysis. Fig.1 shows the mathematical model fitting on load curves from AFM measurements.
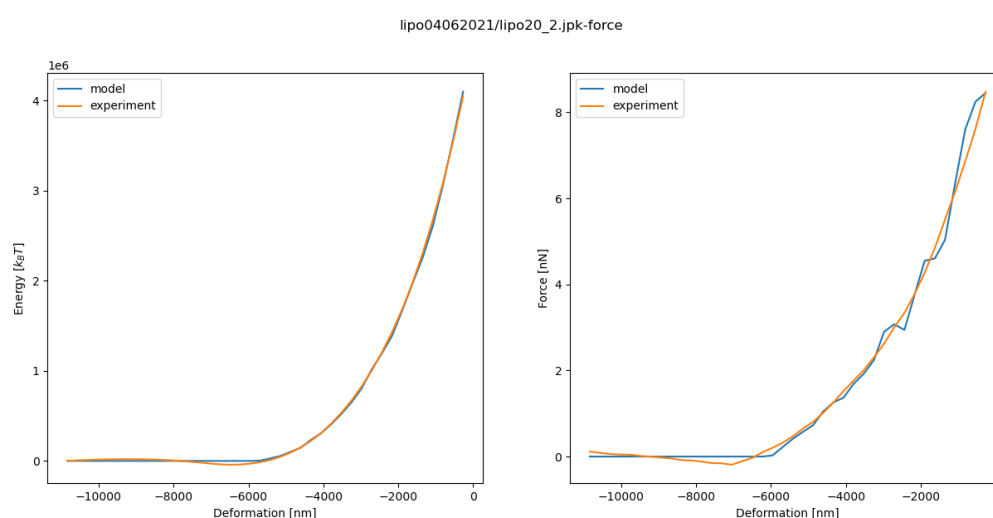
Fig.1 Fitted mathematical model on AFM curves

CONCLUSION

We have developed a method for preparation of mechanical standard for testing of cells using force probe microscopy. We have shown that the stiffness of the construct could be effectively influenced by changing internal environment, e.g. adding hyaluronic acid representing increased viscosity of cytoplasm. Either Hertz or Overbeck model could be used to describe loading curve at low force, but they fail to describe whole region of cell deformation. The shape of the loading curve is considerably affected by adhesion interaction between the substrate and the liposome. We have further shown that the size of the cell should be considered when evaluating the cell stiffness.

ACKNOWLEDGMENT

NUMERICAL ANALYSIS OF DYNAMIC PROPERTIES OF COMPOSITE STRUCTURES

Pavol Michal[1], Milan Vaško[2]

The article deals with the modeling of composite structures with different reinforcement materials and the comparison of their dynamic properties. The main goal of the work is to compare the damping effects of the given structures. The numerical analysis is carried out in the ANSYS Workbench program.

KEYWORDS

Composite material, dynamic properties, damping, numerical analysis

INTRODUCTION

Composite materials are becoming an important part of everyday life, thanks to their unique properties that are used in almost all industries, including technical, research, healthcare, and sports. However, these properties can be influenced by a wide range of factors, one of which is the material of reinforcing fibers and their orientation. In this study, the impact of these factors on dynamic properties, especially on the damping capabilities of the structure, was investigated using ANSYS Workbench software. A disadvantage of numerical analysis is a certain degree of idealization since these are structurally complex materials with a large number of parameters. An effective numerical method is still the subject of research.

Internal damping of composite materials has specific properties. Micro-plastic or viscoelastic phenomena at the interface between the matrix and reinforcement in the form of relative slips are the main sources of internal damping. [1] The internal arrangement of the material and the subsequent distribution of physical fields in the material are the sources of response of the macrostructure. Mechanical components made of materials with specific internal arrangements affect the response of the mechanical system as a macrostructure. [2]

1 NUMERICAL ANALYSIS

Numerical analysis of the given composite structures is performed using Ansys Workbench software. The composite structure itself is designed in the Ansys Composite Preprocessing (ACP) module, where the body geometry, number of layers, and fiber orientation

---

[1] **Ing. Pavol Michal**, Department of Applied Mechanics, Faculty of Mechanical Engineering, University of Žilina. Univerzitná 8215/1, 010 26 Žilina, Slovakia. Tel: +421 41 513 2965.
Email: pavol.michal@fstroj.uniza.sk

[2] **doc. Ing. Milan Vaško, Ph.D.**, Department of Applied Mechanics, Faculty of Mechanical Engineering, University of Žilina. Univerzitná 8215/1, 010 26 Žilina, Slovakia. Tel: +421 41 513 2981.
Email: milan.vasko@fstroj.uniza.sk

are determined. Subsequently, the body properties are transferred to the model in modal analysis, where the body's natural frequencies are determined (Fig. 1). The analysis is then moved to the Harmonic Response module, where the effect of changing fiber orientation on the amplitude of vibration when excited by a force of 10N at the body's natural frequency is examined.
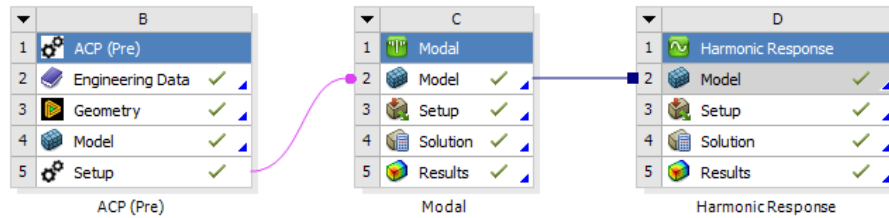
Fig. 1 Project scheme

The types of composite structures are described in Tab. 1. The geometry of the model is a simple rectangular plate with dimensions of 100 x 50 x 4.5 mm (Fig. 2). The materials used are Nylon with chopped carbon fibers (Onyx) as the matrix, and the reinforcement is made up of long fibers of carbon, glass, and kevlar. The material properties of individual fibers are described in Tab. 2. For each material model, 3 fiber orientations are used, 0°, 45°, and 90° with respect to the longer side of the body.

Tab. 1. Composite structures of models

layer	Model 1	Model 2	Model 3
Matrix	Onyx	Onyx	Onyx
Reinforcement	Carbon fiber	Fiber glass	Kevlar fiber
Matrix	Onyx	Onyx	Onyx
Reinforcement	Carbon fiber	Fiber glass	Kevlar fiber
Matrix	Onyx	Onyx	Onyx
Reinforcement	Carbon fiber	Fiber glass	Kevlar fiber
Matrix	Onyx	Onyx	Onyx
Reinforcement	Carbon fiber	Fiber glass	Kevlar fiber
Matrix	Onyx	Onyx	Onyx

Tab. 2. Material properties of fibers [3, 4]

	Unit	Onyx	Carbon fiber	Fiber glass	Kevlar fiber
Young´s modulus 0°	GPa	2,4	135	40	75
Young´s modulus 90°	GPa	1,5	10	8	6
Poisson´s ratio		0,3	0,3	0,28	0,34
Shear modulus	GPa	2,9	5	4	2
Tensile yeld strength	MPa	20	1500	1000	1300
Tensile ultimate strength	MPa	35	1200	600	280
Density	g.cm^{-3}	1,2	1,4	1,5	1,2
Damping ratio		0,1	0,05	0,02	0,081
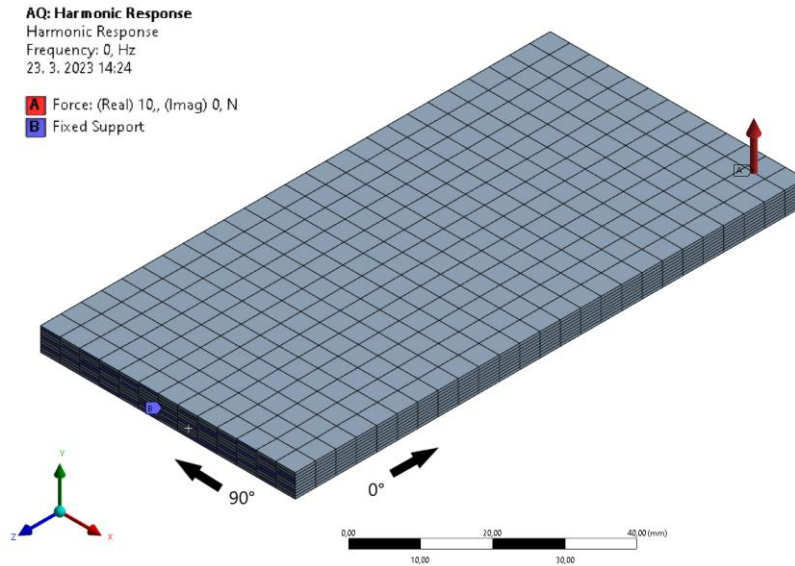
Fig. 2 Geometry and boundary conditions

2 ANALYSIS RESULTS

The result of the analysis is a curve showing the dependency of displacement amplitude on the frequency of vibration (Fig. 3). Fibers oriented at 0° exhibit the smallest amplitudes of displacement, which are excited at higher frequencies compared to fibers oriented at 90°, where higher amplitudes were excited at lower frequencies (Fig. 4, Fig. 5). This implies that the internal damping of the structure is higher for fibers oriented at 90° due to higher internal friction between layers and fibers themselves. Damping ratio for individual fiber directions are shown in Tab. 3. The results of the damping ratio were obtained by processing data from numerical analyses using algorithms programmed in the MATLAB programming language. The Half-power bandwidth method was used to calculate the damping ratio, which involves calculating the damping ratio ζ based on the amplification factor Q (1).

$$\zeta = \frac{1}{2Q}, \qquad Q = \frac{f_n}{\Delta f}, \qquad \Delta f = f_1 - f_2 \tag{1}$$

where f_n is natural frequency, f_1, f_2 are frequencies subtracted from amplitude $\frac{A_{max}}{\sqrt{2}}$
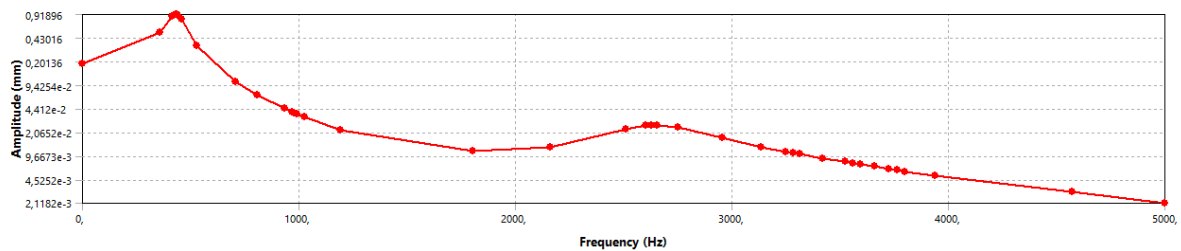
Fig. 3 Graph of amplitude as a function of frequency for the model reinforced with carbon fibers with fiber orientation at 0°.

Tab. 3 Damping ratio ζ for different fiber orientations.

Angle	Carbon fiber	Fiber glass	Kevlar fiber
0°	0,0982	0,03	0,117
45°	0,112	0,032	0,125
90°	0,113	0,033	0,126
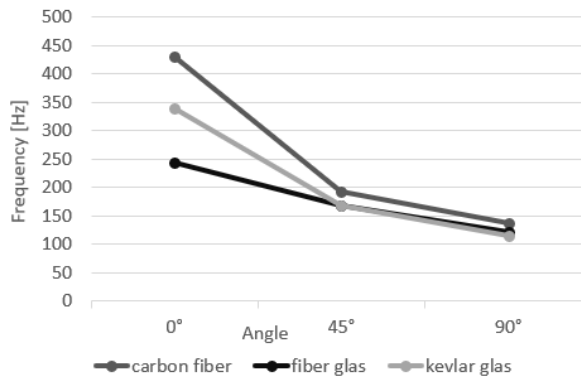
Fig. 4 Dependence of the first natural frequency on the direction of the fibers.
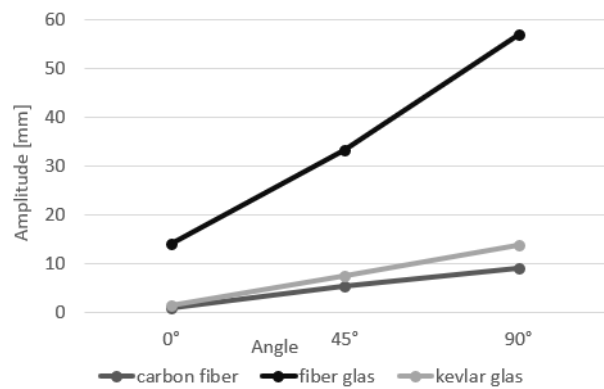
Fig. 5 The dependence of the amplitude of deflection of the first natural frequency on the direction of the fibers.

CONCLUSION

Modal-frequency analysis revealed that changing the orientation of fibers in the composite material structure has an impact on the natural frequencies of the body and, therefore, on the level of internal damping of the body. By changing the fiber orientation from 0° to 90°, the value of the natural frequency decreased and the amplitude of deflection increased for all reinforcement materials.

It is important to pay attention to these properties of composite materials. By correctly evaluating and analyzing them, it is possible to identify areas in various constructions that are susceptible to resonance vibrations. By appropriately modifying the structure of the material in these areas, it is possible to simplify the construction by eliminating the need for various damping elements.

ACKNOWLEDGMENT

LITERATURE

[1] Greif, R.; Hebert, B. Experimental techniques for dynamic characterization of composite materials. Advances in Experimental Mechanics and Biomimetics (ASME - 1992), AD-49/AMD-146:83-97

[2] Tita, V.; Carvalho, J.D.; Lirani, J. A procedure to estimate the dynamic damped behavior of fiber reinforced composite beams submitted to flexural vibrations. Materials research, 2001, 4.4: 315-321.

[3] http://www.performance-composites.com/carbonfibre/mechanicalproperties_2.asp (accessed on 24. March 2023)

[4] Majko, J., Vaško, M., Handrík, M., Sága, M. Tensile Properties of Additively Manufactured Thermoplastic Composites Reinforced with Chopped Carbon Fibre. Materials 2022, Volume 15, Issue 12, https://doi.org/10.3390/ma15124224 (accessed on 24. March 2023)

APPLIED MECHANICS 2023

Grand Hotel Sergijo, April 19ᵗʰ – 21ˢᵗ 2023
Piešťany, SLOVAKIA

STRUCTURAL ANALYSIS OF MECHANICAL AND MECHATRONIC SYSTEMS MADE OF NYLON SPRINGS WITH NEGATIVE THERMAL EXPANSION

JUSTÍN MURÍN[1], VLADIMÍR GOGA[2], JURAJ PAULECH[3], JURAJ HRABOVSKÝ[4], VLADIMÍR KUTIŠ[5], LADISLAV ŠARKÁN[6]

Analytical linear and numerical geometric nonlinear mathematical models of selected nylon spring systems (known as artificial muscle) for the area of small and large elastic elongation and thermoelastic shortening are presented. The author's new finite element of the Nylon Coiled Twisted Spring, (NCTS), with geometric nonlinearity and negative thermal expansion and negative prestressing is used. Results of structural analyzes of selected actuators and passive and active dampers will be discussed. The obtained calculation results will be compared with the linear solution as well as measurements on the physical models.

KEYWORDS

Nylon coiled twisted spring (NCTS). Structural elastic and thermoelastic analysis. Linear and geometric nonlinear springs. Negative thermal expansion. Actuators and dampers.

INTRODUCTION

By twisting the nylon 6 fiber, (also known as fishing line), loaded with a tensile force, a Nylon Coiled Twisted Spring (NCTS) is created that is also known as artificial muscle [1]. As

[1] **Prof. Ing. Justín Murín, Dr.Sc.**, Department of Automotive Mechatronics, Faculty of Electrical Engineering and Information Technology, Slovak University of Technology in Bratislava. Ilkovicova 3, Bratislava, Slovakia. Tel +421 224352523. Email: justin.murin@stuba.sk

[2] **Doc. Ing. Vladimír Goga, Ph.D.**, Department of Automotive Mechatronics, Faculty of Electrical Engineering and Information Technology, Slovak University of Technology in Bratislava. Ilkovicova 3, Bratislava, Slovakia. Tel +421 224352523. Email: vladimir.goga@stuba.sk

[3] **Ing. Juraj Paulech, Ph.D.**, Department of Automotive Mechatronics, Faculty of Electrical Engineering and Information Technology, Slovak University of Technology in Bratislava. Ilkovicova 3, Bratislava, Slovakia. Tel +421 224352523. Email: juraj.paulech@stuba.sk

[4] **Ing. Juraj Hrabovský, Ph.D.**, Department of Automotive Mechatronics, Faculty of Electrical Engineering and Information Technology, Slovak University of Technology in Bratislava. Ilkovicova 3, Bratislava, Slovakia. Tel +421 224352523. Email: juraj.hrabovsky@stuba.sk

[5] **Prof. Ing. Vladimír Kutiš, Ph.D.**, Department of Automotive Mechatronics, Faculty of Electrical Engineering and Information Technology, Slovak University of Technology in Bratislava. Ilkovicova 3, Bratislava, Slovakia. Tel +421 224352523. Email: vladimir.kutis@stuba.sk

[6] **Ing. Ladislav Šarkán, Ph.D.**, Department of Automotive Mechatronics, Faculty of Electrical Engineering and Information Technology, Slovak University of Technology in Bratislava. Ilkovicova 3, Bratislava, Slovakia. Tel +421 224352523. Email: ladislav.sarkan@stuba.sk

a result of twisting, the individual coils are in contact with each other and are compressed by the internal compressive force. The size of this prestressing depends on the mechanical properties of the fiber and its twisting parameters. By applying the selected tensile force, the spring can be safely stretched without impairing its functionality by up to ¾ of its original length [2]. The spring begins to lengthen significantly only after the tensile force overcomes the compressive prestressing. Three areas can be observed from its tensile characteristics. In the first, linear part, there is a very small change in the length of the spring caused by the rigid seating of the spring coils. The second part of the tensile characteristic is linear in its beginning, and the next significant extension is geometrically non-linear. At a certain value of elongation, the coils of the spring begin to unwind. This third part of the tensile characteristic is inadmissible from the point of view of spring functionality. By heating the stretched spring, it starts to shorten significantly. This thermal shortening of the spring is dependent on the amount of warming and on the tensile force that caused this elastic extension. This non-standard property, compared to springs made of other materials, can be used in mechatronic and robotic systems as effective and cheap sensors and actuators. Due to the very good damping effects of these springs, they can also be used for flexible storage of small stationary as well as mobile systems without using an additional damper. [3 – 6].

However, for the optimal design of nylon spring systems, it is necessary to carry out their structural analysis. In this contribution, analytical mathematical models of selected spring systems for the area of small elastic and thermoelastic elongation or spring shortening will be presented. The results of structural analyzes of selected actuators and passive and active dampers will be discussed. Since from the point of view of the possibility of modelling spring systems with large changes in the initial spring length, the paper will present a computational analysis using author's new finite element nylon coiled spring, (NCTS-FE), with geometric nonlinearity, which was assembled at our workplace [7 – 10]. This finite element includes the effect of geometric nonlinearity, negative initial prestressing force as well as negative thermal expansion. The obtained calculation results will be compared with the linear solution as well as measurements on physical models of the analyzed spring systems.

In this abstract, only the results of the linear and nonlinear elastostatic analysis of the passive damper are presented. Additional linear and nonlinear elastostatic and thermoelastic results will be presented in the plenary presentation at the AM2023 conference.

CHAPTER 1 Elastostatic numerical analyzes of the passive damper

For computational evaluation of the geometric nonlinear spring finite element, the real damper, shown in Fig. 1, is analyzed. The damper consists of a cylindrical case closed on both sides by a cap, in which a movable piston is placed. Springs are fixed between the piston and the caps in the initial stretched state. A random one-way dynamic force can act on the piston rod, the maximum amplitude of which is also limited by the initial stretching of the springs on both sides of the piston. The damper is designed by the same springs with linear stiffness constant $k_m = 0.180$ N/mm, the initial compressive prestressing force $F_p = 3$ N and the initial lengths $l_0 = l_1 = l_2 = 85$ mm. Two springs with total stiffness $k_1 = 2k_m = 0.360$ N/mm and total compressional prestressing force $F_{p1} = 2F_p = 6$ N are set on the left side of the damper. From practical point of view, we choose 4 springs on the right side of the damper, whose total stiffness $k_2 = 0.72$ N/mm and the compressive prestressing force $F_{p2} = 2F_{p1} = 12.0$ N. The calculation model of the damper in the in its initial configuration (at time t) is assembled using two serially connected finite elements with unequal stiffnesses according to Fig. 1. Finite

element no. 1 with nodes 1 and 2 has linear stiffness k_1, negative prestressing force F_{p1} and length l_1 in the initial reference position. Finite element no. 2 with nodes 2 and 3 has stiffness $k_2 = pk_1$, negative prestressing force $F_{p2} = pF_{p1}$ and length l_2, while the parameter $p = k_2/k_1 = 2$. Node no. 1 is fixed (its displacement $u_1 = 0$). Node no. 3 is stored in a sliding support. After applying the displacement u_3 at point 3, and the permissible amplitude of the damped dynamic force with maximum amplitude F_2 at point 2, the spring reaches the deformed position at time $t + \Delta t$. For this load system with the prescribed displacement u_3 and force F_2, node 2 is displaced by the value u_2. At the end points of the system, the reactions marked as F_1 and F_3 will occur. In the incremental solution method, the known applied displacement u_3 as well as the force F_2 and the initial prestressing forces F_{p1} and F_{p2} are divided into n load steps.
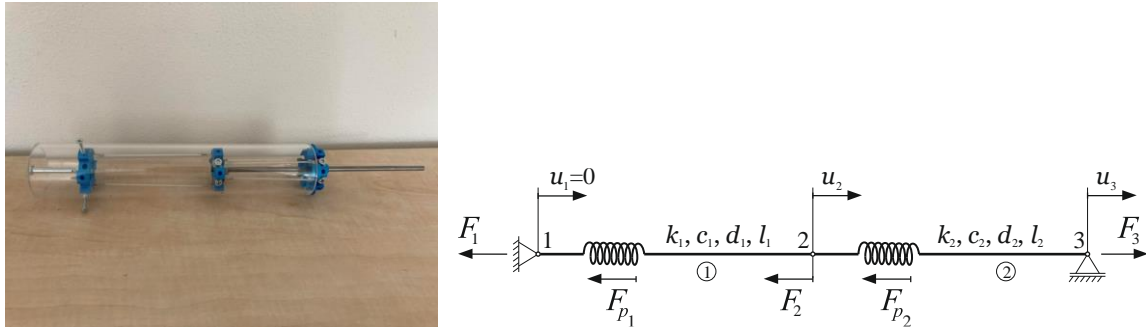
Fig. 1 The physical and finite element models of the damper made of nylon springs

In Tab. 1, the dependence of the maximum allowable force F_2 obtained from the linear model, $F_{2,max,L}$, and the non-linear model, $F_{2,max,NL}$, on the displacement u_3 is summarized.

Tab.1 Dependence of the maximum permissible force F_2 obtained from the linear model, $F_{2,max,L}$, and the non-linear model, $F_{2,max,NL}$, depending on the displacement u_3

u_3 [mm]	10	16.67	20	30	40	50	60
$F_{2,max,L}$ [N]	13.2	18.00	20.40	27.60	34.80	42.00	49.20
$F_{2,max,NL}$ [N]	12.20	16.75	19.15	26.82	35.05	43.87	53.27

The results of the solution in Tab. 1 show that the nonlinearity of the damper begins to manifest itself only at larger initial extensions u_3 of the springs. The measurement on a real damper was performed for an extension of $u_3 = 20$ mm. the maximum value of the force F_2 was 19.2 N. A very good agreement is evident from the comparison of the non-linear calculation results and the measurement for the extension u_3.

CONCLUSION

Nylon twisted coiled springs (NCTS) with negative thermal expansion may be suitable alternative in the design of selected mechanical and mechatronic systems. Their relatively small heating can trigger a large action intervention in the form of tensional force or displacement. For the design of various spring systems, mathematical-physical models are needed for their structural analysis. For reasonably small changes in the length of the springs, it is sufficient to apply the linear theory of elasticity. However, for large permissible changes in the length of the springs, it is necessary to create models based on the nonlinear theory of elasticity. The content of this contribution is focused on the creation of linear and non-linear computational models for elastostatic and thermoelastic analyzes of selected mechatronic and mechanical systems, such as actuators and passive and active dampers. In this short abstract, only the passive damper is analyzed in order to determine the maximum permissible value of the damped force. The results of the nonlinear model differ from the linear model more significantly for large spring

extensions. Experimental measurements of the real damper with the appropriate parameters and for the chosen extension of the springs confirmed the good accuracy of the nonlinear damper model. The analyzed silencer was approved as a utility model [11].The results of several further analyzes as well as the description of the nonlinear nylon spring finite element will be presented in a plenary lecture at the AM2023 conference.

ACKNOWLEDGMENT

LITERATURE

[1] CS. Haines et. al. Artificial Muscles from Fishing Line and Sewing Thread, Science 343, 868-872 (2014), ISSN 1095-9203.

[2] J. Murín, V. Goga, J. Paulech, J. Hrabovsky, L. Šarkan, V. Kutiš, M. Aminbaghai. Modelling and simulation of non-linear thermo-elastostatics of the nylon springs with negative thermal extension. Prepared for publication (2023)

[3] M. Minar, V. Goga, R. Čapková, K. Ondrejička, J. Murín. In Cybernetics & Informatics (2020).

[4] M. Minár and V. Goga and R. Čapková and Ondrejička and J. Murín. Basic parameters of coiled fishing line actuator, in K&I 2020, Proceedings of the 30th International Conference on Cybernetics and Informatics, eddied by J. Cigánek, Š. Kozák, A Kozáková. (Piscataway, New Jersey, 2020), pp. 204-208. DOI: 10.1109/KI48306.2020. 9039870.

[5] J. Murín, J. Paulech, V. Goga, J. Hrabovsky, R. Kmotorka, M. Aminbaghai. AIP Conference Proceedings 2411, 090003 (2021).

[6] J. Murín, V. Goga, J. Hrabovsky, T. Sedlar, V. Kutis, M. Aminbaghai. Thermo-elastic analyzes of new dampers made of polymer springs with negative thermal expansion. IOP Conf. Series: Material Science and Engineering 1199 (2021).

[7] J. Murín, V. Goga and J. Paulech, G. Galik, L. Šarkan,V. Kutiš. Structural analysis of new dampers made of nylon springs. AIP Conference Proceedings 2411, 090003 (2022).

[8] J. Murín, V. Goga, J. Hrabovsky, T. Sedlar, V. Kutis, M. Aminbaghai, Thermo-elastic analyzes of new dampers made of polymer springs with negative thermal expansion. IOP Conf. Series: Material Science and Engineering 1199 (2021).

[9] J. Murín, V. Goga, J. Paulech, G. Galik, L. Šarkan, V. Kutiš. Structural analysis of new dampers made of nylon springs. AIP Conference Proceedings 2411, 090003 (2022).

[10] J. Murín. The formulation of a new non-linear stiffness matrix of a finite element. Computers & Structures, 54, No 5, 933 – 938 (1995).

[11] J. Murin, V. Goga, T. Sedlar. PUV 50026 – 2021. 2021.

INFLUENCE OF FIBER MATERIAL ON SHAPE AND STRESS STATE IN VARIOUS DOMES FOR COMPOSITE PRESSURE VESSELS

ZDENĚK PADOVEC[1], DOMINIK VONDRÁČEK[2], TOMÁŠ MAREŠ[3]

Presented work deals with specially designed domes for filament wound cylindrical pressure vessels. Dome shape can be designed according to material parameters so with the change of the material the shape changes also. Analysis was done for four types of domes (dome with zero transversal stress, with zero transversal strain, with identical strains and dome whose shape minimizes Tsai-Hill criterion) and for two types of fibers (glass and carbon).

KEYWORDS

Filament wound composite, pressure vessel, dome, shell of revolution.

INTRODUCTION

Filament winding technology allows development of the cylindrical part of the pressure vessel together with the dome in one manufacturing operation. The geodesic condition and the utilization of various mechanical properties in different directions can be applied for developing special dome shapes for filament-wound composite pressure vessels [1]. For presented analysis, four dome shapes were chosen - a shell with zero transversal stress σ_T=0 [2], a shell with zero transversal strain ε_T=0 [3], a shell with identical stain ε_L=ε_T [4] and a shell whose shape minimizes Tsai-Hill criterion [5]. The shape itself and the stress state in each dome is a function of material parameters, so two types of fibers were chosen for comparison – glass and carbon (T700).

MATERIALS AND METHODS

The assumptions for the solution comprise:

- an elastic material model of the composite

[1] **Ing. Zdeněk Padovec, Ph.D.**, Department of Mechanics, Mechatronics and Biomechanics, Faculty of Mechanical Engineering, Czech Technical University in Prague. Technická 4, Praha, Czech Republic. Tel +420 224 352 519. Email: Zdenek.Padovec@fs.cvut.cz

[2] **Ing. Dominik Vondráček**, Department of Mechanics, Mechatronics and Biomechanics, Faculty of Mechanical Engineering, Czech Technical University in Prague. Technická 4, Praha, Czech Republic. Tel +420 224 352 523. Email: Dominik. Vondracek@fs.cvut.cz

[3] **Doc. Ing. Tomáš Mareš, Ph.D.**, Department of Mechanics, Mechatronics and Biomechanics, Faculty of Mechanical Engineering, Czech Technical University in Prague. Technická 4, Praha, Czech Republic. Tel +420 224 352 517. Email: Tomas.Mares@fs.cvut.cz

- a thickness of the wall h that is significantly lower than the smallest radius of the shell

- an internal pressure p that leads to membrane loading in the walls of the shell

- a composite wall that is a balanced laminate consisting of two layers with fiber orientations of $\pm\omega$ of the same thickness and volumetric fiber contents

The shell geometry and elastic constants at an arbitrary point of the meridian are functions of the winding angle ω, the wall thickness h, the angle between the axis of revolution and normal to the shell midplane θ, the parallel radius r and both the principal radii R_φ amd R_ψ – see Fig. 1. Let us consider a closed pressure vessel for all the analyzed cases. The membrane stresses (or the in-plane resultant forces) in the meridian and circumferential directions are [5]

$$\sigma_\psi = \frac{N_\psi}{h} = \frac{p\,R_\varphi}{2\,h}$$
$$\sigma_\varphi = \frac{N_\varphi}{h} = \frac{p\,R_\varphi}{2\,h}\left(2 - \frac{R_\varphi}{R_\psi}\right). \tag{1}$$

In a balanced laminate, the total $\tau_{\psi\varphi}=0$; however, each layer exhibits a different shear stress ($+\tau_{\psi\varphi}$ and $-\tau_{\psi\varphi}$). The normal stresses are the same for the whole of the balanced laminate and for each layer. The normal stresses in each layer can be written according to (1), the shear stress in the $+\omega$ layer as

$$\tau_{\psi\varphi} = Q_{61}\,\varepsilon_\psi + Q_{62}\,\varepsilon_\varphi, \tag{2}$$

where Q_{61} and Q_{62} are the elements of a well-known reduced stiffness matrix and ε_ψ and ε_φ are the strains in the meridian and circumferential direction which can be obtained by Hooke´s law. These stresses in the global coordinate system should be transformed into system of the material orthotropy with the use of a transformation matrix (see [6] for example). For a given ratio of the in-plane resultant forces from (1) N_φ/N_ψ (or again with the use of (1), this ratio can be expressed via R_φ/R_ψ), it is possible to obtain the meridian profile of the shell which is a function of the material parameters and the relative size of the polar hole r_0/R for all analyzed domes. Ratio of both principal radii for all analyzed cases can be written as

$$\frac{R_\varphi}{R_\psi} = 2 - \frac{b}{c}, \tag{3}$$

where parameters b and c are function of material parameters in each point of the meridian curve (Young moduli, shear modulus, Poisson ratio, winding angle, strengths, …).
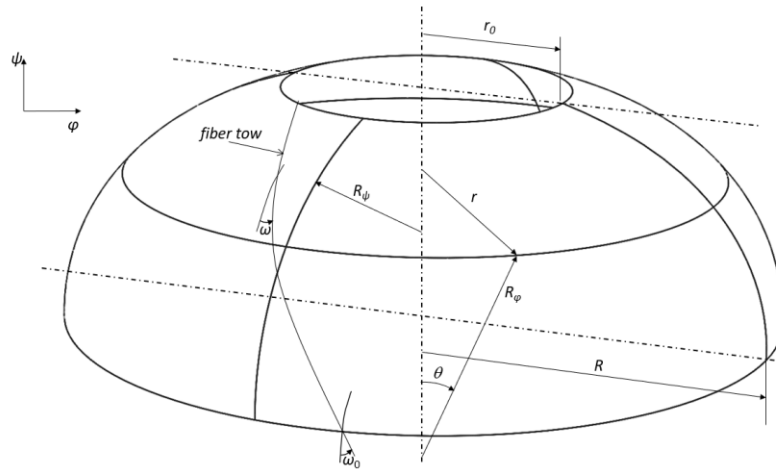

Fig. 1 Shell of revolution of double curvature geometry manufactured by means of helical winding [6]

Two different material systems, a glass/epoxy and carbon/epoxy systems (volumetric fiber content of 60 %) were considered in this study. Solutions were obtained for them with the elastic properties shown in Table 1 and the strength properties shown in Table 2. The other analysis input characteristics comprised a radius of the polar hole of r_0=200 mm, an equator radius of R=500 mm (r_0/R=0.4), internal pressure p=1 MPa and a thickness on the equator of h_0=1.3 mm.

Tab. 1 Elastic properties of lamina in the appropriate directions

Material	E_L [MPa]	E_T [MPa]	G_{LT} [MPa]	v_{LT} [MPa]
Glass/epoxy	46 200	16 513	5 998	0.31
Carbon/epoxy	139 800	9 830	6 395	0.34

Tab. 2 Strength properties of lamina in the appropriate directions

Material	F_{Lt} [MPa]	F_{Lc} [MPa]	F_{Tt} [MPa]	F_{Tc} [MPa]	F_{LT} [MPa]
Glass/epoxy	1 200	600	45	145	65
Carbon/epoxy	2 940	900	50	230	100

RESULTS AND DISCUSSION

Meridian curves of analyzed domes are presented in Fig. 2. From the figure it is obvious that shapes of domes manufactured from glass (except dome with identical strains) are shallower than those manufactured from carbon which is caused by almost two times greater transversal modulus E_T. It means that less material (which is cheaper) is needed for the production of the dome. Computation of the curve shape is stopped when parallel radius reaches the value $1.45r_0$ because in real construction the polar fitting is constructed till this point, and it reinforces the area from r_0 to $1.45r_0$. In Fig. 3 is presented transversal and shear stress in coordinates of material orthotropy. These values were divided by the value $\sigma_{\text{ref}} = pR/2h_0$, which corresponds to the meridian stress on the equator.
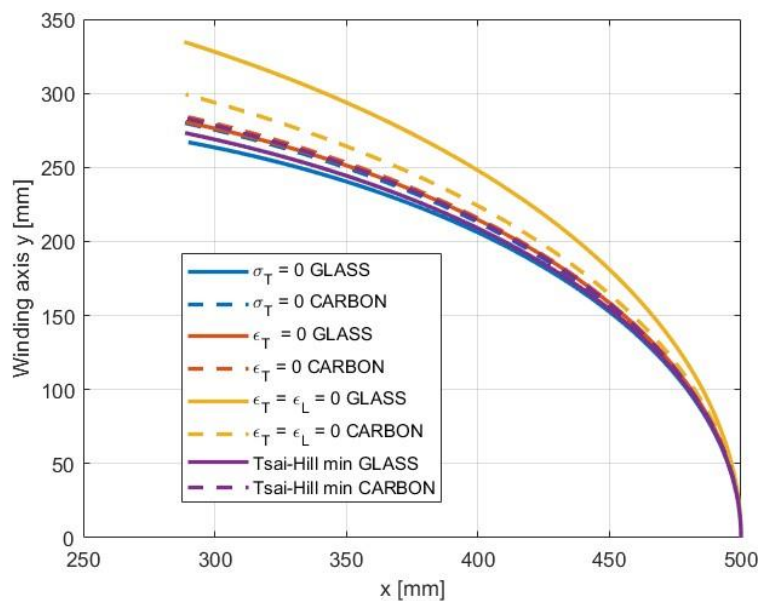

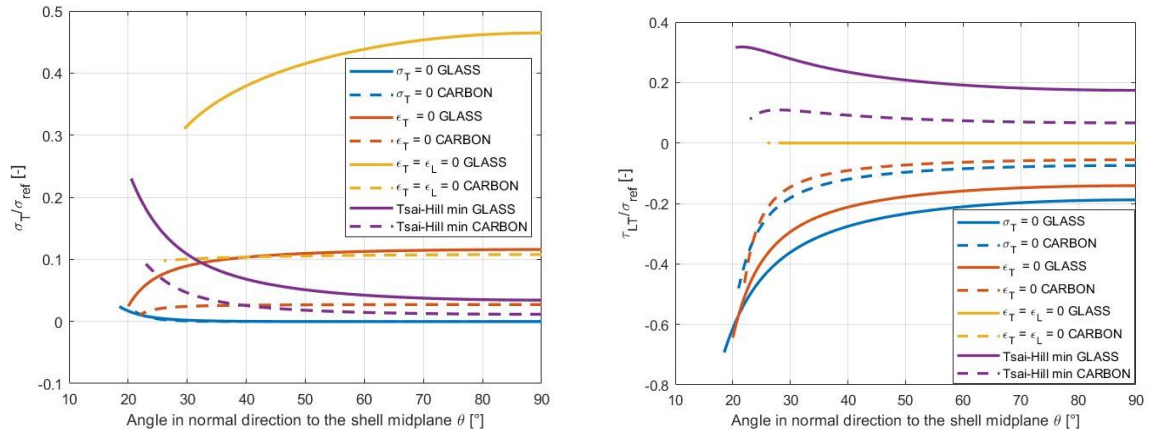Fig. 2 Meridian curves of analyzed domes

Fig. 3 Dimensionless transversal and shear stress in coordinates of material orthotropy

From Fig.3 it is clear that domes manufactured from carbon fiber have lower values of both dimensionless stresses. Curves for transversal stresses in domes from carbon are flatter than those in domes from glass fiber. It is most noticeable for the case of the dome with similar strains, where transversal stress for the carbon case is four times lower than for the glass case. For shear stresses this only applies to the dome which minimizes Tsai-Hill criterion where the shear stress for the carbon case is two times lower than for the glass case.

CONCLUSION

Four types of domes from two different materials for cylindrical pressure vessels were analyzed. Meridian shapes of domes manufactured from glass (except dome with identical strains) are shallower than those manufactured from carbon which means that less material which is cheaper is needed for the manufacturing. On the other hand, we can say that all domes made from the carbon fiber have lower transversal and shear stresses in coordinates of material orthotropy than those manufactured from the glass fiber so the failure index of the carbon domes will be lower than for the domes from the glass fiber at the same load.

ACKNOWLEDGMENT

LITERATURE

[1] Butt, A. M.; Waheed-Ul-Haq, S. Comparative Study for the Design of Optimal Composite Pressure Vessels. Key Engineering Materials 2010, 381-388.

[2] Love, G. G. Structural Analysis of Orthotropic Shells. AIAA Journal 1963, 8 (1), 1843-1847.

[3] Hofeditz, J. T. Structural Design Considerations for Fibrous Glass Pressure Vessels. Modern Plastics 1964, 41, 127-146.

[4] Hojjati, M.; Safavi Ardebili, V.; Hoa, S. V. Design of Domes for Polymeric Composite Pressure Vessels. Composites engineering 1995, 51-59.

[5] Fukunaga, H.; Uemura, M. Optimum Design of Helically Wound Composite Pressure Vessels. Composite structures 1983, 1 (1), 31-49.

[6] Padovec, Z.; Vondráček, D.; Mareš, T. The Analytical and Numerical Stress Analysis of Various Domes for Composite Pressure Vessels, Applied and Computational Mechanics 2022, 16 (2), 151-166.

APPLIED MECHANICS 2023

**Grand Hotel Sergijo, April 19th – 21st 2023
Piešťany, SLOVAKIA**

DEVELOPMENT AND APPLICATION OF A 3D FEM MODEL FOR ROTOR THERMAL BOW PREDICTION

JAN PAŘEZ[1] PATRIK KOVÁŘ[2]

Abstract: This study presents an application of the developed 3D finite element model to an aero engine rotor system under conditions of inhomogeneous temperature field distribution. The mathematical model and the choice of meshing elements of the FEM solver are described. Subsequently, the operating conditions of the rotor system and engine cooling after shutdown are described, where the inhomogeneous temperature field distribution occurs due to heat transfer mechanisms. The result is the calculation of the shaft temperature field and its deformation called rotor thermal bow.

KEYWORDS

Rotor Thermal Bow, Gas Turbines, Finite Element Method, Natural Convection

INTRODUCTION

During operation, the gas turbines are heated by the flow medium. However, when the gas turbine is switched off, the accumulated heat capacity cools down spontaneously. The cooling is based on conjugate heat transfer and radiation between the rotor and stator parts separated by a fluid annular. However, due to natural convection there is a non-uniform distribution of the temperature field [1]. Flow in fluid annuli is caused by the buoyancy of heat flux. The hot air rises upwards and the cold air downwards due to the change in density. This heats the parts in the upper part more, while the lower parts are cooler as showed on Fig. 1. This temperature non-uniformity results in a temperature dependent deformation of the rotor and stator parts called Rotor Thermal Bow [2]. When the gas turbine is
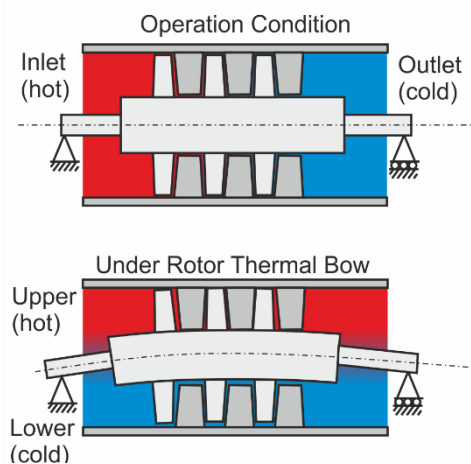
Fig. 1: Gas turbine temperature field distribution

---

[1] **Ing. Jan Pařez**, Department of Mechanics, Biomechanics and Mechatronics, Faculty of Mechanical Engineering, Center of Aviation and Space Research, Czech Technical University in Prague; Technicka 4; 160 00, Prague 6; Czech Republic, Jan.Parez@fs.cvut.cz

[2] **Ing. Patrik Kovář**, Department of Technical Mathematics, Faculty of Mechanical Engineering, Center of Aviation and Space Research, Czech Technical University in Prague; Technicka 4; 160 00, Prague 6; Czech Republic, Patrik.Kovar@fs.cvut.cz

operated again without sufficient cooling, the bowing can cause unintentional contact between the rotor and stator parts and destroy the entire system [5]. This phenomenon has long been known in the power industry [3,4], but is more acute in aero engines as engine designs are forced to minimize radial clearances in order to increase efficiency and temperatures [6].

The paper presents a numerical calculation by the developed FEM solver for rotor system analysis. It was developed for the purpose of complex rotor system analysis in application to aircraft engines. Two identical rotor systems loaded with a non-uniform temperature field due mainly to natural convection cooling will be compared. The first geometry discretized for FEM calculation into nodes and elements will be assumed with homogeneous material. The second geometry is assumed to be composed of a second material with different heat conduction.

FEM MODEL

The finite element method (FEM) solver is based on a set of scripts in Matlab. The control script sequentially executes the partial parts of the calculation. First, the input information of the FEM solver is loaded. Input information is then loaded and consists of the computational mesh geometry, nodes mesh, material and physical properties, and boundary conditions of temperatures and support nodes. From geometry, the computational mesh is created. Finally, a calculation range is selected from the temperature distribution, structural calculation or dynamic analysis.

The computational mesh is formed from the discretized rotor system nodes according to the required number of nodes on the inner radius and the number of radial element layers. In this mesh, the computational region is determined according to the boundaries of the rotor system and nodes at the boundary edge are added. This simply structured mesh is advantageous for the computation of trapezoidal elements. These elements consist of five sets of four nodes each for the front, rear and middle planes in a counterclockwise direction and are created by a for loop for all considered nodes satisfying the conditions of the computational domain. Once the computational mesh, material and physical properties, and boundary conditions of temperatures and node support have been established, the actual computation of the analysis follows. The temperature distribution, structural calculation or dynamic properties calculation range is selected.

The actual calculation of the temperature field and deformations is based on the construction of the heat conduction matrix of the sub-elements in the first step of the temperature field calculation, which are then assembled into a full geometry matrix and boundary conditions added. By finding the solution of this matrix, the temperature distribution for each node of the mesh is obtained. Once the temperature field distribution is determined, the stiffness matrix of the whole geometry composed of the sub-elements is similarly constructed. The displacement of each node of the computational grid is found by finding the solution of this matrix. The whole calculation is solved by a linear calculation.

BOUNDARY CONDITION

Based on the operating conditions of an aircraft gas turbine, the temperature field distribution in the double annulus in the gas turbine cross-sectional area was experimentally and numerically determined. The time dependence of the temperature difference between the upper and lower sides was studied [1]. This difference was used to prescribe the boundary condition
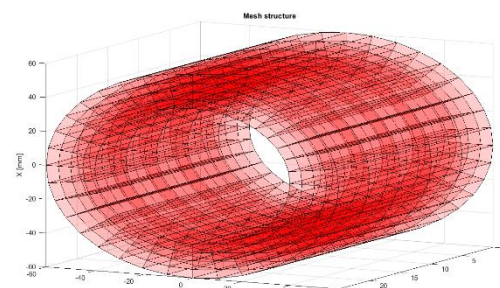

Fig. 2: Discretized geometry of a rotor system

analysis. For the upper side, a temperature of 600 [degC] was prescribed for the nodes. For the lower nodes, the temperature was 400 [degC]. The temperature field distributions for the other nodes were calculated as a function of the constant heat conduction between the neighbor elements. The rotor system corresponds to the rotor system of an aircraft engine. The first bearing is fixed, the second bearing allows axial displacement for thermal expansion. The deflection of the rotor system itself is formed by the temperature differential stretching. The difference between the two chosen geometries is in the application of a bimetallic component with the properties of a thin copper sheet represented into the element. The purpose of choosing this bimetallic component is to achieve a more uniform temperature field due to improved heat conduction around the radius of the geometry, thus reducing the thermal deflection of the chosen geometry. The characteristic dimensions of the geometry are 40 [mm] inner diameter and a length of 100 [mm].

RESULTS

On the boundary conditions described above, two computational variants were created. One with homogeneous material. The other geometry is a combination of the homogeneous material with the addition of an element layer of a second material, namely a layer of copper on the inner radius. The material characteristics are described below in Tab. 1.

Tab. 1: Variants of used materials

	Young modulus [Pa]	Thermal expansion [K^{-1}]	Conductivity [$W*m^{-1}*K^{-1}$]	Temp. max/min [°C]	Max. Deflection [mm]
Material A	2.1e11	12.1e-6	33	600/400	0.793
Material B	0.8e11	24.1e-6	386	600/400	0.348

After the FEM calculation on a simple geometry, the maximum deflection for two cases of geometries was determined as shown in Tab. 1. The first case assumes homogeneous material, where the maximum deflection reached a value of 0.793 [mm]. The second case assumes the addition of a layer of material with better conductivity, in this case a layer of copper was considered. The maximum deflection was determined to be 0.348 [mm]. Thus, a significant improvement of the rotor system properties by heat conduction through the thermal conductor is observed while maintaining the functionality and strength of the rotor system. The error of the calculation tool is assumed in the lower number of selected elements and in the possible calculation of the temperature field. The resulting temperature distribution is shown in Fig. 3 and Fig. 4. To verify the numerical model, further verification on an experimental setup is proposed.
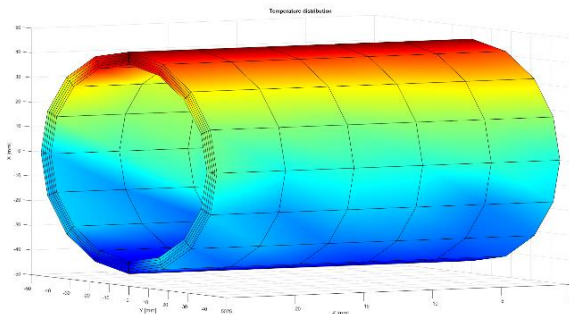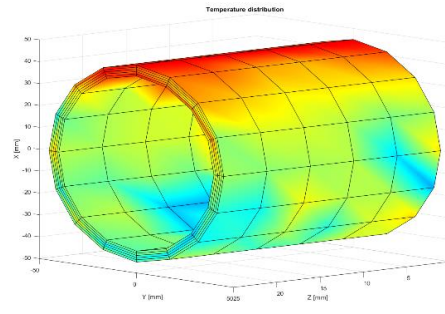

Fig. 3: Variant A, homogeneous material

Fig. 4: Variant B, combined material

CONCLUSION

In this paper the developed FEM solver for analyzing 3D rotor systems was presented. The method of building the computational tool in Matlab environment was described. The construction of the computational mesh from the nodes was also described. The temperature field distribution was calculated for the heat conduction model without considering external natural convection cooling. The structural analysis was computed by a linear calculation. Heat boundary conditions for the upper and lower sides were presented. The rotor supports was chosen in two bearings, one fixed and the other sliding in axial direction. A computational analysis was developed for two cases, where the first is based on homogeneous material with given parameters for steel. For the second case, the effect of a thin copper layer along the inner circumference was investigated. The results plotted in the graphs and table shows the improvement in performance when the heat conductor is used in the rotor system. Thus, the idea of improving the properties in this way is confirmed and will be further investigated.

ACKNOWLEDGMENT

LITERATURE

[1] Pařez, J., et al., Experimental and Numerical Study of Natural Convection in 3D Double Horizontal Annulus, EPJ Web of Conferences. 2022, Vol. 264(1), ISSN 2100-014X.
[2] Pilkington, A., et al. Prediction of natural convection heat transfer in gas turbines. International Journal of Heat and Mass Transfer, 2019, Vol. 141, pp. 233-244.
[3] Pennacchi, P., Vania, A., Accuracy in the identification of a generator thermal bow. Journal of Sound and Vibration, 2004, Vol. 274(2), pp. 273-295.
[4] Marinescu, G., Ehrsam, A., Experimental Investigation Into Thermal Behavior of Steam Turbine Components: Part 2—Natural Cooling of Steam Turbines and the Impact on LCF Life. In: Turbo Expo: Power for Land, Sea, and Air. American Society of Mechanical Engineers, 2012. pp. 1111-1120.
[5] Smith, E. O., Neely, A., Shaft thermal bow modelling in gas turbines-an initial study. In: 21st international symposium on air breathing engines. 2013. pp. 9-13.
[6] Smith, E. O., et al. Enhanced experimental measurements of a gas turbine compressor rotor analogue undergoing thermal bow. In: International symposium on air breathing engines. 2017.

APPLIED MECHANICS 2023

Grand Hotel Sergijo, April 19th – 21st 2023
Piešťany, SLOVAKIA

ANALYSIS OF ELASTOPLASTIC CONTINUUM MECHANICS PROBLEMS APPLYING THE KARRAY-BOUC-WEN MODEL AND VELOCITY SOLUTION USING FEM.

KATARÍNA PIJÁKOVÁ[1], MILAN SÁGA[2], BARBORA DRVÁROVÁ[3], MILAN VAŠKO[4]

This paper uses Matlab to solve elastoplastic problems in continuum mechanics using the finite element method. Nonlinear analysis will focus on trusses, triangles, and tetrahedrons using the rate formulation to solve the equations of state. We will assume an extended Karray-Bouc-Wen model of the physical equations for elastoplastic material behaviour. The problem will be treated in Matlab software and the paper, we will present results from numerical testing of the problem.

KEYWORDS

Velocity formulation, Karray-Bouc-Wen differential model, Plasticity

INTRODUCTION

We use Hooke's law to analyse the behaviour of the structures and assume that the maximum stresses will not exceed the yield strength of the material. However, today's leaner and lighter structures are no longer infinitesimal, but finite. Forming processes cause finite deformations that cannot be described by linear theory, which we call nonlinear material behaviour. Nonlinear behaviour is characterized by the fact that the dependence between load and displacement is not linear and may be due to material behaviour, geometry changes, boundary conditions, or loading. Most continuum mechanics problems are nonlinear and can be classified according to the kinematics of the deformation process and constitutive equations. The most common types of nonlinearities are geometric and physical nonlinearities that exceed the proportionality limit and cause Hooke's law to be invalid.

With the development of computational technology, numerical methods have become very important in nonlinear continuum mechanics, especially the finite element method, which has developed to such dimensions that it can solve many nonlinear problems that could not be solved before. In the next section, we will discuss the incremental and rate equations of nonlinear continuum mechanics, which allow the application of the fundamental principles of plasticity theory.

[1] **Ing. Katarína Pijáková**, Faculty of Mechanical Engineering, University of Žilina, Univerzitná 8215/1, 010 26, Žilina, Slovakia. Tel +421 41 513 2965. Email: Katarina.Pijakova@fstroj.uniza.sk

[2] **prof. Dr. Ing. Milan Sága**, Faculty of Mechanical Engineering, University of Žilina, Univerzitná 8215/1, 010 26, Žilina, Slovakia. Tel +421 41 513 2961. Email: milan.saga@fstroj.uniza.sk

[3] **Ing. Barbora Drvárová**, Faculty of Mechanical Engineering, University of Žilina, Univerzitná 8215/1, 010 26, Žilina, Slovakia. Tel +421 41 513 2965. Email: Barbora.Drvarova@fstroj.uniza.sk

[4] **doc. Ing. Milan Vaško, PhD.**, Faculty of Mechanical Engineering, University of Žilina, Univerzitná 8215/1, 010 26, Žilina, Slovakia. Tel +421 41 513 2950. Email: milan.vasko@fstroj.uniza.sk

Velocity formulation and Karray-Bouc-Wen differential model

The velocity derivation of the equations of state can be realized by applying one of the two variational principles, namely the principle of the minimum of the total potential energy velocity or the principle of the minimum of the complementary energy velocity of the system. Both variational principles can be derived from the principle of virtual work or complementary virtual work. Washizu defined the virtual work principle for quasi-static problems as, for example

$$\int_V \dot{S}_{ij} \cdot \delta \dot{E}_{ij} \cdot dV - \int_A \dot{t}_i \cdot \delta \dot{u}_i \cdot dA = 0, \tag{1}$$

where S_{ij} is a member of II. Piola-Kirchhoff stress tensor, E_{ij} is a term of the Green-Lagrange ratio transformation tensor, t_i is a term of the intensity vector of external forces on the surface A, and u_i is a term of the displacement vector.

Karay and Bouc presented equations for 3-D continuum mechanics problems based on Wen's model and taking into account the associated law of plastic behaviour, Mises' plasticity condition, and Prager's law for material stiffening in the form of

$$\dot{Y}_{ij} + B \cdot \|Y\|^{n-2} \cdot |Y_{rs} \cdot \dot{e}_{rs}| \cdot Y_{ij} + C \cdot \|Y\|^{n-2} \cdot (Y_{rs} \cdot \dot{e}_{rs}) \cdot Y_{ij} = A \cdot \dot{e}_{ij}, \tag{2}$$

where $Y_{ij} = s_{ij} - \frac{2}{3} \cdot \frac{E \cdot E_T}{E - E_T} \cdot \dot{\varepsilon}_{ijp}, \quad B = C = \frac{E}{2 \cdot (1+\mu) \cdot (\sqrt{\frac{2}{3}} \cdot \sigma_y)^n}, \quad A = \frac{E}{(1+\mu)\cdot},$

$\|Y\|$ is the norm of the tensor Y, "| |" is the absolute value operator, sij is the stress deviator term, eij is the strain deviator term, εij is the plastic strain tensor term, n is the power regulating the transition from the elastic to the plastic region. Let us also perform a brief analysis of the Karray-Wen description using the system of nonlinear differential equations (2). Applying the above assumptions in equation (2) instead of Y_{ij}, the deviatoric stress will be s_{ij}. Since the Mises plasticity criterion assumes that the mean plastic strain is zero - there are no volume changes, we can express the mean stress as follows

$$\sigma_S = \frac{E}{3 \cdot (1-2\mu)} \cdot \begin{bmatrix} 1 & 1 & 1 & 0 & 0 & 0 \end{bmatrix} \cdot \boldsymbol{\varepsilon}. \tag{3}$$

Then the stress deviator will be of the form (4).

$$\boldsymbol{s} = \boldsymbol{\sigma} - \frac{E}{3 \cdot (1-2\mu)} \cdot \begin{bmatrix} 1 & 1 & 1 & 0 & 0 & 0 \\ 1 & 1 & 1 & 0 & 0 & 0 \\ 1 & 1 & 1 & 0 & 0 & 0 \\ 0 & 0 & 0 & 0 & 0 & 0 \\ 0 & 0 & 0 & 0 & 0 & 0 \\ 0 & 0 & 0 & 0 & 0 & 0 \end{bmatrix} \cdot \boldsymbol{\varepsilon} = \boldsymbol{\sigma} - \frac{E}{3 \cdot (1-2\mu)} \cdot \boldsymbol{T}_{11} \cdot \boldsymbol{\varepsilon}. \tag{4}$$

We write the deformation deviator in matrix form

$$\boldsymbol{e} = \begin{bmatrix} \frac{2}{3} & -\frac{1}{3} & -\frac{1}{3} & 0 & 0 & 0 \\ -\frac{1}{3} & \frac{2}{3} & -\frac{1}{3} & 0 & 0 & 0 \\ -\frac{1}{3} & -\frac{1}{3} & \frac{2}{3} & 0 & 0 & 0 \\ 0 & 0 & 0 & 1 & 0 & 0 \\ 0 & 0 & 0 & 0 & 1 & 0 \\ 0 & 0 & 0 & 0 & 0 & 1 \end{bmatrix} \cdot \boldsymbol{\varepsilon} = \boldsymbol{T}_{eps} \cdot \boldsymbol{\varepsilon}. \tag{5}$$

By substituting the previous relations into (2) and modifying, we obtain

$$\dot{\sigma} = \left[\boldsymbol{D}_{NL} \cdot \boldsymbol{T}_{eps} + \frac{E}{3 \cdot (1-2\mu)} \cdot \boldsymbol{T}_{11} \right] \cdot \dot{\varepsilon} = \boldsymbol{D}^{EP} \cdot \dot{\varepsilon}, \tag{6}$$

where $\boldsymbol{D}_{NL} = E \cdot \boldsymbol{E}_{6 \times 6} - \|\boldsymbol{s}\|^{n-2} \cdot \boldsymbol{s} \cdot (\boldsymbol{b}_e + \boldsymbol{c}_e)$,
where $\boldsymbol{E}$ is a unit matrix with dimensions 6x6,

$$\boldsymbol{b}_e = B \cdot [|s_x| \cdot sign(\dot{e}_x), |s_y| \cdot sign(\dot{e}_y), |s_z| \cdot sign(\dot{e}_z), |s_{xy}| \cdot sign(\dot{e}_{xy}), |s_{yz}|$$
$$\cdot sign(\dot{e}_{yz}), |s_{zx}| \cdot sign(\dot{e}_{zx})]$$

$\boldsymbol{c}_e = C \cdot [s_x \quad s_y \quad s_z \quad s_{xy} \quad s_{yz} \quad s_{xz}]$.

Equation (6) can be applied to the incremental or rate equations. The advantage of these equations is that we do not have to distinguish between elastic and plastic deformations, because the transition between them is an intrinsic property of this mathematical model.

Implementation of constitutive equations into rate solution of nonlinear problems using Finite Element Method (FEM)

For simplicity, consider infinitesimal deformations. The matrix expression between the relative transformations and displacements in the FEM will be

$$\varepsilon = \boldsymbol{B}_L \cdot \boldsymbol{u} \quad \text{a} \quad \dot{\varepsilon} = \boldsymbol{B}_L \cdot \dot{\boldsymbol{u}}. \tag{7}$$

Substituting (7) into (1), for example, and assuming the elastic-plastic behaviour of the material, we obtain equations of state for the unknown velocity vector of the form

$$\int_V \boldsymbol{B}_L^T \cdot \boldsymbol{D}^{EP} \cdot \boldsymbol{B}_L \cdot dV \cdot \dot{\boldsymbol{u}} - \dot{\boldsymbol{f}} = 0 \quad \Rightarrow \quad \mathbf{K(u)} \cdot \dot{\boldsymbol{u}} = \dot{\boldsymbol{f}}. \tag{8}$$

If we consider small displacements and rotations but large transformations (Green-Lagrange) then the mathematical model of the problem can be written following (1)

$$\int_V \left(\boldsymbol{B}_L + \frac{1}{2}\boldsymbol{B}_{NL} \right)^T \cdot \boldsymbol{D}^{EP} \cdot \left(\boldsymbol{B}_L + \frac{1}{2}\boldsymbol{B}_{NL} \right) \cdot dV \cdot \dot{\boldsymbol{u}} - \dot{\boldsymbol{f}} = 0 \quad \Rightarrow \quad \mathbf{K(u)} \cdot \dot{\boldsymbol{u}} = \dot{\boldsymbol{f}}. \tag{9}$$

For large displacements, rotations, and small deformations, the same $\mathbf{D}^{EP}$ elastoplastic matrix is used. However, for finite deformations, the additive partitioning of the strain tensor into elastic and plastic parts cannot be used. Instead, a multiplicative partition of the strain gradient into elastic and plastic parts is used, which is more difficult.

Algorithmization of elastic-plastic problems in MATLAB

Based on the theory designed for elastic-plastic analysis, we have created a simple version of the MATLAB computational program. It combines the principles of the finite element method, a rate formulation for solving nonlinear continuum mechanics problems, and its application to material nonlinearity described by the Karray-Bouc-Wen equations.

Test example

Using the Karray-Bouc-Wen differential model, we analyse the deformation of the simple finite-element model of the component (FEM Model), which is shown in Fig. 1. Assume a material with Young's modulus of elasticity E=2.1011 Pa, Poisson's number μ=0.3, Yield Stress Re=280 MPa, and the Etang/E ratio is 0.001. The finite element method with tetrahedron 3D elements which had a linear shape function was used for mesh formation. The total number of elements in the mesh is 1718 and the number of nodal points is 643. The body is loaded with a force F(t), its course is shown in Fig. 2.

After using Matlab, which uses the Karray-Bouc-Wen differential model to calculate the deformations and stresses in a given body at specified forces, the program processes the input data and calculates the predicted stress and strain values for each element separately. This data is then used by the main program to produce graphs that show the stress-strain relationships for each element separately. Fig. 3 shows the hysteresis loop for the normal stresses σ_x and σ_z at

the center of gravity of element number 58. Fig. 4 shows the hysteresis loop for the shear stresses τ_{yz} and τ_{zx} at the center of gravity of element number 58.
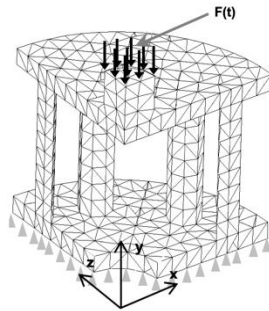

Fig. 1: FEM Model
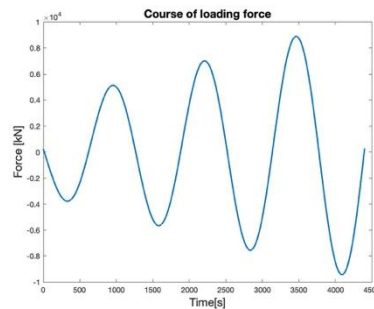
Fig. 2: Course of the loading force F
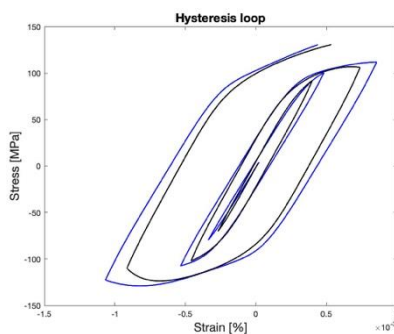
Fig. 3: Hysteresis loop for normal stress σ_x and σ_z
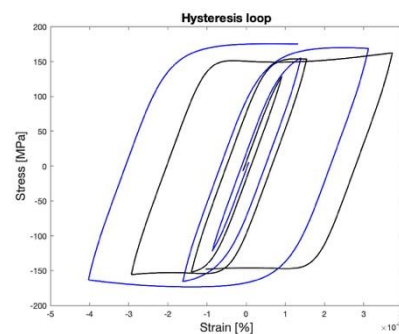
Fig. 4: Hysteresis loop for shear stress τ_{yz} and τ_{zx}

CONCLUSION

This paper aims to demonstrate how we solve problems with nonlinear material properties in mechanics and how we can reliably solve such problems. The paper summarizes the theory of the Karray-Bouc-Wen differential model to calculate the deformation and stress in a given solid for given forces. We then applied this model in a nonlinear analysis in the MATLAB software environment. The presented problem serves as a test problem. The paper was motivated by the subject of computational methods of continuum mechanics and plasticity theory. Results from this paper and work on the program will be included in the assessment of these subjects. In the future, we plan to refine the program to also allow the investigation of the dynamics and durability of various models.

ACKNOWLEDGMENT

LITERATURE

[1] Sága, M., Vavro, J., Kopecký, M. Počítačová analýza a syntéza mechanických sústav. 1.edition. ZUSI Žilina, 2002. Ppt. 267. ISBN-13: 978-80-968605-4-8
[2] Sága, M., Dekýš, V., Žmindák, M., Mazúr, J., Kocúr, R. Príspevok k analýze kumulácie únavového poškodenia pri viacosovom namáhaní. Acta Mechanica Slovaca, Košice 1/2006, ppt. 475 – 484. ISSN 1335-2393

APPLIED MECHANICS 2023

Grand Hotel Sergijo, April 19th – 21st 2023
Piešťany, SLOVAKIA

TOWARDS HYDRODYNAMIC LUBRICATION AND SYSTEM DYNAMICS RELATED TO TEXTURED SURFACES

PAVEL POLACH[1], JAN RENDL[2], LUBOŠ SMOLÍK[3], MILAN OMASTA[4], PETR ŠPERKA[5], MICHAL HAJŽMAN[6]

Hydrodynamic lubrication is an efficient phenomenon for connecting various relatively-moving structural parts in engines, rotors, manipulators, etc. Several approaches to the investigation of the tribological behavior of systems with textured surfaces are introduced. At first, a pin-on-disc setup is used to study the basic properties of the contact employing experiments and computational modelling. The second part of the paper deals with rotor dynamics related to a textured bearing.

KEYWORDS

Hydrodynamic lubrication, Tribology, Textured surfaces, Rotor dynamics

INTRODUCTION

Hydrodynamic sliding contacts are often found in various mechanical components. These are, for example, journal and thrust bearings, piston rings and thrust washers and seals. Low friction, high load-carrying capacity and long service life are the main goals in developing these contacts. One of the most important directions of development is surface texturing.

Targeted surface treatments have various positive benefits. Surface dimples can help to supply contact with lubricant, trap wear particles and reduce direct contact area and level of

[1] **Assoc. Prof. Dr. Ing. Pavel Polach**, New Technologies for the Information Society, Faculty of Applied Sciences, University of West Bohemia, Technická 8, Plzeň, Czech Republic. Tel +420 604 462 384. Email: ppolach@ntis.zcu.cz

[2] **Ing. Jan Rendl, Ph.D.**, New Technologies for the Information Society, Faculty of Applied Sciences, University of West Bohemia, Technická 8, Plzeň, Czech Republic. Email: rendlj@ntis.zcu.cz

[3] **Ing. Luboš Smolík, Ph.D.**, New Technologies for the Information Society, Faculty of Applied Sciences, University of West Bohemia, Technická 8, Plzeň, Czech Republic. Email: carlist@ntis.zcu.cz

[4] **Ing. Milan Omasta, Ph.D.**, Department of Tribology, Faculty of Mechanical Engineering, Brno University of Technology, Technická 2896/2, Brno, Czech Republic. Email: milan.omasta@vut.cz

[5] **Ing. Petr Šperka, Ph.D.**, Department of Tribology, Faculty of Mechanical Engineering, Brno University of Technology, Technická 2896/2, Brno, Czech Republic. Email: petr.sperka@vut.cz

[6] **Assoc. Prof. Ing. Michal Hajžman, Ph.D.**, Department of Mechanics, Faculty of Applied Sciences, University of West Bohemia, Technická 8, Plzeň, Czech Republic. Email: mhajzman@kme.zcu.cz

adhesion. In the hydrodynamic regime, dimples can increase the load-carrying capacity due to local cavitation with asymmetric pressure distribution or inertia-related effects (e.g. [1]).

Surface texturing is an effective way to improve the tribological performance of hydrodynamic contacts. The main problem is that the effect of the texture strongly depends on the operating parameters concerning the mode in which the lubricated contact operates. There is also significant dependence on wall slip, cavitation, thermal effects, etc. A positive effect under certain conditions may be detrimental under other conditions. Due to the complexity of the issue, this topic remains a current subject of research.

The goal of the paper is to introduce several approaches to the investigation of the tribological behavior of systems with textured surfaces. At first, a pin-on-disc setup is used to study the basic properties of the contact employing experiments and computational modelling. The second part of the contribution deals with rotor dynamics related to a textured bearing.

PIN-ON-DISC METHOD

To understand the local effects of texture on tribological properties, it is useful to have direct insight into the contact. In recent years, the cavitation phenomenon has been observed in various surface textures using a high-speed camera in a parallel axial bearing and a pin-on-disc configuration (e.g. [2]). Optical techniques are also suitable for accurate measurement of the thickness of the lubricating film.

The pin-on-disc experimental setup, where a small pin is in contact with a rotating disc, is a common method used for tribological research. Using this method, important tribological characteristics such as transmitted forces, oil film height, temperature, etc. can be investigated and recorded. First of all, it is necessary to set up the proper configuration of the experiment so that all the necessary variables are correctly measured. The second step is the creation of a suitable mathematical model, its solution and analysis. The results provide important insights into the tribological behavior of interacting surfaces [3].

An experimental approach developed at the Department of Tribology Brno University of Technology, which uses optical methods, was used to study the film thickness and load-carrying capacity of the contacts. The experimental test rig consists of a flat static slider on a rotating transparent (glass/sapphire) disc (see Fig. 1). Optical observation is allowed from the bottom. A light-induced fluorescence technique is used to measure the film thickness. This technique is based on the light excitation of a lubricant containing a fluorescent dye that emits light at shifted wavelengths. By separating the emission beam from the excitation, its intensity is proportional to the film thickness. The infrared (IR) thermography technique is used for temperature distribution mapping.
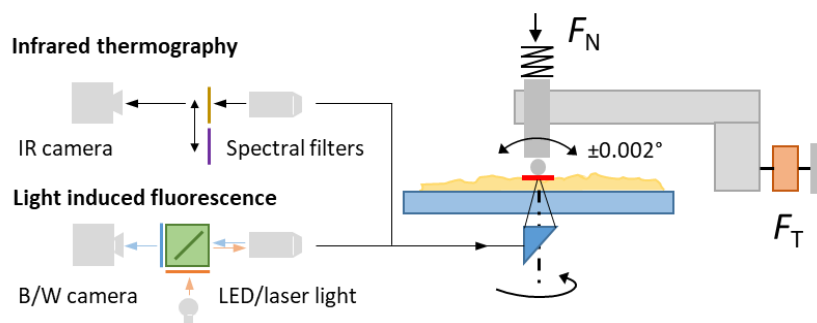

Fig. 1 Scheme of the experimental test rig (taken from [4])

A series of experiments were carried out on the experimental equipment with different texture parameters, geometric configuration (inclination) and operational parameters (load and disc speed). For each texture, the minimum film thickness and friction force as a function of

normal force and velocity were evaluated and compared with smooth surfaces. The experimental results were compared with the numerical simulations to validate the techniques and discuss possible deviations. A pin-on-disc numerical model was developed and analyzed that took into account the operating conditions, the geometry of the test rig and the various types of pins. Two approaches were used to study the hydrodynamic lubrication between the pin and the disc. First, a thin oil film approximation based on Reynolds theory was used. This approach adequately described the lubrication of smooth pins but proved ineffective for textured surfaces. Second, a pin-on-disc CFD model was used to validate the obtained results for a smooth pin and to analyze the textured surfaces. Numerical results were compared with experimentally obtained data. The film height, rotation speed, pin inclination, hydrodynamic force and friction were studied for smooth and textured pins. Typical results are shown in Fig. 2.
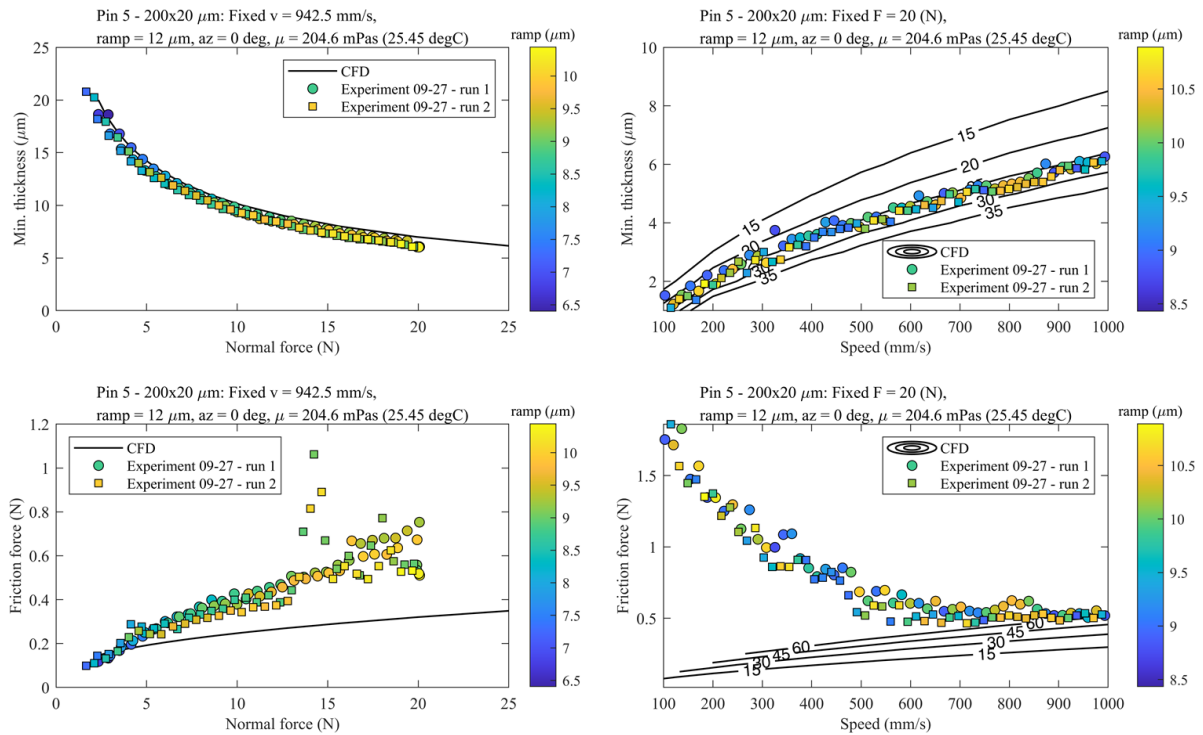
Fig. 2 Experimental results with textured pin compared with results of numerical simulation

ROTOR DYNAMICS WITH TEXTURED BEARINGS

The knowledge obtained from laboratory experiments on a pin-on-rig test device and from the validation of the results of these experiments using numerical simulations can be successfully used for the design of the textures of the journal bearings used to support the rotors. Rotors are supported in journal bearings in most applications because these bearings are cheap and are not prone to fatigue damage, unlike rolling element bearings. However, due to their design with an oil film, journal bearings cause non-linear vibrations and instability of the rotors, and also high power losses. Both the dynamic and tribological properties of the bearing can be improved if several shallow textures are machined on the inner bearing shell. The bearing shells can also contain surface irregularities after the manufacturing process with respect to prescribed engineering tolerances.

Scientific literature deals with journal bearings with textures or with surface roughness relatively often. But the literature is mainly focused on journal bearings without investigating rotor dynamic behavior.

Let's mention at least three publications. Smolík et al. [5] theoretically and experimentally investigate the effects of textures produced by a mechanical indentation on the stability of journal bearings. The research primarily aims at lightly loaded journal bearings used, e.g. in vertical rotors and microturbines. The results show that textures located close to the minimum oil film thickness can noticeably improve stability at low specific loads. Study [6] investigates the combined influence of slip boundary condition and non-Newtonian lubricants on the tribological performance of hydrodynamic textured journal bearing. It has been observed that slip-texture bearings with a change in the rheology of lubricant from Newtonian to pseudoplastic show significant improvement in the maximum pressure, the average rise in temperature, and lubricant-bearing friction force. Pei et al. [7] study the effects of the surface texture on the performance of floating ring bearings. A deterministic lumped-parameter thermal model was employed to estimate the floating ring bearing performance. The results show that textures can considerably affect the floating ring bearing performance, such as significantly increasing the side leakage and reducing the temperature rise.

CONCLUSION

In this paper, the pin-on-disc method used for the investigation of the tribological behavior of systems with textured surfaces is first presented. The specific experimental test rig used for the investigation of tribological properties is introduced, and the experimental results are validated by numerical simulations. In the second part of the paper, the use of textured bearing surfaces in rotor dynamics is briefly presented.

ACKNOWLEDGMENT

LITERATURE

[1] Gropper, D., Wang, L., Harvey, T. J. Hydrodynamic lubrication of textured surfaces: A review of modeling techniques and key findings. Tribology International. 2016, 96, 509-529. ISSN 0301-679X.

[2] Hsu, S. M., Jing, Y., Hua, D., Zhang, H. Friction reduction using discrete surface textures: principle and design. Journal of Physics D: Applied Physics. 2014, 47(33), paper 33/335307. ISSN 0022-3727.

[3] Stachowiak, G. W., Batchelor, A. W. Engineering Tribology. Butterworth-Heinemann, St. Louis, 2013. ISBN 9780750678360.

[4] Hajžman, M., Rendl, J., Smolík, L., Omasta, M., Šperka, P. Methodology for the computational analysis of hydrodynamic lubrication in pin-on-disc experiments. Proceedings of the International Colloquium DYMAMESI 2023. Cracow (Poland), Cracow University of Technology. 2023, 31-34. ISBN 978-80-87012-85-7.

[5] Smolík, L., Rendl, J., Omasta, M., Byrtus, M., Šperka, P., Polach, P., Hartl, M., Hajžman, M. Comprehensive analysis of fluid-film instability in journal bearings with mechanically indented textures. Journal of Sound and Vibration. 2023, 546, paper 117454. ISSN 0022-460X.

[6] Arif, M., Kango, S., Shukla, D. K. Analysis of textured journal bearing with slip boundary condition and pseudoplastic lubricants. International Journal of Mechanical Sciences. 2022, 228, paper 107458. ISSN 0020-7403.

[7] Pei, S., Xu, H., Yun, M., Shi, F., Hong, J. Effects of surface texture on the lubrication performance of the floating ring bearing. Tribology International. 2016, 102, 143-153. ISSN 0301-679X.

Speed control of DC motor – educational model

Ladislav Šarkán[1], Ján Eštok[2], Vladimír Goga[3], Juraj Paulech[4],
Šimon Berta[5], Justín Murín[6]

This paper presents the design of an educational model for speed control of DC motor. The model consists of a pair of two DC motors, one of them is the drive motor, and the other is the generator, which represents the load of the system. The model makes it possible to measure voltage, current and speed of the drive motor. The drive motor speed control system uses a PID controller. Regulator's parameters can be adjusted and thus the quality of regulation process can be monitored.

KEYWORDS

DC motor, Speed control, PID controller, LabView, Educational model

INTRODUCTION

Electric motors convert electrical energy into mechanical rotary motion. Depending on the requirements for the shaft speed, it is possible to use several types of electric motors: AC, DC, BLDC, servomotor, or stepper motor. DC motors are suitable for devices with lower power and continuously adjustable speed, where the speed control to a selected value is often required. The set speed should be maintained by the regulator at the selected value, even if the system is

---

[1] **Ing. Ladislav Šarkán**, Department of Automotive Mechatronics, Faculty of Electrical Engineering and Information Technology, Slovak University of Technology in Bratislava. Ilkovičova 3, Bratislava, Slovak Republic. Email: ladislav.sarkan@stuba.sk

[2] **Bc. Ján Eštok**, Department of Automotive Mechatronics, Faculty of Electrical Engineering and Information Technology, Slovak University of Technology in Bratislava. Ilkovičova 3, Bratislava, Slovak Republic. Email: xestok@stuba.sk

[3] **doc. Ing. Vladimír Goga, Ph.D.**, Department of Automotive Mechatronics, Faculty of Electrical Engineering and Information Technology, Slovak University of Technology in Bratislava. Ilkovičova 3, Bratislava, Slovak Republic. Email: vladimir.goga@stuba.sk

[4] **Ing. Juraj Paulech, Ph.D.**, Department of Automotive Mechatronics, Faculty of Electrical Engineering and Information Technology, Slovak University of Technology in Bratislava. Ilkovičova 3, Bratislava, Slovak Republic. Email: juraj.paulech@stuba.sk

[5] **Ing. Šimon Berta,** Department of Automotive Mechatronics, Faculty of Electrical Engineering and Information Technology, Slovak University of Technology in Bratislava. Ilkovičova 3, Bratislava, Slovak Republic. Email: simon.berta@stuba.sk

[6] **prof. Ing. Justín Murín, Dr.Sc.**, Department of Automotive Mechatronics, Faculty of Electrical Engineering and Information Technology, Slovak University of Technology in Bratislava. Ilkovičova 3, Bratislava, Slovak Republic. Email: justin.murin@stuba.sk

exposed to a change in load or other disturbing influences. Most often, a PID controller is used for this purpose, which adjusts the DC motor power supply based on the difference between the desired and actual motor speed. It is therefore a system in a closed loop, where the measured actual speed represents the feedback of the control system.

If the mathematical model of the controlled system (in our case a DC motor) is known, then it is possible to design a controller based on theory and analyze its operation through computer simulations in appropriate software. However, the actual behavior of the entire system needs to be analyzed by practical measurements on an experimental device. Therefore, the presented educational model for speed control of DC motor was designed. Similar educational models for DC motor speed control can be found in [1, 2, 3].

DESIGN OF THE EDUCATIONAL MODEL

The educational model is shown in Fig. 1. The main part of the model is a pair of two DC motors, one of which is a drive motor, and the other is the generator. The power supply for the motors is 12 VDC. Each motor has a built-in reduction gearbox (gear ratio 14:1) and the drive motor has an optical encoder with two hall sensors for speed measurement. The motor shafts are connected by a flexible clutch. The resistive load of the generator is defined by a set of power resistors connected to the generator i.e., driven motor.
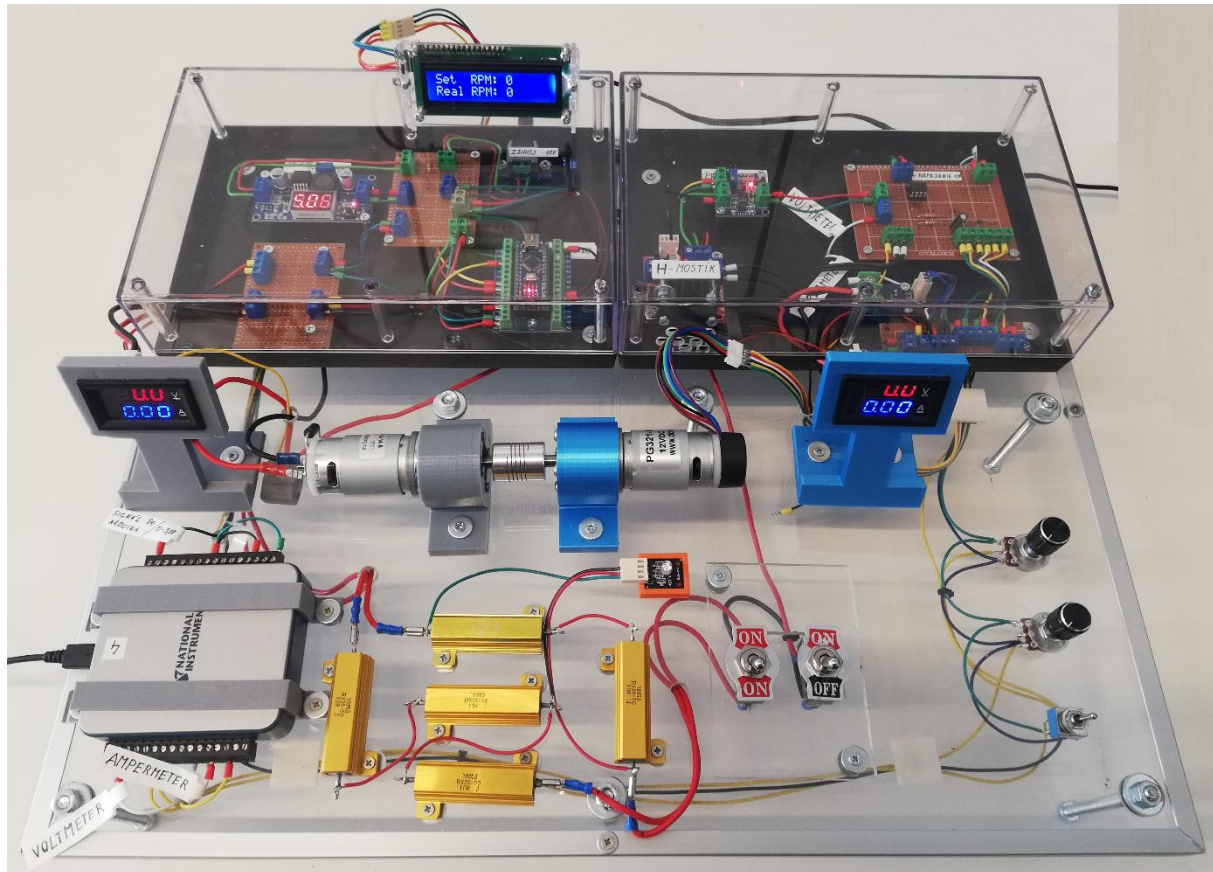
Fig. 1 Education model for speed control of DC motor

The power supply of the entire model is 12 VDC. The drive motor is powered via H-bridge motor driver controlled by a PWM signal from the voltage to PWM converter module, which transforms the voltage analog control signal from the measuring card (National Instruments USB-6001). The measuring card therefore generates a control action voltage signal and at the same time measures the signal from the encoder and evaluates the actual speed of the motor. The card is connected via USB to the computer and the control program is created in the

software LabView. Other measured quantities in LabView are voltage and current on the drive motor. All quantities are also measured by external digital voltmeter-ammeter modules with digital displays (each DC motor has its own measuring module), and the speed of the drive motor is measured by the Arduino Nano platform and its value is displayed on the LCD display.

Model operation is possible in manual or software (LabView) mode. Two rotary potentiometers are used for manual operating mode, and switching to software mode is handled by a toggle switch. The PID controller can be activated only in the software mode. In this case, it is possible to change the controller parameters and monitor the system's response to a change in the desired motor speed or to a change in the generator's resistive load.

Several PCB boards were designed to serve primarily as connection terminals. Most of the electronic modules as well as the PCB boards and wiring are stored in two plastic boxes with a transparent cover. Holders for DC motors and for digital voltmeter-ammeter modules were made using 3D printing technology.

GRAPHICAL USER INTERFACE AND SYSTEM SPEED CONTROL

In Fig. 2 is shown GUI (graphical user interface) created in software LabView. This GUI consists of three indicators: speed, voltage and current of drive DC motor. User can define the desired motor speed (called setpoint) via graphical slider. In the middle part of GUI, there is a graph of the drive motor´s desired and actual speed shown in real time.

Parameters of PID controller are entered in the lower part of GUI and the controller itself is activated by turning on the green button.

Fig. 2 GUI - graphical user interface in LabView

Fig. 3 shows four graphs from the measurement of the drive motor speed (speed setpoint was 300 RPM). In each case, the generator was loaded by connecting a resistive load, which results in decreasing drive motor speed. This situation is represented by the graph in Fig. 3a) when the regulator is deactivated.

A well-tuned PI controller (P = 0.015; T_I = 0.002 min.) adjusts the motor speed in a short settling time and without overshooting, which is shown in Fig. 3b). The PI controller with parameters P = 0.036; T_I = 0.0015 min. regulates the motor speed with significant overshooting and in long settling time, see Fig. 3c). However, the system control is still stable for the reason

that the regulation process settles after a while. Unlike in the next case, where an inappropriately set PI controller (P = 0.015; T_I = 0.0002 min.) will cause system instability, which is shown in Fig. 3d). This condition should be avoided because the desired engine speed can never be reached.

From the graphs in Fig. 3, it can be read that the controller parameters must be appropriately designed so that the regulation process is of sufficient quality. User has the option of setting his own PID parameters during the control process in the GUI.
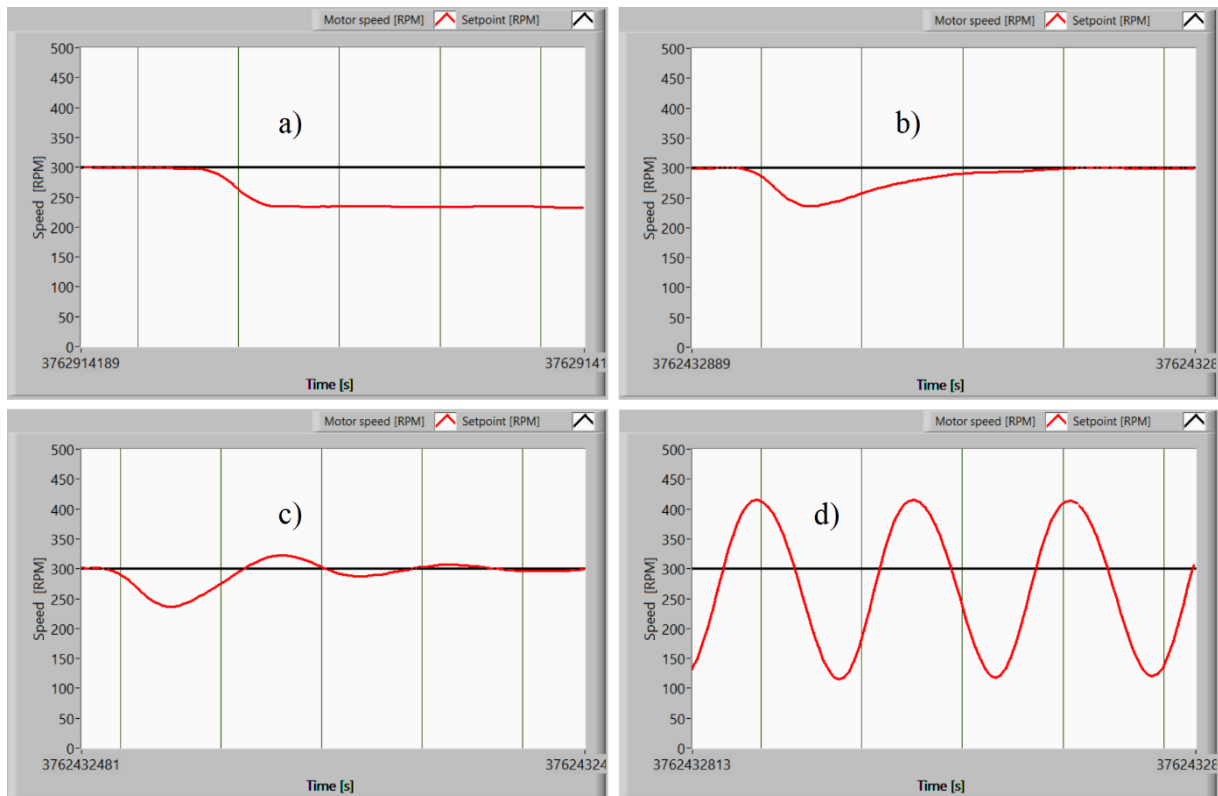
Fig. 3 System control plots

CONCLUSION

A physical educational model of a DC motor speed control was designed. This educational model is a complex mechatronic device, that provides the possibility to evaluate the quality of control process and allows to compare it with the computer simulations. The construction of this device was described, as well as its software environment and operation.

ACKNOWLEDGMENT

LITERATURE

[1] G. Găşpăresc, "PID control of a DC motor using Labview Interface for Embedded Platforms," 2016 12th IEEE International Symposium on Electronics and Telecommunications (ISETC), Timisoara, Romania, 2016, pp. 145-148, doi: 10.1109/ISETC.2016.7781078.

[2] M. Dursun, A. Fenercioglu, "An educational tool for DC motor PID speed controller," Scientific Research and Essays, 2011, pp. 4227-4237, doi: 10.5897/sre11.297.

[3] DC motor training system, Commercial product by Bytronic educational technology. Retrieved from: http://www.bytronic.net/product/dc-motor-training-system/.

Contribution to the creation of computational models in the MSC.Adams

Zdenko Šavrnoch[1], Alžbeta Sapietová[2], Michal Paulec[3]

This paper presents a review of rotating machine dynamics with a focus on the Laval rotor. It presents the creation of a virtual model of the Laval (Jeffcott) rotor in the MSC.ADAMS software environment. Parameters describing the stability of the rotor operation, i.e., the critical angular velocity and the trajectory of the rotor center of gravity (CoG orbit), were monitored and evaluated.

KEYWORDS

Laval's rotor, Jeffcott rotor, rotordynamics, Adams, rotary machines, MATLAB.

INTRODUCTION

Nowadays, the main goal of developments in the field of rotor dynamics is to achieve an ever higher operating speeds, as this, especially in production facilities, ultimately affects productivity gains. An energy machine that rotates at a higher speed can generate or transform more energy. Despite the overall progress in recent years, rotor dynamics remains a highly investigated area, with research focused both on the effective application of previously known concepts to new spheres as well as a better understanding of the behavior of rotating systems. Non-linear and non-stationary rotor dynamics are good examples of areas where extensive and in-depth research is still necessary.

ROTORDYNAMICS

The branch of applied mechanics that deals with the behavior, operation, and diagnostics of rotating machinery and equipment. Rotating machines in their simplest form consist of a rotating element (shaft, disk, etc.) mounted in a supporting structure, bearings (Laval's rotor).

As the rotation speed increases, the magnitude of the amplitude of the oscillations increases, which is excited by the unbalance of the system. The amplitude of the oscillations reaches its maximum values at critical speeds. Typical examples of rotating machines are

---

[1] **Ing. Zdenko Šavrnoch**, Department of Applied Mechanics, Faculty of Mechanical Engineering, University of Zilina. Univerzitná 1, Zilina, Slovakia. Tel +421 41 513 2965. Email: Zdenko.Savrnoch@fstroj.uniza.sk

[2] **prof. Ing. Alžbeta Sapietová, Ph.D.**, Department of Applied Mechanics, Faculty of Mechanical Engineering, University of Zilina. Univerzitná 1, Zilina, Slovakia. Tel +421 41 513 2957. Email: alzbeta.sapietova@fstroj.uniza.sk

[3] **Ing. Michal Paulec**, Department of Applied Mechanics, Faculty of Mechanical Engineering, University of Zilina. Univerzitná 1, Zilina, Slovakia. Tel +421 41 513 2965. Email: Michal.Paulec@fstroj.uniza.sk

turbines (steam, gas), the crankshaft of internal combustion engines, gearboxes, or computer hard drives.

LAVAL ROTOR

When investigating the bending and center of gravity (CoG) trajectories of rotating masses, we can use a simple model of an immaterial shaft and point mass, which represents the rotating masses, bound to that shaft. The system can be characterised by damping, or by the absence of it. Other, parameters by which the system can be described, are the way the shaft is mounted and the deformability of the bodies that form the system.

Laval (Jeffcott) rotor can be assembled in three ways:

- Flexible (compliant) shaft system

- System with rigid shaft and compliant bearings

- System with flexible (compliant) shaft and compliant bearings

COMPUTATIONAL MODEL OF UNDAMPED LAVAL ROTOR

This type of system is characterized by its placement in rigid rotating supports. The rigid disk is mounted symmetrically on a flexible shaft without eccentricity. Initial deflection of the CoG from the central axis (the centerline of the rigid rotational support) is in the vertical direction of the y-axis, proportional to the gravity of the system.
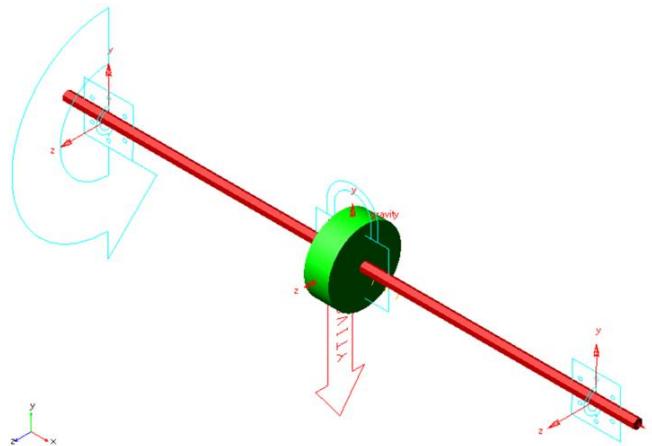
Fig. 1 Disk symmetrically mounted on flexible shaft and rigid supports – rest configuration

An equality must hold in the system between the volumetric forces of the disk and the restoring forces given by the shaft stiffness:

$$m\ddot{z}_T = -kz_H \tag{1}$$

$$m\ddot{y}_T = -ky_H \tag{2}$$

Where: m – disk mass

k – shaft stiffness

$z_H,\ y_H$ – distance of the shaft-disk centerline intersection from the axis of rotation

Shaft bending stiffness in case of symmetrically mounted disk:

$$k = \frac{48EJ}{l^3} \tag{3}$$

Where: E – Young modulus

J – quadratic moment

l – distance between constraints

All material constants are based on the material Steel S235 which was chosen from the material library of MSC.Adams.

Flexible body, shaft, was generated internally in MSC.Adams using tetrahedral elements with linear element order. Adams also allows to import "Modal Neutral File" (.mnf) or "Bulk Data File" (.bdf) files generated externally.

Tab. 1 Other parameters used in the computational model

Parameter	Denotation	Nominal value	Units
Material density (steel S235)	ρ	7801	[kg/m^3]
Young modulus	E	2,07.10^{11}	[Pa]
Disk mass	m_k	0,846	[kg]
Shaft mass	m_h	0,358	[kg]
Shaft length	L_h	585	[mm]
Shaft diameter	d_h	10	[mm]
Disk width	b_k	25	[mm]
Disk diameter	d_k	75	[mm]
Shaft mounting distance from disk	l_b	250	[mm]

SIMULATION RESULTS

Initial angular velocity of the rotor is 130 [rad/s] and its linear ramp is given by the function 130+10·time [rad/s]. Rotor rotates clockwise (CW) and starts at equilibrium.

Tab. 2 Simulation parameters

End Time	15 [s]
Step size	0,0001 [-] / 10 [kHz]

For a better visualization and wider option of diagram modification, were the output data exported from MSC.Adams to MATLAB.
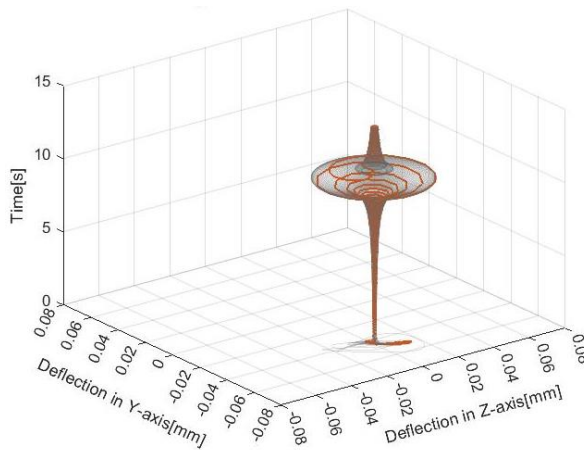
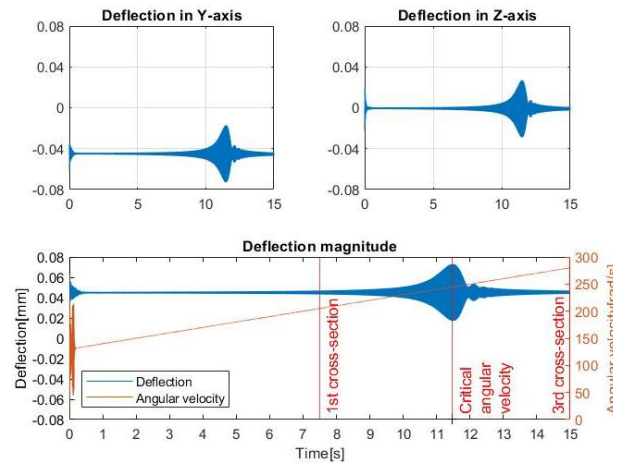Fig. 2 Compound diagram of system CoG deflection - 3D representation

Fig. 3 System CoG deflection 2D representation
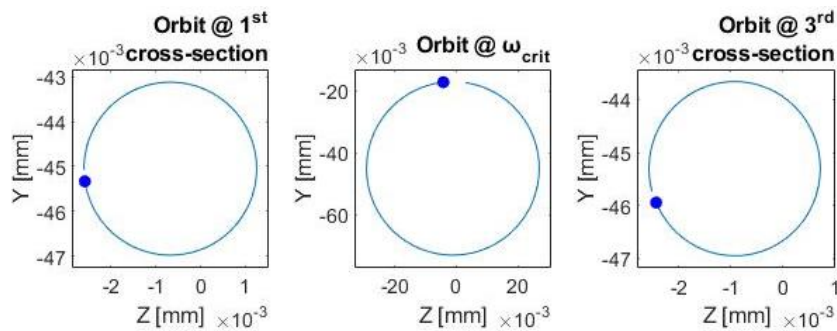
Fig. 4 Square diagrams of system CoG orbit at different speeds

CONCLUSION

The deflection amplitude continuously increases for both monitored axes Y and Z (Fig. 3), while it reaches its maximum at an angular velocity of 244.76 [rad/s] (2337.29 [rpm]). Trajectory, or the orbit described by the CoG of the rotor within one period has the circular shape. The rotational supports have the same stiffness in both Y and Z axes. Thus, the critical angular velocity of the rotor remains the same for both axes. The orbits retain their circular shape due to the absence of play in the rotational supports (Fig. 4). Considering the weight of the disk acting on the flexible shaft causing deflection (Fig. 3 - Deflection in Y-axis) from the initial position of the center of gravity of the bent rotor.

ACKNOWLEDGMENT

LITERATURE

[1] R. Gash, H. Pfützner. Dynamika rotorů. SNTL – Nakladatelství technické literatury, Praha 1980. Číslo publikace 04-226-80.

[2] H.J. Sneck. Machine Dynamics. Prentice-Hall, 1991. ISBN 0-13-543299-5.

[3] A. Sapietová, V. Dekýš, L. Jakubovičová, P. Novák, M. Sapieta. Dynamika riešená v programoch Matlab a MSC.ADAMS. EDIS, Žilina, 2020. ISBN 978-80-554-1841-4.

HYPERSONIC NON-EQUILIBRIUM LAMINAR FLOW SOLVER DEVELOPMENT WITHIN OPENFOAM FRAMEWORK

ADAM TATER[1], JIŘÍ HOLMAN[2]

Under standard conditions, it is possible to describe the compressible fluid flow by the system of highly nonlinear Navier-Stokes equations. This task gets even more complicated when hypersonic speeds are reached. Under conditions of extremely increased temperatures near the flowed surfaces, it is no longer possible to neglect ongoing chemical reactions in the air itself. Present contribution describes basics of the implicit hypersonic flow solver development within OpenFOAM framework.

KEYWORDS

Hypersonic flow; Non-equilibrium flow; LU-SGS method

INTRODUCTION

In past decades, advances in computational fluid mechanics have been possible thanks to the development of computer technology. Nowadays, simulations are becoming almost routine with the use of commercial solvers and under standard atmospheric conditions. This fact changes rapidly in the case of accelerating the flowing medium above the limit of hypersonic flow. This situation is very common in atmospheric re-entry flows. Under these conditions, it is no longer possible to describe the flow of a compressible fluid using a system of Navier-Stokes equations to achieve satisfactory results. It is necessary to include other effects in our considerations.

Firstly, it is the thermochemical non-equilibrium that is considered. A gas is in a state of thermal non-equilibrium when its internal energy cannot be described by a single thermodynamic temperature. Further, it is in chemical non-equilibrium while it does not satisfy chemical equilibrium conditions. Large regions of the hypersonic flow field near surfaces may be in thermochemical non-equilibrium. This is due to the passage of the gas through a strong shock wave, which transforms much of the kinetic energy into random translation motion. The gas is in motion during the transition of the energy back to equilibrium, so the internal energy modes and chemical composition of the gas lag the changes in the translational temperature.

---

[1] **Ing. Adam Tater**, Department of Technical Mathematics, Faculty of Mechanical Engineering, Czech Technical University in Prague. Karlovo náměstí 13, Prague, Czech Republic. Email: adam.tater@fs.cvut.cz

[2] **Ing. Jiří Holman, Ph.D.**, Department of Technical Mathematics, Faculty of Mechanical Engineering, Czech Technical University in Prague. Karlovo náměstí 13, Prague, Czech Republic.

Secondly, finite-rate wall catalysis is the most important effect for correct determination of convective heating. When the wall is noncatalytic, it does not promote recombination at the surface. Thus, it does not contribute the convective heating. If, on the other hand, the surface is catalytic, the chemical energy is released at the surface, and the heat transfer increases. Reality is somewhere between these extreme states and several models of finite-rate wall catalysis exist.

Lastly, vibration-dissociation coupling is another major problematic, because even small changes in the dissociation rates can change the flow field rapidly. It describes a decrease of energy required to dissociate the vibrationally excited molecule. There are also few other effects that need to be considered in certain applications, such as low-density and thermal radiation.

GOVERNING EQUATIONS

We assume that the gas is described by the Navier-Stokes equations extended to account for the presence of chemical reactions and internal energy relaxation. For these equations to be valid, the flow must satisfy the following criteria. Firstly, the gas must be a continuum. Secondly, The mass diffusion fluxes, shear stresses, and heat fluxes must be proportional to the first derivatives of the flow quantities. Thirdly, the internal energy modes must be separable and finally, the flow is only weakly ionized. Under these assumptions and by using the simplest reacting air model, the mass conservation equation for each species s can be written as

$$\frac{\partial \rho_s}{\partial t} + \frac{\partial (\rho_s u_j)}{\partial x_j} + \frac{\partial (\rho_s v_{sj})}{\partial x_j} = w_s, \ s = \{N_2, N, O_2, O, NO\}, \tag{1}$$

where again, ρ_s is the species density and w_s is the chemical source term. These source terms can be evaluated for each species using the law of mass action [1]. The mass averaged velocity is u_j and the diffusion velocity of species s is v_{sj} in the x_j direction. The momentum equation has the familiar form of

$$\frac{\partial (\rho u_i)}{\partial t} + \frac{\partial}{\partial x_j} (\rho u_i u_j + p \delta_{ij} - \tau_{ij}) = 0, \tag{2}$$

where the pressure p is the sum of the partial pressures and τ_{ij} is the shear stress tensor. The total energy conservation equation has the form

$$\frac{\partial E}{\partial t} + \frac{\partial}{\partial x_j} ((E + p) - \tau_{ij} u_i + q_j + \sum \rho_s v_{sj} h_s) = 0, \tag{3}$$

where E is the total energy per unit volume, q_j is the total heat flux vector, and h_s is the species s specific enthalpy. The derivation of the vibrational energy conservation is demanding because the vibrational state is coupled to the chemical state. Molecules that are highly vibrationally excited are more likely to dissociate. Thus, when dissociation occurs, the process removes more vibrational energy from the vibrational energy pool. Likewise, when recombination occurs the newly formed molecule may be formed at an elevated level. A full derivation of this equation is available in [2] and the final form of vibrational energy conservation can be written as

$$\frac{\partial E_v}{\partial t} + \frac{\partial}{\partial x_j} (E_v u_i + \sum E_{vs} v_{si} + \sum q_{vsi}) = \sum Q_{V-Ts} + \sum Q_{CHs}, \tag{4}$$

where $E_{vs} = \sum E_{vs}$. Source terms $\sum Q_{V-Ts}$ and $\sum Q_{CHs}$ are responsible for energy exchange between vibrational and translational modes due to collisions and the dissipation of vibrational energy due to chemical reactions, respectively. Furthermore, the system of equations is closed by an equation of state for an ideal gas analogy.

METHODOLOGY

The above equations can be expressed in the integral form. This form is suitable for the finite volume approximation with assumption of mesh consisting of fixed control volumes as follows

$$\frac{d}{dt}\int_\Omega \boldsymbol{W}dV + \oint_{\partial\Omega}(F - F^v)\cdot d\boldsymbol{S} = 0, \tag{5}$$

where $\boldsymbol{W} = (\rho_{N_2}, \rho_N, \rho_{O_2}, \rho_O, \rho_{NO}, \rho\boldsymbol{U}, E, E_v)$ is the vector of conservative variables and F^v and F are viscous fluxes and inviscid fluxes, respectively. Spatial discretization of conservation laws in their integral form is performed using the finite volume method by taking

$$|\Omega_i|\frac{d\boldsymbol{W}_i}{dt} = -\boldsymbol{R}(\boldsymbol{W})_i = -\sum_{j\in N_i}(F_{ij} - F_{ij}^v)\cdot \boldsymbol{S}_{ij}, \text{where } \boldsymbol{W}_i(t) = \frac{1}{|\Omega_i|}\int_{\Omega_i}\boldsymbol{W}(x,t)dV, \tag{6}$$

where Ω_i is the mesh cell i and N_i is the set of indices of neighbouring cells. The viscous fluxes F_{ij}^v are discretized with the central scheme and the discretization of inviscid fluxes F_{ij} is made using linear reconstructions with the AUSM+up [3] or rotated-hybrid Riemann solver [4]. In case of steady state problem, the time derivative is replaced by the backward difference as

$$|\Omega_i|\frac{\boldsymbol{W}_i^{n+1} - \boldsymbol{W}_i^n}{\Delta t_i} = -\boldsymbol{R}(\boldsymbol{W}^{n+1})_i \approx -\boldsymbol{R}(\boldsymbol{W}^n)_i - \sum_j\frac{\partial \boldsymbol{R}(\boldsymbol{W}^n)_i}{\partial \boldsymbol{W}_j}(\boldsymbol{W}_j^{n+1} - \boldsymbol{W}_j^n), \tag{7}$$

by denoting $\Delta\boldsymbol{W}_j^n = \boldsymbol{W}_j^{n+1} - \Delta\boldsymbol{W}_j^n$ in above equation, it can be rewritten as

$$\sum_j(\frac{|\Omega_i|}{\Delta t_i}\boldsymbol{I} + \frac{\partial \boldsymbol{R}(\boldsymbol{W}^n)_i}{\partial \boldsymbol{W}_j})\Delta\boldsymbol{W}_j^n = -\boldsymbol{R}(\boldsymbol{W}^n)_i. \tag{8}$$

Following steps are analogical to the derivation of matrix-free LU-SGS solver for compressible flows [5]. Firstly, the Jacobian is replaced by its low order thin-layer approximation for viscous terms and the first order Rusanov flux approximation of convective fluxes as

$$F_{ij}\cdot \boldsymbol{S}_{ij} \approx \frac{1}{2}(F(\boldsymbol{W}_i) + F(\boldsymbol{W}_j))\cdot \boldsymbol{S}_{ij} - \frac{\vartheta_{ij}}{2}(\boldsymbol{W}_j - \boldsymbol{W}_i), \tag{9}$$

where ϑ_{ij} is the spectral radius of Jacobian $F_{ij}\cdot \boldsymbol{S}_{ij}$. Thanks to the simple definition of the Rusanov flux, the low order residual can be expressed as

$$\boldsymbol{R}(\boldsymbol{W})_i^{low} = \frac{1}{2}\sum_{j\in N_i}\vartheta_{ij}^*\boldsymbol{W}_i + \frac{1}{2}\sum_{j\in N_i}(F(\boldsymbol{W}_j)\cdot \boldsymbol{S}_{ij} - \vartheta_{ij}^*\boldsymbol{W}_j), \tag{10}$$

where ϑ_{ij}^* includes both the spectral radii of Jacobians of convective terms and the thin-layer approximation of viscous terms, therefore ϑ_{ij}^* must be computed as

$$\vartheta_{ij}^* = \vartheta_{ij} + \frac{|\boldsymbol{S}_{ij}|}{|x_i - x_j|}\max(\frac{4\mu_{ij}}{3\rho_{ij}}, \alpha_{ij}), \tag{11}$$

where $\boldsymbol{x}_i$ and $\boldsymbol{x}_j$ are the position vectors of centers of cells, μ_{ij} is the dynamic viscosity and α_{ij} is the thermal diffusivity. Finally, the product of Jacobians with $\Delta\boldsymbol{W}$ is approximated with finite differences and the system of equations is solved with the LU-SGS method.

Let L $(L_i = \{j \in N_i : j < i\})$ and U $(U_i = \{j \in N_i : j > i\})$ denote the sets of cells belonging to lower and upper part of the matrix, respectively. Then the matrix-free LU-SGS scheme can be written using the following two step procedure

$$D_i\Delta\boldsymbol{W}_i^{(1)} = -\boldsymbol{R}_i - \frac{1}{2}\sum_{j\in L_i}(\Delta F_j^{(1)}\cdot \boldsymbol{S}_{ij} - \vartheta_{ij}^*\Delta\boldsymbol{W}_j^{(1)}), \tag{12}$$

$$D_i\Delta\boldsymbol{W}_i = D_i\Delta\boldsymbol{W}_i^{(1)} - \frac{1}{2}\sum_{j\in U_i}(\Delta F_j\cdot \boldsymbol{S}_{ij} - \vartheta_{ij}^*\Delta\boldsymbol{W}_j), \tag{13}$$

where $\Delta\boldsymbol{W}_i^{(1)}$, $\Delta F_i^{(1)}$, ΔF_i and D_i are computed as

$$\Delta\boldsymbol{W}_i^{(1)} = \boldsymbol{W}_i^{(1)} - \boldsymbol{W}_i^n, \Delta F_i^{(1)} = F(\boldsymbol{W}_i^{(1)}) - F(\boldsymbol{W}_i^n),$$

$$\Delta F_i = F(\boldsymbol{W}_i^{n+1}) - F(\boldsymbol{W}_i^n), D_i = (\frac{|\Omega_i|}{\Delta t_i} + \frac{1}{2}\sum_{j\in N_i}\vartheta_{ij}^*).$$

RESULTS

This research is based on measurements that take place in Calspan-University at Buffalo Research center's hypersonic wind tunnels, specifically on data published in [6]. One of the measured tasks is the hollow cylinder-flare laminar shock wave/boundary layer interaction. Six runs with different boundary conditions were measured. In Fig. 1, results obtained with solver in development (chemical source terms w_s set to zero and no equation for E_v) of the first run are presented and compared with experiment as well as with DPLR solver results by MacLean.
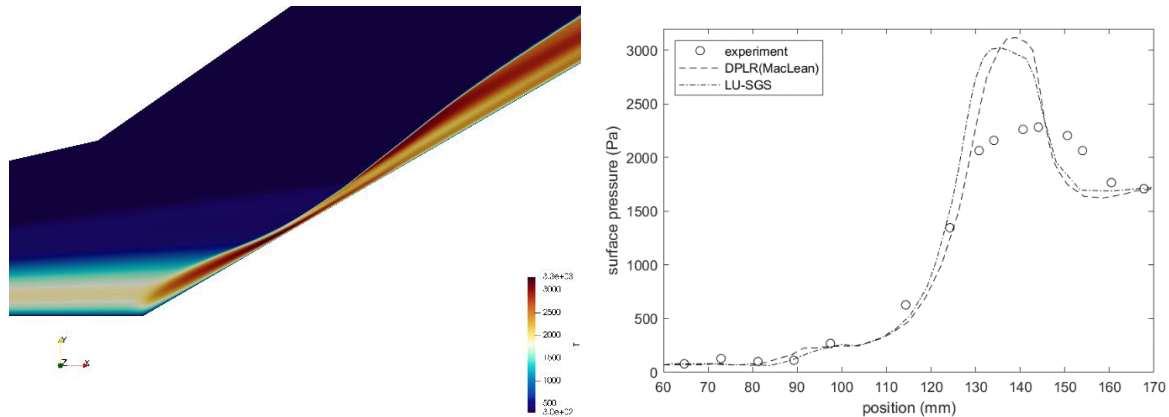

Fig. 1 Hollow cylinder-flare: (left) temperature contours; (right) surface pressure comparison.

CONCLUSION

A coupled matrix-free LU-SGS hypersonic non-equilibrium laminar flow solver was introduced. Comparison of results of hollow cylinder-flare shock wave/boundary layer interaction obtained with introduced solver in development was performed. Further development will be directed towards Reynold's averaged turbulent flow simulations.

ACKNOWLEDGMENT

LITERATURE

[1] Vincenti, Walter Guido. "Introduction to physical gas dynamic." Introduction to physical gas dynamics/Huntington (1975).

[2] Olejniczak, Joseph, and Graham V. Candler. "Vibrational energy conservation with vibration–dissociation coupling: General theory and numerical studies." Physics of Fluids 7.7 (1995): 1764-1774.

[3] Liou, Meng-Sing. "A sequel to AUSM, Part II: AUSM+-up for all speeds." Journal of computational physics 214.1 (2006): 137-170.

[4] Holman, Jiří, and Jiří Fürst. "Rotated-hybrid Riemann solver for all-speed flows." Journal of Computational and Applied Mathematics 427 (2023): 115129.

[5] Fürst, Jiří. "Development of a coupled matrix-free LU-SGS solver for turbulent compressible flows." Computers & Fluids 172 (2018): 332-339.

[6] MacLean, Matthew, Michael S. Holden, and Aaron Dufrene. "Measurements of real gas effects on regions of laminar shock wave/boundary layer interaction in hypervelocity flows." AIAA Aviation, Atlanta, GA (2014).

APPLIED MECHANICS 2023

Grand Hotel Sergijo, April 19th – 21st 2023
Piešťany, SLOVAKIA

CAN STOCHASTIC APPROACH IMPROVE RESIDUAL FATIGUE LIFE ESTIMATION OF RAILWAY AXLES?

DUŠAN TICHOŇ[1], TOMÁŠ VOJTEK[2], PAVOL DLHÝ[3], PAVEL HUTAŘ[4]

Residual fatigue life (RFL) of a railway axle was estimated by probabilistic Monte Carlo simulation of crack propagation, which enabled us to consider statistical distribution of input parameters. Cycle-by-cycle simulation of crack propagation was done based on experimental input data. The results helped to analyze the significance of parameters influencing the fatigue crack growth curve, especially the threshold, which has imminent effect on the resulting RFL.

KEYWORDS

Residual fatigue life, railway axles, Monte Carlo simulation, stochastic crack propagation modelling, EA4T steel.

1 INTRODUCTION

The railway axle plays an essential role in the running system of the train. Axles carry the whole weight of a rolling stock. Fatigue fracture of hollow railway axle [1], [2] resulted in the derailment causing devastating consequences. Hence, it is important to improve the methodology for obtaining RFL. One of the most imminent input parameters is material behavior, especially the threshold value of crack growth rate $K_{max,th}$. Since the threshold itself is affected by many physical phenomena, and we are unable to investigate it on microstructural level and include the effects into calculations, stochastic approach is useful to consider the most important inputs as probabilistic variables with specific scatter on macrostructural level. As any operator or researcher wants to stay conservative, using this methodology the RFL is calculated with probability to reach any specific value (percentiles). More precise estimation of RFL leads to inspection interval optimization and reduces the maintenance costs.

[1] **Ing. Dušan Tichoň**, Institute of Physics of Materials Czech Academy of Sciences, Zizkova 513/22, Brno, Czech Republic; Institute of Applied Mechanics Brno, Ltd., Resslova 972/3, Brno, Czech Republic. Tel +420 532 290 347. Email: tichon@ipm.cz

[2] **Ing. Tomáš Vojtek, Ph.D.**, Institute of Physics of Materials Czech Academy of Sciences, Zizkova 513/22, Brno, Czech Republic. Tel +420 532 290 362. Email: vojtek@ipm.cz

[3] **Ing. Pavol Dlhý, Ph.D.**, Institute of Physics of Materials Czech Academy of Sciences, Zizkova 513/22, Brno, Czech Republic. Tel +420 532 290 347. Email: dlhy@ipm.cz

[4] **doc. Ing. Pavel Hutař, Ph.D.**, Institute of Physics of Materials Czech Academy of Sciences, Zizkova 513/22, Brno, Czech Republic. Tel +420 532 290 351. Email: hutar@ipm.cz

2 LOADING COMPONENTS OF THE RAILWAY AXLE

Failure of common railway axles, see Fig. 1a, is predominantly caused by propagation of surface fatigue cracks that reached critical size under the effect of cyclic stress. The considered fatigue crack presents semi-elliptical shape, as shown in Fig. 1b.
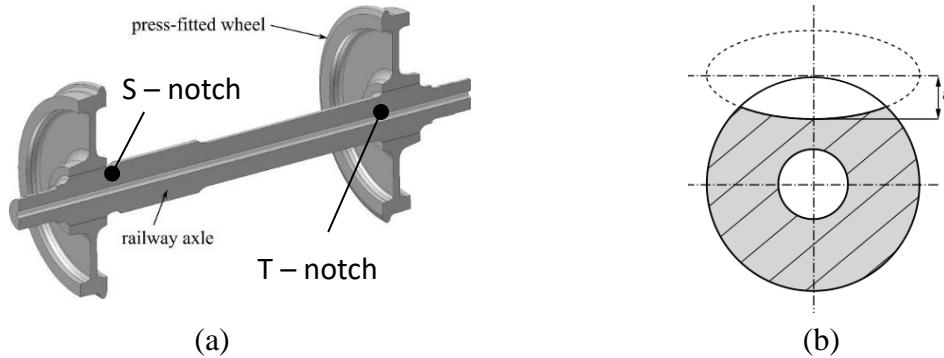

Fig. 1 Investigated railway axle [3] (a), considered semi-elliptical crack shape front (b)

There are three main loading components affecting fatigue crack propagation: dynamic bending, residual stress and press-fit load. Same as in [3], it was expected that the critical position for crack initiation is at one of the notches due to stress concentration. In this work, semi-elliptical crack was considered at the T-notch. The driving force parameter for crack growth is stress intensity factor K (SIF) under Linear Elastic Fracture Mechanics (LEFM) conditions.

i) *Dynamic bending load of a crack at the T-notch*

In [3], FE model was used to calculate the SIF caused only by pure static bending loading $K_{B,s}$. The crack shape was simplified to semi-elliptical with changing aspect ratio according to [4] and its orientation was perpendicular to the axis of the axle. The variation of loading amplitude in real service is described by a load spectrum, shown in Fig. 3a [5]. Dynamic effects are taken into account via so called dynamic coefficient k corresponding to multiple of the static load. The horizontal axis refers to a cumulative number of cycles. Since the real load spectrum is continuous, dynamic coefficient is generated randomly into a load sequence, sorted in descending order to provide more conservative estimation of RFL and to comply with axle fatigue testing. The dynamic bending amplitude sequence was given by (spectrum corresponds to 1000 km of train service):

$$K_{B,d} = k(t) \cdot K_{B,s}(a) \qquad (1)$$

ii) *Residual stress and press-fit load of a crack at the T-notch*

In this work, both residual stress and press-fit load components were considered as deterministic conservative values. According to [6], non-linear contact was modelled to obtain SIFs (K_{PF}) for press-fit load caused by the interference value 0,3 mm between the axle and the wheels, see Fig. 2a. In the case of residual stress, which is induced by machining and heat treatment of axle surface, the assumption of homogenous distribution along the axial direction of the axle was made. In Fig. 2b one can see corresponding SIF values K_{RS} to the mean residual stress profile curve.

iii) *Total load of a crack at the T-notch*

The principle of superposition was used (Eq. (2)) to determine the total SIF $K_{max}(a,t)$ based on the individual SIF components obtained by FE analyses as functions of the crack length a as follows:

$$K_{max}(a,t) = K_{PF}(a) + K_{RS}(a) + K_{B,d}(a,t) \qquad (2)$$

$$K_{min}(a,t) = K_{PF}(a) + K_{RS}(a) - K_{B,d}(a,t) \qquad (3)$$
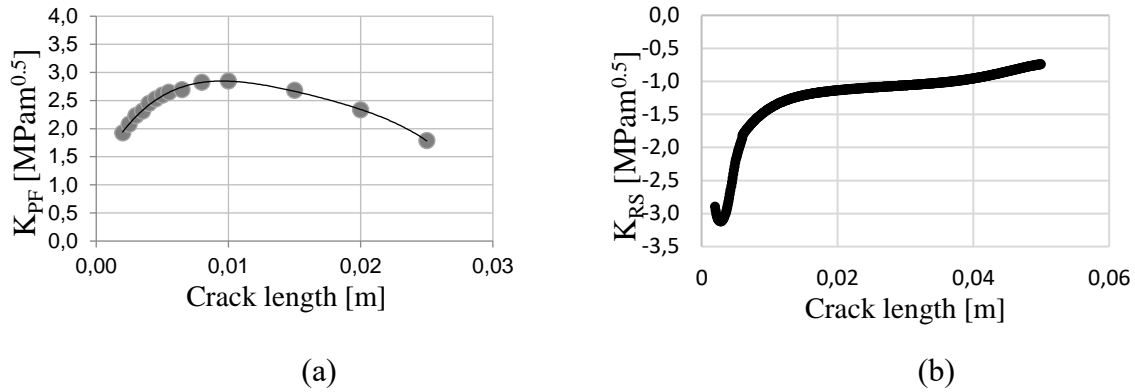

(a)　　　　　　　　　　　　　　　　(b)

Fig. 2 SIF values caused by press-fit load (a), SIF values cause by residual stress (b)

3 CRACK GROWTH MODEL AND SIMULATION OF CRACK PROPAGATION

For our purposes, generally accepted NASGRO model is used to describe crack propagation. As presented in [3], K_{max} is a more suitable parameter controlling crack propagation for applications with low asymmetry ratios R, since there is only small dependence of threshold value $K_{max,th}$ on R inside the interval from -2 up to 0,1.

The simplified form of NASGRO equation for more conservative estimations was used:

$$\frac{da}{dN} \cong \frac{\Delta a}{\Delta N} = C^*(K_{max})^{n^*}\left(1 - \frac{K_{max,th}}{K_{max}}\right)^{p^*}, \qquad (4)$$

where C^*, n^*, p^* are material constants, K_{max} is maximum SIF according to Eq. (2) and $K_{max,th}$ is the threshold SIF value.

During the years at the IPM CAS, many experimental tests for CT and MT specimens made from EA4T steel were performed considering various conditions. To demonstrate the FCGR curve effect on RFL, the CT specimens in normal air humidity were selected. Specimen thickness differs from 3 mm to 6 mm. Further details for experimental data can be found in [6] or [7]. In Fig. 3b experimental FCGR curves for standard hardened EA4T steel are shown. Each of them was separately fitted by the NASGRO model using MATLAB to obtain statistical population for each model parameter. Coefficient of determination, Kolmogorov-Smirnov test
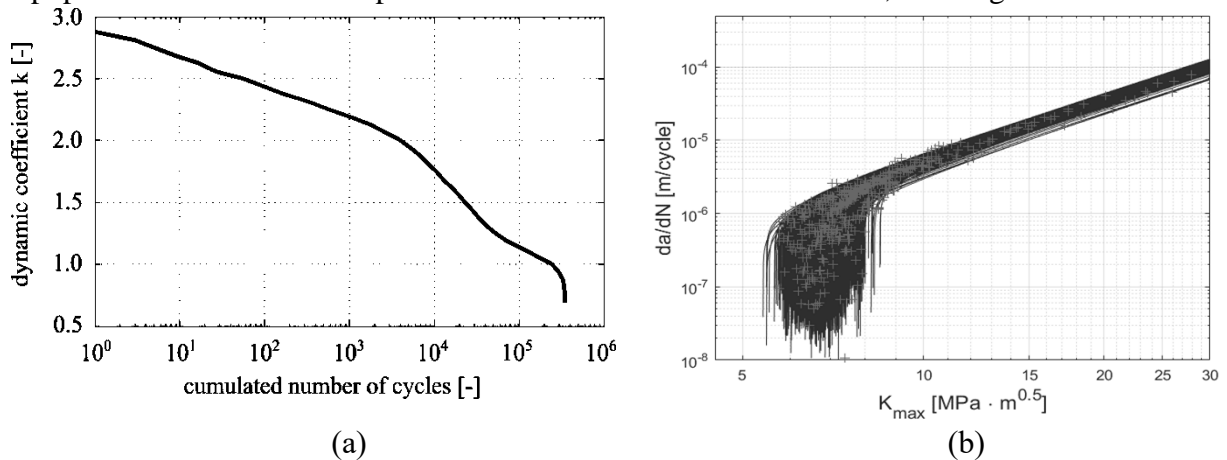

(a)　　　　　　　　　　　　　　　　(b)

Fig. 3 Load spectrum related to the dynamic coefficient [4] (a), Comparison of experimentally measured FCGR curves (grey pluses) and stochastically generated FCGR curves (b)

and Bayesian information criterion, as statistical methods, were used to obtain the best fit for experimental curves and to choose the correct probabilistic distribution function for model parameters. Afterwards, Monte Carlo simulation method was used to simulate the crack propagation path from its initial crack length of $a_0 = 3$ mm to final crack length of $a_f = 25$ mm. In total, 10 000 simulations were run. The results are presented in Fig. 4.
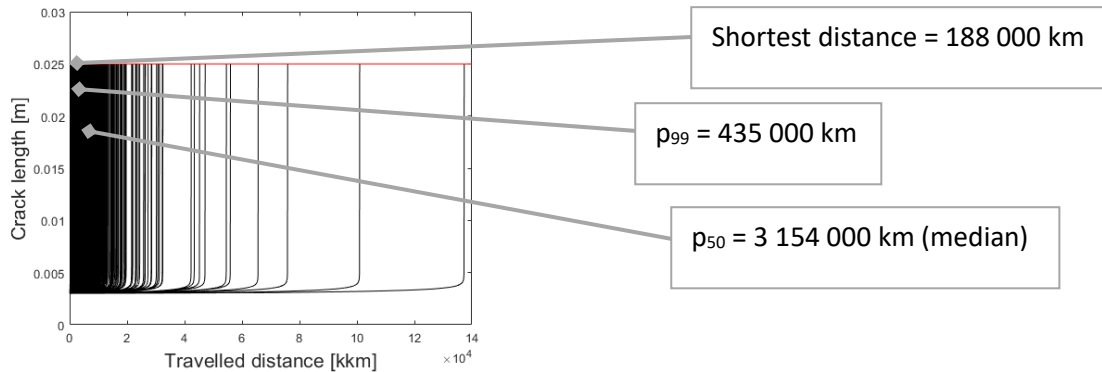

Fig. 4 Travelled distance vs. crack length curves with statistics – median and 99-th percentile

4 CONCLUSION

The proposed stochastic numerical approach offers improvement of methodology of RFL estimation of railway axles. In particular, wide scatter of FCGR curves (especially its threshold values) leads to wide scatter in RFL. To keep the results conservative but not too strict in order to set up periodical inspections, the percentile values provided by this approach can be used, e.g. 99-th percentile. For CT specimens in normal air humidity with various thickness it means that 99% simulations reach at least 435 000 km, while the shortest travelled distance is only 188 000 km.

ACKNOWLEDGMENT

LITERATURE

[1] Baaig, M. Ahmed Ali, S. A. Khan a M. Ansar Ali Baig. High Speed Trains: A Review. *IOSR Journal of Mechanical and Civil Engineering*. 2016, 16(053), 104-109. doi:10.9790/1684-1605304104109

[2] Zerbst, U., S. Beretta, G. Köhler, et al. Safe life and damage tolerance aspects of railway axles – A review: A Review. *Engineering Fracture Mechanics*. 2013, 98(053), 214-271.

[3] Pokorný, P., P. Dlhý, J. Poduška, et al. Influence of heat treatment-induced residual stress on residual fatigue life of railway axles: A classic problem revisited. *Theoretical and Applied Fracture Mechanics*. Elsevier, 2020, 630-635. doi:10.1016/j.tafmec.2020102732

[4] Náhlík, Luboš, Pavel Pokorný, Martin Šeevčík, et al. Fatigue lifetime estimation of railway axles: A classic problem revisited. *Engineering Failure Analysis*. Elsevier, 2017, 139-157.

[5] P. Pokorný, P. Hutař, L. Náhlík: Residual fatigue lifetime estimation of railway axles for various loading spectra. Theor. Appl. Fract. Mech., 82 (2016), pp. 25-32, 10.1016/j.tafmec.2015.06.007

[6] P. Pokorný, T. Vojtek, L. Náhlík, P. Hutař: Crack closure in near-threshold fatigue crack propagation in railway axle steel EA4T. Eng. Fract. Mech., 185 (2017), pp. 2-19, 10.1016/j.engfracmech.2017.02.013

[7] P. Pokorný, L. Náhlík, P. Hutař: Influence of variable stress ratio during train operation on residual fatigue lifetime of railway axles. Procedia Struct. Integr., 2 (2016), pp. 3585-3592, 10.1016/j.prostr.2016.06.447

APPLIED MECHANICS 2023

**Grand Hotel Sergijo, April 19th – 21st 2023
Piešťany, SLOVAKIA**

DETERMINING THE LIFE OF MULTIAXIALLY LOADED WELDED JOINTS USING LOW-CYCLE FATIGUE CRITERIA

ANNA TOŠKOVÁ[1], MARTIN FUSEK[2]

The conference contribution discusses the fatigue criteria used to predict life in the case of multiaxial loading under low-cycle fatigue. In more detail, some critical plane approaches, the effective deformation approach, and energy approaches are discussed. Determining the service life of a cyclically loaded component is a complex problem that is influenced by several factors such as the size of the component or the method of loading. Last but not least, the contribution deals with the possible application of the mentioned criteria for determining the service life of welded joints with an outline of planned experimental research.

KEYWORDS

Multiaxial fatigue, Low-cycle fatigue, welded joints, life prediction, fatigue criteria

INTRODUCTION

Fatigue is one of the fundamental problems in material mechanics. About 85% of machines and equipment are damaged by fatigue. Scientists around the world have been dealing with this problem for many years, but the research is still not complete, mainly because a number of factors affect the fatigue.

A welded joint is the most common non-separable connection of two or more usually metal parts that occur during welding. Creating a weld involves several steps, including preparing the part surfaces, feeding the additive material, heating the parts to working temperature, and finally making the weld. There are many different pressure or fusion welding methods such as friction welding, diffusion welding, laser welding, electric arc welding, or electro-slag welding. Each method has its specific requirements for surface preparation, additive material, heat sources, and other factors. [1]

A weld joint in a component is a notch that causes both an increase in stress and a change in stress. In the places of the notch, cracks are then initiated. The weld joint presents a structural notch due to the difference between the base and weld material. In addition, the shape

[1] **Ing. Anna Tošková**, Department of Applied Mechanics, Faculty of Mechanical Engineering, VSB – Technical University of Ostrava. 17. listopadu 2172/15, Ostrava, Czech Republic. Tel +420 596 993 290. Email: anna.toskova@vsb.cz

[2] **doc. Ing. Martin Fusek, Ph.D.**, Department of Applied Mechanics, Faculty of Mechanical Engineering, VSB – Technical University of Ostrava. 17. listopadu 2172/15, Ostrava, Czech Republic. Tel +420 596 993027. Email: martin.fusek@vsb.cz

of the weld, or the transition between the weld and the base material, can create additional stress concentration.

MULTIAXIAL FATIGUE AND LIFE PREDICTION

The term fatigue refers to the process of material degradation due to repeated stress or loading. If a machine component is subjected to time-varying external forces, it breaks after a certain time as a result of microscopic processes taking place in the material structure. If, on the other hand, the machine part was loaded with an equally large, time-constant external force, the material would not show any signs of failure. In general, a distinction is made between uniaxial and multiaxial loading. Uniaxial loading refers to a situation where the material is loaded in only one direction. However, a number of machine components are loaded multiaxially, when the material is loaded in several directions at the same time. For multiaxially loaded components, the service life must be determined using fatigue criteria. It also depends on the type of multiaxial loading, i.e. whether it is proportional loading, when the individual components of the stress tensor act in phase, or non-proportional loading, when these components act out of phase. [2], [3]

Fatigue criteria in the field of low-cycle fatigue are divided into three categories according to the approach used to determine service life. These approaches and the most used criteria are:

1. Effective deformation approach (e.g. Manson-Coffin)
2. Critical plane approaches
   a. Stress (e.g. Gough-Pollard)
   b. Strain (e.g. Brown-Miller)
   c. Strain-stress (e.g. Fatemi-Socie)
3. Energy approaches (e.g. Smith-Watson-Topfer)

The effective deformation criterion is based on the Manson-Coffin relationship between the amplitude of the total deformation and the number of cycles to damage (see [4], [5], [6]). It is applicable for lifetime estimation only in the case of proportional loading, it is not suitable for non-proportional loading. Critical plane criteria are suitable for life estimates in the case of proportional and non-proportional loading. The principle of the criterion is the search for the critical plane, which is the plane on which the damaging parameter acquires its maximum value. Critical plane stress approach criteria are applicable only in the case of high-cycle fatigue where plastic deformation is negligible. The damaging parameter is stress. The deformation criteria are suitable for both low-cycle and high-cycle fatigue. Among the most used are the Brown-Miller criterion (see [7]), its Kandil modification (see [8]), and the Wang-Brown criterion (see [9]). Deformation is a damaging parameter. These criteria do not take into account non-proportional cyclic hardening. For strain-stress criteria of the critical plane, the primary damage parameter is the strain and the secondary stress. These models (e.g. Fatemi-Socie, see [10]) are also suitable for non-proportional loading. Among the best-known energy criteria is the Smith-Watson-Topfer criterion (see [11]). Another criterion, which differs in its principle from the aforementioned, is Jiang's criterion (see [12]). This model includes the concept of a critical plane, the influence of plastic strain energy, and the principle of material memory taken from the mathematical modelling of cyclic plasticity. Two modifications of this criterion have already been created at the department workplace of the author of the contribution (see [13]). Among other things, the workplace has in-house software for predicting fatigue life using the mentioned criteria.

PREDICTION OF THE FATIGUE LIFE OF WELDED JOINTS

There are several ways to predict the service life of welded joints. In general, we can classify these predictions into three categories, namely:

1. Assessment according to standards (e.g. Eurocode 3, IIW)
2. Assessment based on special methodologies (e.g. Volvo methodology, FEMFAT methodology)
3. Assessment based on own fatigue testing

The first group includes the standard ČSN EN 1993-1-9, the so-called Eurocode 3 (see [14]) and the summary of recommendations issued by the International Institute of Welding (IIW), see [15] for more. These mentioned methodologies represent general procedures for determining lifetime prediction. There are also special methodologies such as Volvo methodology [16], FEMFAT methodology [17], or LOHR methodology [18]. Furthermore, the prediction of fatigue life can be determined using fatigue tests. This method is the most accurate, but the most time-consuming. The IIW standard provides fatigue resistance data in the form of SN curves or cracks growth curves, fatigue assessment is then based on stress range or stress intensity factor range. Fatigue assessment approaches here are based on several types of stress, similar to the Eurocode 3 standard, namely nominal stress, hot-spot stress, and effective notch stress, as well as the approach of fracture mechanics and component testing and subsequent work with experimental data. This lifetime prediction methodology is more suitable for high-cycle fatigue, it is not recommended to be used in the case of low-cycle fatigue when the nominal stress is greater than one and a half times the yield strength of the material.

PLANNED EXPERIMENTAL RESEARCH

Since the beginning of the year, work has been done on the design of two types of welded samples, and experiments with these samples are planned for the following quarter. First, tests will be carried out on samples with a type I butt weld joint (Fig. 1), where the propagation of the crack will be monitored using acoustic emission. These experiments will bring knowledge about changes in the microstructure and about the beginnings of disruption of the material. Furthermore, deformation-controlled biaxial fatigue tests on specimens with circumferential butt welds are planned (Fig. 1). These samples will be loaded proportionally and non-proportionally by several loading paths.
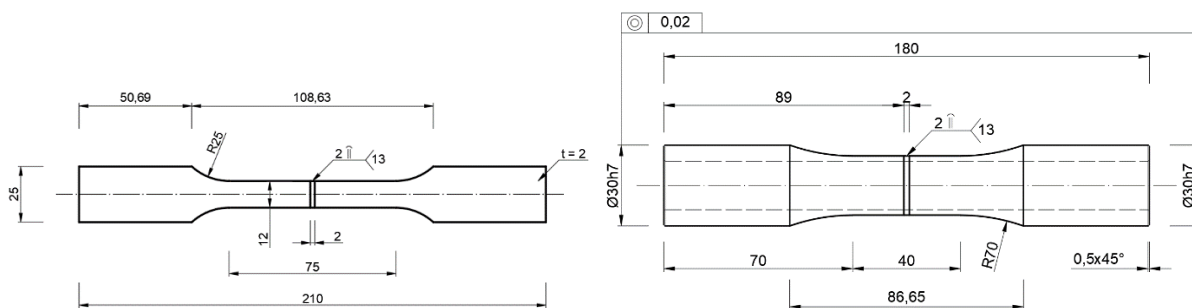

Fig. 1 Designed specimens

CONCLUSION

The conference contribution outlined research in the field of low-cycle fatigue of welded joints. Two types of designed samples were presented, and the planned experimental research was clarified, which will involve experimental determination of the life of the designed samples, including acoustic emission or biaxial testing. This data will then be compared with the lifetime values determined by the department in-house software. This software will not only

be used by the author of the contribution to predict the service life of welded joints but will subsequently also be improved for this use.

ACKNOWLEDGMENT

LITERATURE

[1] KOUKAL, J.; ZMYDLENÝ, T. Svařování. 1, skripta VŠB-TU Ostrava, 2005, 133 s.

[2] DOWLING, Norman E. *Mechanical behavior of materials: engineering methods for deformation, fracture, and fatigue*. 3rd ed. Upper Saddle River: Pearson Prentice Hall, c2007. ISBN 978-0-13-186312-5.

[3] KLESNIL, Mirko a Petr LUKÁŠ. *Únava kovových materiálů při mechanickém namáhání*. Praha: Academia, 1975. Fyzikálně metalurgická řada, sv. 1.

[4] MANSON, S. S. Strain controlled low cycle fatigue of metals. *NASA Technical Note,* 1954, 2933: 2933.

[5] COFFIN JR, L. Fo. A study of the effects of cyclic thermal stresses on a ductile metal. *Transactions of the American Society of Mechanical engineers*, 1954, 76.6: 931-949.

[6] WANG, Yingyu; SUSMEL, Luca. The Modified Manson–Coffin Curve Method to estimate fatigue lifetime under complex constant and variable amplitude multiaxial fatigue loading. *International Journal of Fatigue*, 2016, 83: 135-149.

[7] BROWN, M. W⽥; MILLER, K. J. A theory for fatigue failure under multiaxial stress-strain conditions. *Proceedings of the Institution of Mechanical engineers*, 1973, 187.1: 745-755.

[8] KANDIL, F. A⽥; BROWN, M. W⽥; MILLER, K. J. Biaxial low-cycle fatigue failure of 316 stainless steel at elevated temperatures. In: *Mechanical behaviour and nuclear applications of stainless steel at elevated temperatures*. 1982.

[9] WANG, C. H.; BROWN, M. W. A path-independent parameter for fatigue under proportional and non-proportional loading. *Fatigue & fracture of engineering materials & structures*, 1993, 16.12: 1285-1297.

[10] FATEMI, ALI; SOCIE, D. F. A critical plane approach to multiaxial fatigue damage including out-of-phase loading. *Fatigue & fracture of engineering materials & structures* (Print), 1988, 11.3: 149-165.

[11] SMITH, KNua. A stress-strain function for the fatigue of metals. *Journal of materials*, 1970, 5: 767-778.

[12] JIANG, Yan-yao. A fatigue criterion for general multiaxial loading. *Fatigue & fracture of engineering materials & structures* (Print), 2000, 23.1: 19-32.

[13] FUSEK, Martin; HALAMA, Radim; LICKOVA, D. Two modifications of Jiang criterion for constant amplitude multiaxial loading of AA2124-T851 and SS316L. *Continuum Mechanics and Thermodynamics*, 2020, 1-17.

[14] NUSSBAUMER, Alain; BORGES, Luis; DAVAINE, Laurence. *Fatigue design of steel and composite structures: Eurocode 3: Design of steel structures, part 1-9 fatigue; Eurocode 4: Design of composite steel and concrete structures*. John Wiley & Sons, 2012.

[15] HOBBACHER, A. IIW Recommendations for fatigue design of welded joints and components, Doc. IIW-1823. *WRC Bulletin*, 2008, 520.

[16] Welding manual, design and analysis, 5.501E, Volvo group standard, 1989.

[17] FEMFAT User's Manual Vers. 2.5. Engineering / Technologie Zentrum Steyr, Steyr. 1995.

[18] TURLIER, Didier, et al. New FEA shell element model for seam weld static and fatigue structural assessment. In: *Proc. Int. Conf. Fatigue Design*. 2011.

APPLIED MECHANICS 2023

Grand Hotel Sergijo, April 19th – 21st 2023
Piešťany, SLOVAKIA

DESIGN OF THE MECHANICAL COMPONENT FOR PIEZOELECTRIC ENERGY HARVESTING

MICHAL MILOSLAV ULIČNÝ [1], VLADIMÍR KUTIŠ [2]

Energy harvesting is a significant evolving technological trend of today. Its main use is to power electronics without the need of traditional energy sources. The objective of this work is to create a design of the mechanical component for piezoelectric energy harvesting in the environment of program ANSYS that could be used as a part of a backpack.

KEYWORDS

mechanical design, piezoelectric energy harvesting, FEM, ANSYS

INTRODUCTION

Energy harvesting represents a significant technological trend of this era. Through energy harvesting, energy can be collected from different physical domains. Examples of types of energy harvesting are thermoelectric, electromagnetic, or piezoelectric energy harvesting, which is the focus of this thesis. The benefit of energy harvesting lies in the use of otherwise wasted energy, which can be capitalized by this technology to supply energy to systems that can then perform work. This benefit is also linked to reducing the ecological burden on the planet, which is now at its peak [1]. Energy harvesting could at least partly help to reduce the need to use fossil fuels in order to generate energy to run systems. Kinetic energy is probably the most common form of free energy. This free energy can be observed in common occurrences such as mechanical vibrations, e.g. during the transport of vehicles and the operation of machinery, during ocean tides or during wind blowing. The process by which this energy can be collected and transformed to electricity is called piezoelectric phenomenon.

BASIC PRINCIPLES

The principle of the piezoelectric phenomenon is that if an external mechanical load is applied to the piezoelectric material, the material produces an electrical voltage. This is caused

---

[1] **Ing. Michal Miloslav Uličný**, Department of Mechanics and Mechatronics, Institute of Automotive Mechatronics, Faculty of Electrical Engineering and Information Technology, Slovak University of Technology in Bratislava. Ilkovičova 3, Bratislava, Slovak Republic. Email: michal.ulicny@stuba.sk

[2] **prof. Ing. Vladimír Kutiš, PhD.**, Department of Mechanics and Mechatronics, Institute of Automotive Mechatronics, Faculty of Electrical Engineering and Information Technology, Slovak University of Technology in Bratislava. Ilkovičova 3, Bratislava, Slovak Republic. Tel +421 2 60291 452. Email: vladimir.kutis@stuba.sk

by an internal change in the structure of the material, which causes different electrical potentials. This phenomenon is also referred to as the direct piezoelectric phenomenon. There is also a reverse piezoelectric phenomenon, where the application of an electrical voltage to a piezoelectric material produces a mechanical deformation of its structure, and is called a reverse piezoelectric phenomenon. The piezoelectric phenomenon can be described by constitutive equations using mechanical strain and electrical induction, which is one of the sets of equations that can describe this phenomenon. Although tensor quantities are involved, this mathematical notation is commonly used [2]:

$$\varepsilon = S\sigma + d^T E \tag{1}$$

$$D = d\sigma + \epsilon E \tag{2}$$

Where ε represents the mechanical strain, S represents the mechanical transformation matrix, σ represents the normal stress, d represents the piezoelectric coupling tensor, E represents the electric field, D represents the electric displacement field, and ϵ represents the permittivity.

BACKPACK APLICATION

The energy generated while a person is walking with a backpack was selected as the application of a piezoelectric system for energy harvesting of kinetic energy. In it, the piezoelectric energy harvesting system is integrated into the backpack straps. The design principle assumes that the tension on the straps of the weight-filled backpack, which is on the human back, is uniformly distributed. During walking, a force excitation is generated on the straps in the vertical direction. The idea behind the principle of this application of a piezoelectric energy harvesting system has already been proposed in the paper Energy harvesting through a backpack employing a mechanically amplified piezoelectric stack from the 22nd issue of Mechanical Systems and Signal Processing by J. Feenstra, J. Granstorm, and H. Sodan [3]. A 3D model of their system can be seen in Fig. 1. The aim of this work is to design a mechanical component of the system that, when loaded with a vertical force, develops the highest possible horizontal force applied to the piezoelectric stack located inside the system.
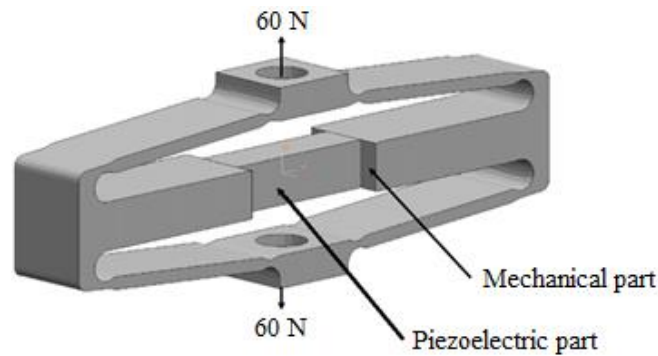

Fig. 1 Original piezoelectric energy harvesting system

MODELLING AND SIMULATION

ANSYS Mechanical tool was used for FEM simulations in this work. The first part of the work consisted of designing the geometry of the mechanical component of the system. Even though the work consists only of a computer simulation of the system, its parameters were not idealized. The loading force was determined according to a backpack load of 4 kg. For the mechanical part of the system, structural steel was chosen as the material, its material properties can be found in Tab. 1 alongside other mechanical parameters. Thus, the aim of the work was to achieve the highest possible output force acting on the piezoelectric part of the system. To achieve this result, joints were implemented in the structure which flex under load and thus

exert a greater horizontal force. Several geometric designs were created for this work, on the order of tens, along with a design that would stress the piezoelectric stack to bend. The final geometry of the mechanical part was created a model which can be seen in Fig. 2, where stress analysis was performed with maximal value 4.56 MPa:
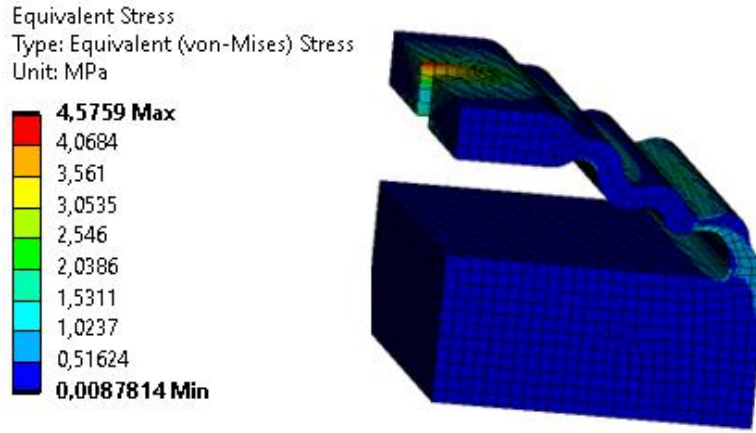

Fig. 2 Quarter model of new piezoelectric energy harvesting system

In Fig. 2 it is also possible to see cut out circular areas through which the piezoelectric system would be integrated to the backpack straps, e.g. via a screw joint, the circles thus represent the area of the screw washer. It also represent the place of mechanical load in numerical simulation and that is the reason why is the maximal stress occurring in that area symbolized with red colour. The design parameters have been determined so that they do not interfere with the human during operation so during the walking. The final dimensions of the geometry and the output force provided are shown in Tab. 1.

Tab. 1 Final output mechanical parameters

Height [mm]	Width [mm]	Depth [mm]	Density [kg/m³]	Young's Modulus [GPa]	Poisson's Ratio [-]	Output force [N]
33.3	36	34.9	7850	200	0.3	18.1

The work continued with piezoelectric analysis where Lead Zirconate Titanate (PZT-5H) was considered as the piezoelectric material. Its properties in matrices are shown in equations (3), (4) and (5).

$$S = \begin{bmatrix} 16.5 & -4.78 & -8.45 & 0 & 0 & 0 \\ -4.78 & 16.5 & -8.45 & 0 & 0 & 0 \\ -8.45 & -8.45 & 20.7 & 0 & 0 & 0 \\ 0 & 0 & 0 & 43.5 & 0 & 0 \\ 0 & 0 & 0 & 0 & 43.5 & 0 \\ 0 & 0 & 0 & 0 & 0 & 42.6 \end{bmatrix} 10^{-12} \left[\frac{m^2}{N} \right] \tag{3}$$

$$d = \begin{bmatrix} 0 & 0 & 0 & 0 & 741 & 0 \\ 0 & 0 & 0 & 741 & 0 & 0 \\ -274 & -274 & 593 & 0 & 0 & 0 \end{bmatrix} 10^{-12} \left[\frac{C}{N} \right] \tag{4}$$

$$\epsilon = \begin{bmatrix} 3130 & 0 & 0 \\ 0 & 3130 & 0 \\ 0 & 0 & 3400 \end{bmatrix} \left[\frac{F}{m} \right] \tag{5}$$

Piezoelectricity analysis is not a standard part of ANSYS, so it was necessary to add the PiezoAndMEMS extension. This extension allows the properties of the piezoelectric material to be defined in the model in the form of transformed equations (1) and (2). Piezoelectric static voltage analysis is shown Fig. 3, where final voltage output was 0.21 V. Next piezoelectric analyses were considered with a representative electrical resistance of 100 Ω and harmonically loaded with a wide range of frequencies. The highest values were provided at 25 kHz, which is not the exact frequency at which this piezoelectric system will operate, but provides a good overview. The output electrical quantities are given in Tab. 2.
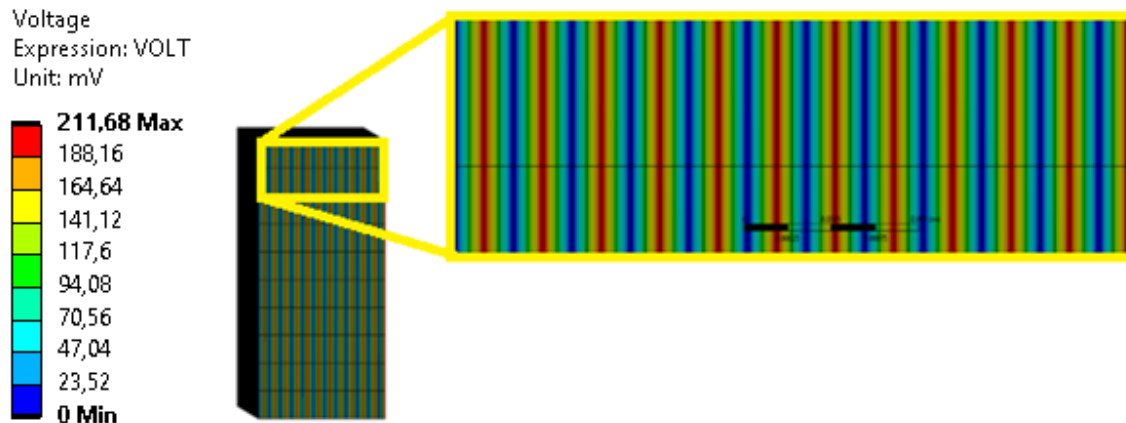

Fig. 3 Piezoelectric static voltage analysis

Tab. 2 Final output electrical parameters with harmonic excitation

Electric voltage [V]	Electric current [A]	Electric power [W]
0.39	0.004	0.00156

CONCLUSION

The aim of this work was to design, create and simulate mechanical part of piezoelectric energy harvesting system. Even after successful simulations and obtained results, there is still a room for improvement for this system and for new ideas. System presented in this work could be beneficial for applications with low-power electronics.

ACKNOWLEDGMENT

LITERATURE

[1] K. O. Yoro and K. Austin, "CO2 emission sources, greenhouse gases, and the global warming effect," in Advances in Carbon Capture, edited by M. R. Rahimpour, M. A. Makarem and M. Farsi (Woodhead Publishing, 2020), pp. 3-28.

[2] KUTIŠ, V. Modelovanie multifyzikálnych procesov a dejov. Bratislava: STU, 2014. isbn 978-80-227-4232-0.

[3] FEENSTRA J., GRANSTROM J., SODANO H. Energy harvesting through a backpack employing a mechanically amplified piezoelectric stack. In Mechanical Systems and Signal Processing, 2008, vol.22, pp. 721-734

APPLIED MECHANICS 2023

Grand Hotel Sergijo, April 19th – 21st 2023
Piešťany, SLOVAKIA

EXPERIMENTAL AND NUMERICAL ANALYSIS OF MATERIAL PROPERTIES OF COMPOSITE SANDWICH STRUCTURES

ANDREJ ÜRGE[1], VLADIMÍR GOGA[2]

This work focuses on the methodology of obtaining material properties of composite sandwich structures. Primarily fibrous composites and their general properties are discussed. The following chapters deal with experimental and numerical methods for determining the material properties of fibre composites and their constituents. Next, determined properties are used to develop a FEM model of a composite sandwich structure. Numerical results are then compared with experimental data.

KEYWORDS

Composite material, fibre reinforcement, matrix, composite sandwich structure, FEM model, micromechanics

INTRODUCTION

Composite materials are generally made up of at least two different materials with their corresponding physical properties. Individual constituents keep their specific characteristics, combination of these constituents forms a composite material that can be used in specific applications. This work focuses mainly on carbon fibre-reinforced polymer (CFRP) composite materials and their combination with different core materials resulting in a so-called composite sandwich structure. CFRPs and composite sandwich structures have been studied and used extensively for decades. It is their very low weight, high stiffness, durability, and ease of manufacturing that made them so popular in aeronautical, aerospace, marine, and many other industries. To achieve desired mechanical properties of a sandwich structure it is necessary to know the mechanical properties of individual constituents. Core manufacturers often provide test results or approximate values of stiffness and strength. In the case of CFRPs mechanical properties experience anisotropy and standardized testing is required in individual material directions to achieve desired properties. The manufacturing method, matrix, and fibre type are

[1] **Ing. Andrej Ürge**, Department of Mechanics and Mechatronics, Institute of Automotive Mechatronics, Faculty of Electrical Engineering and Information Technology, Slovak University of Technology in Bratislava. Ilkovičova 3, Bratislava, Slovak Republic. Tel +421 902 223 900. Email: andrej.urge@stuba.sk

[2] **doc. Ing. Vladimír Goga, PhD.**, Department of Mechanics and Mechatronics, Institute of Automotive Mechatronics, Faculty of Electrical Engineering and Information Technology, Slovak University of Technology in Bratislava. Ilkovičova 3, Bratislava, Slovak Republic. Tel +421 260 291 687. Email: vladimir.goga@stuba.sk

a few of the factors that have an impact on resulting mechanical properties which makes standardized tests very expensive and time demanding. Herein the method for obtaining elastic properties of CFRPs from a single test using micromechanics in combination with FEA is studied. Elastic properties of carbon fibres are numerically derived from standardized test and later used in the numerical analysis of the three-point bending of a sandwich structure. Results of numerical analysis are later compared with experimental results. [1]

MATERIALS

Herein the properties of Toray T700 carbon fibres in combination with DT120 epoxy-based matrix in form of pre-impregnated fabric are analysed. The properties of T700 fibre given by the manufacturer are longitudinal tensile modulus, density, and filament diameter. As for the DT120 epoxy-based matrix, the supplier does not provide elastic properties of a matrix nor properties of the combination with T700 carbon fibre. This means that the customer must either perform the standardized tests of a matrix or use average values of mechanical properties provided by different suppliers. Mentioned fibres and matrix form a unidirectional ply also referred to as lamina. By stacking these plies, laminates are constructed which make up the outer faces of a composite sandwich structure. Two types of cores were studied, the first one was foam core and the second one was aluminium honeycomb core both with the same thickness of 10 mm. Directions L and W referring to the orientation of the cells in the honeycomb core must be distinguished. This means that the core has two different shear moduli depending on cell orientation. The compression modulus of both cores was also provided by the supplier. Mentioned materials were used to manufacture samples of composite sandwich structures and to define part of the material properties in FEA and hand calculations.

MECHANICAL PROPERTIES OF CONSTITUENTS

In terms of mechanical properties matrix can be considered isotropic and the required constants are the tensile modulus of the matrix denoted E_m and its Poisson's ratio denoted v_m. Fibres can be considered transversely isotropic and to describe their behaviour in the elastic region at least five independent material constants are required. The longitudinal and transverse elastic modulus of the fibre is denoted E_{f1} and $E_{f2} = E_{f3}$, respectively. The shear modulus in the longitudinal plane of the fibre is denoted by $G_{f12} = G_{f13}$ and the transverse shear modulus is denoted G_{f23}. Similarly, the longitudinal and transverse Poisson's ratios are denoted $v_{f12} = v_{f13}$ and v_{f23}, respectively. The resulting unidirectional composite lamina can be also considered transversely isotropic, and its material properties are denoted similarly to properties of the fibre, the difference being that the index f will be replaced by c. Densities of fibre, matrix, and lamina are denoted ρ_f, ρ_m and ρ_c, respectively. The number of independent material constants is higher than the number of material properties provided by material suppliers. Standardized testing would be required to achieve remaining material constants. In collaboration with NIAR at the Wichita State University, consortium AGATE has conducted standardized tests of several combinations of fibres and matrices, the results of which are provided to the public. One of the tested laminates is a unidirectional laminate containing Toray T700 carbon fibres. [2] Results of this test were used to back-calculate the properties of the fibre using micromechanics and calculated material constants were later used to calculate homogenized properties of laminate with different fibre volume fraction which is denoted v_f. The final independent material constants can be calculated using the modified rule of mixtures introduced by S.W. Tsai and H.T. Hahn, who introduced the stress portioning parameter η. The following equation can be used to determine the properties of the fibre:

$$P_f = \frac{P_c\left(v_f + \eta\left(1 - v_f\right)\right) - P_m\eta\left(1 - v_f\right)}{v_f} \qquad (1)$$

Where P represents a property and can be substituted with respect to the independent material constant we are trying to calculate. This represents a semiempirical approach for determining transverse tensile modulus and longitudinal shear modulus where $0 \leq \eta \leq 1$ is used as a curve fitting parameter. More on this topic can be found in [3] and [4] where Tsai and Hahn described and studied this parameter.

FINITE ELEMENT ANALYSIS OF REPRESENTATIVE VOLUME ELEMENT

Back calculated material properties of a T700 fibre, estimated properties of DT120 epoxy matrix, the diameter of a fibre, and fibre volume fraction were used to model the representative volume element. Obtained homogenized properties showed appropriate compliance with the test results and hand calculations. The highest deviation was observed in the calculation of the longitudinal shear modulus, where the calculated value was 2% lower compared to the measured value. The same process was repeated for fibre volume fraction 0.546 which was calculated from the datasheet supplied with the unidirectional prepreg fabric. The hand calculation and simulation results were again compared and showed reasonable consistency. Homogenized properties were later used to create a finite element model of a composite sandwich structure.

THREE-POINT BENDING ANALYSIS OF A SANDWICH STRUCTURE

The sandwich structure represents a simple beam with a rectangular cross-section which is simply supported by two supports at a distance L. Perpendicular to the top surface of the beam, at a distance $L/2$, the force F_3 will be applied. The outer faces are considered parallel, have a thickness t_v, and are separated by a core that has a thickness t_j. Overall thickness is the sum of the thicknesses $t_j + 2 \cdot t_v$, denoted by h. Distance between the mid surfaces of outer faces will be denoted by t_s and the overall width of the beam will be b. The described beam is shown in Fig. 2 and the real test setup is shown in Fig. 3.
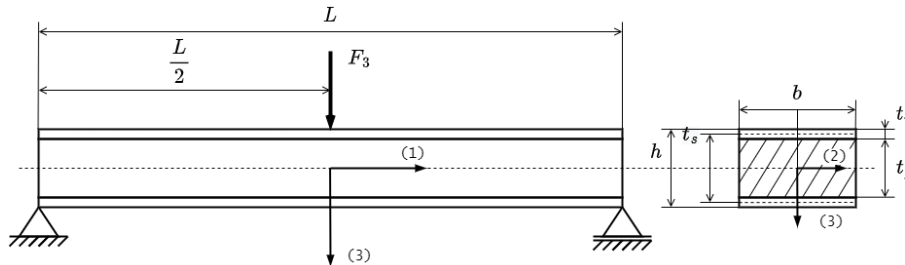

Fig. 2 Three-point bending schematic

Fig. 3 Three-point bending experiment setup

Maximum deformations of the test specimens at different load steps were measured and compared with the results from FEA and simple hand calculations. Five test specimens were manufactured, tested, and modelled with different numbers of unidirectional layers and two different cores and orientations. Calculated values of maximum deformations and results of the

FEA showed good compliance, however, compared to the results of the experiment the resulting values were 15% lower at most, indicating that the manufactured samples had lower bending stiffness. In the calculation and FEA, it is assumed that all the fibres are parallel and oriented exactly at 0 degrees. This is not the case for the samples produced, although attention has been paid to the orientation of the fibres, it is virtually impossible to manufacture an "ideal" sample. A comparison of maximum deformations of individual test samples can be found in Fig. 4.
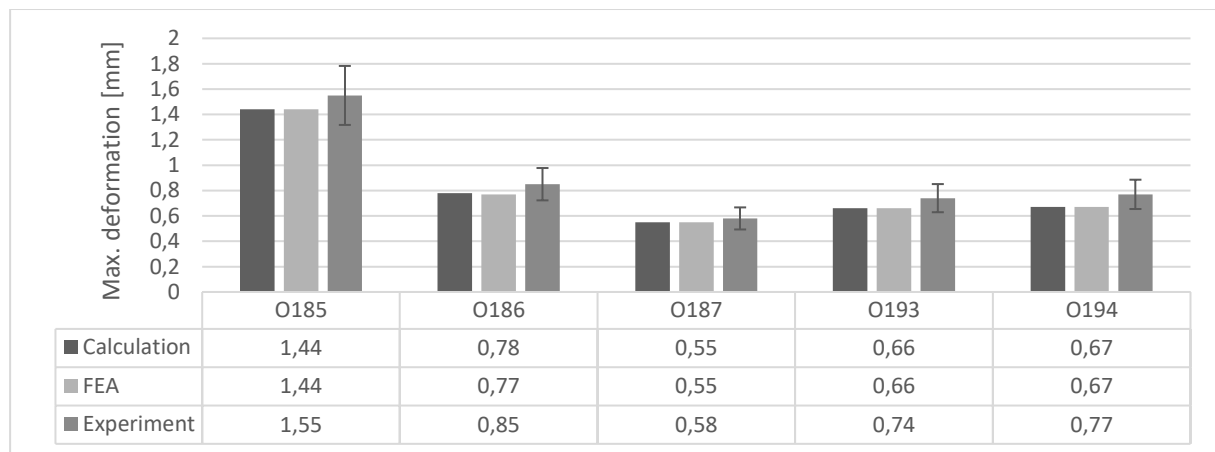

	O185	O186	O187	O193	O194
■ Calculation	1,44	0,78	0,55	0,66	0,67
■ FEA	1,44	0,77	0,55	0,66	0,67
■ Experiment	1,55	0,85	0,58	0,74	0,77

Fig. 4 Comparison of experimentally and numerically obtained values of maximum deformation of individual specimens (15% error shown)

CONCLUSION

This work aimed to determine the elastic properties of the given carbon fibre and use them to model the behaviour of the composite sandwich structure. A modified rule of mixtures was used to determine the fibre properties and the RVE of the CFRP was modelled and analysed. Next, the model of the sandwich structure was created using different core materials and facing laminates. The results of the FEA were compared to the results of the experiment and simple hand calculation showed good compliance. More on this topic can be found in [5].

ACKNOWLEDGMENT

LITERATURE

[1] ZWEBEN, Carl. Mechanical engineer's handbook: Composite Materials. John Wiley & Sons, Ltd, 2015. ISBN 9781118985960.

[2] TOMBLIN, J., MCKENNA, J., NG, Y., RAJU, K. S. FiberCote Graphite Unitape T700 24K / E765. Wichita, KS: National Institute for Aviation Research Wichita State University, 2004

[3] TSAI, Stephen W., HAHN, H. Thomas. Introduction to composite materials. 1st Edition. New York, NY: Routledge, 1980. ISBN 9780203750148.

[4] TSAI, S.W. Theory of Composites Design. Austin, TX: Think Composites, 1992. ISBN 9780961809034.

[5] ÜRGE, A., Experimental and numerical analysis of mechanical properties of a composite sandwich construction. [Experimentálna a numerická analýza mechanických vlastností kompozitnej sendvičovej konštrukcie]. Bratislava, 2022. Master's Thesis. STU FEI, in Slovak language

NOVEL APPROACH FOR MASS SENSING USING NON-LINEAR MICROMECHANICAL RESONATORS.

JIŘÍ VENSKÝ[1], OLDŘICH ŠEVEČEK[2], PETR SKALKA[3], IVO STACHIV[4], MICHAL KOTOUL[5]

The contribution deals with a numerical modelling and analysis of micro/nano-mechanical resonators operating in the non-linear regime which is intended to be utilized for an enhancement of the resonator sensing range eventually its sensitivity. In this work we aim to present an alternative/novel way for solution of such a problem.

KEYWORDS

Mass spectrometry, FE simulation, resonator, resonant frequency

INTRODUCTION

Resonators are micro/nano beams (both cantilever and double side suspended configuration) which are utilized e.g., as mass spectrometers for measurement or detection of molecules or other very small particles [1,2]. Mass of the attached particles is determined by change of the resonator's natural frequencies. This approach assumes linear behavior of the resonator, however their accuracy in detection lowers in case of very light or heavy particles in relation to the resonators mass (optimal mass ratio m/M is around 0.01) [3]. Approach suggested in this work enables a determination of particle mass just from the displacement in resonators centre and the value of nonlinear eigenfrequency. Other attempts can be found in other papers – see e.g. [4,5].

---

[1] **Ing. Jiří Venský**, Institute of Solid Mechanics, Mechatronics and Biomechanics, Brno University of Technology, Faculty of Mechanical Engineering, Technická 2896/2, 61669, Brno, Czech Republic, Email: 191582@vutbr.cz

[2] **Ing. Oldřich Ševeček, Ph.D.**, Institute of Solid Mechanics, Mechatronics and Biomechanics, Brno University of Technology, Faculty of Mechanical Engineering, Technická 2896/2, 61669 Brno, Czech Republic, Email: sevecek@fme.vutbr.cz

[3] **Ing. Petr Skalka, Ph.D.**, Institute of Solid Mechanics, Mechatronics and Biomechanics, Brno University of Technology, Faculty of Mechanical Engineering, Technická 2896/2, 61669 Brno, Czech Republic, Email: skalka@fme.vutbr.cz

[4] **Ing. Ivo Stachiv, Ph.D.**, Institute of Physics, Czech Academy of Sciences, Na Slovance 1999/2, 182 00 Praha 8, Czech Republic, Email: stachiv@fzu.cz

[5] **Prof. RNDr. Michal Kotoul, DrSc.**, Institute of Solid Mechanics, Mechatronics and Biomechanics, Brno University of Technology, Faculty of Mechanical Engineering, Technická 2896/2, 61669 Brno, Czech Republic, Email: kotoul@fme.vutbr.cz

FE MODEL AND SIMULATIONS

Non-linear transient simulations are complex and time consuming, therefore beam elements (BEAM189) with a rectangular cross-section were employed instead of 3D solid model. Attached particle is simulated using the MASS21 element added to the corresponding node along the resonator. Resonator dimensions were set to $BxHxL = 60x2x350\mu m$. Excitation is implemented as a sinusoidal, time dependent displacement u_z on both ends with an amplitude equal to $(n*g)/(2*\pi*f)$ where n is a multiple of gravity constant g and f is current excitation frequency. Material is considered as a pure silicon with the Young´s modulus E=160GPa, Poisson´s ratio v=0.22 and density ρ=2330kg/m^3. Damping is set via BETAD command in Ansys as 1e-11.

The idea of this method is based on determining the amplitude and frequency upon passing the instability. The analysis is transient with a step by step increasing frequency. Excitation acceleration is expressed as a multiple of gravity constant and in this demonstration is set to 500g. Each sinus cycle is divided into 50 steps. Using parametric simulation, instability points are determined for various positions of the particle and mass ratios. This creates so called characteristic maps of the resonator (either as 3D plot or a contour graph).

RESULTS

To determine the position and mass of the particle, two maps are used. A_1=f(x_m,m/M) and f_1= f(x_m,m/M) (see Fig.1 and Fig.2). Upon the measurement a repeated frequency sweep is performed over the first resonant frequency on the resonator. When no particle is attached to the resonator, the natural frequency and maximal amplitude upon passing the instability remains unchanged. Once a particle is attached, instability point changes and the new amplitude A_1 and frequency f_1 are used for a determination of the particle mass and its position. Lines in Fig.1 and Fig.2 show all admissible mass positions and m/M ratios fulfilling the measured values of A_1 and f_1. The position and mass ratio are then determined through an intersection of these two curves. The symmetry of the resonator results in two solutions for the particle position x_m, that are always the same distance from the centre of the resonator. Mass ratio m/M (which is how the particle mass is determined since resonators mass is known) has just a single solution.
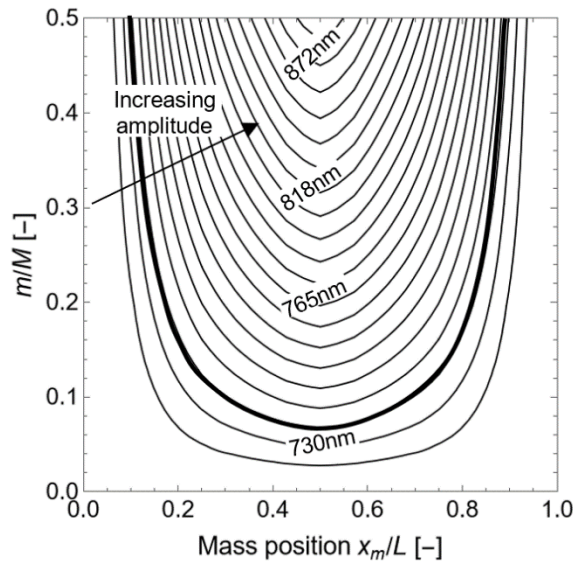

Fig. 1 Contour plot of amplitudes A_1(500g) at the instability point calculated at resonator´s centre as a function of the particle position x_m and mass ratio m/M. Thick line stays for the experimentally determined amplitude isoline.
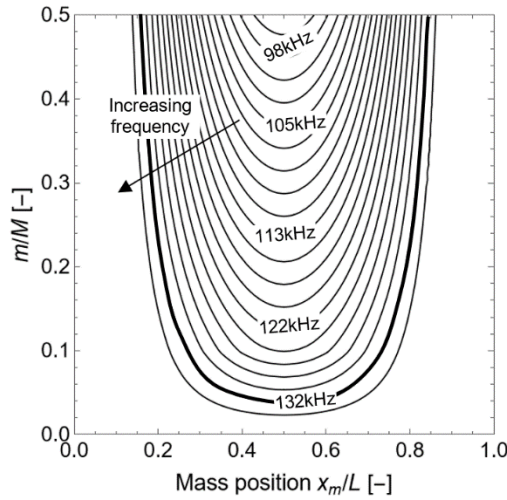
Fig. 2 Contour plot of frequencies f_1(500g) at the instability point as a function of the particle position x_m and mass ratio m/M. Thick line stays for the experimentally determined frequency isoline.

It is important to note that when the excitation and corresponding vibrational amplitudes are too low then the error in determination of the particle mass will be significant. Error analysis will be a subject of the subsequent studies. The measurement sensitivity can be easily tunes just by applied excitation acceleration that can be adjusted for the measurement of certain range of particle masses and desired accuracy. This procedure will still require to define resonator´s amplitude and frequency maps for different excitation conditions.

Further, an analysis of resonators mechanical stresses was carried out. Stresses in the critical location of the resonator (in vicinity of the clamping) at the transition of the instability point in order to avoid resonator´s failure. Studied resonators are intended to be prepared from SOI wafers where the Silicon layer has a monocrystalline form and strengths of these materials are in order of GPa. Meanwhile stresses reached in the analysis did not reach hundreds of MPa for numerous values of the mass ratio.

CONCLUSION

This paper proposes an alternative approach for detection of small particles, in the range of molecules, using micro (nano) mechanical resonators working in nonlinear regime. The position and mass of the particle is determined by the natural frequency and resonators displacement in the middle upon a sweep over its natural frequency. This approach allows tunability of the measurement conditions to reach the optimal accuracy. The accuracy can also be improved by higher excitation acceleration applied to the resonator.

Physical operational limits of the resonator in a non-linear regime were further investigated. In case of the considered operational regime the stresses on the resonator are significantly below its tensile strength.

The proposed method still has issues which have to be further investigated. Primarily the influence of the nonsymmetrical position of the attached particle as well as influence of the particle stiffness. Both might influence coordinates of the instability point in the amplitude-frequency characteristic. Further, it is necessary to map the accuracy of this method based on standard error of experimental and measurement devices and lastly determine optimal regimes for particles with various masses.

LITERATURE

[1] D. Z. Keifer and M. F. Jarrold, 'Single-molecule mass spectrometry', Mass Spectrom. Rev., vol. 36, no. 6, pp. 715–733, Nov. 2017.

[2] A. K. Naik, M. S. Hanay, W. K. Hiebert, X. L. Feng, and M. L. Roukes, 'Towards single-molecule nanomechanical mass spectrometry', Nat. Nanotechnol., vol. 4, no. 7, pp. 445–450, Jul. 2009.

[3] I. Stachiv, L. Gan, C.-Y. Kuo, P. Šittner, and O. Ševeček, 'Mass Spectrometry of Heavy Analytes and Large Biological Aggregates by Monitoring Changes in the Quality Factor of Nanomechanical Resonators in Air', ACS Sensors, vol. 5, no. 7, pp. 2128–2135, Jul. 2020.

[4] M. Yuksel, E. Orhan, C. Yanik, A. B. Ari, A. Demir, and M. S. Hanay, 'Nonlinear Nanomechanical Mass Spectrometry at the Single-Nanoparticle Level', Nano Lett., vol. 19, no. 6, pp. 3583–3589, Jun. 2019.

[5] X. Wang, X. Wei, D. Pu, and R. Huan, 'Single-electron detection utilizing coupled nonlinear microresonators', Microsystems Nanoeng. 2020 61, vol. 6, no. 1, pp. 1–7, Oct. 2020.

OPTIMIZATION OF A 3D PRINTED ANKLE-FOOT-ORTHOSIS

ONDŘEJ ZOUFALÝ[1], KATARÍNA MENDOVÁ[2], MATEJ DANIEL[3]

Ankle-foot-orthoses are biomechanical devices used for stabilizing the joints, improving the gait pattern and functioning of the affected lower limb. This work deals with optimizing a 3D printed ankle-foot-orthosis for children affected by cerebral palsy. AFO will be optimized in terms of stiffness and different structures improving foot stability, gait pattern and reducing muscle forces and metabolic cost.

KEYWORDS

Ankle-foot-orthosis, AFO, Optimization, Gait analysis

INTRODUCTION

Digital orthotics and 3D printed orthoses improves comfort, functionality, and aesthetics. Cerebral palsy affects ability to move and maintain balance. AFO helps patients with the gait and stability of the ankle joint. Manufactured 3D printed AFO can be easily fitted on the patient's foot and be optimized from material and different structures perspective. Main objective of optimization is to improve stability of the ankle joint, gait pattern and provide proprioception which helps with coordination.[1]

CHAPTER 1 Model of AFO

The model is made in Blender software due to easy procedure of fitting the AFO on the patient's foot. Blender is an open-source software for 3D graphics modelling where models consist of vertices, edges and faces. Another advantage is implementation of Python interface which enables you to automatize the procedure of making a model.

Since every shape of the foot is different, a model of general shape was made. The model consists of perforation for local lightening, so putting the orthosis on is easier, and humps that press the foot on its proprioceptive points. Blender uses so-called *modifiers*, which enable to fit

---

[1] **Ing. Ondřej Zoufalý**, Department of Mechanics, Biomechanics and Mechatronics, Faculty of Mechanical Engineering, Czech Technical University in Prague, Technická 4, Prague 6. Tel +420 602 250 784. Email: ondrej.zoufaly@fs.cvut.cz

[2] **Ing. Katarína Mendová,** Department of Mechanics, Biomechanics and Mechatronics, Faculty of Mechanical Engineering, Czech Technical University in Prague, Technická 4, Prague 6. Tel +420-22435-2690. Email: katarina.mendova@fs.cvut.cz

[3] **Prof. RNDr. Matej Daniel, Ph.D.**, Department of Mechanics, Biomechanics and Mechatronics, Faculty of Mechanical Engineering, Czech Technical University in Prague, Technická 4, Prague 6. Tel +420-22435-2518. Email: matej.daniel@cvut.cz

general shaped AFO model onto a model of patient's foot. With *modifiers* it is also easy to change the properties (such as thickness, shape of perforation etc…) for a particular patient.
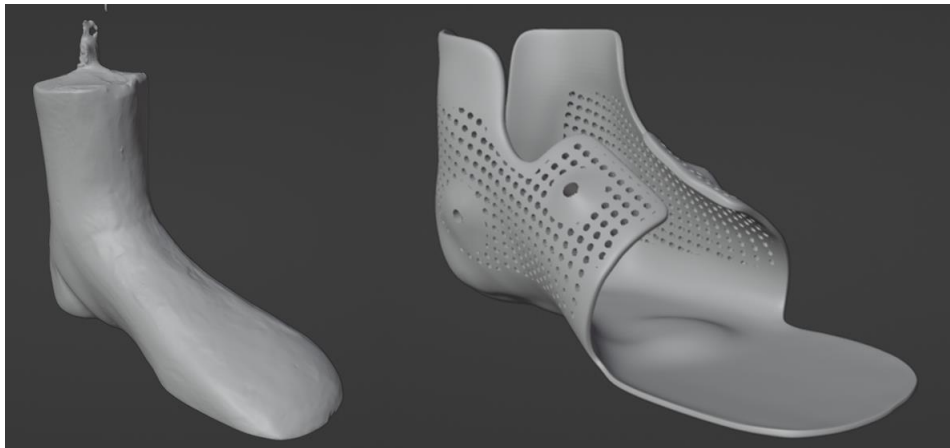

Fig. 1 Model of the patient's foot (left model), fitted AFO (right side)

CHAPTER 2 Structures with two-directional bending stiffness structures

Children with cerebral palsy often struggle with dorsiflexion of the foot and suffer from a foot drop. That means the first contact with the ground is with the toes instead of the heel. To fix this problem we will try to implement a two directional bending stiffness structures that would be stiff enough in one bending direction to help with stabilizing the foot and flexible enough in the other direction to ensure physiological flexion of your toes during the last part of the standing phase.[2]
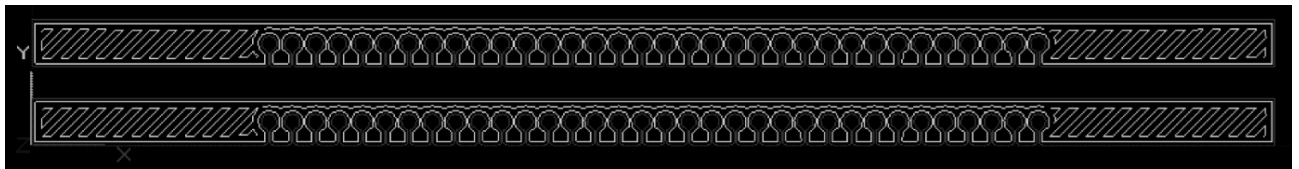

Fig. 2 Structures with two directional bending stiffness

CONCLUSION

3D printed orthosis are much more complex than manually manufactured AFOs. So far, we have figured out an automatized process of making a fitted 3D model of AFO. In the future there will be gait analysis experiments of healthy children and children with cerebral palsy. We will compare the change of gait pattern of disabled children from the state of not wearing AFO to wearing AFO relative to healthy children gait pattern.

ACKNOWLEDGMENT

LITERATURE

[1] ROMKES, Jacqueline a Reinald BRUNNER. Comparison of a dynamic and a hinged ankle–foot orthosis by gait analysis in patients with hemiplegic cerebral palsy. Gait and Posture. 2002, 15(1), 18-24.

[2] WRIGHT, Ed a Sally A. DIBELLO. Principles of Ankle-Foot Orthosis Prescription in Ambulatory Bilateral Cerebral Palsy. Physical Medicine and Rehabilitation Clinics of North America. 2020, 31(1), 69-89. ISSN 10479651.

Láka ťa elektromobilita? Staň sa súčasťou nášho R&D tímu v Schaeffler Kysuce

V Schaeffler Kysuce staviame moderné výskumné a vývojové centrum, ktoré bude prinášať inovatívne riešenia v oblasti elektromobility pre automobilky z celého sveta.

Už dnes naši kolegovia vyvíjajú kompletné integrované elektrické pohonné systémy. A neskôr to budú aj mechatronické riešenia pre autonómne riadenie vozidiel.

Výnimočnosť nášho nového centra podčiarkuje aj fakt, že viaceré riešenia, ktoré naši kolegovia navrhnú, sa budú na Kysuciach aj vyrábať.

Pridať sa k nám môžeš už teraz!
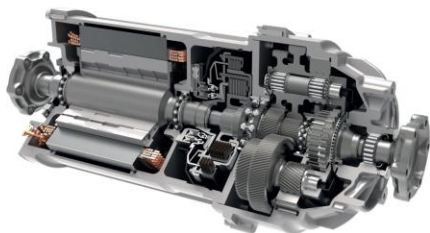
Veríme, že možnosť vyvíjať technologické riešenia pre udržateľnú mobilitu, ktoré dokážu zvýšiť dojazd a bezpečnosť vozidiel, bude motiváciou pre mnohé mladé talenty, ako si aj ty.

Túto príležitosť si nemôžeš nechať ujsť!

Benefity

Naši zamestnanci si môžu vybrať zo širokej škály atraktívnych benefitov.

- Jazykové kurzy
- Vzdelávanie a rozvoj talentov
- Finančné bonusy
- Stabilita nadnárodnej spoločnosti
- Odborný a kariérny rast

SCHAEFFLER

- Pružná pracovná doba a home office
- 37,5 hod. pracovný týždeň
- Odmena za zlepšovacie návrhy
- Sociálne príspevky
- Atraktívne odmeňovanie

Kontakt

Ak sa chceš dozvedieť viac, navštív našu stránku
https://emobility-schaeffler.sk

Aktuálny zoznam voľných pozícií nájdeš na:
jobs.schaeffler.com
www.emobility-schaeffler.sk/kariera

Na tvoje otázky radi odpovieme aj telefonicky na
+421 910 867 840

Zaujali sme ťa? Neváhaj a prihlás sa!

We pioneer motion

Naštartuj svoju kariéru v Schaeffler

KTO SA CHCE OTOČIŤ NA MIESTE, MUSÍ MYSLIEŤ INAK AKO OSTATNÍ.

Daj nám o sebe vedieť

Schaeffler – spoločnosť s perspektívou!

Skupina Schaeffler ako popredný svetový dodávateľ pre automobilový a ostatný priemysel je už 75 rokov priekopníkom vynálezov a vývoja v oblastiach pohybu a mobility. Vďaka inovatívnym technológiám, produktom a službám pre elektromobilitu, pohonom efektívnym z hľadiska CO_2, Priemyslu 4.0, digitalizácii a obnoviteľnej energii je spoločnosť spoľahlivým partnerom pre efektívnejší, inteligentnejší a udržateľnejší pohyb a mobilitu.
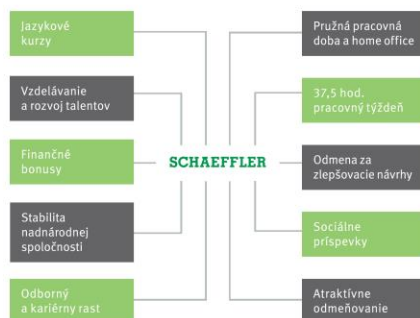
už **30** rokov na Slovensku

Schaeffler so svojimi dvoma závodmi v Skalici a Kysuckom Novom Meste a 9000 zamestnancami, patrí k najväčším zamestnávateľom na Slovensku.

Schaeffler Kysuce vyvíja a vyrába riešenia pre oblasť elektromobility pre motory, prevodovky a podvozky. Ide napríklad o modulárnu, vysoko integrovanú technologickú platformu pre elektromotory, hybridné pohonné jednotky, plne elektrické nápravy, elektrické parkovacie brzdy alebo mechatronické stabilizátory náklonu vozidla. Jeho súčasťou bude aj nové výskumno-vývojové centrum, ktoré sa bude špecializovať na nové technologické riešenia v oblasti mobility pre svetové automobilové značky.

Výrobné portfólio **Schaeffler Skalica** tvoria ložiskové riešenia, kliety i krúžky, lineárne a priame pohony, servisné prvky, produkty na údržbu výrobných liniek a inteligentné monitorovacie systémy. Súčasťou závodu je aj špeciálne mechatronické laboratórium, výskum a vývoj nových riešení.

Prepoj svoje vedomosti s praxou

Vyber si z našej ponuky a začni kariéru s nami

Si absolvent VŠ v odboroch mechatronika, elektrotechnika, strojárstvo so zameraním na programovanie, fyzika, alebo iného podobného zamerania? Komunikuješ aktívne anglicky (slovom i písmom)? Zaujímaš sa o novinky v oblasti automotive a návrhu systémov pre elektrické a hybridné vozidlá?

Čo ponúkame?
Uplatnenie v nasledovných oblastiach:

- návrh systémov,
- tvorba dizajnu,
- vývoj softvéru,
- požiadavkové inžinierstvo,
- simulácie komponentov a systémov,
- skúšobníctvo a test manažment,
- projektové riadenie,
- analýzy nákladov a iné oblasti pre podporu projektov.

Čaká ťa:

- práca s najmodernejšími technológiami v medzinárodnom tíme,
- odborné zaškolenie seniornými kolegami,
- jazykové vzdelávanie,
- sebarealizácia na zodpovednej pozícii s možnosťou odborného a profesijného rastu.

Schaeffler Kysuce
Dr. G. Schaefflera 1
02401 Kysucké Nové Mesto
SchaefflerKysuce@schaeffler.com

Schaeffler Skalica
Dr. G. Schaefflera 1
90901 Skalica
SchaefflerSkalica@schaeffler.com

www.emobility-schaeffler.sk
www.schaeffler.sk

PROČ VYUŽÍVAT SOFTWARE ANSYS

Díky Ansys simulacím budete inovovat rychleji a efektivněji

SLUŽBY OD SVS FEM

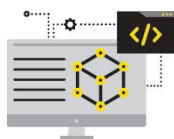## Spolupracujte s námi na svých projektech, ve vědě i výzkumu

UDÁLOSTI

Ansys online a prezenčně jako student i jako expert

Proč Ansys od SVS FEM?

+ Expertní technická podpora
+ Více jak 30 let zkušeností a důvěry našich zákazníků
+ Oddělení vlastního vývoje ACT – Ansys rozšíření na míru pro Vaši společnost

Software a hardware pro inovace

Expertní technická podpora

Změříme to za Vás

Vypočítáme to za Vás

Pořádáme:

- **Školení**
  Naučte se Ansys
- **Semináře**
  Zdokonalte se v Ansys
- **Webináře**
  Pochopte proč Ansys
- **Konference**
  Když je Ansys Vaše práce

- **Soutěže**
  Vyhrajte s Ansys
- **Ansys Update**
  Buďte první u novinek
- **Ansys Academy**
  Certifikujte se online
- **Ansys Advisors**
  Buďte ambasadorem

Reference:

BOSCH   Danfoss   Honeywell

Garrett   ZF   SIGMA   Continental
ADVANCING MOTION

Nevíte, jak na měření nebo výpočet?

Jsme připraveni jít do toho s Vámi. V každé fázi Vaší cesty za inovacemi jsme schopni poskytnout odborné poradenství a rychle pro Vás najít nejvhodnější řešení.

Co kdybyste začali tím, že Ansys jen zdarma vyzkoušíte?

www.svsfem.cz   Vyzkoušejte Ansys

TESTEK, a.s., technická služba technickej kontroly a znalecká organizácia v odbore cestná doprava, ponúka tieto služby:
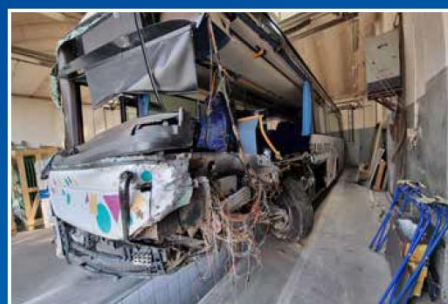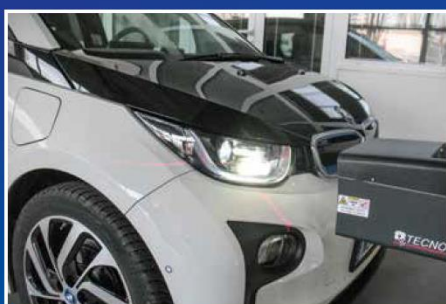
- ◼ vypracovanie znaleckých posudkov a expertíz v odbore cestná doprava,
- ◼ kalkulácia nákladov na opravu vozidla,
- ◼ odborné posúdenie technického stavu vozidla,
- ◼ meranie a kontrola odrazivosti reflexných značení,
- ◼ mobilná aplikácia na čítanie chybovej pamäte OBD a meranie pozdĺžnej dynamiky vozidla TESTEK expert,
- ◼ odborná príprava a skúšky z overenia znalostí o vozidlách podľa zákona č. 106/2018 Z. z.

Prevádzka:
Vajnorská 137
83104 Bratislava

Poštové spojenie:
P.O. Box 42
82017 Bratislava 217

Tel.: +421 2 546 51 311
e-mail: testek@testek.sk
web: www.testek.sk